Doctorate Program in Materials Science

PhD Thesis

Carbon-Based Atomically Dispersed Transition Metal Atom Electrocatalysts

Zhifu Liang

Director: Prof. Jordi Arbiol i Cobos

Co-Director: Prof. Andreu Cabot i Codina

Institut Català de Nanociència i Nanotecnologia (ICN2), CSIC & BIST

Institut de Recerca en Energia de Catalunya (IREC)

Department of Chemistry, Faculty of Sciences

Universitat Autònoma de Barcelona (UAB)
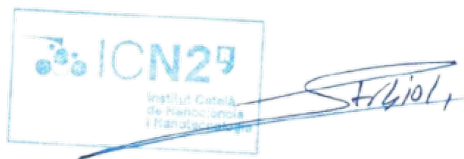
Jordi Arbiol i Cobos, ICREA Professor at Institut Català de Nanociència i Nanotecnologia (ICN2), CSIC & BIST, **Andreu Cabot i Codina**, ICREA Professor at Institut de Recerca en Energia de Catalunya (IREC)

CERTIFY

that Mr. **Zhifu Liang**, MSc in Coordination Chemistry, carried out the work entitled "**Carbon-Based Atomically Dispersed Transition Metal Atom Electrocatalysts**" under their direction and qualifies for the degree of Doctor in Materials Science.

And for that record, sign this certificate.

Prof. Jordi Arbiol i Cobos,   Prof. Andreu Cabot i Codina,

Zhifu Liang

Bellaterra, February 2022

Table of Content

Acknowledgments

I will finish my PhD study in UAB with the completion of this thesis. Along the way, I studied far away from my hometown, and especially encountered the Covid-19 pandemic in the middle. The completion of this thesis would have not been possible without the help of many people. I would like to express my thanks to all those who gave me their support during my PhD thesis.

First of all, I would like to express my deepest gratitude to my supervisor, ICREA Prof. Dr. Jordi Arbiol at Institut Català de Nanociència i Nanotecnologia (ICN2) for accepting me to pursue my PhD at ICN2 and UAB in Barcelona. Thank you so much for letting and supporting me in doing my favorite research topics, and giving me the freedom to follow my own feelings. Thanks a lot for your support on my research work and your patience and constructive corrections and suggestions for my papers and PhD thesis. Thanks for your excellent guidance, advice and support for my research during my PhD study, which pave me the way to be a good researcher and will be helpful for my future scientific career. It has been a great honor to learn from you to be a positive and optimistic researcher and mentor in my future. I also appreciate the relaxed research environment in your research group so that I could well balance my work and life.

I would like to express my thanks to ICREA Prof. Dr. Andreu Cabot at Institut de Recerca en Energia de Catalunya (IREC). Thanks a lot for accepting to be my co-supervisor and giving me the opportunity to work in your lab to conduct my research work. Thanks a lot for your patience and constructive corrections and suggestions for my papers and PhD thesis. Thanks a lot for your great help and excellent guidelines on my experiments. I have learned a lot from your attentive, logical and rigorous attitude for research, which will also pave my way to be a good researcher in my future.

Thanks to all members in GAe⁻N group (ICN2), Pengyi, Sara, Jérémy, Chiara, Ying, Xu, Ting, Marc and Christian, they gave me a friendly and comfortable scientific

1

Finally, I am especially grateful to my parents, thank you for your support and understanding along the way. You will always be my strong backing and my eternal warm harbour. Thank you for your nurturing grace, all the achievements are inseparable from your support and encouragement. As in an ancient Chinese poem said, "谁言寸草心，报得三春晖" (such kindness of warm sun, can't be repaid by grass). Thanks a lot to my sister and my brother for their support, especially taking care of the family when I've been away for three years and haven't come home.

Thanks to my dearest Liqun for her love, accompany and encouragement in the past years.

Abstract - English

Currently, environmental pollution and energy shortages are getting more and more attention from the international community. Most of the society's production uses catalysts, so developing high-efficiency catalysts is an effective way to solve the environmental and energy problems. Atomically dispersed metal atom catalysts are a new type of catalysts with dispersion of metal atoms, and unique electronic and geometry structure, which have exhibited excellent catalytic performance in lithium-sulfur batteries, electrochemical CO_2 reduction, electrocatalytic conversion of organic molecules and other important catalytic reactions. The design and synthesis of efficient atomically dispersed metal atom catalysts and the study of their mechanisms have become a hot frontier in the field of catalysis. This thesis is focused on developing novel atomically dispersed metal atom catalysts based on porous two-dimensional covalent organic frameworks and applied to lithium-sulfur batteries and electrocatalysis, and also explore the relationship between structure and catalytic performance at the molecular level, and provide strategies for designing efficient atomically dispersed metal atom catalysts at the atomic scale.

The research context of this dissertation is divided into 4 parts:

Part 1: A two-dimensional (2D) layered organic material, C_2N, loaded with atomically dispersed iron as effective sulfur host in LSBs. X-ray absorption fine spectroscopy and density functional theory calculations proved the structure of the atomically dispersed Fe/C_2N catalysts. As a result, Fe/C_2N-based cathodes demonstrated a significantly improved rate performance and long-term cycling stability. Fe/C_2N-based cathodes displayed initial capacities up to 1540 mAh g^{-1} at 0.1 C and 678.7 mAh g^{-1} at 5 C, while retaining 496.5 mAh g^{-1} after 2600 cycles at 3 C with a decay rate as low as 0.013% per cycle. Even at a high sulfur loading of 3 mg cm^{-2}, They deliver remarkable specific capacity retention of 587 mAh g^{-1} after 500 cycles at 1 C. This work provides a rational structural design strategy for the

development of high-performance cathodes based on atomically dispersed catalysts for lithium-sulfur batteries.

Part 2: A highly efficient 2D nickel organic framework containing a large density of highly dispersed salophen NiN_2O_2 active sites toward electrochemical CO_2RR to methanol. We demonstrated that by tuning the ligand environment of the salophen NiN_2O_2, the electrocatalytic activity of the material toward CO_2 reduction could be significantly improved. We particularly proved that by introducing a carbonyl group at the ligand environment of the Ni active sites, the electrochemical CO_2 reduction activity was highly promoted and its product selectivity reached a high Faradaic efficiency of 27 % toward the production of methanol at -0.9 V vs RHE. The salophen-based π-d conjugated metal-organic framework presented here thus provided the best performance toward CO_2 reduction to methanol among the previously developed nickel-based electrocatalysts.

Part 3: The nickel organic framework in **part 2** was expanded to other electrocatalytic applications, which exhibited outstanding catalytic activity and durability toward the oxidation of methanol (CH_3OH), ethanol (CH_3CH_2OH) and benzyl alcohol ($C_6H_5CH_2OH$), the smaller molecule exhibited higher catalytic performance. These outstanding electrocatalytic activities for alcohol electrooxidation were attributed to the presence of the carbonyl group in the ligand chemical environment, which enhances the adsorption for alcohol, as revealed by density functional theory calculations. Our work not only introduced a new atomically dispersed Ni-based catalyst, but also demonstrated a new strategy for designing and engineering high-performance catalysts through the tuning of their chemical environment.

Part 4: A novel tetraaza[14]annulene (TAA) organic framework synthesized by a non-template method was reported for the first time. The framework was used as ligand to construct a cobalt-based complex (Poly-TAA-Co) with CoN4 structure which was supported on multi-wall carbon nanotubes (CNTs) to work as an atomically dispersed efficient molecular based electrocatalyst for the CO_2 reduction

5

reaction (CO_2RR). The resulting catalyst (Poly-TAA-Co-CNT) exhibited excellent performance, with a 90% CO faradaic efficiency, a low overpotential (390 mV) and good stability in 0.5 M $KHCO_3$ aqueous solution. Density functional theory calculations confirmed the Co-TAA to be excellent active sites for electrocatalytic CO_2RR. This work not only inspired the design of novel organic frameworks based on TAA macromolecules, but also paved the way to the development and application of new molecular-based catalysts for electrocatalytic CO_2RR.

Resum - Català

Actualment, la contaminació ambiental i l'escassetat d'energia reben cada cop més atenció per part de la comunitat internacional. La major part de la producció de la nostra societat utilitza catalitzadors, de manera que el desenvolupament de catalitzadors d'alta eficiència és una manera eficaç de resoldre els problemes ambientals i energètics. El catalitzador d'àtoms metàl·lics dispersos atòmicament és un nou tipus de catalitzador amb dispersió d'àtoms metàl·lics, una estructura electrònica i geomètrica única, que ha mostrat un excel·lent rendiment catalític en les bateries de sofre - liti, en la reducció electroquímica de CO_2, la conversió electrocatalítica de molècules orgàniques i en d'altres reaccions catalítiques importants. El disseny i la síntesi d'un catalitzador eficient basat en àtoms metàl·lics dispersos atòmicament i revelar el seus mecanismes s'han convertit en una frontera de gran interès en el camp de la catàlisi. Aquesta tesi se centra a desenvolupar nous catalitzadors d'àtoms metàl·lics dispersos atòmicament basats en marcs orgànics covalents bidimensionals porosos i aplicats a bateries de sofre - liti i electrocatàlisi, i també explorar la relació entre estructura i rendiment catalític a nivell molecular, proporcionar estratègies per dissenyar a escala atòmica catalitzadors eficients basats en àtoms metàl·lics atòmicament dispersos.

El context de recerca d'aquesta tesi es divideix en 4 parts:

Part 1: Un material orgànic en capes bidimensionals (2D), C_2N, carregat amb ferro dispersat atòmicament com a hoste efectiu pel sulfur en bateries de sofre - liti. L'espectroscòpia fina d'absorció de raigs X i els càlculs teòrics de densitat funcional (DFT) demostren l'estructura dels catalitzadors Fe/C_2N dispersos atòmicament. Com a resultat, els càtodes basats en Fe/C_2N demostren un rendiment de velocitat significativament millorat i una estabilitat de cicle a llarg termini. Els càtodes basats en Fe/C_2N mostren capacitats inicials de fins a 1540 mAh g^{-1} a 0,1 C i 678,7 mAh g^{-1} a 5 C, mentre que conserven 496,5 mAh g^{-1} després de 2600 cicles a 3 C amb una taxa de decadència tan baixa com 0,013 % per cicle. Fins i tot amb una càrrega

elevada de sofre de 3 mg cm^{-2}, ofereixen una retenció de capacitat específica notable de 587 mAh g^{-1} després de 500 cicles a 1 C. Aquest treball proporciona una estratègia de disseny estructural racional per al desenvolupament de càtodes d'alt rendiment basats en catalitzadors dispersos atòmicament per a bateries de sofre - liti.

Part 2: Un marc orgànic de níquel 2D altament eficient que conté una gran densitat de llocs actius de salofèn NiN$_2$O$_2$ altament dispersos per tal de fer el pas de CO$_2$RR electroquímic a metanol. Demostrem que ajustant l'entorn dels lligands del salofèn NiN$_2$O$_2$, es pot millorar significativament l'activitat electrocatalítica del material cap a la reducció de CO$_2$. En particular, demostrem que mitjançant la introducció d'un grup carbonil a l'entorn de lligands dels llocs actius de Ni, l'activitat electroquímica de reducció del CO2 està molt promoguda i la seva selectivitat arriba a una alta eficiència Faradaica del 27% per la producció de metanol a -0,9 V vs RHE. . El marc organo-metàl·lic conjugat π-d basat en salofèn que es presenta aquí ofereix així el millor rendiment cap a la reducció de CO$_2$ a metanol d'entre tots els electrocatalitzadors basats en níquel desenvolupats anteriorment.

Part 3: El marc orgànic de níquel de la **part 2** es va ampliar a altres aplicacions electrocatalítiques. S'ha trobat que presenta una activitat catalítica i una durabilitat excepcionals cap a l'oxidació de metanol (CH$_3$OH), etanol (CH$_3$CH$_2$OH) i alcohol benzílic (C$_6$H$_5$CH$_2$OH), la molècula més petita presenta un efecte catalitzador de més alt rendiment. Aquestes activitats electrocatalítiques destacades per a l'electrooxidació de l'alcohol s'atribueixen a la presència del grup carbonil a l'entorn químic del lligand, que millora l'adsorció de l'alcohol, tal com revelen els càlculs teòrics de densitat funcional (DFT). El nostre treball no només introdueix un nou catalitzador basat en Ni dispersat atòmicament, sinó que també demostra una nova estratègia per dissenyar catalitzadors d'alt rendiment mitjançant l'ajust del seu entorn químic.

Part 4: Es va reportar per primera vegada la síntesi d'un nou marc orgànic de tetraaza[14]annulene (TAA) mitjançant un mètode sense plantilla. El marc s'utilitza com a lligand per construir un complex basat en cobalt (Poly-TAA-Co) amb estructura CoN4 que es recolza en nanotubs de carboni de paret múltiple (CNT) per

funcionar com un electrocatalitzador molecular eficient basat àtoms dispersats per a la reacció de reducció de CO_2 (CO_2RR).

El catalitzador resultant (Poly-TAA-Co-CNT) presenta un rendiment excel·lent, amb una eficiència faradaica del 90% de CO, un sobrepotencial baix (390 mV) i una bona estabilitat en solució aquosa de $KHCO_3$ 0,5 M. Els càlculs teòrics de densitat funcional van confirmar que el Co-TAA tenia excel·lents llocs actius per al CO_2RR electrocatalític. Aquest treball no només inspira el disseny de nous marcs orgànics basats en macromolècules TAA, sinó que també obre el camí per al desenvolupament i l'aplicació de nous catalitzadors de base molecular per al CO_2RR electrocatalític.

Resumen - Castellano

Actualmente, la contaminación ambiental y la escasez de energía están recibiendo cada vez más atención por parte de la comunidad internacional. La mayor parte de la producción de nuestra sociedad utiliza catalizadores, por lo que desarrollar catalizadores de alta eficiencia es una forma eficaz de resolver los problemas ambientales y energéticos. Los catalizadores basados en átomos metálicos dispersos atómicamente son un nuevo tipo de catalizadores con dispersión de átomos metálicos, estructura electrónica y geométrica única, que ha mostrado un excelente rendimiento catalítico en baterías de litio-azufre, reducción electroquímica de CO_2, conversión electrocatalítica de moléculas orgánicas y otras reacciones catalíticas importantes. El diseño y la síntesis de catalizadores eficientes basados en átomos metálicos dispersos atómicamente y revelar su mecanismo se han convertido en una frontera de gran interés en el campo de la catálisis. Esta tesis se centra en el desarrollo de nuevos catalizadores de átomos metálicos dispersos atómicamente basados en marcos orgánicos covalentes bidimensionales porosos y aplicados a baterías de litio-azufre y electrocatálisis, y también explora la relación entre la estructura y el rendimiento catalítico a nivel molecular, y proporciona estrategias para el diseño atómicamente eficiente de catalizadores de átomos metálicos dispersos a escala atómica.

El contexto de investigación de esta tesis se divide en 4 partes:

Parte 1: Un material orgánico en capas bidimensionales (2D), C_2N, cargado con hierro disperso atómicamente como huésped efectivo de azufre en baterías de litio-azufre. La espectroscopia fina de absorción de rayos X y los cálculos teóricos de densidad funcional prueban la estructura de los catalizadores de Fe/C_2N dispersos atómicamente. Como resultado, los cátodos basados en Fe/C_2N demuestran un rendimiento de velocidad significativamente mejorado y una estabilidad cíclica a largo plazo. Los cátodos basados en Fe/C_2N muestran capacidades iniciales de hasta 1540 mAh g^{-1} a 0,1 C y 678,7 mAh g^{-1} a 5 C, al tiempo que retienen 496,5 mAh g^{-1} después de 2600 ciclos a 3 C con una tasa de caída tan baja como 0,013 % por ciclo.

Incluso con una alta carga de azufre de 3 mg cm^{-2}, ofrecen una retención de capacidad específica notable de 587 mAh g^{-1} después de 500 ciclos a 1 C. Este trabajo proporciona una estrategia de diseño estructural racional para el desarrollo de cátodos de alto rendimiento basado en catalizadores dispersos atómicamente para baterías de litio-azufre.

Parte 2: Un marco orgánico de níquel 2D altamente eficiente que contiene una gran densidad de sitios activos de salofeno NiN$_2$O$_2$ altamente dispersos hacia CO$_2$RR electroquímico a metanol. Demostramos que al ajustar el entorno del ligando del salofeno NiN$_2$O$_2$, la actividad electrocatalítica del material hacia la reducción de CO$_2$ puede mejorarse significativamente. En particular, demostramos que al introducir un grupo carbonilo en el entorno del ligando de los sitios activos de Ni, la actividad electroquímica de reducción de CO$_2$ se promueve en gran medida y su selectividad alcanza una alta eficiencia Faradaica, del 27 %, hacia la producción de metanol a -0.9 V vs RHE. El marco orgánico-metálico conjugado π-d basado en salofeno presentado aquí proporciona el mejor rendimiento hacia la reducción de CO$_2$ a metanol entre todos los electrocatalizadores basados en níquel desarrollados previamente.

Parte 3: El marco orgánico basado en níquel de la **parte 2** se amplió a otras aplicaciones electrocatalíticas, donde exhibe una actividad catalítica y una durabilidad sobresalientes hacia la oxidación de metanol (CH$_3$OH), etanol (CH$_3$CH$_2$OH) y alcohol bencílico (C$_6$H$_5$CH$_2$OH), la molécula más pequeña exhibe una mayor capacidad catalítica y rendimiento. Estas actividades electrocatalíticas sobresalientes para la electrooxidación del alcohol se atribuyen a la presencia del grupo carbonilo en el entorno químico del ligando, lo que mejora la adsorción del alcohol, como lo revelan los cálculos teóricos de densidad funcional. Nuestro trabajo no solo presenta un nuevo catalizador basado en Ni disperso atómicamente, sino que también demuestra una nueva estrategia para el diseño y la ingeniería de catalizadores de alto rendimiento a través del ajuste de su entorno químico.

Parte 4: Se reportó por primera vez la síntesis de un nuevo marco orgánico de tetraaza[14]anuleno (TAA) mediante un método sin plantilla. El marco se utiliza

como ligando para construir un complejo basado en cobalto (Poly-TAA-Co) con estructura CoN4 que se apoya en nanotubos de carbono (CNT) de pared múltiple para funcionar como un electrocatalizador de base molecular eficiente dispersado atómicamente para la reacción de reducción de CO_2 (CO_2RR). El catalizador resultante (Poly-TAA-Co-CNT) muestra un excelente rendimiento, con una eficiencia faradaica de CO del 90 %, un sobrepotencial bajo (390 mV) y una buena estabilidad en solución acuosa de $KHCO_3$ 0,5 M. Los cálculos teóricos de densidad funcional confirmaron que los Co-TAA son excelentes sitios activos para el CO_2RR electrocatalítico. Este trabajo no solo inspira el diseño de nuevos marcos orgánicos basados en macromoléculas TAA, sino que también allana el camino para el desarrollo y la aplicación de nuevos catalizadores de base molecular para CO_2RR electrocatalítico.

Abbreviations

SACs	single-atom catalysts
DACs	double atom catalyst
ADMACs	atomically dispersed metal atom catalysts
STEM	
EELS	
HAADF	high-angle annular dark-field
AC	aberration-corrected
MOFs	Metal organic frameworks
2D	two dimension
COFs	covalent organic frameworks
PCMs	porous carbon matrices
ALD	atomic layer deposition
PRS	photochemical reaction strategy
CNTs	carbon nanotubes
Pc	phthalocyanine
XAFS	X-ray absorption fine structure
STM	scanning tunneling microscopy
FT-IR	fourier-transform infrared spectroscopy
SEM	Scanning electron microscopy
EDS	energy-dispersive X-ray spectroscopy
SPM	scanning probe microscopy
AFM	atomic force microscopy
NMR	Nuclear Magnetic Resonance
LSBs	Lithium-sulfur batteries
LiPSs	long-chain lithium polysulfides
DFT	density functional theory
CO_2RR	carbon dioxide reduction reaction
HER	hydrogen evolution reaction

FE	faradaic efficiency
AOR	alcohol oxidation reaction
ORR	oxygen reduction reaction
OER	oxygen evolution reaction
BOR	benzyl alcohol oxidation reaction
EIS	electrochemical impedance spectroscopy
CV	cyclic voltammetry
PBE	Perdew-Burke-Ernzerhof
PAW	project augmented wave
E_{ads}	adsorption energy
HRTEM	high resolution transmission electron microscopy
FFT	fast fourier transform
XRD	powder X-ray diffraction
TGA	thermogravimetric analysis
XPS	X-ray photoelectron spectroscopy
WT	wavelet transform
BET	Brunauer–Emmett–Teller
CN	coordination numbers
CP	chronopotentiometry
CV	cyclic voltammograms
TABQ	Tetramino-benzenequinone
TAB	1,2,4,5-Benzenetetramine tetrahydrochloride
HBC	2,5-dihydroxyterephthalaldehyde

Chapter 1

Introduction: Atomically Dispersed Metal Atom Catalysts

1.1 Introduction

Catalysis science is not only a very important topic of scientific research, but also it is closely related to all fields of human society. What's more, it is also a major contributor to the world economy.[1] According to the reports, 30% of global production is related to catalysis and about 90% of the chemical manufacturing involves at least one catalytic process. [2-4] At present, with the progress of society, there is an exacerbated consumption and depletion of traditional fossil energy. The increasingly serious global energy shortage and environmental pollution are two major problems facing today's society, which can be mitigated with the development of efficient catalysts. We need more efficient catalysts in energy technologies to meet our requirements for low cost, high output and sustainable development. Besides, environmental protection also requires high-performance catalysts able to decompose the rapidly increasing industrial waste, for instance. Furthermore, we also need more sensitive analytical methods to detect the environment more accurately, which is also closely related to the application of catalysts. [5-6]

The main goal in the field of catalysis research is to develop efficient, active, selective and stable catalysts.[7] We typically differentiate between two types of catalysts, homogeneous and heterogeneous catalysts. Homogeneous catalysts have the advantage of high activity and high selectivity in the catalytic process due to the nature of dispersed active sites. However, since it is not easy to recover the homogeneous catalyst from the system, the catalyst cannot be recycled, which may increase the amount of waste and even pollute the environment. On the contrary, heterogeneous catalysts do not have the problem of causing waste, but they usually have the disadvantages of low selectivity and low atom utilization. Supported metal catalysts may have excellent catalytic performance, such as high activity and selectivity. Therefore, they are widely used in many important industrial catalytic reactions. The catalytic performance of the supported catalyst is closely related to the size of the metal active component on the carrier. The high activity of the supported metal cluster catalyst is attributed to the presence of its metal active components in

the form of highly dispersed nanoclusters on a carrier with a high specific surface area. This large dispersion allows making full use of the catalytic active sites, thereby improving the reaction activity and metal atom utilization. [8-12] To optimize the catalytic activity of each metal atom on the supported metal catalyst, researchers continue to reduce the particle size of the active metal. The size of the catalyst can affect its catalytic behavior. This phenomenon is called the size effect of the nanocatalyst. [13] The coordination environment and electronic structure of the catalyst surface atoms will change as the size of the catalyst decreases, especially in certain specific nanoscale size ranges. In the past, many studies have found that sub-nano clusters have better catalytic activity or selectivity than nano-scale particles.[14-19] Theoretically, the limit of the dispersion of supported metal catalysts is that the metal is uniformly distributed on the support in the form of single atoms. This is not only an ideal state for supported metal catalysts, but also allows the study of catalytic processes at the atomic level.

In the reaction process, for the high loading metal catalysts, only a few metal active components play the role of catalytic active sites for the traditionally supported metal catalysts. However, in comparison, all-metal atoms in single-atom catalysis will work as catalytic active centers, so that the atomic utilization rate is close to 100%. [20-22] Especially in the case of noble metal catalysts, their extensive use undoubtedly increases the cost of the processes, which makes them less interesting for their large-scale utilization in industrial production. Therefore, to maximize the catalytic efficiency of precious metals and reduce manufacturing costs, the development of single-atom catalysts has become the primary choice for catalytic applications. Different from nano or sub-nano catalysts (**Figure 1.1**), when metal species are dispersed at the atomic scale, they show some novel properties, such as high surface area energy, quantum size effects, unsaturated coordination environment, interaction between metal and support and so on. It is precisely because of these characteristics that are significantly different from nano- and sub-nano particles that atomic-level dispersed catalysts have superior catalytic performance. [23]
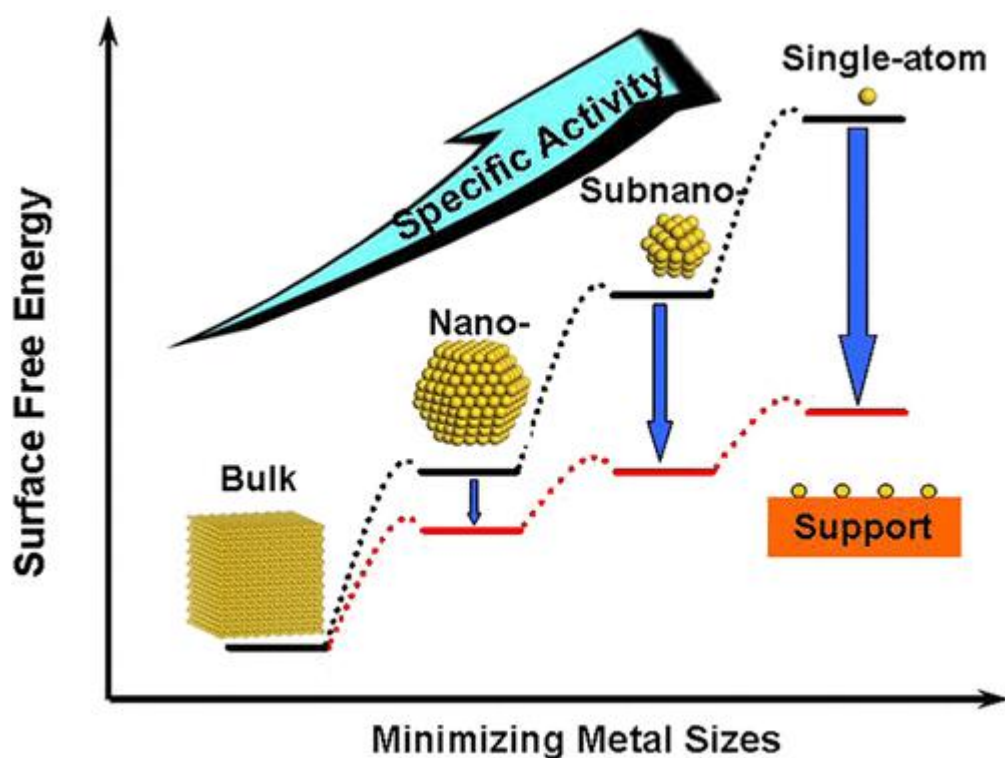
Figure 1.1 Schematic illustrating the changes of surface free energy and specific activity per metal atom with metal particle size and the support effects on stabilizing single atoms. [24]

Since 2011, when Zhang and his co-workers reported the synthesis of single platinum atom catalysts by loading Pt on the surface of FeO_x by co-precipitation method and proposed the concepts of single-atom catalyst (SAC),[25] atomically dispersed catalysts have become the frontier of catalysis research. They are a type of special supported catalyst, where the metal atom is atomically dispersed on the support (metal, metal oxide, carbon, molecular sieve). The atomically dispersed metal atom works as a catalytic active site, similar to the homogeneous catalyst, providing great potential for achieving high activity and selectivity in catalytic reactions and revealing the reaction mechanism. The atomically dispersed catalysts not only include the uniform characteristics of homogeneous catalysts, but also contain the characteristics of heterogeneous catalysts, such as stable and easy to be separated (recycled), so they become a bridge between homogeneous and heterogeneous catalysts.[26] According to the number of metal atoms in the metal active sites, the atomically dispersed metal atom catalysts can be categorized into single-atom catalysts, double-atom catalysts,

and metal nanocluster catalysts.

Currently, atomically dispersed catalysts exhibit important applications in many research fields, such as electrocatalysis,[27] photocatalysis,[28] thermocatalysis,[29] fine chemical synthesis,[30] fuel cells,[31] sodium-sulfur batteries,[32] zinc-air batteries, [33] and so on (**Figure 1.2**).
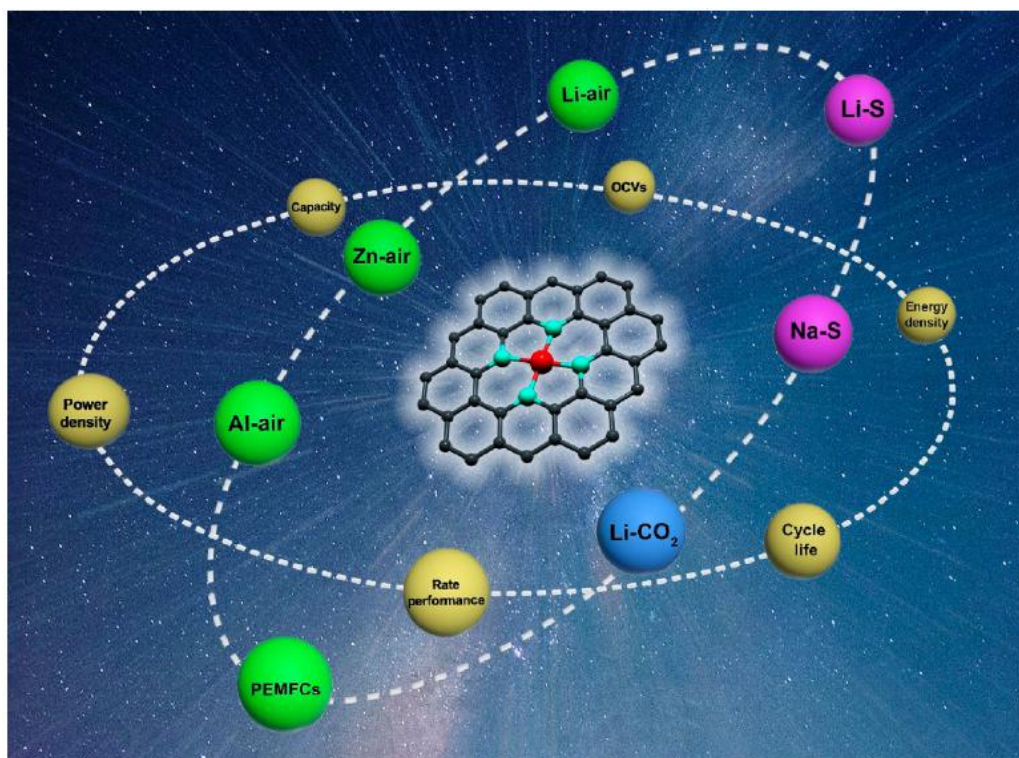
Figure 1.2 Atomically dispersed catalysts and their potential functions in next-generation electrochemical energy storage and conversion devices. [34]

1.2 Preparation of Atomically Dispersed Metal Atom Catalysts (ADMACs)

The most important thing to prepare atomically dispersed catalysts is to ensure that the metal atom is atomically dispersed on the surface of the support. To achieve the preparation of ADMACs stable and efficient, many design and synthesis strategies have been developed. The various strategies for synthesizing ADMACs will be introduced in the following.

1.2.1 Wet Chemistry Methods

Normally, the wet chemistry approaches contain co-precipitation,[25] impregnation,[35-36] photochemical reduction,[37] and so on. In the wet-chemistry routes, first, the metal precursors are anchored on different supports and then the process is followed by drying and annealing. At last, the atomically dispersed metal catalysts with uniformly active sites can be obtained after further reduction and activation. Although these methods still present some challenges, such as low loading content and poor dispersion of the metal active sites, wet-chemistry approaches have extensively been used as effective methods to prepare atomically dispersed metal atom catalysts. [38-39]
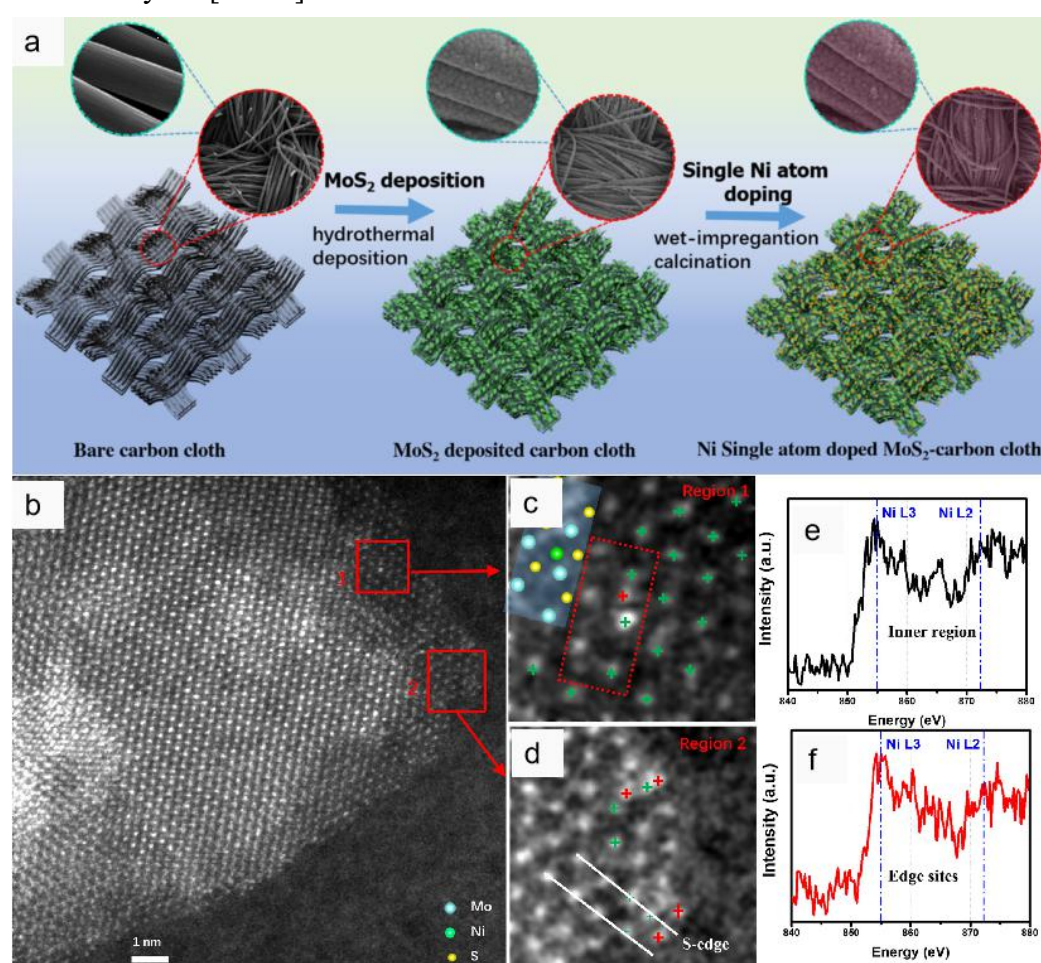
Figure 1.3. a) Schematic illustration of the preparation of Ni_{SA}-MoS_2 and Ni_C-MoS_2. b) Atomic resolution STEM images of Ni_{SA}-MoS_2/CC and corresponding higher-magnification views of (c) region 1 and (d) region 2; Ni atoms marked with a red cross, Mo atoms marked with a green cross) Corresponding Ni EELS spectra of (e) inner region 1 and (f) edge sites at region 2; (the atomic model of the red dashed

rectangle area in panel b are inserted at the top left corner with S atoms as yellow balls, Ni atoms as green balls, and Mo atoms as light-blue balls). [42]

As an example of this approach, Choi and co-workers synthesized an atomically dispersed Pt catalyst by using a conventional wet-impregnation of H_2PtCl_6 on the as-prepared S-doped zeolite carbon template.[40] The highly incorporated S-coordinated Pt with 5 % content was spatially constrained in the zeolite micropores. The mesoporous carbon nitride's cavities were used to anchor isolated Ru atoms, while the Ru atom was mobilized as demonstrated by first-principles calculations.[41] A second exemplifying work is that of Gu and co-workers, who reported a nickel atom decorated MoS_2 catalyst produced by immersing MoS_2/CC (carbon cloth) in a $NiCl_2$ ethanol solution and then applying a calcination step (**Figure 1.3**).[42] Metal clusters appeared if the annealing temperature exceeded 600 ℃ for 2 h. From **Figure 1.3b-c**, atomically dispersed Ni atoms could be loaded onto the hexagonal site of the basal plane and also in the S-edge by coordinating with neighboring S atoms.

1.2.2 MOFs derivative methods

Metal organic frameworks (MOFs) have become a hot type of material in the past decades. Their interest resides on their porous morphology with ultra-high surface area, modifiable surface, and abundant adjustable channels, [43] formed by self-assembly of metal ions or clusters and organic ligand through coordination interaction. MOFs not only can be used as atomically dispersed catalysts directly, but also work as good precursors to derivate atomically dispersed catalysts by pyrolysis. So far, MOFs and their derivative materials have been extensively explored in applications such as batteries, catalysis, hydrogen storage, gas separation and so on.[44] Compared to the atomically dispersed catalysts prepared by other methods, MOFs-based atomically dispersed catalysts have the following advantages:[45] 1) Their highly ordered porosity can significantly enhance the mass transfer during the reaction process and therefore increase the catalytic activity.[46] 2) MOFs have rich chemical adjustability and rich structure diversity, consequently, the structure of the fixed single-atom and double-atom metal active sites can be easily and precisely

controlled.[47] 3) MOFs-based catalysts can achieve a high loading content of metal active sites. 4) The metal species used as active sites can be widely diverse, and it is effective to realize the synergistic effect between chemical components.[48] For all these reasons, atomically dispersed catalysts supported by MOFs and their derivatives have great potential applications in energy conversion and catalysis. [49]

To prepare atomically dispersed catalysts based on MOFs, the first derivative method is to pyrolyze the as-prepared MOFs. Yang and his co-workers prepared a precursor with a core-shell structure PS@ZIF-8 by growing ZIF-8 with Zn metal node on carboxylated polystyrene nano (PS) spheres, then the precursor was annealed at high temperature to obtain the Zn monoatom dispersed catalyst HPC-800.[50] Yin et. al pyrolyzed the as-prepared dual atom ZnCo-ZIF MOFs precursor to remove Zn species and obtain the single cobalt atom catalysts Co SAs/N-C.[51] Wang and his co-workers proposed a coordinated-assisted strategy to accurately control the atomically dispersed Ruthenium atoms supported on nitrogen-doped porous carbon.[52] In their report, first, the UiO-66-NH$_2$ with abundant suspended-NH$_2$ groups was synthesized, then the Ru ion was introduced in the MOFs (UiO-66-NH$_2$) through the strong coordination interaction between Ru^{3+} and -NH$_2$. After the pyrolysis at high temperature and etching by the HF, the atomically dispersed Ru atom catalysts (Ru SAs/N-C) formed (**Figure 1.4**).
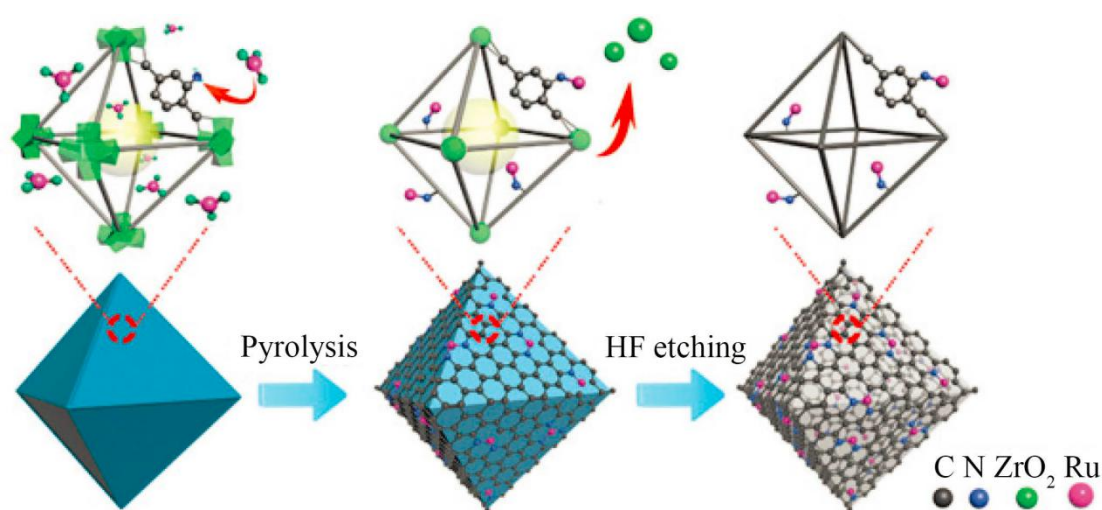
Figure 1.4 The preparation of Ru SAs/N-C catalysts. [52]

Even though the pyrolysis of MOFs is a universal method to prepare atomically

dispersed metal atom catalysts, it also has some drawbacks, such as it is hard to increase the metal loading, hard to control the coordination structure and ligand structure environment, it is difficult to prepare them in large quantities and so on. So, the best strategy is to use the MOFs as atomically dispersed metal catalysts directly. Recently, Ye and colleagues reported the dispersion of isolated Co active centers into MOF-525 with porphyrin unit.[53] The porphyrin structure unit can not only be used for anchoring the isolating active centers, but also to regulate the coordination geometry of the isolated Co centers which works as the co-catalysts for photocatalytic CO_2 reduction. Chen and co-workers developed tricycloquinazoline-based 2D conductive MOFs as promising atomically dispersed copper atom electrocatalysts for the reduction of CO_2 to methanol. [54] Chen et. al reported a MOF with efficient electrocatalytic oxygen reduction activity via tunning d–π Conjugation through the regulation of the ligand structure. [55]

1.2.3 Defect Immobilized Strategies

Defects appear widely in nanomaterials, such as caves, step edges and intrinsic defects, which are useful to immobilize atomically dispersed metal atoms and tune the geometric and electronic structure for enhancing the reaction activity. [56-57] Depending on the support, defect vacancies mainly consist of the absence of a metal cation, oxygen, sulfur, nitrogen, carbon and so on. Among them, the cation defect vacancy is widely used to trap the isolated metal atoms. Li et al. loaded isolated Pt atoms on the intrinsic defects of a TiO_2 support (Pt1/def-TiO_2) and demonstrated that this system could perform as an efficient photocatalyst. [58] Notably, the atomically dispersed Pt atoms promote the adjacent TiO_2 moieties to generate surface oxygen vacancies and Ti^{3+} defects, giving rise to an excellent performance for photocatalytic hydrogen evolution. DeRita and his colleagues utilized the anatase Ti defects to immobilize the Pt atoms to synthesize atomically dispersed Pt atom catalysts (Pt_{iso}/TiO_2).[59] Wan and co-workers prepared atomically dispersed Au catalysts (Au-SA/Def-TiO_2) with a Ti-Au-Ti structure by constructing the oxygen defect vacancy on the TiO_2 nanosheets to trap the isolated Au atoms (**Figure 1.5**). [60]

Carbon defects are also a common type of defects, which can provide effective anchoring sites for atomically dispersed metal atoms through the strong electron transfer between carbon and metal atoms. [61]
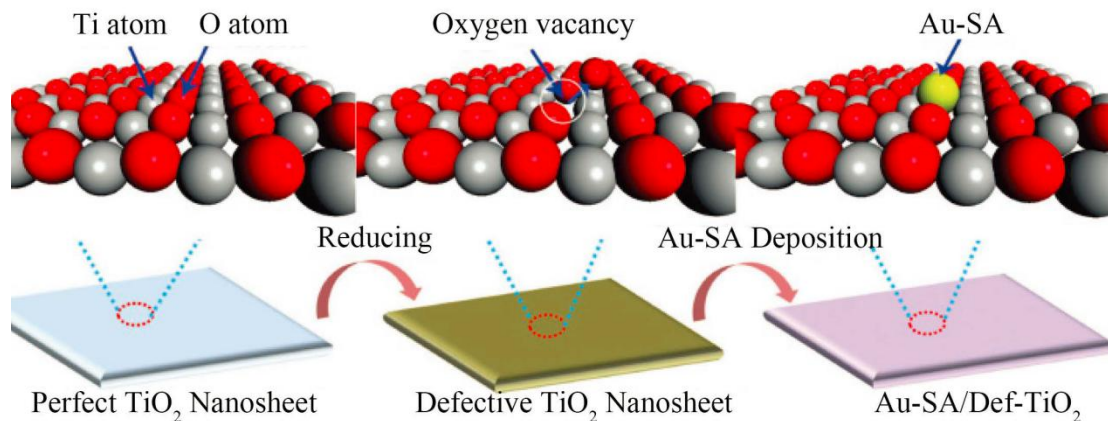
Figure 1.5. The preparation of Au-SA/Def-TiO$_2$ catalysts. [60]

1.2.4 Space Confinement Strategies

The main target of the space confinement strategy is to use the presence of cages in some materials to confine the atomically dispersed metal atoms. The common types of materials with a high density of cages are MOFs, COFs, zeolites, porous carbon matrices (PCMs) and so on, where the presence of a crystal structure with cages plays a very important role in the formation of atomically dispersed metal atom catalysts. Liu and his colleagues prepared single-atom catalysts (M-ISAS@Y, M=Pt, Pd, Ru, Rh, Co, Ni, Cu) supported on Y-zeolite through encapsulating metal diethylamine precursor in β cages and high temperature pyrolysis carbonization (**Figure 1.6**). [62] Chen and his co-workers reported the synthesis of a single tungsten atom catalyst by annealing and etching the precursor previously obtained by encapsulating the WCl5 into the cages of UIO-66-NH2 framework. [63]
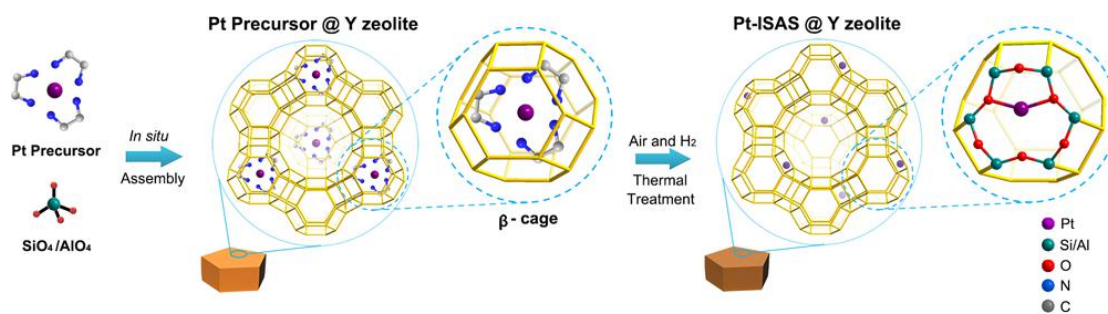
Figure 1.6. Schematics for the preparation of the M-ISAS@Y catalyst [62]

1.2.5 Photochemical Reaction Strategy

The photochemical reaction strategy (PRS) refers to the use of ultraviolet rays to irradiate the metal ion solution to effectively control the nucleation process between the reduced metal atoms, thereby preparing the atomically dispersed metal atom catalysts. The principle of PRS is to decrease the diffusion rate and local concentration, so that the reduced metal atoms exist in the form of atomic dispersion. Liu and his colleagues reported a photochemical strategy for the fabrication of an atomically dispersed Pd catalyst (Pd1/TiO$_2$) with a 1.5% content of Pd by irradiating the mixture of H$_2$PdCl$_4$ solution and ethylene glycolate (EG)-stabilized ultrathin TiO$_2$ nanosheets under low-density UV light in a xenon lamp (**Figure 1.7**). [37] The Pd$_1$/TiO$_2$ catalyst exhibited high catalytic activity and stability in hydrogenation of C=C bonds in aldehydes.
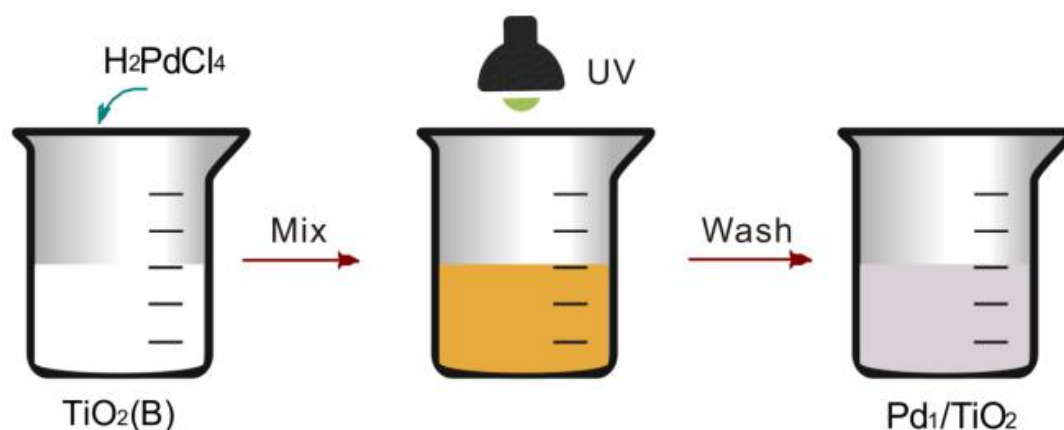
Figure 1.7. Scheme of the fabrication of Pd$_1$/TiO$_2$ catalyst by photochemical reaction strategy. [37]

1.2.6 Other Synthesis Strategies

In addition, to prepare atomically dispersed metal atom catalysts, some other synthesis methods have been developed. Here, a short introduction of the alternative synthesis approaches is summarized, including atomic layer deposition (ALD), ball milling, molecular catalysts anchored on the support.

ALD belongs to the high-vacuum physical deposition techniques, which can control the deposition of diverse structures on different substrates precisely. During the ALD process, the substrate is exposed to the vapor precursors. Sun and his co-workers reported the synthesis of platinum atoms anchored on a graphene nanosheet through the ALD method. [64] First, the graphene nanosheet was exposed to the Pt precursor of (methylcyclopentadienyl)-trimethylplatinum (MeCpPtMe3), then the precursor reacted with the oxygen on graphene nanosheet. After repeating the ALD with controllable cycles, the single-Pt atom dispersion on graphene nanosheets was obtained.

Ball milling methods, due to their simplicity, eco-friendliness and scalability have been widely applied for preparing catalytic materials.[65] Recently, the ball-milling approach has aroused interest for the direct preparation of atomically dispersed metal atom catalysts.[66,67] Bao et al. reported the synthesis of graphene confined metal-N4 catalysts via the combination of graphene nanosheets and iron phthalocyanine (FePc) by ball milling, which resulted in the reconstruction of the FePc in FeN4-embedded graphene nanosheet. [68]

More recently, molecular-based atomically dispersed metal atom catalysts with fine-tuned steric, electronic, electrostatic and chelating properties/abilities[69] have been engineered and optimized (e.g. through ligand modification) for electrocatalysis. Wu and his co-workers prepared a cobalt atom catalyst by immobilizing cobalt phthalocyanine on carbon nanotubes (CNT), which was used to reduce CO_2 to methanol with appreciable activity and selectivity. [70] Ni and co-workers reported the loading of a d–π metal coordination polymer on carbon nanotubes by π–π packing interaction to form a cobalt-based SAC for an efficient oxygen reduction reaction. Su

et al. obtained the anchoring of cobalt phthalocyanine on carbon nanotubes by chemical bond linkage, which also works as electrocatalysts for CO_2 reduction (**Figure 1.8**). [71]
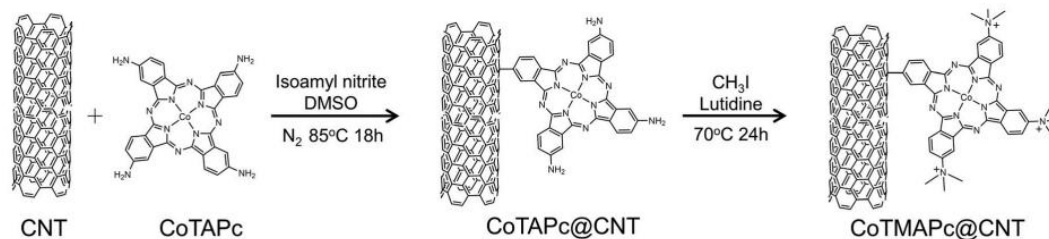
Figure 1.8. Scheme for the synthesis of CoTMAPc@CNT. [71]

1.3 Characterization Methods for ADMACs

Following the synthesis of atomically dispersed metal atom catalysts, the microstructure, chemical state, electronic structure and coordination structure must be investigated by advanced modern characterization methods, as well as the relationship between structure and the catalytic performance, which is of great significance for further designing superior catalysts. Currently, the most efficient characterization methods to fully analyze atomically dispersed metal atom catalysts are atomic resolution aberration-corrected high-angle annular dark-field scanning transmission electron microscopy (AC HAADF-STEM), X-ray absorption fine structure (XAFS), Scanning Tunneling Microscopy (STM) and Fourier-transform infrared spectroscopy (FT-IR).

1.3.1 Atomic resolution Aberration Corrected High-Angle Annular Dark-Field Scanning Transmission Electron Microscopy (AC HAADF-STEM)

Scanning electron microscopy (SEM) and transmission electron microscopy (TEM) are widely used to visualize the morphology and structure of catalysts.[72] Aberration-corrected high-angle annular dark-field scanning TEM (AC HAADF-STEM) with sub-angstrom scale resolution is the most intuitive and indispensable technique for probing the atomic dispersion of the metal atoms within the catalysts at the atomic scale.[73] Under HAADF conditions, the different atom

elements exhibit a different image intensity due to their difference in atomic number (Z-contrast). In this way, the intensity imaged in HAADF STEM is barely proportional to Z^2, so the different atom species can be easily distinguished by observing their brightness. For example, metal atoms display brighter points compared to carbon atoms in single metal atom catalysts loaded on graphite, because the Z-contrast is different between metal atoms and carbon atoms and the atomic number of the metal atom is larger. Du and his co-workers prepared single cobalt atom catalysts (Co-N/G) supported on nitrogen-doped graphene, however, while the isolated cobalt atoms could not be directly observed by TEM, they were clearly detected by HAADF-STEM.[74] As shown in **Figure 1.9**, the double atom catalyst (DACs) Ir2@α-Fe₂O₃ was successfully characterized by HAADF-STEM. [75] In **Figure 1.9a, b**, the double atom Ir2 can be clearly recognized as the bright two-point structure, the other lighter grey spots in the background display Fe atoms on the substrate. Furthermore, there no single Ir atoms or nanoparticles are observed, confirming the pure as-prepared double Ir atoms catalysts. Energy-dispersive X-ray spectroscopy (EDS) also further confirmed that no Ir clusters were observed (**Figure 1.9d**).
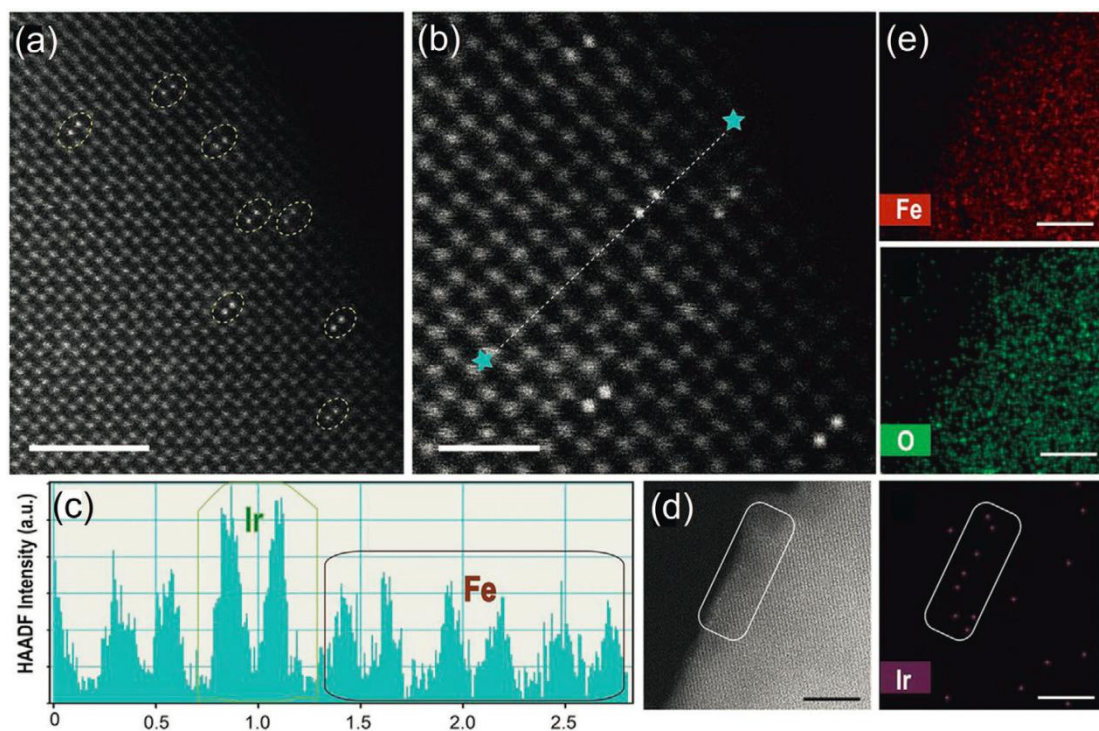
Figure 1.9 HAADF-STEM characterization if Ir2@α-Fe₂O₃.[75]

1.3.2 X-ray Absorption Fine Structure (XAFS)

Synchrotron-radiation X-ray absorption fine structure (XAFS) which includes X-ray absorption near-edge structure (XANES) and extended X-ray absorption fine structure (EXAFS), is the most accurate and effective technique to confirm the local coordination environment and electronic structure. [76] The XAFS technique has been widely applied in transition metal-based catalysts due to its element specificity, chemical state and sensitivity to short-range interaction. The electronic structure and chemical valence state can be analyzed by the features of peaks and shoulders in XAFS spectrum. In addition, the structure information including coordination number, bond distance, oxidation state, and degree of disorder can be revealed by the EXAFS spectrum.[77] As shown in **Figure 1-10a**, the absorption peak in the Zn K-edge XANES spectrum for Zn-N-C-1 is close to those of ZnO and Zinc phthalocyanine (ZnPc), implying that the oxidation state of Zinc in Zn-N-C-1 is +2. **Figure 1-10b** corresponds to the Fourier transform (FT) of the EXAFS spectra, which shows a peak at around 1.53 Å for the Zn-N-C-1 sample, confirming the existence of the Zn-N bond, and the absence of Zn-Zn metal bonds. These latest results confirm the atomic dispersion of Zn atoms. Furthermore, the EXAFS fitting in **Figures 1.10c** and **1.10d** suggest a ZnN4 coordination structure in Zn-N-C-1 catalyst.
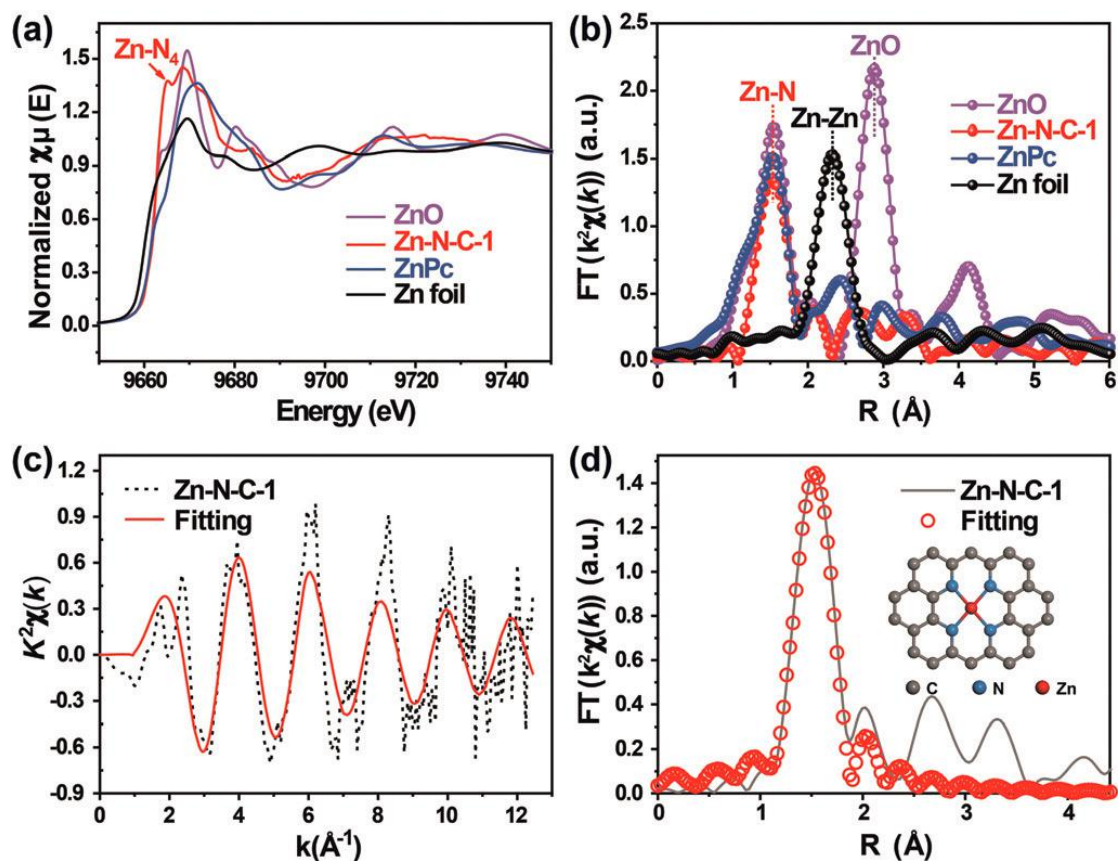
Figure 1.10. a) Zn K-edge XANES spectra of Zn-N-C-1, ZnO, ZnPc, and Zn foil. b) Fourier transforms (FTs) of the k2-weighted c(k) functions of the EXAFS spectra for the Zn K-edge. c, d) Corresponding EXAFS fitting curves in k and R space, respectively; inset shows a model of the Zn environment. [78]

1.3.3 Scanning Probe Microscopy (SPM)

Scanning probe microscopy (SPM) is one of the important characterization methods to confirm the presence of active sites for the atomically dispersed metal atom catalysts, especially for localizing the single metal atoms supported on the two-dimensional graphene-like structures. The most typical SPMs are scanning tunneling microscopy (STM) and atomic force microscopy (AFM). The STM not only can be used to reveal the information of electronic and geometric structures, but also to distinguish elements with similar atomic numbers on 2D graphene-like materials, indirectly, while the AFM can be applied to obtain the number of layers and the morphology of the catalysts. Deng and his co-workers confirmed the atomic dispersion of iron and the incorporation of FeN4 active sites in graphene support

through low-temperature scanning tunneling microscopy. [79]

1.3.4 Fourier-Transform Infrared Spectroscopy (FT-IR)

In addition to the above-mentioned methods of characterization for atomically dispersed metal atom catalysts, Fourier-transform infrared spectroscopy (FT-IR) can also be used to detect the vibration mode of molecules adsorbed on the surface to characterize the properties of active sites.[80] FT-IR characterization techniques can be applied to conduct a qualitative analysis of polar chemical bonds and functional chemical groups with infrared activity. [81-82] However, FT-IR cannot confirm whether the dispersed state of the metal is at atomic scale or bulk scale because of the negligible infrared activity of metallic bonds. The principle of FT-IR is that utilizing infrared spectroscopy to detect the interaction between support and adsorbed molecules, the intermediate product was detected by FT-IR, then the characteristics of the active center of the catalyst can be inferred by detecting the strength and vibration frequency of the tested model and correction. Qiao and his colleagues presented the FT-IR spectrum of CO adsorbed on the surface of single Pt atoms and Pt clusters, respectively. [25] The band at 2080 cm^{-1} was assigned to CO linearly bonded to Pt$^{\delta+}$ with independence of frequency, indicating isolated Pt atoms. The characteristic peaks of CO molecules on the surface of single metal atoms are different compared to those of nanoparticles and bulk counterparts. Gallenkamp et al. confirmed the presence of single iron atoms by FT-IR, XAFS and Nuclear Magnetic Resonance (NMR) analyses, and further analyzed the atomic composition and electronic structure of Fe-N-C active sites. [83]

1.4 The Applications of Atomically Dispersed Metal Atom Catalysts

The mutual conversion between electrical energy and chemical energy through electrocatalytic reactions is an important task in the field of clean energy. Developing stable and efficient catalysts with industrial application prospects, and clean energy conversion technologies has become a frontier hotspot of research in related fields. The current common electrocatalytic reactions are water splitting reactions,

electrocatalytic carbon dioxide reduction, alcohol fuel cells, lithium-sulfur batteries, zinc-air batteries and so on. Recently, the application of atomically dispersed metal catalysts in the field of electrocatalysis and energy conversion research areas has produced a lot of research results.

1.4.1 Lithium-Sulfur Batteries

Lithium-sulfur batteries (LSBs), composed of a lithium metal anode and sulfur cathode, have a high theoretical capacity (1672 mAh g^{-1}), are based on sulfur which has a high natural abundance and low cost and are potentially safe (**Figure 1.11a**). LSBs are one of the most attractive candidates to replace lithium-ion batteries and become the next competitive battery generation. [84] The sulfur in the cathode is existing as S_8, during the discharge process, the S_8 reacts with the lithium-ion to form the long-chain lithium polysulfides (LiPSs), Li_2S_x ($4 \leq x \leq 8$). As the discharge progress, the long-chain LiPSs are reduced to short-chain LiPSs, until the formation of the final discharge product, namely Li_2S. [85-86] The charging process is just the opposite.

The typical discharge process is categorized into four steps (**Figure 1.11b**).[87] The first step is that the elemental sulfur S_8 is reduced to soluble Li_2S_8, which can be dissolved into the liquid electrolyte.

$$S_8 + 2Li \rightarrow Li_2S_8 \qquad (1)$$

Then in the second step, the high order Li_2S_8 is reduced to the low order lithium polysulfides (L_2S_x, $4 \leq x < 8$)

$$Li_2S_8 + 2Li \rightarrow Li_2S_n + Li_2S_{8-n} \qquad (2)$$

For the third step, LiPS is transformed to insoluble Li_2S_2 or Li_2S. During this process, the two pathways are competing, and the major capacity of a lithium-sulfur battery originates from this process.

$$2Li_2S_n + (2n-4)Li \rightarrow nLi_2S_2 \qquad (3)$$

Or

$$2Li_2S_n + (2n-2)Li \rightarrow nLi_2S \qquad (4)$$

The final step corresponds to a solid-solid process between Li_2S_2 and Li_2S, which is

kinetically slow and with high polarization.

$$Li_2S_2 + 2Li \rightarrow 2Li_2S \tag{5}$$
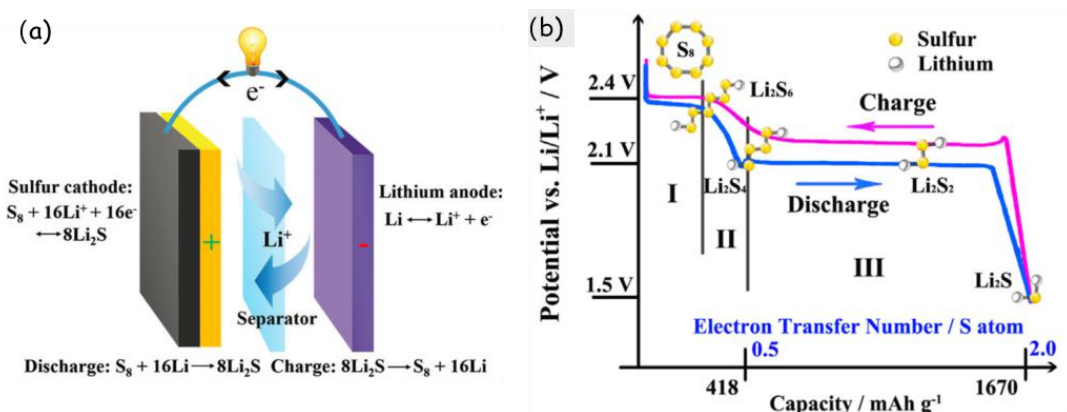
Figure 1.11 (a) LSB structure. [88] (b) Charge/discharge curves for LSBs. [85]

Even though the principles of the LSB look very simple, there are still many key technical problems to be solved to construct ideal LSBs with high energy density, high stability and safety. [89-92] First, the elemental sulfur, Li_2S_2 and Li_2S have a low electrical conductivity, resulting in an increased internal resistance and poor reaction kinetics, which is not leading to a high rate performance of the battery. Second, the large volume change between S8 and Li_2S reaches 80% during charge/discharge processes, which causes the active substance to fall off and the internal structure to collapse, resulting in bad stability. Third, LiPS are generated from the cathode during the discharge process, which are easily dissolved into the electrolyte and diffused to the anode under the action of a concentration gradient. This phenomenon, known as the "shuttle effect", leads to the inactivation of some sulfur, low utilization of lithium, low stability and low coulomb efficiency of LSBs. In addition, the lithium dendritic phenomenon causes a serious safety problem and a short circuit inside the battery.[93]

To address the critical problems, researchers mainly concentrated on the following aspects: (1). The sulfur was loaded on the conductive support to form the composites to enhance the conductivity, among them, carbon-based materials have been the most widely used. (2). Trapping the dissolved LiPSs within the cathode or hindering their diffusion by using a separator are good solutions. (3). Improve the battery electrolyte system, such as using a solid electrolyte. (4). Protect the lithium anode.

A strong interaction between sulfur species and hosts is necessary for efficiently

anchoring LiPSs within the cathode, such as physical confinement by porous structure and chemical adsorption through increasing the polarity of the host materials by doped heteroatoms.[94] As for the atomically dispersed metal atom catalysts, the fully exposed metal centers can be used as ideal active sites for adsorbing and promoting the LiPSs redox kinetic conversion. In addition, the structural tunability of its atomic level precision provides new possibilities for accurately exploring the relationship between catalyst structure and activity and exploring the conversion mechanism of lithium polysulfide at the atomic level.[95-102] Recently, Du and his co-workers reported a single cobalt atom catalyst anchored on nitrogen-doped graphene (Co-N/G) which was used as cathode materials for lithium-sulfur batteries with excellent performance. [103.] The stable Co-N-C active sites in the N-graphene serving as a bifunctional catalyst, not only showed good chemical adsorption ability for LiPSs, but also played an important role in boosting the redox kinetic conversion of polysulfides. The Li-S cells were assembled with a S@Co-N/G based cathode exhibiting a capacity decay rate of just 0.053% per cycle during 500 cycles at 1 C current density. Even though when the mass loading of sulfur was increased to 6 mg cm^{-2}, the electrode displayed a high areal capacity of 5.1 mAh cm^{-2}, and the capacity decay rate was only 0.029% per cycle over 100 cycles at 0.2 C. The in-situ XANES further confirmed that the Li2S formed during the initial discharge process on the Co-N/G support which also promoted the transformation rate. Furthermore, DFT calculations show that the Co-N/G electrode promotes the formation and decomposition of Li_2S during the discharge and charge processes, respectively (**Figure 1.12 a, b**).
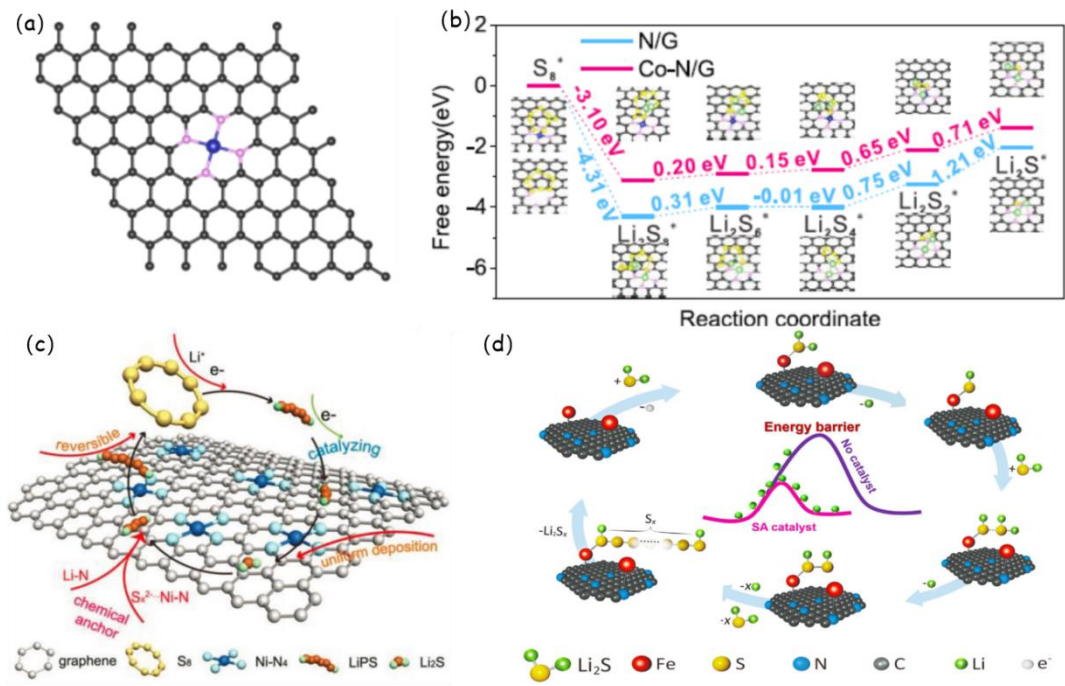
Figure 1.12 (a) Structures of Co-N/G used in first-principles calculations. (b) Energy profiles for the reduction of LiPSs on N/G and Co-N/G substrates. (insets) The optimized adsorption conformations of intermediate species on N/G and Co−N/G substrate. Energy profiles of the decomposition of Li$_2$S cluster on N/G (c) Single nickel atom catalyst. (d) A proposed mechanism for SAFe catalyzed Li$_2$S delithiation reaction.[103]

Zhang et al. synthesized a single nickel atom catalyst (Ni@NG) loaded in nitrogen-doped graphene (**Figure 1.12 c**),[104] Their results confirmed that the active site Ni-N4 in Ni@NG can be used to trap the polysulfides and suppress the "shuttle effect". Furthermore, the charge transfer between the Ni-N4 active sites and LiPSs promote the redox kinetic conversion of polysulfides. Wang and his colleagues proposed a catalyst based on uniformly atomically dispersed iron atoms loaded on porous nitrogen-dopped carbon matrices with a nanostructured Li$_2$S (Li$_2$S@NC:SAFe). Besides serving as an iron atom supporter, the conductive matrix (NC) could also work for immobilizing polysulfides and preventing the shuttle effect.[105] When the composite worked as cathode for the Li-S cells, the cells exhibited ultra-high-rate performance, cycle stability and capacity of 589 mAh g^{-1} at 12 C. Interestingly, the decay rate was only 0.06% per cycle over 1000 cycles at 5 C.

DFT calculations displayed that the single iron atom catalyst reduced the energy barrier of Li-S bond breakage and lithium-ion diffusion. They proposed the following mechanism for the role of the single iron atom catalyst: First, the coordination interaction between the Fe atom and Li_2S elongate and weaken the Li-S bond, leading to the decoupling of lithium ions from the intermediate [N-Fe...S-Li2]. After that, the intermediate will promote the formation of a polysulfide chain by utilizing a series of Li_2S species by the repeated delithiation during the charging process. Once the polysulfide chain detaches from the active site, the Li2S continues the coordination with Fe for the next subsequent delithiation reaction. This mechanism provides a good reference for the subsequent exploration of the reaction mechanism during the charging and discharging process of LSBs (**Figure 1.12d**).

Besides, atomically dispersed catalysts have been developed for the application of Li-S batteries widely [106-108]. However, most of them stay on graphene-based atomic catalysts and lack the understanding of the interaction between metal atoms and supports and the influence of coordination environment and ligand environment on catalytic activity. The following aspects need to be considered in the future development of catalysts that are efficiently applied to LSBs:

(1) Suitable conductive support. Doping with heteroatoms and the periodic porous structure of the cathode materials of LSBs are beneficial to increase the loading of sulfur and trapping polysulfides. In this way, COFs with good conductivity and regular periodic porous structure are good candidates as support materials in the cathode of LSBs, especially when concerning atomically dispersed metal atom catalysts based on two-dimensional COFs.

(2) The optimized coordination structure and the atom coordination. Even though most atomically dispersed metal atom catalysts present the MN4 structure, also a FeN2 structure was reported.[109] However, there is still a need for more exploration for the relation between the coordination structure and the LSBs performance. Furthermore, it is also worth exploring the coordination of the metal atoms with other atoms (such as S, O, P, and so on).

(3) Design of double metal atoms or cluster catalysts. The simple structure of

single-atom catalysts provides convenience for studying the conversion process of lithium polysulfide with atomic precision. However, it has a limited effect on the complex long-chain LiPS. In this way, it would be possible to design multi-atom catalysts to promote the redox kinetic conversion of polysulfide by taking advantage of their synergistic interaction.

(4). The large-scale synthesis of atomically dispersed metal atom catalysts, which would be helpful for the commercial application in LSBs.

1.4.2 Electrochemical CO2 reduction

The environmental problems caused by the CO_2 greenhouse gas produced by the burning of fossil fuels have always been a hot spot of concern. In order to alleviate the environmental hazard caused by greenhouse gases and the depletion of non-renewable energy, it is urgent to develop new technologies for efficiently processing CO_2. Electrochemical reduction of carbon dioxide (CO_2RR) to valuable fuels and chemicals is a promising technology to promote the carbon cycle. The general process of electrocatalytic CO_2 reduction is shown in **Figure 1.13**. The anode of the electrolytic cell undergoes the water oxidation reaction to generate protons (H^+) and release oxygen, protons diffuse through the ion exchange membrane to the cathode, then the cathode of the electrolytic cell undergoes electroreduction of CO_2 to generate CO or other hydrocarbon products.

Figure 1.13 Illustration of the electrochemical CO_2 reduction process and the possible products generated in an electrochemical reaction cell.[110]

Over the past decades, a large amount of metal-based electrocatalysts were reported. [111] In this way, Ag and Au based electrocatalysts can be active for the conversion of CO_2 to CO with high Faradaic efficiency (FE), exceeding 90%. [112-113] In addition, copper-based electrocatalysts are commonly used for the electrochemical conversion of CO_2 to deeply reduced hydrocarbon products, such as methane,[114] ethylene,[115] ethanol[116] and acetate. [117] (**Figure 1.14**)

Figure 1.14 Schematic mechanism of different metal electrocatalysts for CO_2 reduction reaction in aqueous solution [110]

Table 1-1 exhibits the typical products obtained from the electrochemical CO_2RR and the corresponding equilibrium potentials. In the reversible hydrogen electrode (RHE) scale, the equilibrium potentials (E^0) of most products from CO_2RR are higher than 0 V, indicating that the reaction is thermodynamically more favorable compared to the hydrogen evolution reaction (HER). However, the kinetics of CO_2RR are usually much more sluggish than those of HER, which means that both reactions compete in parallel on many electrodes. [118] Therefore, it is very important to synthesize an ideal catalyst with high selectivity for electrochemical CO_2RR.

Atom-dispersed metal catalysts have high atom utilization efficiency due to the high dispersibility of metal atoms. The unsaturated coordination structure and homogeneity of the metal atom active site promise a similar spatial structure and electron interaction between catalyst and CO_2, which favors the selectivity of the specific product in electrochemical CO_2 reduction.

Table 1-1 Electrochemical reaction equation for CO₂RR

Chemical Equation	E_0/(V vs RHE)
$2H^+ + 2e^- \rightarrow H_2$	0
$CO_2 + 2H^+ + 2e^- \rightarrow H_2O + CO$	-0.10
$CO_2 + 2H^+ + 2e^- \rightarrow HCOOH$	-0.12
$CO_2 + 4H^+ + 4e^- \rightarrow HCHO + H_2O$	-0.1
$CO_2 + 6H^+ + 6e^- \rightarrow CH_3OH + H_2O$	0.03
$CO_2 + 8H^+ + 8e^- \rightarrow CH_4 + 2H_2O$	0.17
$2CO_2 + 8H^+ + 8e^- \rightarrow CH_3COOH + 2H_2O$	0.11
$2CO_2 + 12H^+ + 12e^- \rightarrow C_2H_4 + 4H_2O$	0.07
$2CO_2 + 12H^+ + 12e^- \rightarrow C_2H_5OH + 3H_2O$	0.08
$3CO_2 + 18H^+ + 18e^- \rightarrow C_3H_7OH + 5H_2O$	0.10
$2CO_2 + 2H^+ + 2e^- \rightarrow H_2C_2O_4$	-0.50

Recently, many atomically dispersed metal atom catalysts have been reported for efficient electrochemical CO₂RR. Diercks et al. reported a molecular-based electrocatalyst that was based on two-dimensional COFs embedded with cobalt porphyrin.[119] The proposed COFs favored the efficient charge transfer, displaying a high FE of CO product which was over 87% and a current density of 65 mA cm-2 at -0.55 V. Wu et al. found that the electroreduction of CO₂ to methanol could be achieved on cobalt phthalocyanine supported on carbon nanotubes (CoPc/CNT), [120] with a FE of above 40% and a current density of 10 mA cm-2 at -0.94 V. In this study, CO was the important reaction intermediate, which was further reduced to methanol through a proposed domino process (**Figure 1.15**). In addition, they also hypothesized that there exists a synergistic interaction between CNT and CoPc in catalyzing the conversion of CO₂ to methanol-based on the different performance by using different

support (Vulcan XC72, Ketjenblack, CNT). Gu and his colleagues reported efficient single iron atom catalysts (Fe-N-C) for the CO_2 conversion, with a FE of CO over 90% at a really low overpotential of 80 mV. [121] Interestingly, Fe^{3+} was detected throughout the CO_2RR process by in-situ XANES measurements. They further confirmed that the pyrrole type of N coordinated with Fe^{3+} would favor the stability of the Fe^{3+} valence state, and that there was weaker CO absorption on $Fe^{3+}N-C$ sites compared to that on $Fe^{2+}-N-C$.
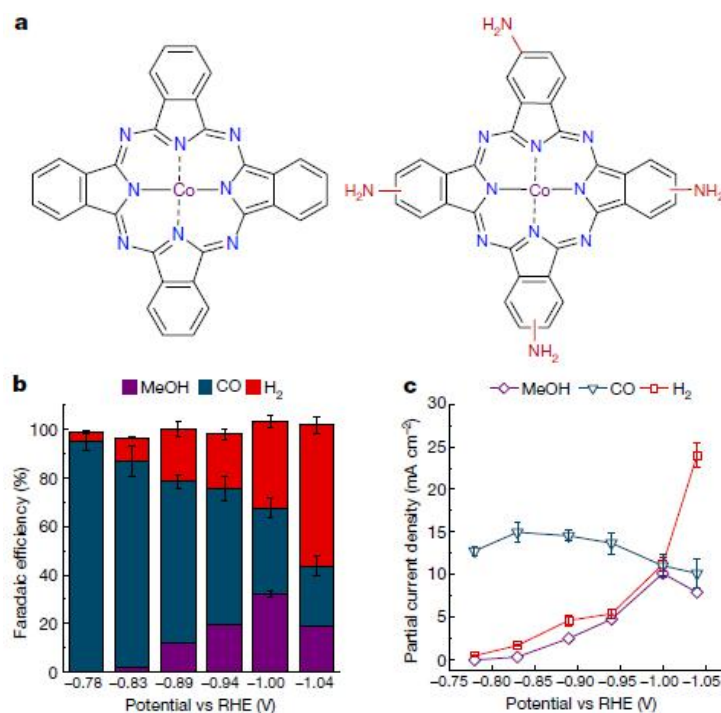
Figure 1.15 Electrocatalytic performance of CoPc-NH$_2$/CNT for CO_2 reduction to methanol. (a) Structural comparison between CoPc and CoPc-NH$_2$. (b, c) Potential-dependent product selectivity (FE; b) and partial current density. (c) for CO_2 electroreduction catalyzed by CoPc-NH$_2$/CNT. Error bars represent the standard deviation on the three measurements. [120]

Not only single-atom or double-atom catalysts are explored for the electrochemical CO_2 reduction. In the catalytic reaction involving a variety of reactants, reaction intermediates and products, the simple structure of the active center also makes the application of single-atom catalysts encounter challenges. Designing an active center, which contains multiple metal atoms can increase multiple reaction sites for complex reactions, leading to the integration of the functions of those multiple atoms together,

and maybe adding also synergistic effects. [122] Li Y. and his co-workers reported silver-based dual-atom catalysts supported by graphene (Ag2/Graphene), with the AgN3-AgN3 coordination structure. [123] The two silver atoms at the metal active site of the catalyst adsorb the C and O atoms in the CO_2 molecule respectively. This adsorption structure reduces the activation barrier of the CO_2 molecule, which leads to the formation of COOH reaction intermediates, thereby reducing the choice of CO products with faradaic efficiency (FE) of 93.4%. In the carbon dioxide reduction reaction, the catalyst not only directly affects the adsorption and activation of CO_2, but also has a synergistic effect on the process of adsorbing H_2O. Jiao et al. reported a double copper atom catalyst (Cu^0-Cu^{x+}) supported on one-dimensional Pd10Te3 nanowires. The $Pd_{10}Te_3$ surface defect of the nanowires was utilized to anchor the copper atom pair. Cu^{x+} adsorbs H_2O molecules, and the adjacent Cu^0 adsorbs CO_2 molecules, thereby promoting the activation of CO_2. The Faradaic efficiency of CO generation was found above 92%, and the competing hydrogen evolution reaction was almost completely suppressed. Experimental characterization and theoretical calculations showed that the adsorption configuration reduced the activation energy barrier, making the catalyst have higher selectivity, catalytic activity and stability at a relatively low potential.[124]

Not only the homonuclear diatomic catalysts were developed for electrochemical CO_2 reduction, but also there are some research reports on heteronuclear diatomic catalysts for CO2RR. Anchoring two different metal atoms together can further develop new catalysts aimed at improving the selectivity and activity of the reaction, enriching the types and functions of the catalysts, and having good application prospects. Wei and his colleagues synthesized a double atom catalyst with the N4-Ni-Sn-N4 coordination structure. This catalyst displayed high activity and selectivity for HCOOH generation, the yield of HCOOH was 36.7 $mol·h^{-1}$ g_{Sn}^{-1}. The FT-IR measurements and DFT calculations exhibited that the introduction of Ni could regulate the electronic structure of Sn, enhancing the adsorption of Sn on CO_2 molecules, promoting their conversion into *OCHO intermediates, and finally producing HCOOH. [125]

1.4.3 Electrochemical Synthesis of Fine Chemicals

Normally, industrial-scale carboxylic acid (R-COOH) production almost completely needs a resource- and energy-intensive oxidation process, where high temperature, elevated pressure and costly catalysts are used to overcome the kinetic limitation. It is therefore challenging and interesting to develop new sustainable and environmentally friendly routines for producing R-COOH to alleviate the emerging rigorous energy and environmental problems. Electrocatalysis can play an important role in overcoming the abovementioned problems and meeting the corresponding requirements. It is becoming evident that the electrochemical oxidation of alcohol with hydrogen generation is a potential cost-effective and clean routine to produce RCOOH.[126-133] The electrochemical oxidation of alcohol to produce R-COOH has several advantages, such as high energy efficiency, high selectivity, that the reaction is operated under ambient pressures and room temperature conditions, that the electricity needed can be used from renewable energy sources (solar, wind and so on), the process can be designed in large scale, and the process can be integrated with hydrogen generation electrocatalysis or the production of other valuable chemicals or fuels.[134-136] More interesting, the alcohol oxidation reaction (AOR) to carboxylic acetate could also be integrated into the oxygen reduction reaction (ORR) to work as fuels cells to generate electricity.[137]

During the past decades, many electrocatalysts have been reported for the electrochemical alcohol oxidation, but most are based on high-cost and low-abundance elements such as platinum and palladium, [138-140] Several non-precious transition metal catalysts have been proposed for alcohol electro-oxidation.[141-143] Among them, nickel-based catalysts are considered the most promising candidates owing to their high catalytic activity, low price, and notable abundance. Cui et al. reported hierarchically structured and highly branched Ni-Cu alloy networks which exhibited superior activities for electrochemical methanol oxidation reaction (MOR) with a larger peak current density of 140 mA cm^{-2} and long-term stability.[144] Wu and his co-workers synthesized a new

three-dimensional microporous MOF with Cubane [Ni4(OH)4] clusters which can work as an electrocatalyst for the MOR. The optimal hybrid material showed excellent electrocatalytic performance with a high mass-specific peak current of 527 mA mg^{-1} and a peak current density of 29.8 mA cm^{-2} at a very low potential (0.6V). [145] Li and his colleagues reported nickel-molybdenum-nitride nanoplates supported on carbon fiber cloth (Ni-Mo-N/CFC), which were used for the electrolytic production of hydrogen at the cathode and value-added formate obtained by the oxidation of glycerol at the anode. The faraday efficiency for H2 evolution was 99.7 % and the one for formate production was 95%. [133] Huang et al. reported an amorphous Ni, Co hydroxide nanosheet loaded on Ni foam (A-Ni-Co-H/NF), with a large active area and low charge transfer resistance, which was used to catalyze the electrocatalytic benzyl alcohol oxidation reaction (BOR). Surprisingly, the electrocatalytic reaction achieved an industrial-scale current density above 400 mA cm^{-2} before the appearance of the OER, and displayed ultrafast reaction kinetics for BOR. The faradaic efficiency of Ph-COOH was about 100%, more interestingly, the spending time was really fast (15 min) at room temperature and atmospheric pressure (**Figure 1.16**). [146]
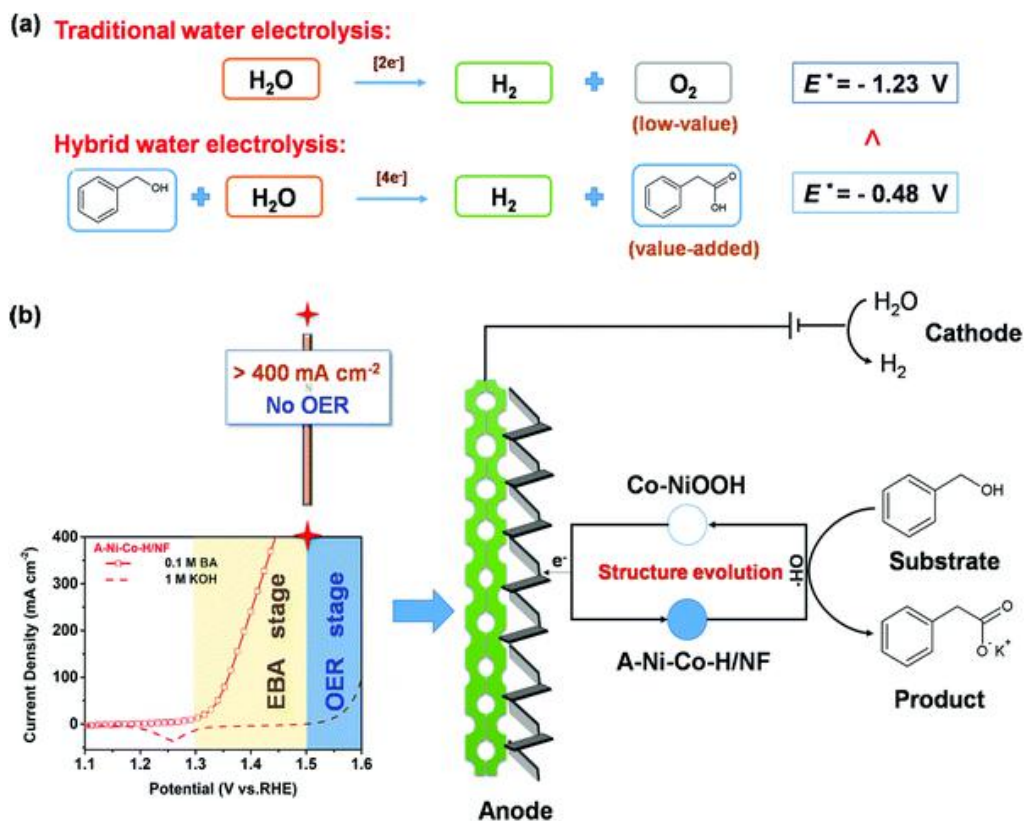
Figure 1.16 (a) The related reactions of traditional water electrolysis and hybrid water electrolysis. (b) Electrocatalytic H_2 generation combined with the generation of high-purity Ph-COOH. [146]

1.5 The Research Content and Purpose of This Thesis

At present, atomic-level dispersed metal atom catalysts have become a research hotspot in the field of energy and environmental catalysis, due to their unique electronic and geometric structure, showing interesting applications in many fields, such as photocatalysis, electrocatalysis, organic catalysis, batteries and so on. This thesis mainly focuses on utilizing novel two-dimensional COFs and MOFs materials to design and develop novel high-efficiency atomically dispersed metal atom catalysts for cathode materials of high-efficiency LSBs, electrochemical alcohol oxidation and carbon dioxide reduction reactions, and further conduct in-depth exploration at the atomic level to improve catalysis strategies for the regulation of catalytic performance, providing guidance for the development of efficient atomically dispersed catalysts.

This thesis specifically includes the following different systems:

A novel catalyst based on atomically dispersed iron in a 2D covalent organic framework (Fe/C₂N), which has been shown as an efficient sulfur host material for LSBs. Double iron atoms are coordinated to nitrogen in the C_2N pores. These atomically dispersed Fe atoms not only improve the material polarity to immobilize the soluble polysulfides, but also act as catalytic active sites to promote the reaction kinetics between sulfur, polysulfide, and Li_2S. As a result, S@Fe/C₂N-based cathodes exhibit excellent electrochemical performance, showing a high capacity and a remarkable rate performance at different current densities, while keeping outstanding cycling stability.

An atomically-dispersed nickel 2D molecular organic framework containing abundant carbonyl (C=O) functional groups within the nickel ion coordination environment. Its atomic structure and how the outstanding electrocatalytic activities and durabilities are obtained for the electrochemical-oxidation of methanol, ethanol, and benzyl alcohol have been analyzed, are related to the alcohol adsorption ability of the carbonyl functional groups and the high unsaturated coordination number of the nickel ions within this new catalyst.

A conjugated nickel organic framework with abundant carbonyl groups in the ligand near the nickel catalytic active site is described and explored as electrocatalyst CO₂RR to methanol in aqueous medium. The unique chemical structure and uniformly distributed catalytic active centers in the proposed nickel organic framework, combined with the high electrical conductivity of carbon nanotubes (CNT), results in electrocatalysts with high catalytic activities, excellent durability and notable selectivity for CO₂RR to methanol. This work not only provides new insights into the synthesis of an atomically dispersed material under mild and controllable conditions, but also demonstrates a novel strategy to design effective CO₂RR electrocatalysts by tuning the ligand chemical environment.

Finally, a non-template synthesis method was used to construct a new type of Tetra[14]annulene based π-d conjugated cobalt organic framework with atomically dispersed cobalt, namely, Poly-TAA-Co with CoN4 structure. This molecular complex

is loaded on a conductive support, namely multi-wall CNTs, and applied for the efficient electrochemical CO_2RR. The obtained results have been rationalized by means of density functional theory (DFT) calculations.

References

[1] R. Lang, X. Du, Y. Huang, X. Jiang, Q. Zhang, Y. Guo, K. Liu, B. Qiao, A. Wang, T. Zhang, *Chem. Rev.*, 2020, 120, 11986.

[2] N. Mizuno, M. Misono, Chemical Reviews, 1998, 98, 199-218.

[3] A. Wang, J. Li, T. Zhang, *Nature Reviews Chemistry*, 2018, 2, 65-81.

[4] J. C. Védrine, *Catalysts*, 2017, 7, 341.

[5] M. Stratakis, H. Garcia,*Chemical Reviews*, 2012, 112, 4469-4506.

[6] Y. Wang, N. Zhao, B. Fang, H. Li, X. T. Bi, and H. Wang, Chemical Reviews, 2015, 115, 3433-3467.

[7] S. Y. Chen, Catalytic Reactor engineering. Beijing: Chemical Industrial Press. 2011. 7.

[8] M. Haruta , T. Kobayashi , H. Sano, N. Yamada , *Chem. lett.*, 1987, 16 (2), 405.

[9] H. G. Boyen, G. Kastle, F. Weigl, B. Koslowski, C. Dietrich, P. Ziemann, J. Spatz, S. Riethmuller, C. Hartmann, M. Moller, *Science*, 2002, 297,1533.

[10] M. Valden, X. Lai, D. W. Goodman. *Science*, 1998, 281, 1647.

[11] A. Uzun, V. Ortalan, Y. Hao, N. D. Browning, B. C. Gates, *ACS Nano* 2009, 3, 3691.

[12] W. E. Kaden, T. Wu, W. A. Kunkel, S. L. Anderson, *Science*, 2009, 326, 826.

[13] S. Cao, F. Tao, Y. Tang, Y. Lia, J. Yu, *Chem. Soc. Rev.,* 2016, 45, 4747-4765

[14] A. A. Herzing, C. J. Kiely, A. F. Carley, P. Landon, G. J. Hutchings, *Science*, 2008, 321, 1331-1335.

[15] M. Turner, V. B.Golovko, O.P. Vaughan, P. Abdulkin, A. Berenguer-Murcia, M. S. Tikhov, B. F. Johnson, R. M. Lambert, *Nature*, 2008, 21, 981-983.

[16] S. Vajda, M. Pellin, J. Greeley, et al. *Nature Mater.,* 2009, 8, 213-216.

[17] K. Judai, S. Abbet, A. S. Wörz, U. Heiz, and C. R. Henry, J. Am. Chem. Soc. 2004, 126, 9, 2732-2737.

[18] Y. Lei, F. Mehmood, S. Lee, J. Greeley, B. Lee, S. Seifert, R. E. Winans, J. W. Elam, R. J. Meyer, P. C. Redfern, D. Teschner, R. Schlögl, M. J. Pellin, L. A. Curtiss, S. Vajda, Science, 2010, 9, 224-8.

[19] B. Qiao, A. Wang, L. Li, Q. Lin, H. Wei, J. Liu, and T. Zhang, ACS Catal., 2014, 4, 7, 2113-2117.

[20] X. Zhang, H. Shi, B. Xu, Angew. Chem. Int. Ed., 2005, 44, 7132-7135.

[21] J. M. Thomas, Z. Saghi, P. L. Gai, Topics in Catalysis, 2011, 54, 588-594.

[22] D. Pierre, W. Deng, M. F.-Stephanopoulos, Topics in Catalysis, 2007, 46, 363-373.

[23] Y. Shi, C. Zhao, H. Wei, J. Guo, S. Liang, A. Wang, T. Zhang, J. Liu, T. Ma, *Adv. Mater.,* 2014, 26, 8147-8153

[24] Single-Atom Catalysts: A New Frontier in Heterogeneous Catalysis. *Acc. Chem. Res*. 2013, 46, 8, 1740-1748

[25] B. Qiao, A. Wang, X. Yang, L. F. llard, Z. Jiang, Y. Cui, J. Liu, J. Li, T. Zhang, *Nature Chemistry*, 2011, 3, 634-641.

[26] L. Zhang, A. Wang, J. T. Miller, X. Liu, X. Yang, W. Wang, L. Li, Y. Huang, C. Mou, T. Zhang, *ACS Catal*., 2014, 4, 1546-1553.

[27] P. Yin, T. Yao, Y. Wu, L. Zheng, Y. Lin, W. Liu, H. Ju, J. Zhu, X. Hong, Z. Deng, G. Zhou, S. Wei, Y. Li, *Angew. Chem. Int. Ed.,* 2016, 55, 10800-10805.

[28] Q. Yang, C. Yang, C. Lin, H. Jiang, *Angew. Chem. Int. Ed.*, 2019, 58, 3511-3515.

[29] Y. Zhu, W. Sun, W. Chen, T. Cao, Y. Xiong, J. Luo, J. Dong, L. Zheng, J. Zhang, X. Wang, C. Chen, Q. Peng, D. Wang, Y. Li, *Adv. Funct. Mater.,* 2018, 28,1802167.

[30] L. Zhang, A. Wang, J. T. Miller, X. Liu, X. Yang, W. Wang, L. Li, Y. Huang, C. Mou, T. Zhang, ACS Catal., 2014, 4, 1546-1553.

[31] J. Li, Z. Wei, D. Liu, D. Du, Y. Lin, M. Shao, Topics in Current Chemistry, 2019, 377, 4.

[32] M. Qiao,Y. Wang, Q. Wang, G. Hu, X. Mamat, S. Zhang, S. Wang, *Angew. Chem., Int. Ed.* 2020, 59, 2688-2694.

[33] L. Yang, L. Shi, D. Wang, Y. Lv, D. Cao, *Nano Energy*, 2018, 50, 691-6983.

[34] Wang, F. Chu, J. Zeng, Q. Wang, T. Naren, Y. Li, Y. Cheng, Y. Lei, F.Wu, *ACS Nano*, 2021, 15, 210−239

[35] L. Lin, W. Zhou, R. Gao, et al., *Nature*, 2017, 544, 80-83

[36] L. Nie, D. Mei, H. Xiong, B. Peng, Z. Ren, X. Hernandez, A. DeLaRiva, M.

Wang, M. Engelhard, L. Kovarik, A. Datye, Y. Wang, *Science*, 2017, 358, 1419-1423

[37] P. Liu, Y. Zhao, R. Qin, S. Mo, G. Chen, L. Gu, D. M. Chevrier, P. Zhang, Q. Guo, D. Zang, B. Wu, G. Fu, N. Zheng, *Science*, 2016, 352, 797-801.

[38] Y. Yang, Y. Yang, Z. Pei, K. Wu,C. Tan, H. Wang, L. Wei, A. Mahmood, C. Yan, J. Dong, S. Zhao, Y. Chen, *Matter*, 2020, 3, 1442-1476.

[39] Y. Wang, K. Qi, S. Yu, et al., *Nano-Micro letter*, 2019, 11, 102.

[40] C. Choi, M. Kim, H. Kwon, et al., *Nature Commun.,* 2016, 7, 10922.

[41] S. Tian, Z. Wang, W. Gong, W. Chen, Q. Feng, Q. Xu, C. Chen, C. Chen, Q. Peng, L. Gu, H. Zhao, P. Hu, D. Wang, Y. Li, *J. Am. Chem. Soc.*, 2018, 140, 11161.

[42] Q. Wang, Z. Zhao, S. Dong, D. He, M. Lawrence, S. Han, C. Cai, S. Xiang, P. Rodriguez, B. Xiang, Z. Wang, Y. Liang, M. Gu, *Nano Energy*, 2018, 53, 458.

[43] H. Furukawa, K. E. Cordova, M. O'Keeffe, O. M. Yaghi, *Science* 2013, 341, 6149.

[44] W. Xia, A. Mahmood, R. Zou, Q. Xu, *Energy Environ. Sci.*, 2015, 8, 1837.

[45] C. Hou, H. Wang, C. Li, Q. Xu, *Energy Environ. Sci.*, 2020, 13, 1658-1693.

[46] Y.Zhang, S. Ni, C. Chong, J. Xu, X. Mu, X. Zhang, *Applied Materiasl Today*, 2021, 23, 101029.

[47] J. Liu, D. Cao, H. Xu, D. Cheng, *Nano select*, 2021, 2, 251-270.

[48] J. Liu, D. Zhu, C. Guo, A. Vasileff, S. Qiao, *Advanced Energy Materials*, 2017, 7, 1700518.

[49] Y. Pan, R. Abazari, Y. Wu, J. Gao, Q. Zhang, *Electrochemistry Communications*, 2021, 126, 107024.

[50] Q. Yang, C. Yang, C. Lin, H. Jiang, *Angew. Chem. Int. Ed.,* 2019, 58, 3511-3515.

[51] P. Yin, T. Yao, Y. Wu, L. Zheng, Y. Lin, W. Liu, H. Ju, J. Zhu, X. Hong, Z. Deng, G. Zhou, S. Wei, Y. Li, *Angew. Chem., Int. Ed.* 2016, 55, 10800.

[52] X. Wang, W. Chen, L. Zhang, T. Yao, W. Liu, Y. Lin, H. Ju, J. Dong, L. Zheng, W. Yan, X. Zheng, Z. Li, X. Wang, J. Yang, D. He, Y. Wang, Z. Deng, Y. Wu, Y. Li, *J. Am. Chem. Soc.* 2017, 139, 9419.

[53] H. Zhang, J. Wei, J. Dong, G. Liu, L. Shi, P. An, G. Zhao, J. Kong, X. Wang, X. Meng, J. Zhang, J. Ye. *Angew. Chem., Int. Ed.* 2016, 55, 14310.

[54] J. Liu, D. Yang, Y. Zhou, G. Zhang, G. Xing, Y. Liu, Y. Ma, O. Terasaki, S. Yang, L. Chen, *Angew. Chem. Int. Ed.*, 2021, 60, 14473.

[55] Y. Ni, L. Lin,Y. Shang, L. Luo,L. Wang,Y. Lu,Y. Li, Z. Yan, K. Zhang, F. Cheng, J. Chen, *Angew. Chem., Int. Ed.*, 2021,133, 17074-17078.

[56] Y. Li, R. Zhang, W. Zhou, X. Wu, H. Zhang J. Zhang, *ACS Nano*, 2019, 13, 5533-5540.

[57] Y. Li, S. Zuo, Q. Li, X. X. Wu, J. Zhang, H. Zhang, J. Zhang, *Nano Letter*, 2021, 21, 1848-1855.

[58] Y. Chen, S. Ji, W. Sun, Y. Lei, Q. Wang, A. Li, W. Chen, G. Zhou, Z. Zhang, Y. Wang, L. Zheng, Q. Zhang, L. Gu, X. Han, D. Wang, Y. Li, *Angew. Chem., Int. Ed.* 2020, 59, 1295-1301.

[59] L. DeRita, J. Resasco, S. Dai, et al., *Nature Materials,* 2019, 18, 746-751.

[60] J. Wan, W. Chen, C. Jia, L. Zheng, J. Dong, X. Zheng, Y. Wang, W. Yan, C. Chen, Q. Peng, D. Wang, Y. Li, *Adv. Mater.*, 2018, 30, 1705369.

[61] L. Zhang, Y. Jia, G. Gao, X. Yan, N. Chen, J. Chen, M. Soo, B. Wood, D. Yang, A. Du, X. Yao, X. (2018). *Chem*, 2018, 4 , 285-297.

[62]Y. Liu, Z. Li, Q. Yu, Y. Chen, Z. Zhao, G. Zhao, S. Liu, W. C. Cheong, Y. Pan, Q. Zhang, L. Gu, L. Zheng, Y. Wang, Y. Lu, D. Wang, C. Chen, Q. Peng, Y. Liu, L. Liu, J. Chen, Y. Li, *J. Am. Chem. Soc.*2019, 141, 9305.

[63] W. Chen, J. Pei, C. T. He, J. Wan, H. Ren, Y. Wang, J. Dong, K. Wu, W. C. Cheong, J. Mao, X. Zheng, W. Yan, Z. Zhuang, C. Chen, Q. Peng, D. Wang, Y. Li, *Adv. Mater*. 2018, 30, 1800396.

[64] S.H. Sun, G.X. Zhang, N. Gauquelin, N. Chen, J.G. Zhou et al., *Sci. Rep*. 2013, 3, 1775.

[65] C. Xu, S. De, A. M. Balu, M. Ojeda, R. Luque, Chemical Communications, 2015, 51, 6698-6713.

[66] X. Cui, H. Li, Y. Wang, Y. Hu, L. Hua, H. Li, et al., *Chem*, 2018, 4, 1902-1910.

[67] T. Gan, Q. He, H. Zhang, H. Xiao, Y. Liu, Y. Zhang, H. Ji, *Chemical Engineering Journal*, 389, 124490.

[68] D. Deng, X. Chen, L. Yu, X. Wu, Q. Liu, et al., *Sci. Adv.*, 2015, 1, e1500462.

[69] E. Boutin, L. Merakeb, B. Ma, B. Boudy, M. Wang, J. Bonin, E. Anxolabehere-Mallart, M. Robert, *Chem. Soc. Rev*., 49 (2020), 5772-5809.

[70] Y. Wu, Z. Jiang, X. Lu, et al. *Nature,* 2019*, 575*, 639-642.

[71] J. Su, J.-J. Zhang, J. Chen, Y. Song, L. Huang, M. Zhu, B. I. Yakobson, B. Z. Tang, R. Ye, *Energy & Environmental Science*, 2021, 14, 483-492.

[72] A. K. Datye, *J. catal*., 2003, 216,144.

[73] C. Kübel, A. Voigt, R. Schoenmakers, M. Otten, D. Su, T. Lee, A. Carlsson, J. Bradley, *Microsc Microanal*. 2005, 11, 378-400.

[74] Z. Du, X. Chen, W. Hu, C. Chuang, S. Xie, A. Hu, W. Yan, X. Kong, X. Wu, H. Ji, L. Wan, *Journal of the American Chemical Society*, 2019, 141, 3977-3985.

[75] Y. Zhao, K. Yang, Z. C. Wang, X. Yan, S. Cao, Y. Ye, Q. Dong, X. Zhang, J. Thorne, L. Jin, K. Materna, A. Trimpalis, H. Bai, S. Fakra, X. Zhong, P. Wang, X. Pan, J.-H. Guo, M. Flytzani-Stephanopoulos, G. G Brudvig, V. Batista, and D. Wang, *PNAS*, 2018, 115, 2902-2907.

[76] Christina H. M. van Oversteeg, H. Q. Doan, Frank M. F. de Groot, T. Cuk, *Chem Soc. Rev.,* 2017, 46, 102.

[77] H. Jin, C. Guo, X. Liu, J. Liu, A. Vasileff, Y. Jiao, Y. Zheng, S. Qiao, *Chemical Review*, 2018, 118, 6337.

[78] J. Li, S. Chen, N. Yang, M. Deng, S. Ibraheem, J. Deng, J. Li, L. Li, Z. Wei, *Angew. Chem. Int. Ed.*, 2019, 58, 7035-7039.

[79] D. Deng, X. Chen, L. Yu, X. Wu, Q. Liu, Y. Liu, H. Yang, H. Tian, Y. Hu, *Science Advances*, 2015, 1, e1500462.

[80] X. Li, X. Yang, J. Zhang, Y. Huang, B. Lin, *ACS Catal*., 2019, 9, 2521.

[81] R. N. Panda, M. F. Hsieh, R. J. Chung, T. S. Chin, *J. Phys. Chem .Solid*, 2003, 64, 193.

[82] T. Xu, X. Huang, *Fuel*, 2010, 89 (9), 2185-2190.

[83] C. Gallenkamp, U. I. Kramm, V. Krewald, *Chem. Commun*., 2021, 57, 859-862.

[84] W. Lim, S. Kim, C. Jo, J. Lee, *Angew. Chem. Int. Ed.*, 2019, 58, 18746-18757.

[85] J. Liang, Z. Sun, F. Li, H. Cheng, *Energy Storage Mater.*, 2016, 2, 76-106.

[86] J. Schuster, G. He, B. Mandlmeier, T. Yim, K. Lee, T. Bein L. Nazar, *Angew.*

Chem. Int. Ed. Engl., 2012, 51(15):3591-3595.

[87] S. Zhang, *J. Power Sources*, 2013, 231, 153.

[88] Z. Wei Seh, Y. Sun, Q. Zhang, Y. Cui, *Chem. Soc. Rev.*, 2016, 45, 5605-5634.

[89] J. Zhu, P. Zhu, C. Yan, X. Dong, X. Zhang, *Progress in Polymer Science*, 2019, 90, 118. 90.

[90] H. Peng, J. Huang, X. Cheng, Q. Zhang, *Advanced Energy Materials*, 2017, 7, 1700260.

[91] Z. Seh, W. Li, J. Cha, et al., *Nat. Commun.*, 2013, 4, 1331.

[92] Y. Guo, H. Li, T. Zhai, *Advanced Materials*, 2017, 29, 1700007.

[93] R. Xu, J. Lu, K. Amine, *Advanced Energy Materials*, 2015, 5, 1500408.

[94] S. Jing, P. Ding, Y. Zhang, H. Liang, S. Yin, P. Tsiakaras, *Ionic*, 2019, 25, 5297.

[95] Z. Zhuang, Q., Kang, D. Wang, et al., *Nano Research*, 2020, 13, 1856-1866.

[96] L. Fang, Z. Feng, L. Cheng, R. Winans, T Li, *Small Methods*, 2020, 4, 2000315.

[97] K. Xu, M. Zhu, L. Zhu, D. Li, W. Zhang, T. Huang, Y. Zhu, Y. Qian, Journal of Materials Chemistry A, 2020, 8 (15): 7100-7108.

[98] B. Li, L. Kong, C. Zhao, Q. Jin ,X. Chen, H. Peng, J. Qin, J. Chen, H. Yuan, Q. Zhang, J. Huang, *InfoMat*, 2019, 1, 533-541.

[99] J. Wang, L. Jia, H. Lin, Y. Zhang, *ChemSusChem*, 2020, 13, 3404-3411.

[100] Y. Li, G. Chen, J. Mou, Y. Liu, S. Xue, T. Tan, W. Zhong, Q. Deng, T. Li, J. Hu, C. Yang, K. Huang, M. Liu, *Energy Storage Materials*, 2020, 28, 196-204.

[101] Q. Shao, L. Xu, D. Guo, Y. Su, J. Chen, *Journal of Materials Chemistry A*, 2020, 8, 23772-23783.

[102] F. Wang, J. Li, J. Zhao, Y. Yang, C. Su, Y. L. Zhong, Q.-H. Yang, J. Lu, *ACS Mater. Lett*. 2020, 2, 1450-1463.

[103] Z. Du, X. Chen, W. Hu, C. Chuang, S. Xie, A. Hu, W. Yan, X. Kong, X. Wu, H. Ji, L.-J. Wan, *J. Am. Chem. Soc.*, 2019, 141, 3977-3985.

[104] L. Zhang, D. Liu, Z. Muhammad, F. Wan, W. Xie, Y. Wang, L. Song, Z. Niu, Jun Chen, *Adv. Mater.*, 2019, 31, 1903955.

[105] J. Wang, L. Jia, J. Zhong, Q. Xiao, C. Wang, K. Zang, H. Liu, H. Zheng,J. Luo, J. Yang, H. Fan, W. Duan, Y. Wu, H. Lin, Y. Zhang, *Energy Storage Materials*, 2019,

18: 246-252.

[106] G. Zhou, S. Zhao, T. Wang, S. Z. Yang, B. Johannessen, H. Chen,C. Liu, Y. Ye, Y. Wu, Y. Peng, C. Liu, S. P. Jiang, Q. Zhang, Y. Cui, *Nano Lett.*, 2020, 20, 1252-1261.

[107] K. Zhang, Z. Chen, R. Ning, S. Xi, W. Tang, Y. Du, C. Liu, Z. Ren, X. Chi, M. Bai, C. Shen, X. Li, X. Wang, X. Zhao, K. Leng, S. Pennycook, H. Li, H. Xu, K. Loh, K. Xie, *ACS Appl. Mater. Interfaces*, 2019, 11, 25147-25154.

[108] J. Xie, B. Li, H. Peng, Y. Song, M. Zhao, X. Chen, Q. Zhang, J. Huang, *Advanced Materials*, 2019, 31, 1903813.

[109] Y. Qiu, L. Fan, M. Wang, X. Yin, X. Wu, X. Sun, D. Tian, B. Guan, D. Tang, N. Zhang, *ACS Nano*, 2020, 14, 16105.

[110] W. Zhang, Y. Hu, L. Ma, G. Zhu, Y. Wang, X. Xue, R. Chen, S.Yang, Z. Jin, *Adv. Sci.*, 2018, 5, 1700275.

[111] Y. Hori, H. Wakebe, T. Tsukamoto, O. Koga, *Eletrochim Acta*, 1994, 39, 1833-1839.

[112] Y. Wang, L. Cao, N. J. Libretto, X. Li, C. Li, Y. Wan, C. He, J. Lee, J. Gregg, H. Zong, D. Su, J. T. Miller, T. Mueller, C. Wang, *J. Am. Chem. Soc.* 2019, 141, 16635.

[113] K. Qi, Y. Zhang, J. Li, C. Charmette, M. Ramonda, X. Cui, Y. Wang, Y. Zhang, H. Wu, W. Wang, X. Zhang, D. Voiry, *ACS Nano*, 2021, 15, 4, 7682-7693.

[114] K. P. Kuhl, E. R. Cave, D. N. Abramc, Thomas F. Jaramillo, *Energy Environ. Sci.*, 2012, 5, 7050-7059.

[115] R. Reske, H. Mistry, F. Behafarid, B. R. Cuenya, and P. Strasser, *J. Am. Chem. Soc.* 2014, 136, 19, 6978-6986.

[116] L. Gao, X. Li, Z. Yao, H. Bai, Y. Lu, C. Ma, S. Lu, Z. Peng, J. Yang, A. Pan, H. Huang, *J. Am. Chem. Soc.* 2019, 141, 18083.

[117] W. Luc, X. Fu, J. Shi, et al., *Nat. Catal.*, 2019, 2, 423-430.

[118] Y. Hori, A. Murata, R. Takahashi, *J. Chem. Soc. Faraday Trans.*, 1 1989, 85, 2309-2326.

[119] C. S. Diercks, S. Lin, N. Kornienko, E. A. Kapustin, E. M. Nichols, C. Zhu, Y. Zhao, C. J. Chang, O. M. Yaghi, *J. Am. Chem. Soc.*, 2018, 140, 1116.

[120] Y. Wu, Z. Jiang, X. Lu, et al., *Nature*, 2019, 575, 639-642.

[121] J. Gu, C. Hsu, L. Bai L, H. Chen, X. Hu, *Science*, 2019, 364,1091-1094.

[122] Y. Pan, C. Zhang, Z. Liu, C. Chen, Y. Li, *Matter*, 2020, 2, 78-110.

[123] Y. Li, C. Chen, R. Cao, Z. Pan, H. He, K. Zhou, Applied Catalysis B: Environmental, 2020, 268, 118747.

[124] J. Jiao, R. Lin, S. Liu, et al., *Nature Chem.*, 2019, 11, 222-228.

[125] W. Xie, H. Li, G. Cui, J. Li, Y. Song, S. Li, X. Zhang, J. Y. Lee, M. Shao, M. Wei, *Angew. Chem., Int. Ed.*, 2021, 60, 7382.

[126] B. You, N. Jiang, X. Liu and Y. Sun, *Angew. Chem., Int. Ed.*, 2016, 55, 9913-9920.

[127] B. You, X. Liu, N. Jiang and Y. Sun, *J. Am. Chem. Soc.*, 2016, 138, 13639-13646.

[128] S. Verma, S. Lu and P. J. A. Kenis, *Nat. Energy*, 2019, 4, 466-474.

[129] D. A. Bulushev, J. R. H. Ross, *ChemSusChem*, 2018, 11, 821.

[130]X. Zhu, X. Dou, J. Dai, X. An, Y. Guo, L. Zhang, S. Tao, J. Zhao, W. Chu, X. C. Zeng, C. Wu and Y. Xie, *Angew. Chem., Int. Ed.*, 2016, 55, 12465-12469.

[131] L. Song, N. Fu, B. G. Ernst, W. H. Lee, M. O. Frederick, R. A. DiStasio, Jr. and S. Lin, *Nat. Chem.*, 2020, 12, 747-754.

[132] G. Wen, Q. Gu, Y. Liu,et al., *Angew. Chem., Int. Ed.*, 2018, 57, 1-6.

[133] Y. Li, X. Wei, L. Chen, J. Shi and M. He, *Nat. Commun.*, 2019, 10, 5335.

[134] M. Li, X. Deng, K. Xiang, Y. Liang, B. Zhao, J. Hao, J. L. Luo, X. Z. Fu, ChemSusChem, 2020, 13, 914.

[135] X. Chen, Y. Liu, J. Wu, Mol. Catal., 2020, 483, 110716.

[136] D. R. Palo, R. A. Dagle, J. D. Holladay, Chem. Rev. 2007, 107, 3992.

[137] L. Du, Y. Shao, J. Sun, G. Yin, C. Du, Y. Wang, *Catal. Sci. Technol*. 2018, 8, 3216.

[138] Y. Tong, X. Yan, J. Liang, S. X. Dou, *Small*, 2021, 17, 1904126.

[139] M. A. F. Akhairi, S. K. Kamarudin, *Int. J. Hydrogen Energy*, 2016, 41, 4214.

[140] D. Si, B. Xiong, L. Chen, J. Shi, *Chem Catalysis*, 1, 941-955.

[141] S.Rezaee, S. Shahrokhian, *Appl. Catal., B*, 2019, 244, 802;

[142] A. Badalyan, S. S. Stahl, *Nature*, 2016, 535, 406.

[143] G. M. K. Tolba, N. A. M. Barakat, A. M. Bastaweesy, E. A. Ashour, W. Abdelmoez, M. H. El-Newehy, S. S. Al-Deyab, H. Y. Kim, *J. Mater. Sci. Technol.*, 2015, 31, 97

[144] X. Cui, P. Xiao, J. Wang, M. Zhou, W. Guo, Y. Yang, Y. He, Z. Wang, Y. Yang, Y. Zhang, Z. Lin, *Angew. Chem. Int. Ed. Engl.*, 2017. 56, 4488-4493.

[145] Y. Wu, J. Tian, S. Liu, B. Li, J. Zhao, L. Ma, D. Li, Y. Lan, X. Bu, *Angew. Chem. Int. Ed.*, 2019, 58, 12185-12189.

[146] H. Huang, C. Yu, X. Han, H. Huang, Q. Wei, W. Guo, Z. Wang, J. Qiu, *Energy Environ. Sci.*, 2020,13, 4990-4999.

Chapter 2

Atomically dispersed Fe in C₂N based Catalyst as Sulfur Host for Efficient Lithium-Sulfur Batteries
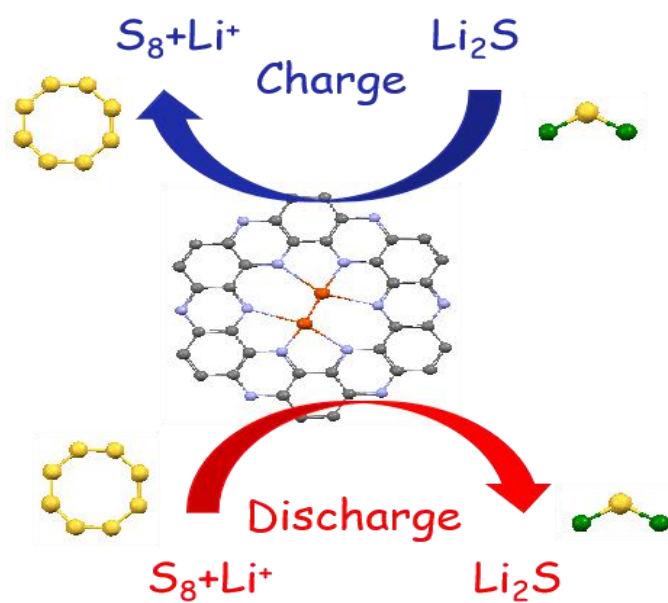
2.1 Introduction

Lithium-sulfur batteries (LSBs) are considered one of the main candidate technologies for next generation energy storage systems. The main advantages of LSBs are their high theoretical capacity (~1675 mAh g^{-1}) and high energy density (~2600 Wh kg^{-1}), which is about five times higher than that of lithium-ion batteries.[1-4] Besides, sulfur, the active cathode material, is highly abundant in the earth crust and it has a low cost and no major environmental, health, and safety issues.[5] While LSBs are extremely appealing, some serious drawbacks still impede their practical application. These drawbacks include the low electrical conductivity of sulfur and lithium sulfides, the sluggish Li-S reaction kinetics, the large volume changes during lithiation/delithiation and the shuttle effect of soluble lithium polysulfide (LiPS) Li_2S_x (3<x≤8). The latter has associated an irreversible loss of active material at the cathode and the corrosion of the lithium metal anode, overall resulting in a rapid capacity fading and a poor coulombic efficiency that greatly reduce the rate performance, cycling stability and lifespan of LSBs.[6][7]

An effective strategy to increase electrical conductivity and accommodate volume changes is the use of high surface area and high porosity carbon-based materials as sulfur hosts,[15] e.g. mesocarbon,[8] graphene,[9] porous carbon,[10] carbon nanotubes,[11] conducting polymers such as polyaniline [12] or covalent organic frameworks (COFs).[13][14] These porous materials also limit LiPS diffusion by hampering their transport, but they just weakly physically interact with LiPS, which is insufficient to inhibit the shuttle effect. To overcome this limitation, heteroatoms with stronger electronegativity, e.g. O, N, S, P, have been introduced in carbon-based materials to improve their interaction with LiPS.[16-18] While several of these heteroatom-doped carbon-based sulfur hosts have demonstrated improved electrochemistry performance, this strategy is far from its optimization. The main difficulty toward optimizing these complex materials is the intricate characterization of the heteroatom dispersion, which translates in a very challenging control of the materials parameters during synthesis and an unreliable characterization of the

electrochemical mechanisms and the structure-performance relationships.

Recently, 2D organic materials with a periodic porous structure, large surface area, and controllable chemical composition and functionality have been demonstrated as excellent sulfur hosts in LSBs.[19][20] On the other hand, single-atom catalysts (SACs) based on atomically dispersed metal atoms have demonstrated outstanding catalytic performances in several reactions, including Li-S redox reactions.[21-25] Besides maximizing the metal dispersion, the main advantage of SACs is their high surface energy, which allows decreasing the energy barrier of several catalytic processes.

C_2N, a 2D graphene-like layered organic material was synthesized for the first time in 2015 through a wet chemistry method by Beak and co-workers.[43] Since then, several C_2N-based materials have been developed for their application in electrocatalysis and batteries, e.g Ru/C_2N for hydrogen evolution,[26][27] Fe/C_2N for oxygen reduction,[28] and C_2N for lithium-ion batteries.[29] In C_2N, pores are surrounded by six pyridine nitrogen atoms, which can be either coordinated with a metal atom or used themselves as traps for polysulfides and lithium ions, as predicted theoretically.[30] Using DFT calculations, Lin and co-workers further predicted that metal atoms embedded in C_2N as SACs could hinder the shuttle effect and accelerate the electrochemical conversion between sulfur and Li_2S.[31] Nevertheless, the extremely challenging preparation of C_2N-based catalysts containing an atomic metal distribution has so far prevented to experimentally corroborate these expectations.

Here, we report on the synthesis of atomically and uniformly dispersed iron on C_2N frameworks (Fe/C_2N). These new catalysts present several advantages as sulfur host in LSBs. Firstly, C_2N frameworks show a high polarity and excellent electrical conductivity due to the abundance of pyrazine nitrogen and their planar two-dimensional (2D) π-conjugated properties. Secondly, C_2N is a highly porous and high surface area framework, allowing the efficient transport of lithium ions and the effective absorption of polysulfide. Thirdly, two iron atoms can be trapped in each hole, coordinating to the neighbor nitrogen atoms, to act as active sites for the conversion reaction of polysulfide during the charging and discharging processes. For

all these reasons, the produced Fe/C$_2$N based catalysts were tested as sulfur cathode host materials in LSBs.

2.2 Experimental Section

2.2.1 Materials

Ethylenediamine (99%), 1,3-dioxolane (DOL, 99.5%), lithium nitrate (99.98%), lithium sulfide (99.9%), and chloroanilic acid (98%) were purchased from Alfa Aesar. Sulfuric acid (95%~98%), N-methyl-pyrrolidone (NMP, 99.99%), diethyl ether (99.9%), iron (III) nitrate nonahydrate (>98%), and tetraethylene glycol dimethyl ether (99%) were purchased from Sigma-Aldrich. Lithium bis(trifluoromethanesulfonyl) imide (LiTFSI) (99%) was purchased from Acros Organics and dimethoxymethane (DME, 99%) is from Honeywell. All chemicals were used without further purification.

2.2.2 Synthesis of hexaaminobenzene (HAB):[32]

First, chloroanilic acid was placed into a 15 mL glass vial which was put in a 0 °C ice bath, under vigorous stirring. Next, 5.64 mL ethylenediamine and a few drops of concentrated sulfuric acid were added. Then the ice bath was removed, and the obtained solution was warmed up to room temperature. Afterward, the solution was transferred to a 15 mL Teflon autoclave, the autoclave was kept at 80 °C for 72 h to complete the amination reactions. The solution was cooled to room temperature. The obtained mixture was vacuum filtrated using a polytetrafluoroethylene (PTFE) membrane (0.47 μm), rinsed with diethyl ether and degassed ethanol three times, and freeze-dried overnight. The identity of the final product was confirmed by ^{1}H NMR . ^{1}H NMR (400 MHz, H$_2$O-d_2, δ): 3.39 (s, 2H, NH2). (**Figure 2-1**)
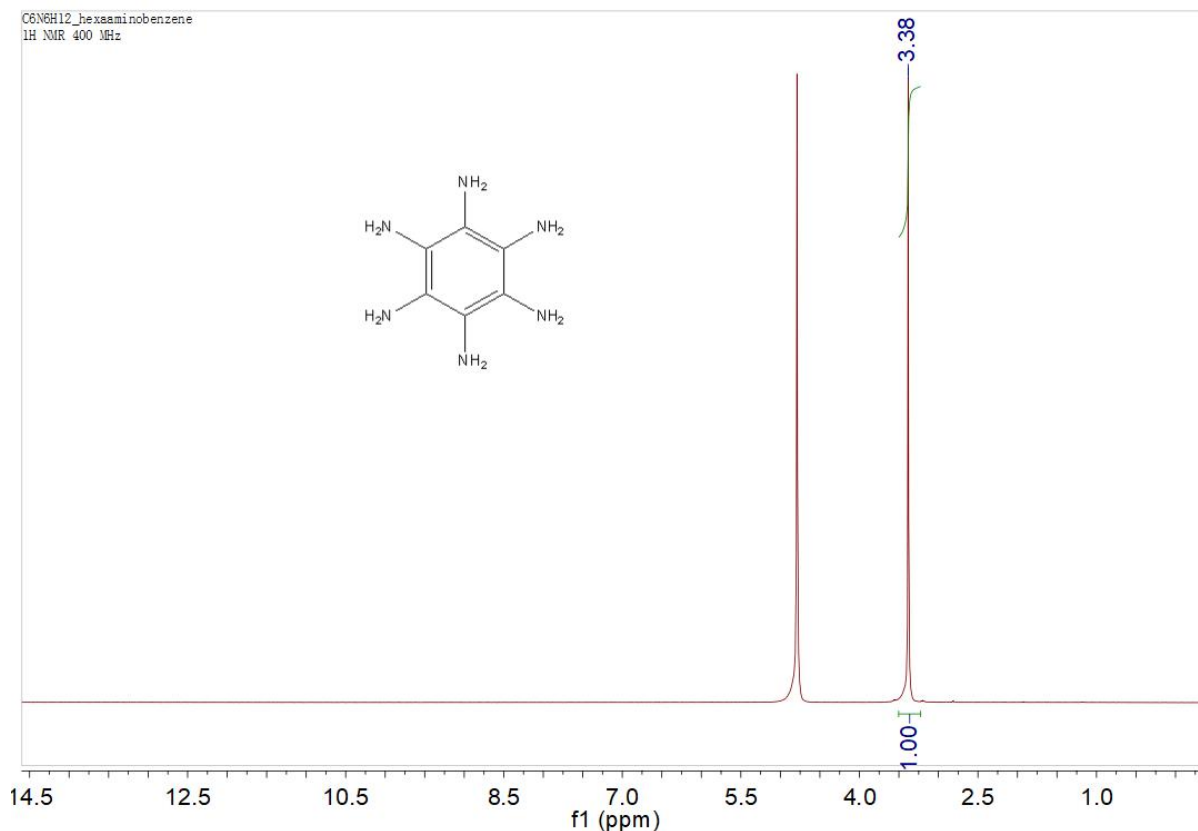
Figure 2.1. ^{1}H NMR spectrum of hexaaminobenzene (HAB)

2.2.3 Synthesis of C$_2$N:[33]

In a typical reaction experiment, an equal mol ratio of hexaaminobenzene and chloroanilic acid, and degassed NMP were put into a three-necked round bottom flask under argon gas placed in an ice bath. Under vigorous stirring, a few drops of concentrated sulfuric acid were added. Then the ice bath was removed, and the mixture was warmed up to room temperature. The resulting solution was heated to 175 °C for 12 h. After cooling to room temperature, the mixture was vacuum filtrated, and washed with ethanol and water for three times and freeze-dried for 24 h. Finally, the obtained black solid was annealed at 450 °C for 3 h under argon gas with a ramp rate of 5 °C/min.

2.2.4 Synthesis of Fe/C$_2$N

C$_2$N (200 mg) and iron(III) nitrate nonahydrate (404 mg) were added to 15 mL ethanol. The resulting solution was stirred for 48 h at room temperature, and then

vacuum filtrated and dried at 60 °C in an oven. The obtained precursor was annealed at 700 °C for 3 h. After that, the black solid was placed into 10 mL 3M HCl solution and stirred for 2 days to remove iron nanoparticles. The material was centrifuged, washed with water and ethanol for several times, and finally vacuum dried at 120 °C for 12 h.

2.2.5 Preparation of S@C$_2$N and S@Fe/C$_2$N composites

Following a typical melt-diffusion procedure, Fe/C$_2$N (or C$_2$N) was mixed with sublimated sulfur in a mass ration of 1:3 through uniform milling, then transferred to a clean vial, placed in a Teflon autoclave, sealed under argon gas and heated for 12 h at 155 °C. To remove the redundant sulfur outside of the Fe/C$_2$N, the powder was immersed in a 10 mL CS$_2$ and ethanol solution (1:4, volume ratio) for 10 min twice.

2.2.6 Li$_2$S$_4$ adsorption tests

Sulfur and Li$_2$S with a molar ratio of 3:1 were mixed with appropriate amounts of DME and DOL (volume ratio of 1:1) under vigorous stirring overnight, until a homogeneous dark brown solution was formed. To test the adsorption ability for polysulfide, 20 mg active materials (Fe/C$_2$N, C$_2$N and Super P) were covered by a 3.0 mL 10×10^{-3} M Li$_2$S$_4$ solution in a glass vial, kept shaking and ageing overnight.

2.2.7 Electrochemical measurements

To prepare the cathodes, active materials (S@C$_2$N, S@Fe/C$_2$N), Super P and PVDF binders were mixed with a mass ratio of 8:1:1 dispersing in N-methyl-2-pyrrolidone (NMP, 99.99%, Sigma-Aldrich). The obtained homogeneous slurry was cast on an aluminium foil current collector and then vacuum dried at 60 °C overnight. The sulfur was loaded in small plates (with a diameter of 12 mm) and was stamped in a coated aluminium film with about 1 mg cm^{-2}. For the high sulfur loading, we used a coating of 3.0 mg·cm^{-2}. The coin cells were assembled in an argon-filled glove box for the electrochemical tests. The anode used was a Li foil and Celgard 2400 membranes were used as separators. 1.0 M lithium bis(trifluoromethanesulfony) imide (LiTFSI)

and 0.2 M $LiNO_3$ dissolved in the mixed solvent of DOL and DME (1:1 v/v) were used as the electrolyte. Each coin cell contained about 20 μL of the electrolyte. To allow the electrolyte to penetrate the electrode sufficiently, all coin cells were aged for several hours before testing. Galvanostatic charge/discharge (GCD) measurements were conducted between 1.7 and 2.8 V (vs. Li^+/Li) in a Neware BTS4008 battery cycler. A battery tester BCS-810 from BioLogic was used to perform the cyclic voltammetry (CV) tests with different scan rates, ranging from 0.1 to 0.4 mV s^{-1}. Electrochemical impedance spectroscopy (EIS) tests were conducted in the frequency range from100 kHz to 0.01 Hz.

2.2.8 Symmetric cell assembly and tests

The electrodes for the symmetric cell were prepared using the same method as that for the lithium-sulfur battery. The working and counter electrodes utilized two pieces of the same electrode (with an average loading of ~ 0.5 mg cm^{-2}). Each coin cell contained 40 μL of electrolyte (0.5 M Li_2S_6 and 1 M LiTFSI in DOL/DME (v/v = 1/1)). CV tests were carried out at a scan rate of 10 mV s^{-1} and EIS measurements were performed in a frequency range from 100 kHz to 0.01 Hz.

2.2.9 Li_2S_2 nucleation and dissolution tests

Standard 2032 coin cells were used to analyze the nucleation and dissolution of the Li_2S. Equal amounts of Fe/C_2N and C_2N catalysts were dispersed uniformly in ethanol. Then, the catalysts were loaded on carbon paper to work as cathodes. Li foil worked as anode. The catholyte consisted of 20 μL of 0.25 M Li_2S_8 and 1.0 M LiTFSI in tetraethylene glycol dimethyl ether solution. In the case of the anolyte, it consisted of 20 μL of 1.0 M LiTFSI solution without Li_2S_8 in the same solvent as the catholyte. To transform the polysulfide Li_2Sx (x=6, 8) to Li_2S_4 we used the following procedure. The cells were kept at 2.05 V until the current dropped to 0.01 mA. Fresh coin cells were assembled to perform the dissolution of Li_2S, which were discharged at 0.10 mA to 1.80 V firstly, following galvanostatically discharge at 0.01 mA to 1.80 V for reducing S species into solid Li_2S, completely. Subsequently, the cells were

potentiostatically charged at 2.40 V for transforming the Li_2S into polysulfide until the charge current was lower than 0.01 mA.[49]

2.2.10 Materials characterization

Crystal structures were characterized using powder XRD in a Bruker AXS D8 Advance X-ray diffractometer. (Cu-Kα radiation, λ = 1.5106 Å, 40 kV and 40 mA; Bruker, Germany). TGA was performed under air or nitrogen gas at a heating rate of 10 °C/min using a Thermogravimetric Analyzer Q200. SEM images were obtained in a ZEISS Auriga Field emission scanning electron microscopy (FE-SEM) operating at 20 kV. HRTEM studies were conducted in a FEI Tecnai F20 microscope at an operating voltage of 200 kV. HAADF-STEM images and elemental mapping were obtained in a spherical aberration-corrected transmission electron microscope FEI Titan 80-300 at 300 kV and FEI Titan G2 80-200 ChemiSTEM with four EDX detectors and operated at 200 kV. X-ray photoelectron spectroscopy (XPS) data was obtained by using 150 W and a Phoibos 150 MCD-9 detector. The XANES and EXAFS were performed at the Beijing Synchrotron Radiation Facility (BSRF). The obtained XAFS data were analyzed according the standard procedures using ATHENA program.[52] The nitrogen adsorption-desorption isotherms were recorded in a Tristar II 3020 Micromeritics system at 77 K. The specific surface area and the pore size distribution were calculated by Brunauer–Emmett–Teller (BET) and Barrett-Joyner-Halenda (BJH) methods.

2.2.11 DFT Calculation

The spin-polarized DFT computations were implemented using the Perdew-Burke-Ernzerhof (PBE) functional, as performed in the VASP package.[54] The project augmented wave (PAW) approach was used with a kinetic cutoff energy of 450 eV. According to previous literature,[55] the molecule $C_{36}N_{12}H_{12}$ with one hole was used to represent the periodic C_2N system. To avoid the neighboring image interactions, a 2×2×1 supercell of Fe/C_2N was created and a vacuum spacing of 15 Å was inserted along the normal direction. The first Brillouin zone was sampled with

$3\times3\times1$ and $5\times5\times1$ Γ-centered k-points grids for geometric optimization and electronic structure calculations. All atoms were relaxed to their equilibrium positions when the total energy change was finally converged to 10^{-5} eV/atom; and the force on each atom was converged to 0.04 eV/Å. The adsorption energy (E_{ads}) is calculated through the following Equations based on the energy difference of the system before and after LIPS adsorption.[22]

2.3 Results and Discussions

2.3.1 Characterization of Prepared Samples

Fe/C_2N composites were synthesized as illustrated in **Figure 2.2a**. First, C_2N was prepared via a polycondensation reaction and a subsequent annealing process.[32][33] Next, Fe/C_2N was obtained by a pyrolysis treatment of a mixture of C_2N and iron (III) nitrate. Fe/C_2N displayed a granule-type morphology, as observed by scanning electron microscopy (SEM) (**Figure 2.3a**). High resolution transmission electron microscopy (HRTEM) analysis showed no iron nanoparticles attached or near the Fe/C_2N structure (**Figure 2.3b**); and the corresponding fast Fourier transform (FFT) or power spectra of the Fe/C_2N structure indicated C_2N to present an amorphous or a low crystallinity structure. As shown in Figure 1b and the enlarged image in Figure 1c, isolated Fe atoms (labeled in yellow) and double iron atom sites (labeled in red) which showed a low crystallinity structure were clearly observed using high angle annular dark field (HAADF)-aberration corrected (AC) scanning transmission electron microscopy (STEM), further these STEM images in **Figure 2.2b,c** supported that there was a homogenous distribution of iron. Energy-dispersive X-ray spectroscopy (EDS) elemental mapping (**Figure 2.2d and 2.3c**) showed that Fe, C, N and O are uniformly distributed. It is worth noting that the presence of oxygen was mainly due to the solution used for the TEM sample preparation and the fact that the C_2N structure present high polarity holes with high affinity for trapping oxygen and moisture. To confirm this low crystallinity structure and to discard any electron beam damage during HRTEM characterization, Fe/C_2N was further analyzed by powder X-ray diffraction (XRD, **Figure 2.3d**).
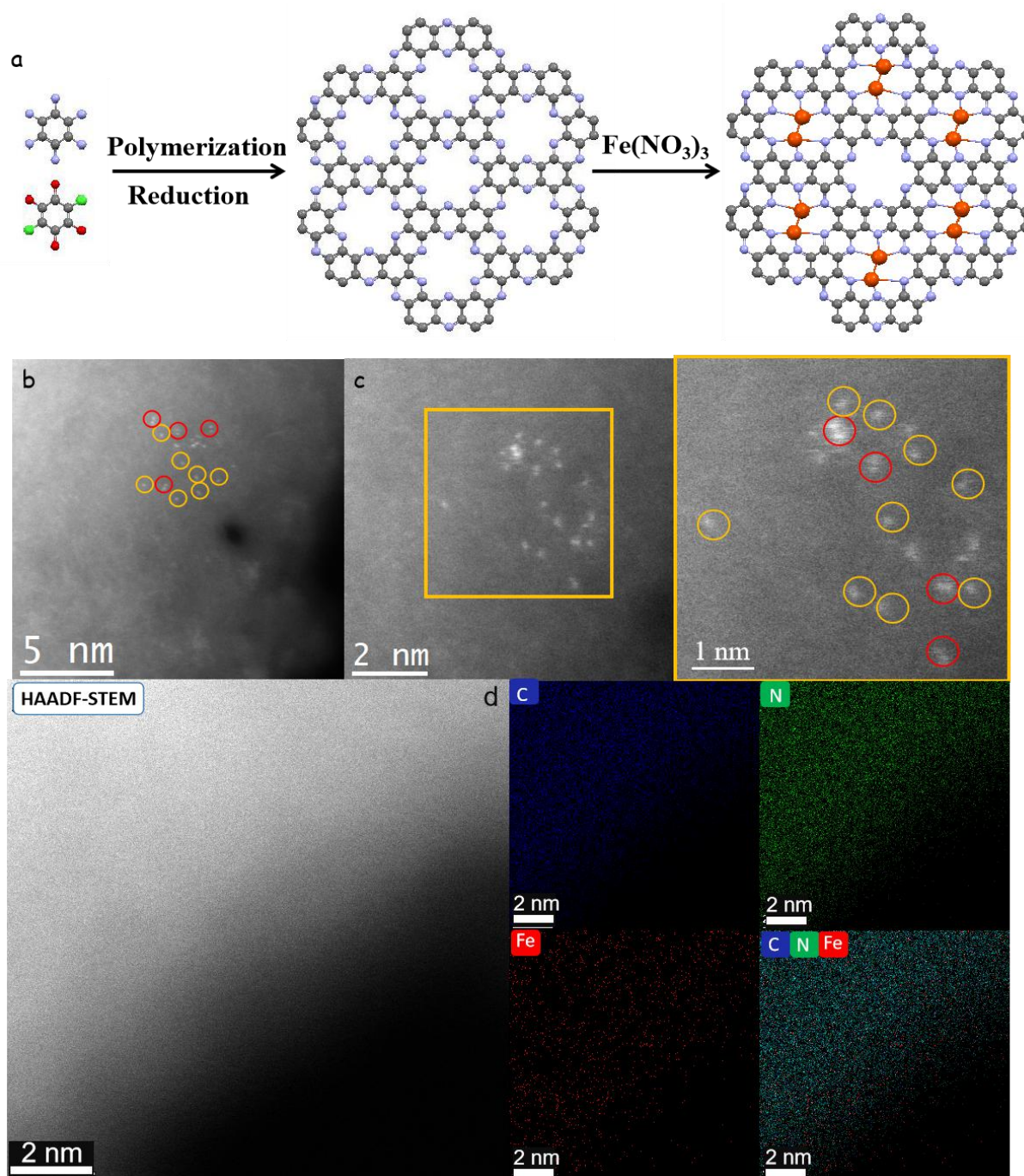
Figure 2.2. (a) Schematic illustration of the synthesis route for the Fe/C_2N 2D layered material (blue = nitrogen, grey = carbon, red = oxygen, green = chlorine, orange = iron). (b), (c) HAADF-STEM images of a Fe/C_2N catalyst showing the presence of atomically dispersed iron species: double iron clusters are circled in red and single iron atoms are circled in yellow. (d) High magnification STEM-HAADF image and atomic resolution EDS elemental mapping showing the elemental distribution in a Fe/C_2N sample.

66

XRD confirmed the C_2N to present a low crystallinity, with a main broad and weak diffraction peak at about 26.5°. This peak, common for graphene-like materials, corresponded to a 0.33 nm d-spacing of the (002) crystal plane of the C_2N layered structure. It is important to highlight that no peak corresponding to an iron-based lattice structure was observed. The latter experimental evidence confirmed the absence of Fe-related nanoparticles or clusters, thus pointing toward an atomic dispersion of Fe which is consistent with SEM-EDX, HRTEM and HAADF-AC-STEM results.
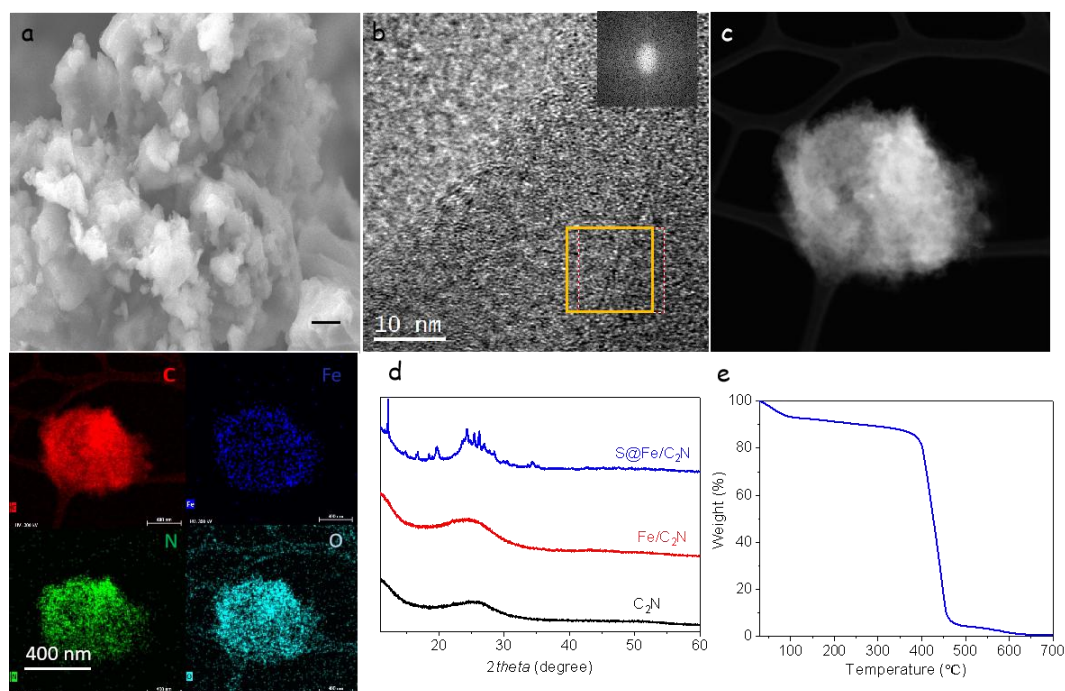
Figure 2.3 (a) SEM image of a Fe/C_2N catalyst (scale bar = 0.2 μm); (b) HRTEM image of a Fe/C_2N catalyst. (c) STEM-HAADF image and EDS elemental mapping (scale bar = 400 nm) showing the elemental distribution in a Fe/C_2N sample. (d) XRD patterns of $S@Fe/C_2N$, Fe/C_2N and C_2N; (e) TGA profile of Fe/C_2N under air.

Thermogravimetric analysis (TGA) showed the weight of Fe/C_2N samples to decrease to a 0.9 % when heating them to 700°C under air (**Figure 2.3e**). The remaining 0.9% mass was associated to Fe_2O_3, which is consistent with a 0.67 wt% iron content in the initial Fe/C_2N.

X-ray photoelectron spectroscopy (XPS), which confirmed the Fe concentration to be around 1 wt% (**Figure 2.4a**). Additionally, XPS was used to analyze the sample

chemical structure. The high-resolution N 1s XPS spectrum was fitted with three bands at 406.5 eV, 402.5 eV and 399.6 eV, which correspond to oxidized nitrogen (406.5 eV and 402.5 eV)[35][51] and pyrazine nitrogen (399.6 eV)[43] (**Figure 2.4b**). The C1s XPS spectrum was resolved into four bands (**Figure 2.4c**), associated to C=C (284.3 eV), C-N (285.1 eV), C=O (287.3 eV) and the C-heteroatom (288.9 eV).[26] The high-resolution Fe 2p XPS spectrum (**Figure 2.4d**) was fitted with 4 bands corresponding to two iron oxidation states. The main two bands were located at 724 eV ($2p_{1/2}$) and 710 eV ($2p_{3/2}$) and corresponded to a Fe^{2+} chemical state. The second doublet at 712.7 eV ($2p_{1/2}$) and 726.5 eV ($2p_{3/2}$) was assigned to satellite peaks.[35] From the linear combination fitting, the average valence state of the Fe atom is +1.767.
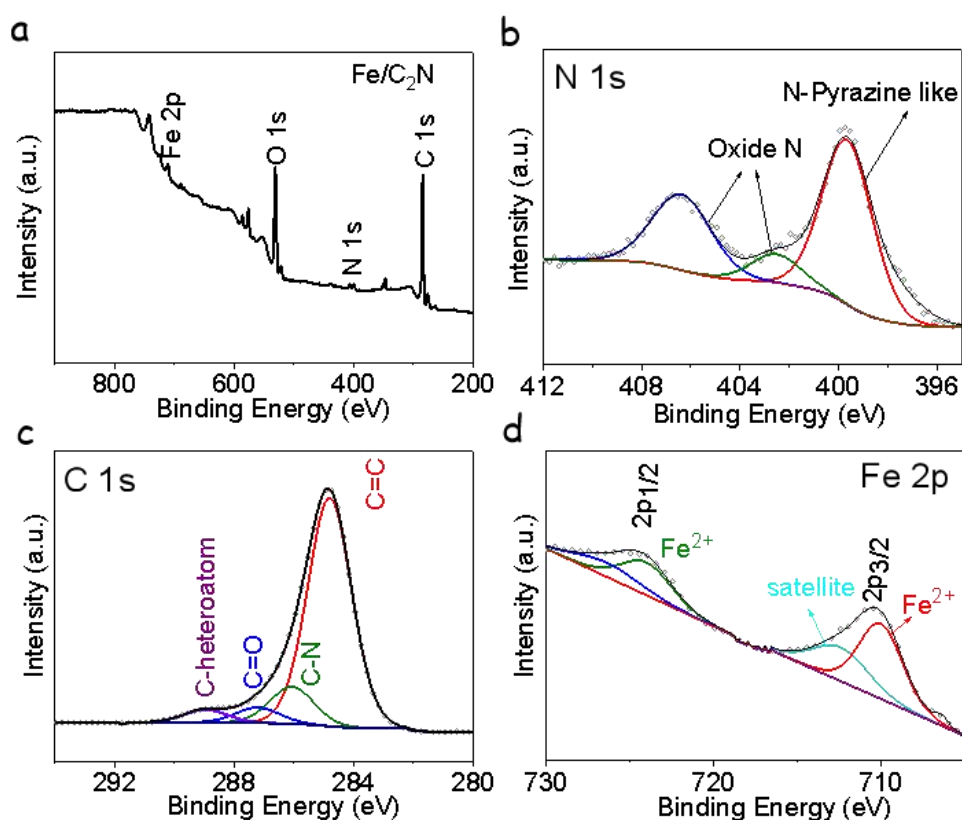
Figure 2.4 (a) XPS survey spectrum of Fe/C2N. (b)-(d) High resolution XPS spectra obtained from Fe/C_2N: (b) N 1s; (c) C 1s ; (d) Fe 2p.

To further reveal the chemical structure of Fe/C_2N and particularly the valence state of iron, X-ray absorption near-edge structure (XANES) analyses were carried out using an Fe foil and Fe_2O_3 as references. As shown in **Figure 2.5a**, the edge structure of

Fe/C$_2$N in the XANES spectra is much closer to that of Fe$_2$O$_3$ than to Fe, meaning that the valence state of Fe in Fe/C$_2$N is higher than that of the metallic state, in agreement with XPS results. The XANES spectrum of Fe/C$_2$N also displayed a small peak at 7112.9 eV, which is similar to that in iron phthalocyanine.[34][45] This peak indicated the presence of a Fe-N bond in Fe/C$_2$N catalysts.[35] Fourier transform was applied to the extended X-ray absorption fine structure (FT-EXAFS) spectra shown in **Figure 2.5b** and further used to investigate the coordination structure of Fe/C$_2$N. For the Fe foil, the main peak at 2.2 Å stands for the Fe-Fe bond, while for the Fe$_2$O$_3$, the peaks at 1.5 Å and 2.6 Å were associated to Fe-O and Fe-Fe bonds, respectively.[36][46] The FT-EXAFS spectrum of Fe/C$_2$N displayed a peak at 1.76 Å, in between that of Fe-Fe and Fe-O bonds. This peak was attributed to a Fe-N bond, demonstrating the coordination of in iron with nitrogen in Fe/C$_2$N. To obtain a higher detail of the Fe coordination within Fe/C$_2$N, the EXAFS spectra at the Fe K-edge was fitted (**Figure 2.5c**, **Table 2-1**). Fitting results showed that the coordination number of Fe-N is 3, and the average coordination number of Fe-Fe is 1.5, which discarded the presence of iron and iron oxide nanoparticles, consistently with SEM-EDX, HRTEM, XRD and XPS results. Notice that for atomically iron dispersed in the sample, the coordination number of Fe-Fe bond in our EXAFS fitting results is 1.5, which is consistent with HAADF-AC-STEM results, further confirming the successful iron atomic dispersion.[37]
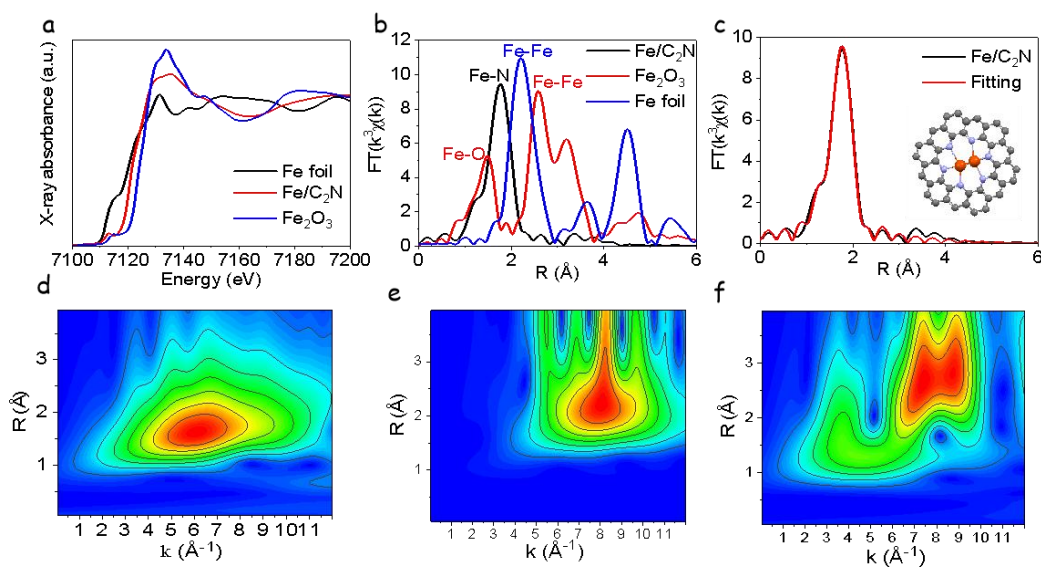
Figure 2.5. (a) XANES spectra of a Fe/C_2N sample and the reference Fe foil and Fe_2O_3. (b) k3-weighted FT-EXAFS spectra corresponding to the Fe K-edge. (c) EXAFS fitting curves in R space for the Fe/C_2N sample. (d) Wavelet transform plot for Fe/C_2N. Wavelet tansforms for the k3-weight Fe K-edge EXAFS information of reference samples: (a) Fe foil; (b) Fe_2O_3.

A wavelet transform (WT) analysis of the K3-weight EXAFS signal was carried out to further characterize the atom back scattering (**Figure 2.5d-f**). The reference Fe foil exhibited a WT maximum at 8.0 $Å^{-1}$, associated to Fe-Fe. The reference Fe_2O_3 exhibited two WT maxima, at 8.0 $Å^{-1}$ and 4.0 $Å^{-1}$, corresponding to Fe-Fe and Fe-O, respectively. Instead, Fe/C_2N displayed a single WT maximum located at 5.9 $Å^{-1}$, which was assigned to Fe-N.

Samples	Shell	CN	R(Å)	σ2	ΔE_0	R factor
Fe foil	Fe-Fe	8	2.46±0.01	0.0050	5.1±1.0	0.0055
	Fe-Fe1	6	2.84±0.01			
Fe/C_2N	Fe-N	3.0±0.1	1.97±0.02	0.0031	5.4±1.5	0.0016
	Fe-Fe	1.5±0.1	2.11±0.01	0.0029		

**Table 2-1** EXAFS fitting parameters at the Fe K-edge for various samples (S_0^2=0.76) *CN*: coordination numbers; [b]*R*: bond distance; [c]σ^2: Debye-Waller factors; [d] ΔE_0: the inner potential correction. *R* factor: goodness of fit. S_0^2 was set to 0.76, according to the experimental EXAFS fit of Fe foil reference by fixing CN as the known crystallographic value; δ: percentage.

2.3.2 Batty Performance and DFT Calculation
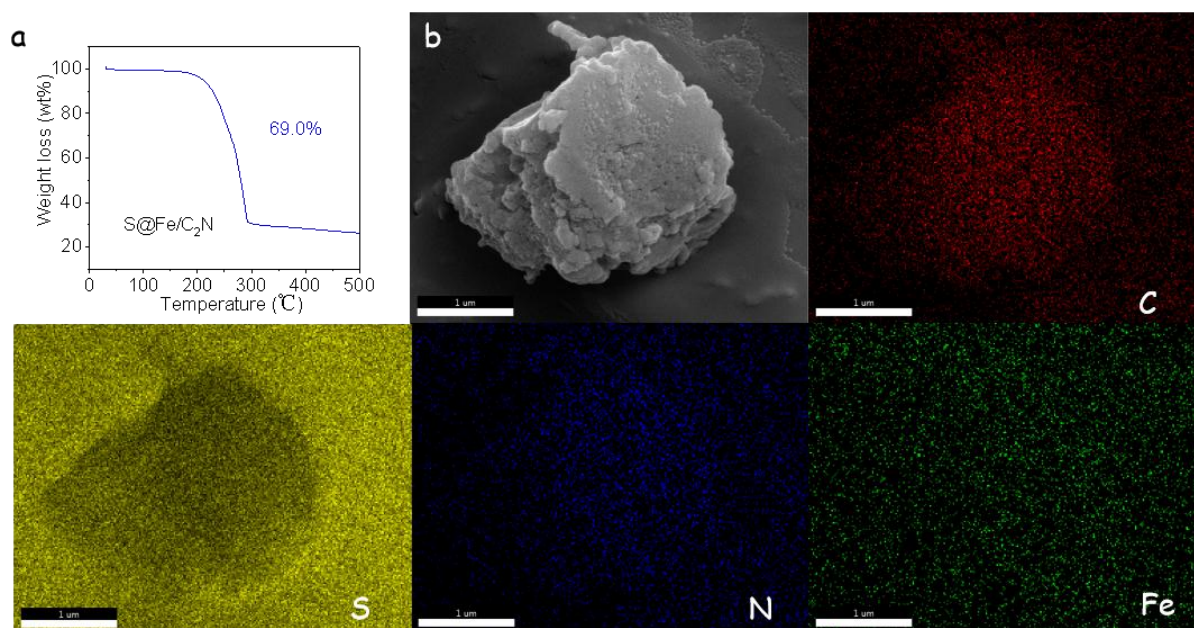
Figure 2.6 a) TGA profile from S@Fe/C$_2$N under nitrogen. (b) SEM EDX mapping of S@Fe/C$_2$N (scale bar = 1 μm).

To investigate the performance of Fe/C$_2$N as sulfur host in LSB cathodes, Fe/C$_2$N composites were loaded with ca. 70 wt% of elemental sulfur using the melt-impregnation method. In the following, the Fe/C$_2$N sample loaded with elemental sulfur will be named as S@Fe/C$_2$N. The XRD pattern obtained on the S@Fe/C$_2$N sample (**Figure 2.3d**) displayed the peak corresponding to the orthorhombic sulfur phase, confirming the presence of sulfur. TGA quantified the final percentage of sulfur in the S@Fe/C$_2$N composite to be 69 wt% (**Figure 2.6a**). EDX analysis showed the sulfur to be uniformly distributed on the surface of Fe/C$_2$N (**Figure 2.6b**). The Brunauer–Emmett–Teller (BET) specific surface area of Fe/C$_2$N was 223.4 m^2 g^{-1}, and it decreased with the sulfur loading to the 13.1 m^2 g^{-1} measured for S@Fe/C$_2$N. In parallel, the overall pore volume decreased from 0.10 to 0.04 cm^3 g^{-1} after sulfur loading. These results further confirmed sulfur to be infiltrated in the material cavities and pores (**Figure 2.7**). [23]
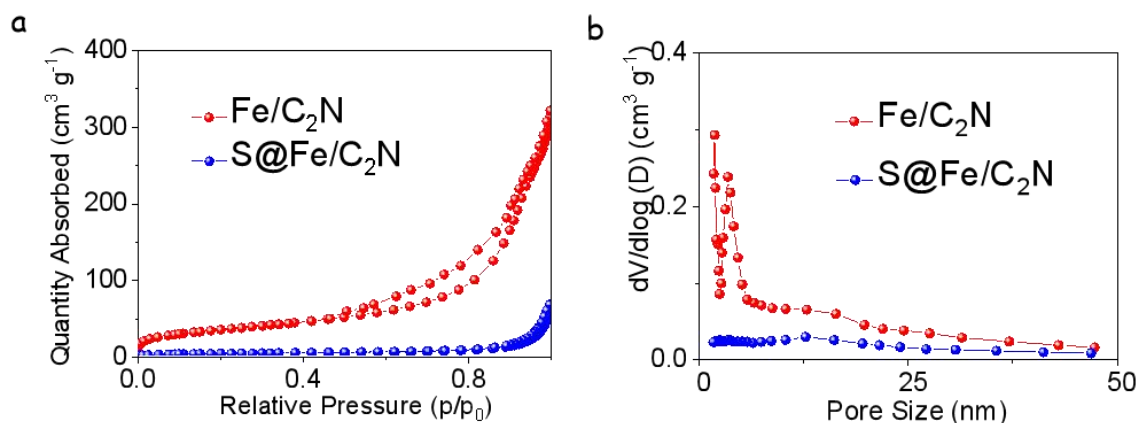
Figure 2.7. (a) N_2 adsorption-desorption isotherms of Fe/C_2N and S@Fe/C_2N. (b) Pore size distribution of Fe/C_2N and S@Fe/C_2N.

We evaluated the ability of Fe/C_2N to adsorb LiPS by immersing the same amount (20 mg) of Super P, C_2N and Fe/C_2N into a 10 mM solution of Li_2S_4. After 24 h, the solutions containing C_2N and Fe/C_2N were completely transparent, while the blank solution and the solution containing Super P showed a dark orange color (**Figure 2.8a**). These results demonstrate the excellent ability of C_2N-based materials for LiPS adsorption. The high-resolution Fe 2p and N 1s XPS spectra obtained on the Fe/C_2N before and after Li_2S_4 adsorption are displayed in **Figure 2.8b-c**. After Li_2S_4 adsorption, the Fe 2p and N 1s peaks showed a significant shift to higher binding energies, which denoted a strong chemical interaction between Li_2S_4 and Fe/C_2N
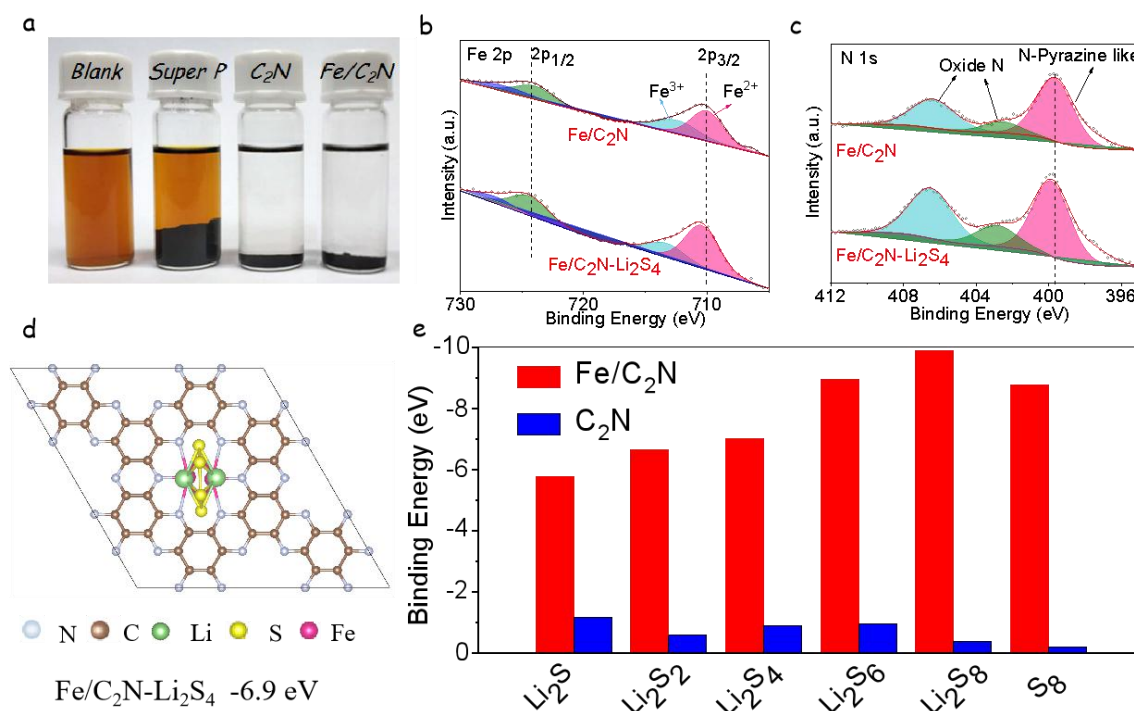
Figure 2.8 (a) Adsorption test: Digital photograph of the Li_2S_4 solution before and after (24 h) the addition of Super P, C_2N and Fe/C_2N, as marked in each flask cap. (b) High resolution XPS spectra of Fe 2p from Fe/C_2N before and after the Li_2S_4 adsorption test. (c) High resolution of XPS spectra of N 1s from Fe/C_2N before and after the Li_2S_4 adsorption test. (d) Adsorption configurations for Li_2S_4 on Fe/C_2N. (e) Binding energies between LiPS (Li_2S, Li_2S_2, Li_2S_4, Li_2S_6, Li_2S_8 and S_8) and C_2N or Fe/C_2N as calculated by DFT.

To further investigate the strong interaction between LiPS and Fe/C_2N, density functional theory (DFT) calculations were conducted. For comparison, the interaction between LiPS and C_2N was also calculated. Based on the XPS and XAFS results, the Fe-Fe double atom on C_2N was used as model for the DFT calculations and C_2N as reference. **Figure 2.8d** shows the optimized adsorption configuration with Li_2S_4. **Figure 2.9** exhibits the optimized adsorption configuration with LiPS species (Li_2S, Li_2S_2, Li_2S_4, Li_2S_6, Li_2S_8 and S_8) on C_2N and Fe/C_2N. The corresponding binding energies are displayed in **Figure 2.8e**. DFT calculations showed the absolute binding energies for Fe/C_2N with LiPS species to be higher than those for C_2N, indicating that Fe/C_2N has a stronger ability to absorb soluble LiPS. These results are consistent with the absorption test of Li_2S_4, suggesting that Fe/C_2N could be effective to suppress the

"shuttle effect" of LiPS.
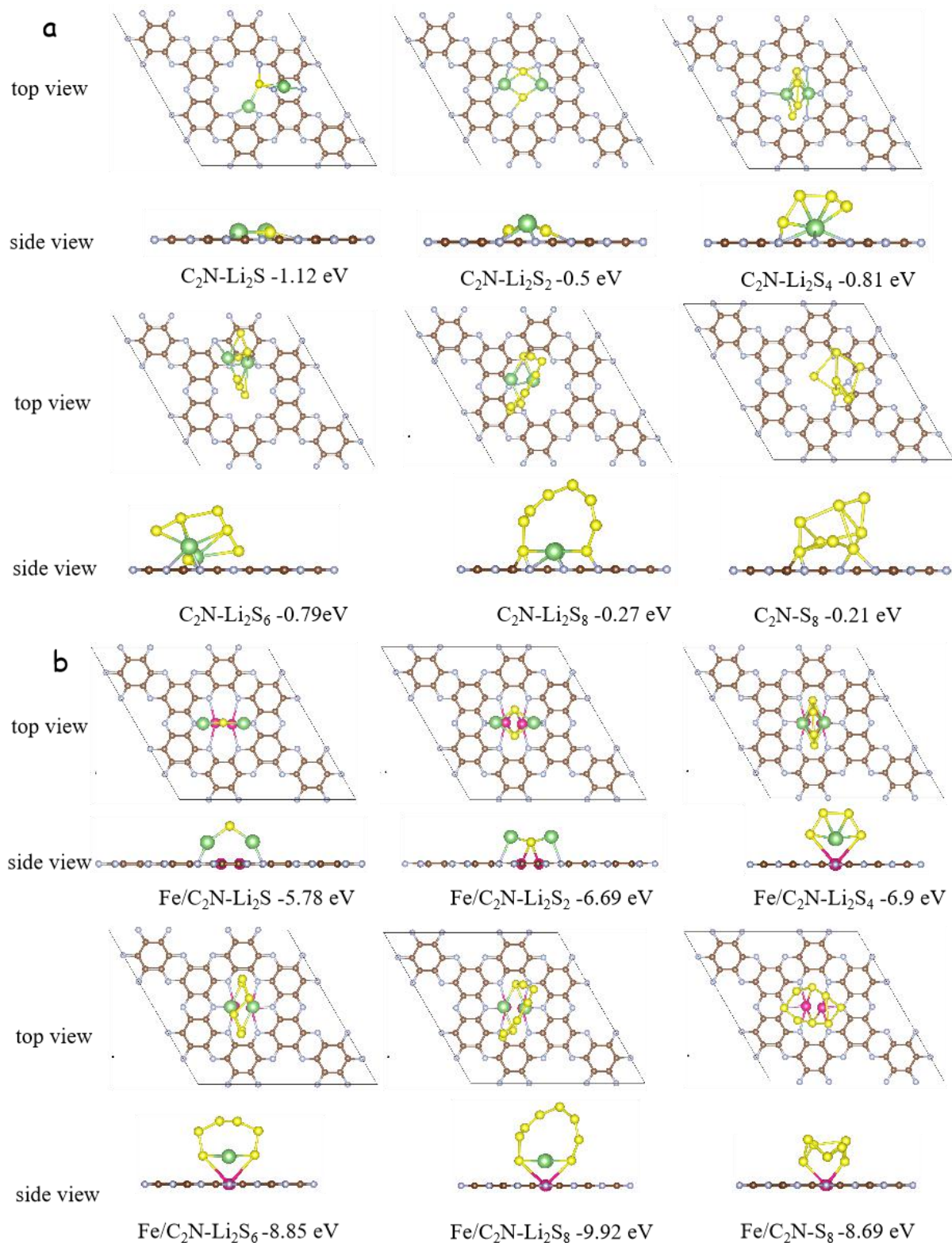
Figure 2.9. Schematic diagram of DFT calculation results for C_2N and Fe/C_2N with LiPS (Li_2S, Li_2S_2, Li_2S_4, Li_2S_6, Li_2S_8 and S_8): (a) C_2N. (b) Fe/C_2N. (light blue=nitrogen, brown=carbon, green=lithium, yellow=sulfur, pink=iron)
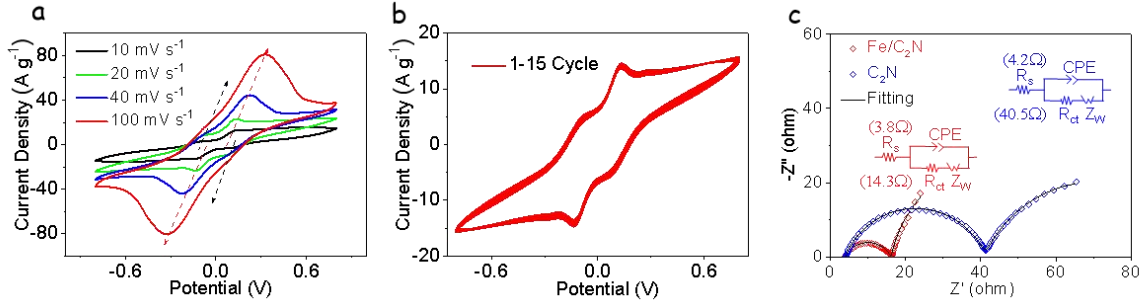
Figure 2.10. (a) CV profiles of S@C$_2$N electrode in symmetric cells at scan rate from 10 mV/s to 100 mV/s. (b) CV curves of symmetric cells from 1 to 15 cycles. (c) EIS spectrum of symmetric cells based on Fe/C$_2$N and C$_2$N sulfur host materials.

With the Fe/C$_2$N-based electrode, redox peaks were clearly defined even when the scanning rate was increased from 10 mV s^{-1} to 100 mV s^{-1} (**Figure 2.10a**). These results pointed out the important role played by the atomically dispersed Fe on the catalytic reaction of polysulfides. Besides, the excellent overlapping of the CV curves obtained from symmetric cells based on Fe/C$_2$N electrodes indicated excellent process reversibility and cell stability (**Figure 2.10b**).

Electrochemical impedance spectroscopy (EIS) analysis (**Figure 2.10c**) showed the charge transfer resistance of the Fe/C$_2$N-based electrode to be much lower than that of C$_2$N. Here it is important to take into account that the activation process is also related to the decreasing of the charge-transfer resistance after cycling. Therefore, our results provide strong evidence that the Fe/C$_2$N based electrodes have a better reaction response than that of the C$_2$N electrodes between polysulfides and Li$_2$S$_2$/Li$_2$S during charging and discharging process.

To prove the electrocatalytic activity of Fe/C$_2$N for polysulfide conversion, CV tests of symmetric cells with identical working and counter electrodes were conducted in 0.5 M Li$_2$S$_6$. Electrodes were prepared using a slurry-casting process. Fe/C$_2$N-based electrodes displayed two cathodic and two anodic symmetric peaks at ±0.13 and ±0.08 V (**Figure 2.11a**), which are associated with the electrochemical oxidation and reduction of Li$_2$S$_6$.[38][39] More specifically, the cathodic peak at –0.13 V and the anodic peak at 0.13 V are related to the reaction:

$$S_6^{2-} + 10e^- + 12Li^+ \leftrightarrow 6Li_2S \qquad (1)$$
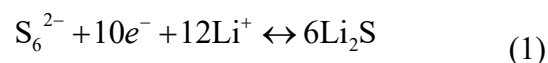
and the cathodic peak at 0.08 V and the anodic peak at –0.08 V to the reaction:

$$4S_6^{2-} \leftrightarrow 8e^- + 3S_8 \tag{2}$$
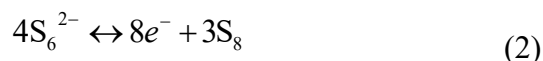
On the other hand, redox peaks were barely observed in the CV profiles of symmetrical cells based on C_2N. C_2N-based cells were also characterized by much lower current densities than those based on Fe/C_2N.
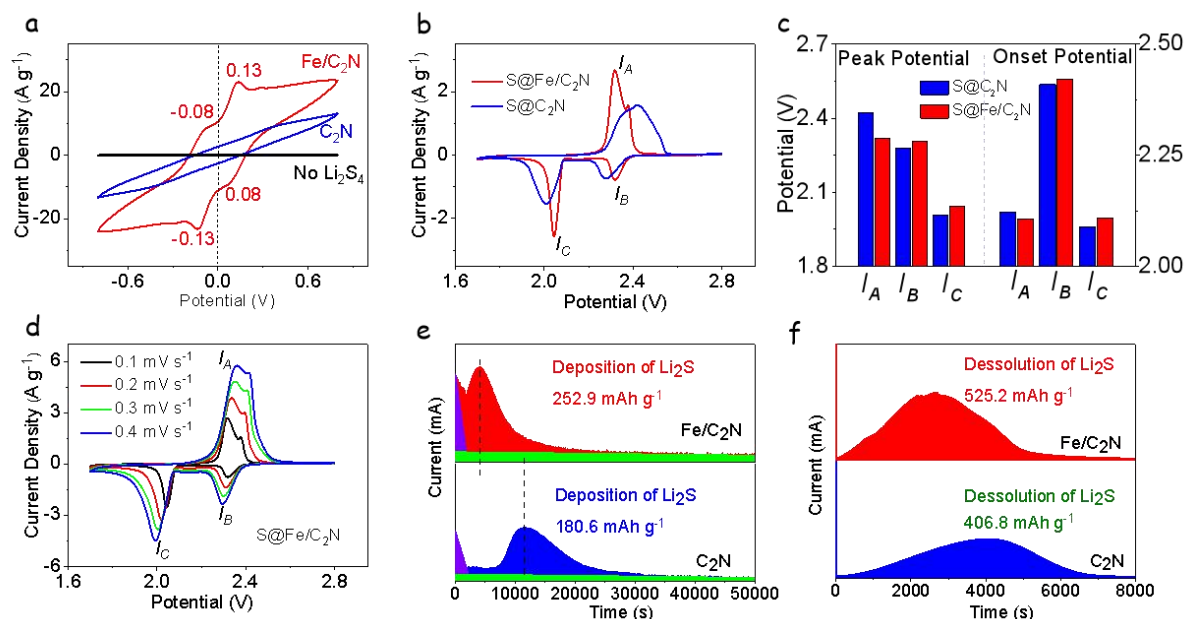
Figure 2.11 (a) CV curves of symmetrical cells with 20 mV s^{-1} scan rate. (b) CV profiles of Li-S cells with S@Fe/C$_2$N and S@C$_2$N cathodes with 0.1 mV s^{-1} scan rate. (c) Peak potential and onset potential of asymmetrical Li-S cells based on the CV curves. (d) CV profiles of the S@Fe/C$_2$N electrode with scan rates from 0.1 mV s^{-1} to 0.4 mV s^{-1}. (e) Potentiostatic discharge profiles at 2.04 V on Fe/C$_2$N and C$_2$N electrodes with Li$_2$S$_8$ catholyte. (f) Potentiostatic charge profiles at 2.32 V to evaluate the dissolution kinetics of Li$_2$S.

CV curves of Li-S coin cells based on S@Fe/C$_2$N and S@C$_2$N cathodes are shown in **Figure 2.11a**. These CV curves were found to almost overlap during the first cycles, indicating good reversibility of the sulfur redox reaction (**Figure 2.11b**). S@Fe/C$_2$N-based cells displayed a peak at 2.32 V (I_B) during the cathodic scan attributed to the transformation reactions:

$$S_8 + 2e^- + 2Li^+ \rightarrow Li_2S_8 \tag{3}$$

$$3Li_2S_8 + 2e^- + 2Li^+ \rightarrow 4Li_2S_6 \qquad (4)$$

$$2Li_2S_6 + 2e^- + 2Li^+ \rightarrow 3Li_2S_4 \qquad (5)$$
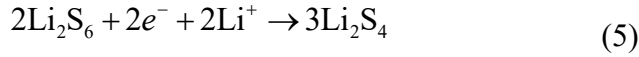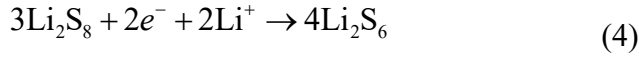
The second reduction peak in the cathodic scan at 2.04 V (I_C) corresponds to the reactions:[40][41]

$$Li_2S_4 + 2e^- + 2Li^+ \rightarrow 2Li_2S_2 \qquad (6)$$

$$Li_2S_2 + 2e^- + 2Li^+ \rightarrow 2Li_2S \qquad (7)$$
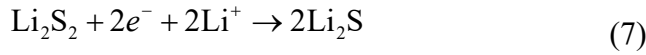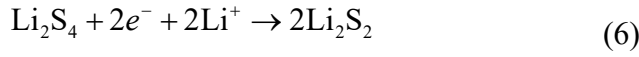
For the S@C$_2$N-based cells, cathodic peaks appeared broader and shifted to lower potentials, 2.3 V (I_B) and 2.0 V (I_C).

During the anodic scan, S@Fe/C$_2$N cells displayed two overlapping peaks at 2.35-2.40 V (I_A), that are attributed to the oxidation reaction from Li$_2$S$_2$/L$_2$S to S$_8$. Broader peaks, shifted around 50 mV to higher potentials (2.40-2.45 V) were obtained for the S@C$_2$N cell. Overall, S@Fe/C$_2$N cathodes displayed cathodic peaks at a more positive potential and anodic peaks at more negative potentials than S@C$_2$N, suggesting improved kinetics for the polysulfide transformation reaction (**Figure 2.11c**). As displayed in **Figure 2.11c**, S@Fe/C$_2$N cathodes were characterized by higher onset potentials for the reduction peaks and lower onset potentials for the oxidation peaks, further demonstrating the important catalytic role played by the atomically dispersed iron in S@Fe/C$_2$N cathodes.
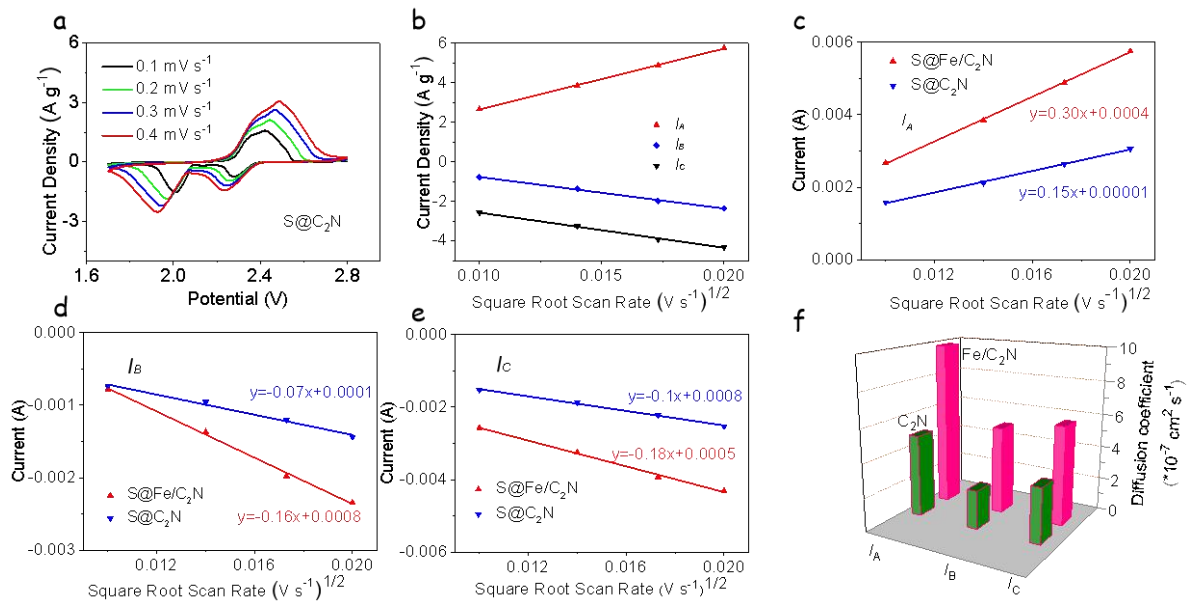
Figure 2.12 (a) CV profiles of S@C$_2$N electrode at scan rate from 0.1 mV/s to 0.4 mV/s. (b) Plot of CV of S@Fe/C$_2$N electrode peak current of I_A, I_B, I_C *vs* the square root of the scan rate. (c) Anodic oxidation reaction (peak I_A : Li$_2$S$_2$/Li$_2$S$\leftrightarrow$S$_8$) *vs* the square root of the scan rate. (d) First cathodic reduction process (peak I_B: S$_8\leftrightarrow$Li$_2$S$_x$). (e) Second cathodic reduction reaction (peak I_C: Li$_2$S$_x\leftrightarrow$Li$_2$S$_2$/Li$_2$S). (f) Diffusion coefficient of S@Fe/C$_2$N and S@C$_2$N electrodes calculated from I_A, I_B, I_C respectively.

CV measurements at various scanning rates, from 0.1 mV s^{-1} to 0.4 mV s^{-1}, were conducted to explore the reaction kinetics. As shown in **Figures 2.11d** and **2.12a**, an increase of the scan rate did not modify the shape of the redox peaks, indicating good electrochemical stability. The linear relationship between the potential of the reduction and oxidation peak maxima and the square root of the scan rate pointed toward a diffusion-limited process (**Figure 2.12b**). Thus, the Li$^+$ ion diffusion coefficients (D_{Li+}) were calculated through the Randles-Sevcik equation: [42][44]

$$I_P = (2.69 \times 10^5) n^{1.5} S D_{Li^+}^{0.5} C_{Li^+} \upsilon^{0.5} \qquad (8)$$

where I_P represents the peak current, n is the electron transferred number, S is the geometric area of the electrode, D_{Li+} represents the lithium ion diffusion coefficient, C_{Li}^+ is the concentration of lithium ions and v is the potential scanning rate. n, S and C_{Li}^+ are constant in this equation, so D_{Li+} can be determined from the slope of I_P vs $v^{0.5}$. Slopes of the cathodic and anodic peaks were significantly higher for S@Fe/C$_2$N (**Figure 2.12c-e**) than for S@C$_2$N electrodes, implying higher D_{Li+} values for the former (**Figure 2.12f**). This result suggested a faster transport of lithium ions and a related more efficient conversion of polysulfides in S@Fe/C$_2$N than in S@C$_2$N electrodes.

To further evaluate the catalytic effect of the electrode materials on the reversible reaction between polysulfide and Li$_2$S, potentiostatic nucleation and dissolution experiments were carried out. As shown in **Figure 2.11d**, the deposition of Li$_2$S on Fe/C$_2$N electrodes was considerably faster and at a larger current density under 2.05 V than on C$_2$N. Based on Faraday's law, the Fe/C$_2$N electrode exhibited a precipitation

capacity of 252.9 mAh g^{-1}, well above that of the C_2N electrode (180.8 mAh g^{-1}). Similarly, the potentiostatic Li_2S dissolution experiment (**Figure 2.11e**) showed the Fe/C_2N electrode to be characterized by a much higher current density and dissolution capacity (525.2 mAh g^{-1}) than C_2N (406.8 mAh g^{-1}). These results further proved that the atomically dispersed iron in C_2N enhanced the deposition and kinetic dissolution of Li_2S.

Overall, the dispersion of iron atoms not only provided strong polysulfide interaction sites through the enhancement of the C_2N polarity but also acted as excellent active sites for the reversible transformation of Li_2S.
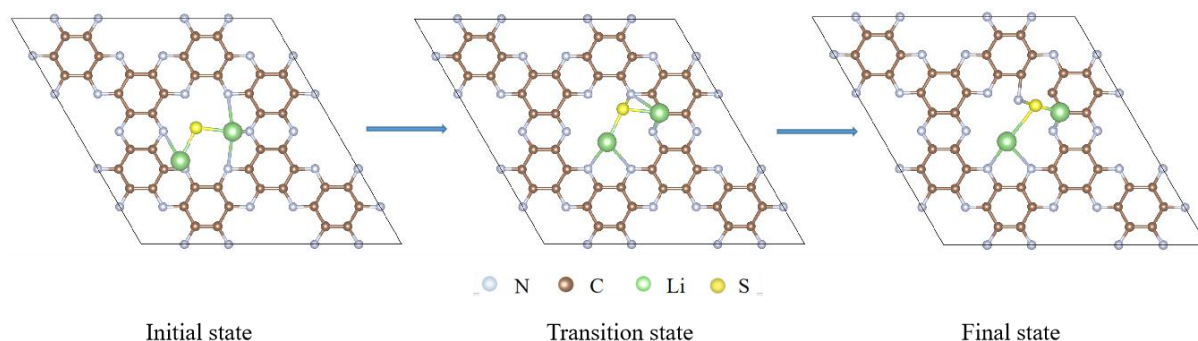
Figure 2.13 Schematic diagram of states of Li_2S decomposition on C_2N.

DFT calculations were conducted to reveal in detail the redox kinetics of the LiPS conversion. **Figures 2.13** and **2.14a** exhibit the initial state, transition state and final state of Li_2S decomposition on Fe/C_2N and C_2N. The calculated energy barrier for Li_2S decomposition on Fe/C_2N and C_2N surface was 0.62 eV and 1.52 eV, respectively (**Figures 2.14b**). These results demonstrate that Fe/C_2N can greatly reduce the Li_2S decomposition energy barrier and enhance the redox reversibility between Li_2S and LiPSs. Next, the Gibbs free energies were calculated for the S reduction pathways of both S@C_2N and S@Fe/C_2N cathodes. The optimized configuration of the intermediates and their Gibbs free energy profiles are exhibited in **Figure 2.14c**. The largest increase of Gibbs free energy was obtained for the conversion from Li_2S_2 to Li_2S species, suggesting this step as the rate-limiting for the total discharge process.[22] The free energy increase was lower for Fe/C_2N (0.89 eV) than for C_2N (0.92 eV), which suggested that the reduction of S is more thermodynamically favorable on Fe/C_2N than on C_2N substrate.
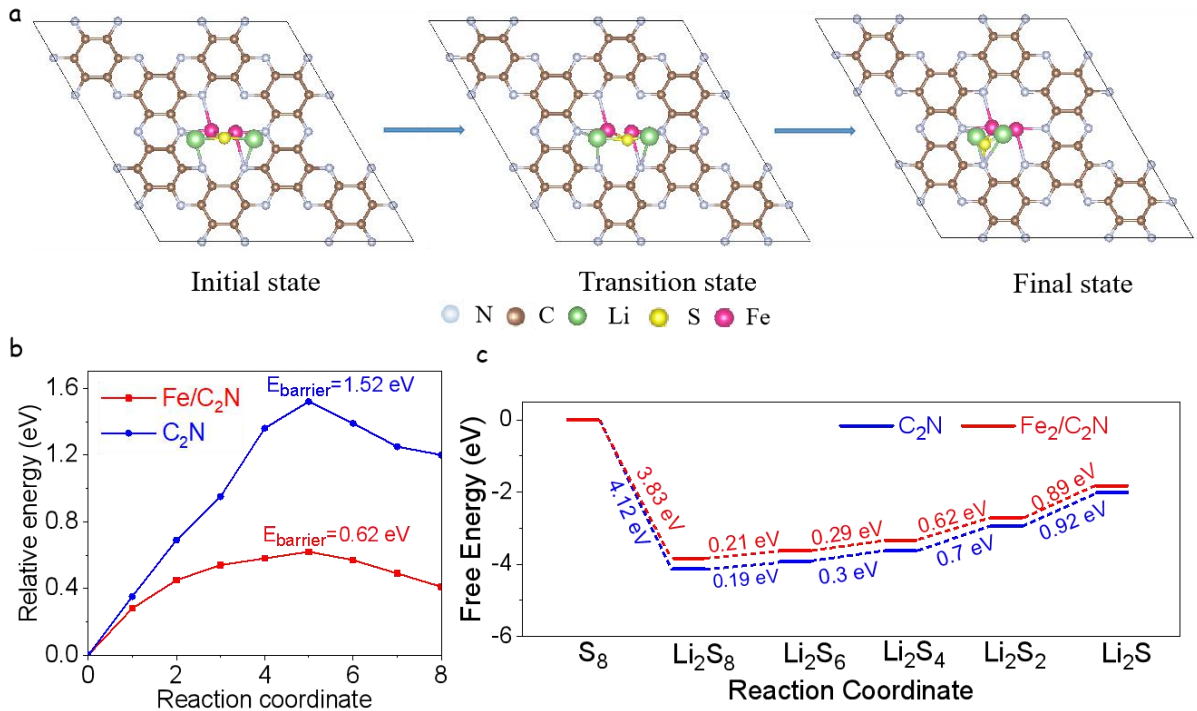
Figure 2.14 (a) The optimized adsorption configuration of Li_2S decomposition on Fe/C_2N. (b) Energy barrier profiles of Li_2S cluster decomposition on C_2N and Fe/C_2N along with different reaction coordinates. (c) Energy profiles of the reduction of Fe/C_2N and C_2N substrate respectively.

In **Figure 2.15a,** the galvanostatic charge-discharge curves for S@Fe/C_2N and S@C_2N electrodes at a current rate of 0.1 C are displayed. The voltage jump of the blue charging curve at the initial charging period, which reflects the overpotentials of Li_2S activation. This demonstrates the C_2N electrode displays a higher overpotential than the Fe/C_2N electrode, verifying the accelerated activation process of Li_2S in the presence of Fe/C_2N. The discharging curve is associated with the multistep sulfur reaction mechanism. Two clear discharge and one charge plateaus are observed in both cases. The first discharge plateau, at around 2.3 V, is attributed to the reduction of sulfur to soluble LiPS ($S_8 \rightarrow S_6^{2-} \rightarrow S_4^{2-}$). The second discharge plateau, at about 2.1 V, corresponds to the conversion of soluble LiPS into lithium sulfide ($S_4^{2-} \rightarrow Li_2S_2 \rightarrow Li_2S$).[50] Defining Q1 and Q2 as the capacity of the first discharge and the second discharge plateaus, respectively, the ratio between Q2 and Q1 (Q2/Q1) can be considered as a measure of the catalytic activity of the electrode material. The

higher the capacity ratio value, the better the catalytic ability.[47,48] **Figure 2.15b** shows the capacity ratio for the S@Fe/C$_2$N electrode to be quite large (Q2/Q1=2.86), well above the ratio measured for the S@C$_2$N electrode (Q2/Q1=2.35). This result is consistent with the superior catalytic activity towards polysulfides redox reaction of the Fe-loaded electrode.

As shown in **Figure 2.15b**, the polarization potential, i.e. the difference between the oxidation potential and the second reduction potential, of the S@Fe/C$_2$N electrode (ΔE=142.3 mV) was significantly lower than that of the S@C$_2$N electrode (ΔE= 180.9 mV). The lower overpotential for the phase conversion between soluble LiPS and insoluble Li$_2$S$_2$/Li$_2$S during the charge (**Figure 2.16a**) and discharge (**Figure 2.16b**) processes, further confirmed the improved redox kinetics of S@Fe/C$_2$N.

Figures 2.15c and **2.16c** exhibit the galvanostatic charge-discharge voltage profiles at various current densities ranging from 0.1 C to 5 C. The two discharge plateaus and the charge plateau were clearly observed even at the highest charge/discharge rates. **Figure 2.15d** shows the specific capacities at different discharge rates of the two electrode types tested. S@Fe/C$_2$N cathodes were characterized with average discharge capacities of 1480, 1250, 1085, 955, 856.4, 774 and 683 mAh g^{-1} at current rates from 0.1 C to 5 C, well above the capacities obtained for S@C$_2$N cathodes (**Figure 2.15d**).
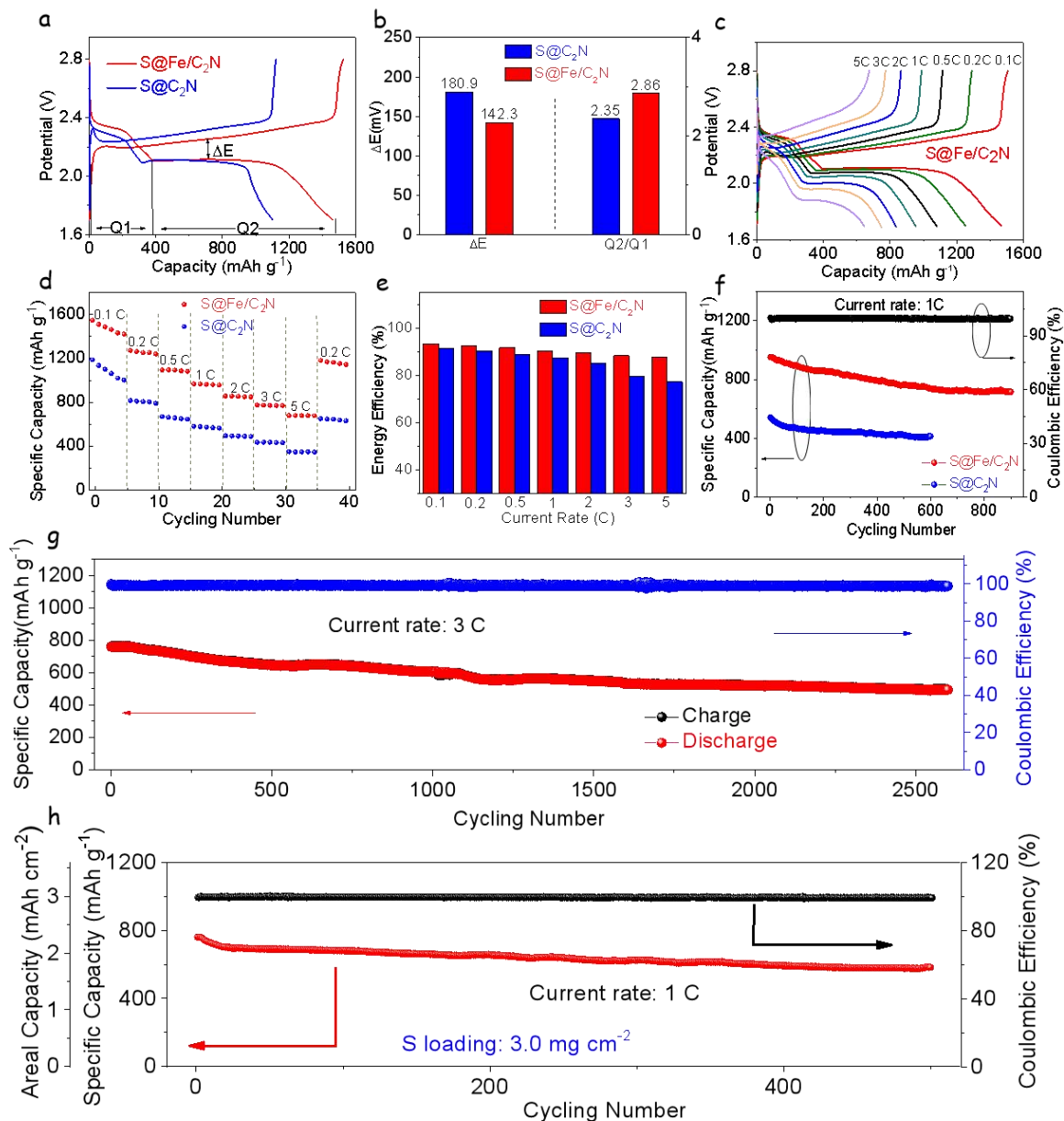
Figure 2.15 Electrochemical performance of Fe/C₂N and C₂N-based electrodes. (a) Galvanostatic charge-discharge profiles of S@Fe/C₂N and S@C₂N electrodes with a 0.1 C current rate. (b) Values of Δ*E* and Q2/Q1 resulted from the charge/discharge curves. (c) Galvanostatic charge-discharge profiles of S@Fe/C₂N at various rates. (d) Rate capabilities at current rates from 0.1 C to 5 C. (e) Energy efficiency at various current rates. (f) Capacity retention of S@Fe/C₂N and S@C₂N electrodes at 1 C. (g) Capacity retention of S@Fe/C₂N electrode at 3 C. (h) Capacity retention at 1 C with 3.0 mg cm⁻² sulfur loading.

Besides, when switching back the current rate from 5 C to 0.2 C, fairly similar

average capacities were recovered, 1172 mAh g^{-1} for the S@Fe/C$_2$N electrode, which pointed toward an excellent stability.
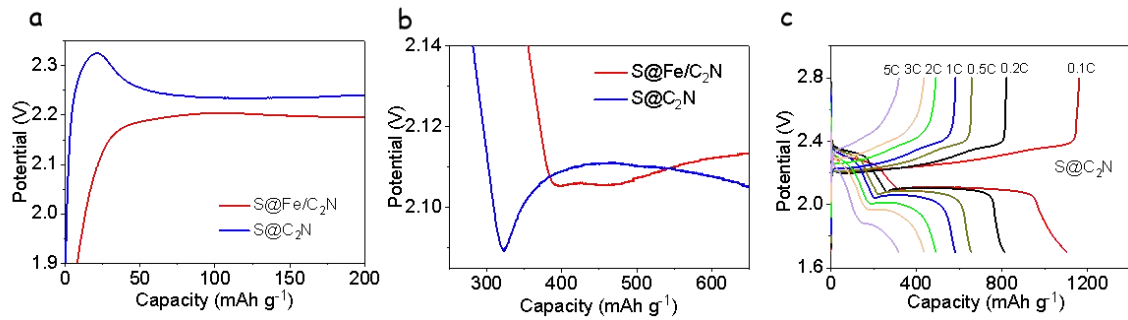
Figure 2.16 (a) Charge curves of S@Fe/C$_2$N and S@C$_2$N electrodes exhibiting the overpotentials for the transformation from Li$_2$S$_x$ to Li$_2$S$_2$/Li$_2$S. (b) Discharge curves of S@Fe/C$_2$N and S@C$_2$N electrodes exhibiting the overpotentials for the transformation from Li$_2$S$_2$/Li$_2$S to Li$_2$S$_x$. (c) Charge/discharge curves of S@C$_2$N electrode at various current densities from 0.1 C to 5 C.

The energy efficiency of the energy storage device was calculated using the following formula: $E = \int UIdt$. As shown in **Figure 2.15e**, the S@Fe/C$_2$N electrode was characterized by higher energy efficiency, up to 93 % at 0.1C, than S@C$_2$N, which is consistent with the lower polarization potential of the former, in turn associated with the exceptional catalytic properties of Fe/C$_2$N.

The cycling performance of S@Fe/C$_2$N and S@C$_2$N electrodes at 1C are shown in **Figure 2.15f**. S@Fe/C$_2$N electrodes displayed not only two-fold higher capacities than S@C$_2$N but also improved stability. S@Fe/C$_2$N electrodes maintained a discharge capacity of 716.5 mAh g^{-1} after 900 cycles, with a coulombic efficiency of 99.7%. This value corresponds to a capacity retention of 75.14%, i.e. an average capacity reduction rate of 0.0276% per cycle. **Figure 2.15g** displays the cycling performance of the S@Fe/C$_2$N electrode at 3C current rate. At this high current rate, the initial discharge capacity was 764.1 mAh g^{-1}. After 2600 cycles, the capacity was still 496.5 mAh g^{-1}, which corresponds to a 0.013% average capacity attenuation per cycle.
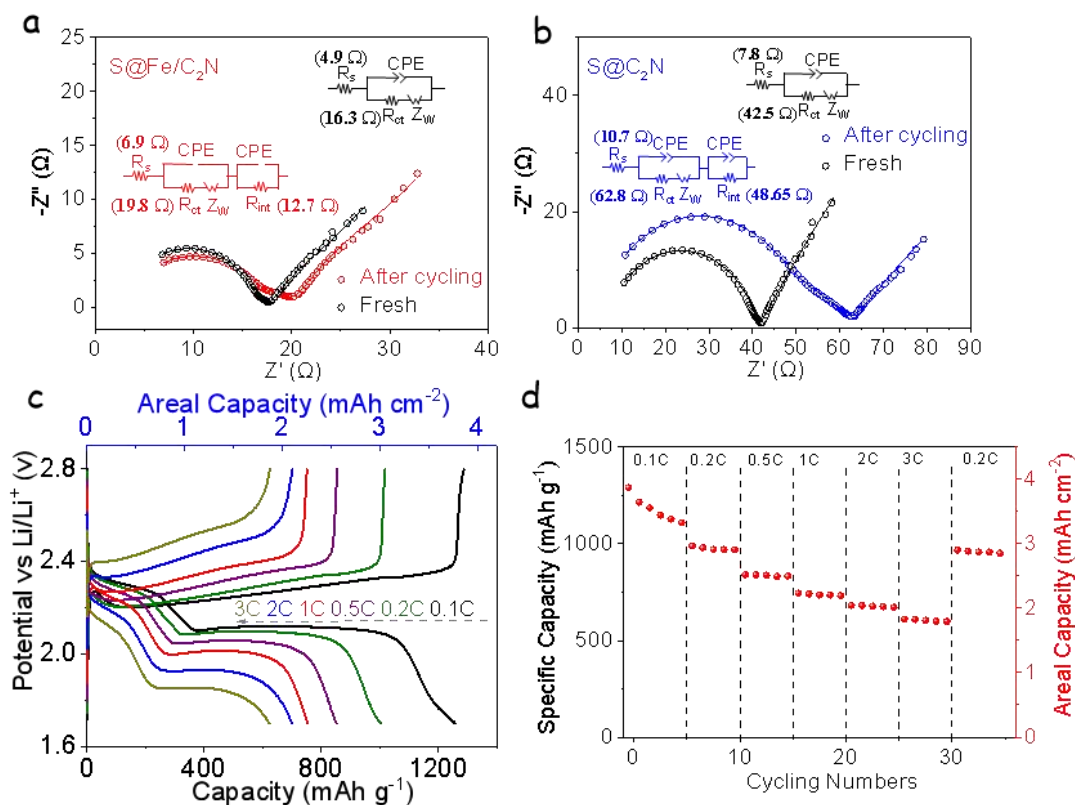
Figure 2.17. (a) EIS spectra obtained on coin cells fabricated with the S@Fe/C2N cathode, for the fresh cell and after cycling at 1 C for 100 cycles respectively. (b) EIS spectra obtained on the coin cells fabricated with the S@C2N cathode corresponding fresh cell and after cycling at 1 C for 100 cycles. (c) Charge/discharge profiles. (d) Rate capability of S@Fe/C2N electrode with sulfur loading of 3 mg cm^{-2} at different current densities.

Figures 2.17a,b display results from EIS analysis before the first discharge and after 200 cycles at 1 C. Comparing the S@C$_2$N with the S@Fe/C$_2$N electrode, the latter showed a much lower Rct, indicating improved electrode kinetics.

To explore the potential practical application of Fe/C$_2$N-based cathodes, electrodes with higher sulfur loading were produced and tested. Galvanostatic charging and discharging profiles at various current rates from a S@Fe/C$_2$N electrode with 3.0 mg cm^{-2} sulfur loading are shown in **Figure 2.17c**. One charging plateau and two discharging plateaus were clearly observed even at current rates up to 3 C. The average specific capacities were 972 mAh g^{-1} at 0.1 C and 610 mAh g^{-1} at 3 C, corresponding to areal capacities of 2.8 mAh cm^{-2} and 1.8 mAh cm^{-2}, respectively.

Figure 2.17d shows the rate performances of the S@Fe/C$_2$N electrode with a high sulfur load, which displayed average discharge capacities of 1189.5, 966, 839.5, 734.7, 680.6, 601.3 and 605 mAh g^{-1} at current rates from 0.1 C to 3 C. Besides, the long-term cycling test of this electrode displayed the initial capacity of 760 mAh g^{-1} to decrease at a rate of 0.046% per cycle to 584.6 mAh g^{-1} after 500 cycles, which corresponds to a 76.92% capacity retention (**Figure 2.15h**). During this process, a coulombic efficiency above 99.3% was maintained. These results suggest our materials show excellent LSBs performance.
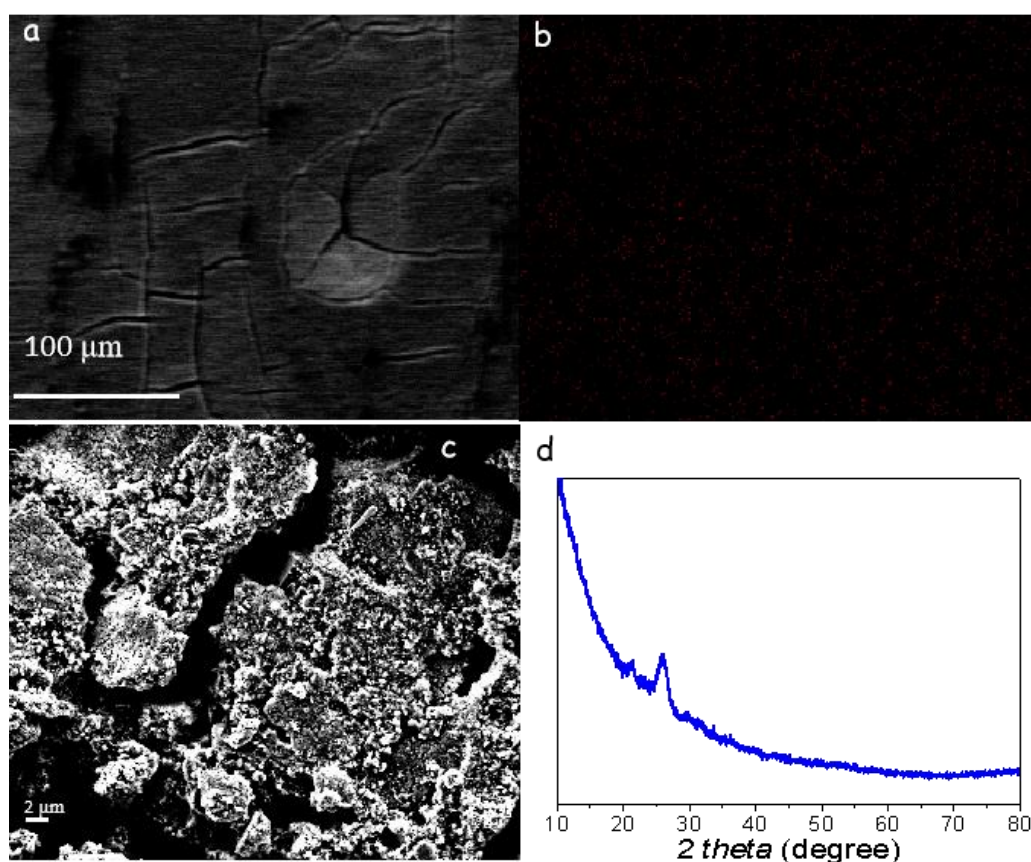
Figure 2.18. (a) SEM image of the Li-anode after cycling; (b) EDS mapping images of Li-anode showing a low sulfur signal after cycling. (c) SEM image of the S@Fe/C2N cathodes after charging at 1.7 V. (d) XRD spectrum after charging at 1.7 V.

To further analyse the advantages of Fe/C$_2$N for efficient LSBs performance,[53] an EDS mapping of the Li-anode after cycling was conducted. On the EDS maps, only a very small amount of sulfur was observed (**Figures 2.18a,b**), which means that the

Fe/C$_2$N as cathode in the LSBs can inhibit the "shuttle effect" of the polysulfides efficiently. On the other hand, SEM characterization (**Figure 2.18c** of the cathode after cycling was also performed. At the full-discharged state of 1.7 V, the cells were disassembled to investigate the morphology of Fe/C$_2$N after cycling. The corresponding SEM image displayed nanoparticles that were uniformly distributed on the surface of Fe/C$_2$N rather than aggregating into large bulk agglomerates. Combined with the Li$_2$S nucleation measurement through potentiostatic discharge profiles, the results further demonstrated that Fe/C$_2$N catalyst regulate the deposition behavior of Li$_2$S. To evaluate the stability of the Fe/C$_2$N structure during cycles, we conducted XRD measurements (**Figure 2.18d**) of the cathode after charging. Diffraction peaks corresponding to Fe nanoparticles or aggregates were not observed, meaning that the atomically dispersed iron atoms, which act as active sites, are kept stable and isolated during cycling.

Overall, the above results demonstrate that Fe/C$_2$N-based cathodes show an excellent electrochemical performance associated to the following properties: 1) The abundant presence of pyrazine nitrogen and pores in the C$_2$N structure, which can immobilize LiPS and thus minimize the shuttle effect; 2) The high electrical conductivity of Fe/C$_2$N which maximizes the sulfur utilization; and 3) The presence of atomically dispersed iron, which is coordinated to nitrogen and work as efficient active sites to promote the polysulfide conversion reaction kinetics.

2.4 Conclusions

In summary, a novel catalyst based on atomically dispersed iron in a 2D organic material (Fe/C$_2$N) has been shown as an efficient sulfur host material for LSBs. Combination of XPS, XANES, EXAFS, atomic resolution AC-HAADF-STEM and DFT calculations confirmed that the synthesized Fe/C$_2$N presents atomically dispersed iron. Iron atoms, which are in some cases found to group in pairs, are coordinated to nitrogen in the C$_2$N pores. These atomically dispersed Fe atoms not only improve the material polarity to immobilize the soluble polysulfides, but also act as catalytic active sites to promote the reaction kinetics between sulfur, polysulfide

and Li$_2$S. As a result, S@Fe/C$_2$N-baed cathodes exhibit excellent electrochemical performance, showing a high capacity and a remarkable rate performance at different current densities, while keeping outstanding cycling stability. This work demonstrates that atomically dispersed metal atoms within the unique C$_2$N structure can help to achieve excellent electrochemical performance. The present strategy can be utilized to design active materials not only for LSBs, but also for other energy conversion and storage systems.

References

[1] H.-J. Peng, J.-Q. Huang, X.-B. Cheng, Q. Zhang, *Adv. Energy Mater.*, 2017, *7*, 1700160.

[2] A. Manthiram, S. H. Chung, C. Zu, *Adv. Mater.*, 2015, *27*, 1980-2006.

[3] P. G. Bruce, S. A. Freunberger, L. J. Hardwick, J. M. Tarascon, *Nat. Mater.*, 2011, *11*, 19-29.

[4] L. Lin, F. Pei, J. Peng, A. Fu, J. Cui, X. Fang, N. Zheng, *Nano Energy*, 2018, *54*, 50-58.

[5] J. Song, M. J. Choo, H. Noh, J. K. Park, H. T. Kim, *ChemSusChem*, 2014, *7*, 3341-3346.

[6] Q. Pang, X. Liang, C. Y. Kwok, L. F. Nazar, *Nat. Energy*, 2016, *1*, 16132.

[7] M. Hagen, D. Hanselmann, K. Ahlbrecht, R. Maça, D. Gerber, J. Tübke, *Adv. Energy Mater.*, 2015, *5*, 1401986.

[8] B. Zhang, X. Qin, G. R. Li, X. P. Gao, *Energy Environ. Sci.*, 2010, *3*, 1531-1537.

[9] J.-Z. Wang, L. Lu, M. Choucair, J. A. Stride, X. Xu, H.-K. Liu, *J. Power Sources*, 2011, *196*, 7030-7034.

[10] G. Li, W. Lei, D. Luo, Y.-P. Deng, D. Wang, Z. Chen, *Adv. Energy Mater.*, 2018, *8*, 1702381.

[11] Y. S. Su, A. Manthiram, *Chem. Commun.*, 2012, *48*, 8817-8819.

[12] P. Wei, M. Q. Fan, H. C. Chen, X. R. Yang, H. M. Wu, J. Chen, T. Li, L. W. Zeng, C. M. Li, Q. J. Ju, D. Chen, G. L. Tian, C. J. Lv, *Renew. Energy*, 2016, *86*, 148-153.

[13] H. Liao, H. Wang, H. Ding, X. Meng, H. Xu, B. Wang, X. Ai, C. Wang, *J. Mater. Chem. A*, 2016, *4*, 7416-7421.

[14] T. Sun, J. Xie, W. Guo, D. S. Li, Q. Zhang, *Adv. Energy Mater.*, 2020, *10*, 1904199.

[15] Y. Yang, G. Zheng, Y. Cui, *Chem. Soc. Rev.*, 2013, *42*, 3018-3032.

[16] X. Zhou, J. Tang, J. Yang, J. Xie, B. Huang, *J. Mater. Chem. A*, 2013, *1*, 5037-5044.

[17] X. G. Sun, X. Wang, R. T. Mayes, S. Dai, *ChemSusChem*, 2012, *5*, 2079-2085.

[18] F. Sun, J. Wang, H. Chen, W. Li, W. Qiao, D. Long, L. Ling, *ACS Appl. Mater. Interfaces*, 2013, *5*, 5630-5638.

[19] Y. Cao, C. Liu, M. Wang, H. Yang, S. Liu, H. Wang, Z. Yang, F. Pan, Z. Jiang, J. Sun, *Energy Storage Mater.*, 2020, *29*, 207-215.

[20] X. Chen, Y. Xu, F. H. Du, Y. Wang, *Small Methods*, 2019, *3*, 1900338.

[21] J. Wang, L. Jia, J. Zhong, Q. Xiao, C. Wang, K. Zang, H. Liu, H. Zheng, J. Luo, J. Yang, H. Fan, W. Duan, Y. Wu, H. Lin, Y. Zhang, *Energy Storage Mater.*, 2019, *18*, 246-252.

[22] Z. Du, X. Chen, W. Hu, C. Chuang, S. Xie, A. Hu, W. Yan, X. Kong, X. Wu, H. Ji, L. J. Wan, *J. Am. Chem. Soc.*, 2019, *141*, 3977-3985.

[23] J. Xie, B. Q. Li, H. J. Peng, Y. W. Song, M. Zhao, X. Chen, Q. Zhang, J. Q. Huang, *Adv. Mater.*, 2019, *31*, e1903813.

[24] L. Zhang, D. Liu, Z. Muhammad, F. Wan, W. Xie, Y. Wang, L. Song, Z. Niu, J. Chen, *Adv. Mater.*, 2019, *31*, e1903955.

[25] Y. Li, J. Wu, B. Zhang, W. Wang, G. Zhang, Z. W. Seh, N. Zhang, J. Sun, L. Huang, J. Jiang, J. Zhou, Y. Sun, *Energy Stor. Mater.*, 2020, *30*, 250-259.

[26] J. Mahmood, F. Li, S. M. Jung, M. S. Okyay, I. Ahmad, S. J. Kim, N. Park, H. Y. Jeong, J. B. Baek, *Nat. Nanotechnol.*, 2017, *12*, 441-446.

[27] J. Mahmood, S.-M. Jung, S.-J. Kim, J. Park, J.-W. Yoo, J.-B. Baek, *Chemistry of Materials.*, 2015, *27*, 4860-4864.

[28] J. Mahmood, F. Li, C. Kim, H.-J. Choi, O. Gwon, S.-M. Jung, J.-M. Seo, S.-J. Cho, Y.-W. Ju, H. Y. Jeong, G. Kim, J.-B. Baek, *Nano Energy*, 2018, *44*, 304-310.

[29] J. Xu, J. Mahmood, Y. Dou, S. Dou, F. Li, L. Dai, J. B. Baek, *Adv. Mater.*, 2017, *29*.

[30] J. Wu, L.-W. Wang, *J. Mater. Chem. A*, 2018, *6*, 2984-2994.

[31] H. Lin, R. Jin, A. Wang, S. Zhu, H. Li, *Ceramics Int.*, 2019, *45*, 17996-18002.

[32] S. S. Shinde, C. H. Lee, J.-Y. Jung, N. K. Wagh, S.-H. Kim, D.-H. Kim, C. Lin, S. U. Lee, J.-H. Lee, *Energy Environ. Sci.*, 2019, *12*, 727-738.

[33] S. S. Shinde, C. H. Lee, J. Y. Yu, D. H. Kim, S. U. Lee, J. H. Lee, *ACS Nano,* 2018, *12*, 596-608.

[34] N. Ramaswamy, U. Tylus, Q. Jia, S. Mukerjee, *J. Am. Chem. Soc.*, 2013, *135*, 15443-15449.

[35] F. Xiao, G.-L. Xu, C.-J. Sun, M. Xu, W. Wen, Q. Wang, M. Gu, S. Zhu, Y. Li, Z. Wei, X. Pan, J. Wang, K. Amine, M. Shao, *Nano Energy*, 2019, *61*, 60-68.

[36] A. Zitolo, V. Goellner, V. Armel, M. T. Sougrati, T. Mineva, L. Stievano, E. Fonda, F. Jaouen, *Nat. Mater.*, 2015, *14*, 937-942.

[37] W. Ye, S. Chen, Y. Lin, L. Yang, S. Chen, X. Zheng, Z. Qi, C. Wang, R. Long, M. Chen, J. Zhu, P. Gao, L. Song, J. Jiang, Y. Xiong, *Chem*, 2019, *5*, 2865-2878.

[38] H. Lin, L. Yang, X. Jiang, G. Li, T. Zhang, Q. Yao, G. W. Zheng, J. Y. Lee, *Energy Environ. Sci.*, 2017, *10*, 1476-1486.

[39] H. Lin, S. Zhang, T. Zhang, H. Ye, Q. Yao, G. W. Zheng, J. Y. Lee, *Adv. Energy Mater.*, 2019, *9*, 1902096.

[40] S. S. Zhang, *J. Power Sources,* 2013, *231*, 153-162.

[41] Y. Li, J. Fan, J. Zhang, J. Yang, R. Yuan, J. Chang, M. Zheng, Q. Dong, *ACS Nano*, 2017, *11*, 11417-11424.

[42] X. Zhu, W. Zhao, Y. Song, Q. Li, F. Ding, J. Sun, L. Zhang, Z. Liu, *Adv. Energy Mater.*, 2018, *8*, 1800201.

[43] Mahmood, J. Lee, E. K. Jung, M. Shin, D. Jeon, I. Y. Jung, S. M. Choi, H. J. Seo, J. M. Bae, S. Y. Sohn, S. D. Park, N. Oh, J. H. Shin, H. J. Baek, J. B. *Nat. Commun.*, 2015, 6, 6486.

[44] G. Zhou, H. Tian, Y. Jin, X. Tao, B. Liu, R . Zhang, Z. W. Seh, D. Zhuo, Y. Liu, Sun, J. Zhao, J. C .Zu, D. S. Wu, Q. Zhang, Y. Cui, *Proc. Natl. Acad. Sci.*, 2017, 114, 840.

[45] J. F. Kimer, W. Dow, W. R. Scheidt. *Inorg. Chem.,* 1976, 15, 1685-1690.

[46] Y. Chen, Ji, S. Wang, Y. Dong, J. Chen, W. Li, Z. Shen, R. Zheng, L. Zhuang, Z. Wang, Y D. Li, *Angew. Chem. Int. Ed.,* 2017, *129*, 7041-7045.

[47] D. Su, M. Cortie, H. Fan, G. Wang, *Adv. Mater.,* 2017, *29*, 1700587.

[48] C.-Y. Fan, Y.-P. Zheng, X.-H. Zhang, Y.-H. Shi, S.-Y. Liu, H.-C. Wang, X.-L. Wu,

H.-Z. Sun, J.-P. Zhang, *Adv. Energy Mater.,* 2018, *8*, 1703638.

[49] C. Zhang, J. J. Biendicho, T. Zhang, R. Du, J. Li, X. Yang, J. Arbiol, Y. Zhou, J. R. Morante, A. Cabot, *Adv. Funct. Mater.,* 2019, *29*, 1903842.

[50] H. Yuan, H.-J. Peng, B.-Q. Li, J. Xie, L. Kong, M. Zhao, X. Chen, J.-Q. Huang, Q. Zhang, *Adv. Energy Mater.* 2019, *9*, 1802768.

[51] W. Cheng, Lu. Weng, Y. Li, A. Lau, C K. Chan, C. Chan, *Aerosol Science and Technology*, 2013, 47, 1118-1124.

[52] B. Rave , M. Newville, ATHENA, *J. Syncrotron Radiat.*, 2005, 12, 537-541.

[53] J-Y. Wei, X-Q. Zhang, L-P. Hou, P. Shi, B-Q. Li, Y. Xiao, C. Yan, H. Yuan, J-Q. Huang, *Adv. Mater.*, 2020, 32, 2003012.

[54]. G, Kresse, J. Furthmüller, *Comp. Mater. Sci.*, 1996, 6, 15.

[55]. J. Wu, L. Wang, *J. Mater. Chem*. A, 2018, 6, 2894-2994.

Chapter 3

Molecular Engineering to Introduce Carbonyl Between Nickel Salophen Active Sites to Enhance the Electrochemical CO_2 Reduction to Methanol
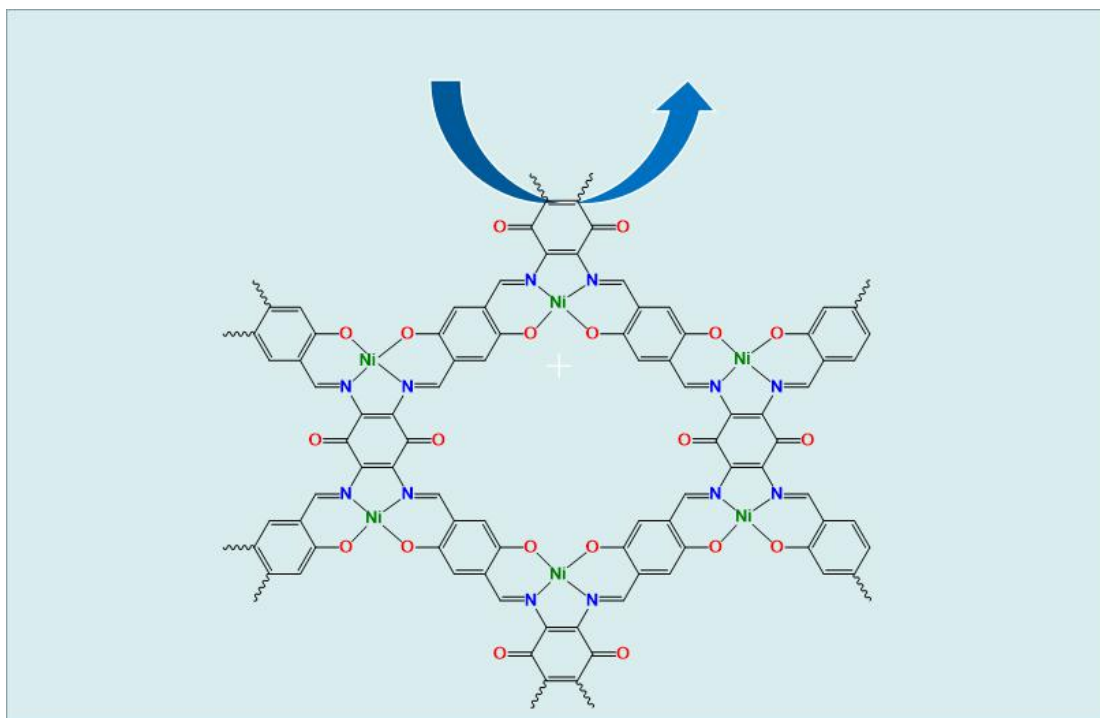
3.1 Introduction

The electrochemical conversion of carbon dioxide (CO_2) to valuable chemicals using renewable electricity can enable the cost-effective capture and reuse of this greenhouse gas.[1,2] Hydrocarbons and alcohols are the most desired products from the CO_2 reduction reaction (CO_2RR). Among them, methanol is particularly appealing owing to its numerous uses and its liquid phase at ambient temperature that facilitates storage and transportation. Thus, numerous materials have been explored as CO_2RR catalysts for methanol production, including metal oxides, [7] metal chalcogenides,[8-10] copper-based single atom catalysts,[11-12] molecular-based catalysts such as cobalt salophen complexes,[38-39] cobalt phtholocyamine [13-15] and its derivatives.[4] However, despite the relative simplicity of the methanol molecule, the reduction of CO_2 to methanol with high selectivity and stability has been demonstrated extremely challenging and mainly CO and formate have been reported as the CO_2RR products.[3-6]

Most of the CO_2RR catalysts developed in the last decades are complex nanomaterials that present unclear structure-performance correlation and uncertain reaction mechanisms, which complicates their optimization.[6,19-21] More recently, molecular catalysts with fine-tuned steric, electronic, electrostatic and chelating properties/abilities [22] have been engineered and optimized (e.g. through ligand modification) for CO_2RR. When supported on conductive substrates, some of these molecular catalysts, such as metalloporphyrin and metallophthalocyanine, have shown low overpotentials and high CO_2RR conversion efficiency and selectivities.[3][16][23-26] In the last few years, two-dimensional (2D) conductive metal-organic frameworks with tunable pore structure and functionality, and with abundant catalytic active sites, have arisen as exceptional candidate catalysts for CO_2RR.[4,18,27-30] While several reports have detailed the influence of the metal, ligand type and coordination number on CO_2RR performance,[17][29] the analysis and exploitation of the strong influence that the ligand microenvironment near the active center has on the CO_2RR remain unexplored.

In this chapter, a conjugated nickel organic framework with abundant carbonyl groups in the ligand near the nickel catalytic active site is described and explored as electrocatalyst CO_2RR to methanol in aqueous medium. The unique chemical structure and uniformly distributed catalytic active centers in the proposed nickel organic framework, combined with the high electrical conductivity of carbon nanotubes (CNTs), results in electrocatalysts with high catalytic activities, excellent durability and notable selectivity for CO_2RR to methanol. The present work not only provides new insights into the synthesis of this atomically dispersed material under mild and controllable conditions, but also demonstrates a novel strategy to design effective CO_2RR electrocatalysts by tuning the ligand chemical environment.

3.2 Experimental Section

3.2.1 Materials

Dichloromethane (99%), methanol (99%), Dimethyl sulfoxide (DMSO), N,N-dimethylformamide (DMF) (98%), salicylaldehyde (99%), 1,2-diaminobenzene (98%) and hydrazine hydrate (98%) were purchased from Alfa Aesar. Tetrachloro-p-benzoquinone (99%), potassium phthalimide (98%), N-methyl-pyrrolidone (NMP, 99.99%), 2,5-dimethoxyterephthalaldehyde (97%), 1,2,4,5-benzenetetraamine tetrahydrochloride (TAB), hexane (95%), boron tribromide (99.99%), and Nafion (10%) were purchased from Sigma-Aldrich. Benzyl alcohol (99%), nickel acetate tetrahydrate (99%), and potassium hydroxide (85%) were from Acros Organics. Acetonitrile (98%) and ethanol (99.5%) were purchase from Honeywell. All chemicals were used without further purification. Carbon Nanotube was ordered from Sailed Technology. The oxidation treatment of carbon nanotube (CNTs) was followed as the literature.[41]

3.2.2 Characterization

The crystal structure of the materials was characterized by means of powder X-ray diffraction (XRD) measured in a Bruker AXS D8 Advance X-ray diffractometer. (Cu-Kα radiation, λ = 1.5106 Å, 40 kV and 40 mA; Bruker, Germany). [13]C

cross-polarization with magic angle-spinning (CP-MAS) solid-state nuclear magnetic resonance (NMR) spectra were measured on a Bruker ARX 400 MHz spectrometer. Thermogravimetric analysis (TGA) was performed under air and nitrogen gas at a heating rate of 5 °C/min using a Thermogravimetric Analyzer Q200. Scanning electron microscopy (SEM) images were obtained in a Zeiss Auriga Field emission scanning electron microscope (FE-SEM) operating at 20 kV. High-resolution transmission electron microscopy (HRTEM) studies were conducted in a FEI Tecnai F20 microscope at an operating voltage of 200 keV. High angle annular dark-field (HAADF)-scanning transmission electron microscopy (STEM) images and elemental mapping were measured in a spherical aberration corrected transmission electron microscope FEI Titan G2 80-200 ChemiSTEM with four energy-dispersive X-ray spectroscopy (EDX) detectors and operated at 80 and 200 keV. X-ray photoelectron spectroscopy (XPS) data was obtained with a Phoibos 150 MCD-9 detector. The Ni K-edge X-ray absorption fine structure (XAFS) spectra were measured at the Canadian Light Source, beamline SXRMB. The samples were pressed onto a double-sided carbon tape and the data was recorded in X-ray fluorescence mode. The XAFS data was processed with the Athena program. [42] Extend X-ray absorption fine structure (EXAFS) was analyzed using the IFEFFIT package [43] and the EXAFS fitting was performed with FEFF6L.[44] For EXAFS fitting, spectra were fitted in R-space, from 1.0 Å to 2.76 Å. The R-space EXAFS signal was obtained by a variable k^n-weighted Fourier transform (n = 1, 2, 3) of the EXAFS signal $\chi(k)$ over a k-range of 3.00 Å^{-1} to 11.7 Å^{-1}. The coordination numbers of Ni-N and Ni-O paths were both fixed at 2, and the bond lengths, energy shift, and the Debye-Waller factors were optimized to yield the best fit. Nitrogen adsorption-desorption isotherms were recorded in a Tristar II 3020 Micromeritics system at 77 K. The specific surface area was calculated by Brunauer-Emmett-Teller (BET) method.

3.2.3 Synthesis of 2,5-dihydroxyterephthalaldehyde (HBC)
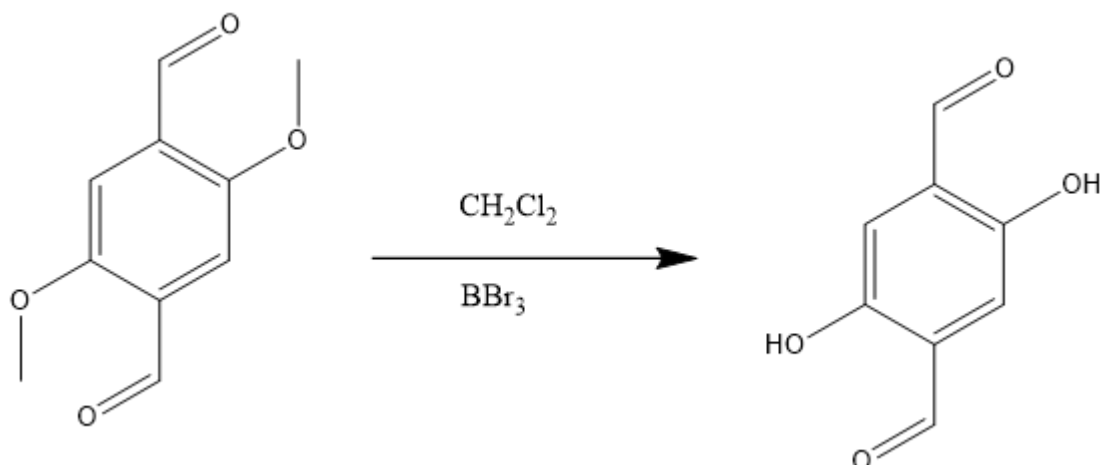
2,5-dimethoxyterephthalaldehyde (250 mg, 1.285 mmol) and 25 mL dichloromethane were placed to 50 mL round bottom three-neck flask with magnetic stirring for 10 min. Then 3.22 mL BBr$_3$ (1 M in hexane) was added to the above solution slowly at ice bath. After stirring for 3 hours at room temperature, 5 mL water was added slowly. Organic solvents were then removed by flow argon, and the obtained yellow precitipate was vacuum filtrated and washed with water several times, then washed with acetone to obtain a bright yellow compound 2,5-hydroxyterephthalaldehyde (HBC) with a yeld of 75 %. (IR O-H:3260 cm^{-1}, -CHO: 2881, -C=O: 1664 cm-1) ^{1}H-NMR (400 MHz, DMSO-d_6, δ): δ 10.33 (m, 4H), 7.25 (s, 2H). [45]

3.2.4 Synthesis of Tetramino-benzenequinone (TABQ)
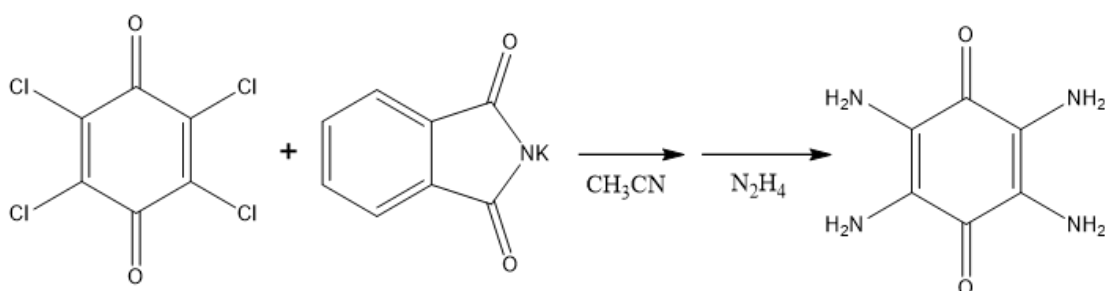
5.0 g of tetrachloro-p-benzoquinone and 15.0 g of potassium phthalimide were put into 100 nL falsk, then 50.0 mL of acetonitrile were added and magnetically stirred at 80 °C for 12h. After cooling down to room temperature naturally, the precipitate was filtrated by vacuum, and washed with hot DMF for several times, then washed with

MILIQ water and ethanol for several times. Then vacuum dried at 60 ℃ for overnight. 10.0 g brown-yellow powder of tetra(phthalimido)-benzoquinone was got. [46-47] The obtained tetra(phthalimido)-benzoquinone was transferred into a 100 mL round bottom flask, then 40.0 mL of hydrazine hydrate solution was dropped slowly. After being magnetically stirring and kept at 65 ℃ for 2 h, the purple tetramino-benzoquinone (TABQ) was obtained with a yield of 26 %. (IR -NH2: 3367 cm^{-1}, -C=O: 1668 cm-1, C-(C=O)-C 1140 cm^{-1}) ^{1}H-NMR (400 MHz, DMSO-d_6, δ): δ 4.55 (s, 8H). [48-49]

3.2.5 Synthesis of Ni-2D-O-SA

HBC (166 mg, 1 mmol), TABQ (84 mg, 0.5 mmol), nickel acetate tetrahydrate (1 mmol, 248.8 mg) and 5 mL NMP were placed into a 15 mL glass vial, The obtained mixture was sonicated for 30 min to form a homogenous dispersion. The glass vial was put into a 25 mL Teflon-lined stainless-steel autoclave. The autoclave was sealed and maintained at 120 ℃ for 72 h. The obtained black precipitate was filtrated and then washed with DMF and methanol for several times, Soxhlet extracted by methanol for 24 h, then dried under vacuum at 60 ℃ for 24 h to give a black powder with ~83% yield ($C_{11}N_2O_3NiH_4·2H_2O$, Elemental Analysis, calculated: C, 43.05; H, 2.63; N, 9.13; Found: C, 42.04; H, 3.14; N, 8.36).

3.2.6 Synthesis of Ni-2D-SA

The preparation procedure of Ni-2D-SA is similar as Ni-2D-O-SA, the precursor TABQ was replaced by 1,2,4,5-benzenetetraamine tetrahydrochloride (TAB).[50] ($C_{11}N_2O_2NiH_5·H_2O$ elemental analysis Calculated: C, 48.24; H, 2.58; N, 10.23; Found: C, 47.34; H, 3.24; N, 9.26)

3.2.7 Synthesis of Ni-2D-O-SA/CNT composites

30 mg Ni-2D-O-SA, 5 mL NMP and 70 mg pre-oxidized carbon nanotubes (CNTs) were added into a 15 mL glass vial. The obtained mixture was sonicated for half an hour, and stirred at 100 ℃ for 12 h, The obtained black composite was collected by

vacuum filtration and washed with ethanol for several times, and then vacuum dried at 60 °C for 24 h.

3.2.8 Synthesis of Ni-2D-SA/CNT composites

Ni-2D-SA-CNT composites were synthesized by using the same procedure as for Ni-2D-O-SA-CNT, just the precursor of Ni-2D-SA was replaced by Ni-2D-O-SA.

3.2.9 Synthesis of model complex Ni-salophen (Ni-SA)
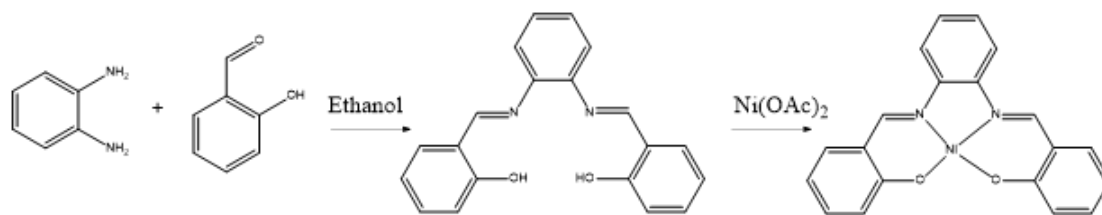
First, the salophen ligand was synthesized by placing 108 mg (1 mmol) of 1,2-diaminobenzene in 15 mL three-neck flask. Then 6 mL Ethanol were added and the mixture was heated to 70 °C under stirring, after that, 2 mmol of salicylaldehyde were added to the above mixture. The mixture was refluxed for 24 h. After cooling to room temperature, the obtained precipitates were vacuum filtrated and washed with EtOH for several times. Finally, the yellow powder was dried under vacuum at 60 °C overnight. To prepare the Ni-salophen (Ni-SA), 60 mg of Ni(CH$_3$COO)$_2 \cdot$4H$_2$O, 90 mg of salophen ligand and 6 mL of MeOH were put into a 15 mL flask. The obtained mixture was heated to 60 °C with magnetic stirring for one day under argon. The mixture was filtrated by vacuum and washed with MeOH for several times. Finally, the reference complex Ni-SA was dried under vacuum at 60 °C overnight.

3.2.10 Electrochemical Measurements
Electrode preparation

1 mg of catalyst was dispersed in the mixture of isopropanol (475 μL) and Nafion (5%, 25μL) by sonication for 1h to obtain uniformly inks. Then, the inks were dropped on the carbon paper (1*1 cm^2) under the infrared grill light. After dropping, the electrodes were further dried by infrared grill light at least 20 min before test.

Electrochemical measurements

All electrochemical measurements were performed in a gas-tight H-type glass cell containing a Nafion 117 membrane using a Biologic VMP3 multichannel potentiostat workstation at room temperature. The electrolyte (0.1 M $KHCO_3$) was saturated with CO_2 before each experiment by bubbling CO_2 for 20 min. In a typical three-electrode test system, a graphite rod and an Ag/AgCl electrode were used as the counter electrode and the reference electrode, respectively. All working electrodes were dried by infrared grill light at least 20 min before test. Each fresh sample was measured with a chronoamperometric step for 1h at each potential. The roughness factors were determined by measuring the double-layer capacitance with cyclic voltammetry in the potential range of open circuit potential $\pm$ 50 mV at varying scan rates (2, 5, 10, 20, 50, 100 mV s^{-1}). All potentials were converted to the RHE using the relationship: E(RHE) = E(Ag/AgCl) + 0.197 + 0.059*pH. The pH of 0.1 M $KHCO_3$ saturated with CO_2 is 6.8, which is measured by a pH-meter. The potentiostat workstation was set to compensate 85 % of the ohmic drop, and no further iR correction was performed.

Electrochemical CO_2 reduction reaction (CO_2RR) product analysis

During electrolysis, CO_2 gas (99.995%) was delivered into the cathodic compartment containing CO_2-saturated electrolytes at a rate of 20 sccm and vented into online gas chromatography (GC) equipped with a combination of molecular sieve 5A. Methane and carbon monoxide were detected by a methanizer-flame ionization detector, and the hydrogen was detected by a thermal conductivity detector. Every 20 minutes, 1 mL of gas was sampled to determine the concentration of gaseous products. After electrolysis, the liquid products in catholyte were quantified by Nuclear Magnetic Resonance (NMR). Specifically, 500 μL of catholyte was taken out after 1 h of CO_2 electroreduction. It was then mixed with 150 uL of internal standard. The internal standard was obtained by dissolving 2.5 mM Dimethyl sulfoxide (DMSO) into D_2O solvent. After that, the mixture was then transferred into a NMR sample tube for measurement.

Calculation of the Faradaic efficiency of methanol ($FE_{methanol}$)

The FE$_{methanol}$ was calculated by the following formula:

$$FE_{methanol} = \frac{C_{methanol} \times V \times N_A \times 6e}{N_{total}}$$

Where C$_{methanol}$ is the concentration of methanol in the electrolyte, V is the volume of electrolyte, N$_A$ is Avogadro's constant, N$_{total}$ is the total number of electrons measured during the entire CO$_2$RR.

The concentration of methanol (C$_{methanol}$) was obtained using the calibration curves shown in the following. The calibration curves were made by measuring standard solutions of methanol.
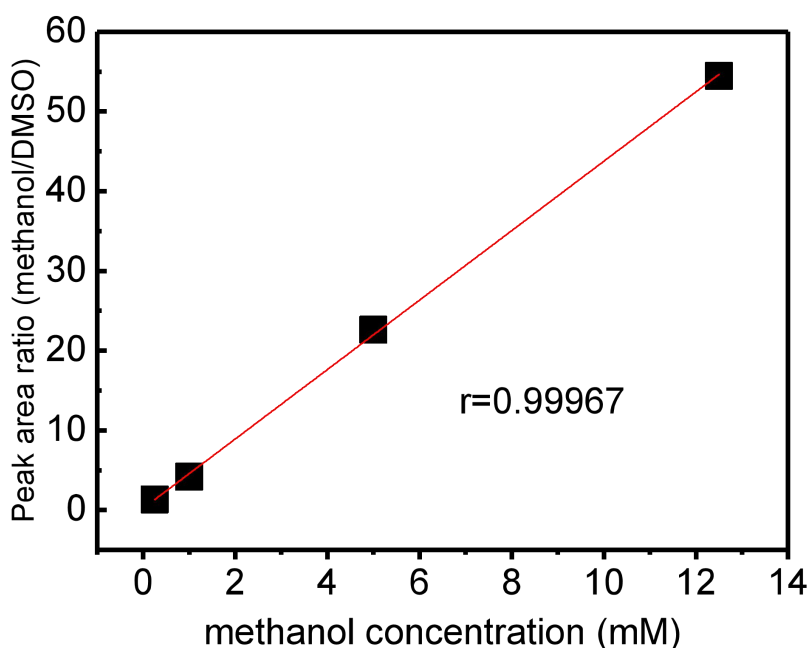
Figure 3.1 Calibration curves for methanol.

The peaks were quantified by integrating the area. the relative peak area can be calculated as follows:

$$\text{Relative peak area ratio (methanol)} = \frac{\text{singlet peak area at 3.23ppm (methanol)}}{\text{singlet peak area at 2.6 ppm (DMSO)}}$$

3.2.11 DFT Calculations

All the data were calculated from density functional theory (DFT) by the Vienna ab initio Simulation Package (VASP). [51] [52] The generalized gradient approximation of Pardew-Burke-Ernzerhof (PBE) method with van der Waals correlation was conducted to optimize the geometric structures. [53] The convergence criteria was 0.05 eV/Å in force and 1×10^{-5} eV in energy, while the plane wave cutoff was 500 eV.

The Monkhorst–Pack mesh k-point grids was 1×1×1 for all models. All of the vacuum thicknesses were higher than 15 Å.

The whole process of CO_2 electrochemical reduction to methanol for comparison we choose consists the following steps:

$$CO_2(g) \rightarrow *OHCO \rightarrow *HCOOH \rightarrow *CHO \rightarrow *CH_2O \rightarrow *CH_2OH \rightarrow *CH_3OH \rightarrow *+CH_3OH$$

$$CO_2 \rightarrow *COOH \rightarrow *CO \rightarrow *COH \rightarrow *CHOH \rightarrow *CH_2OH \rightarrow CH_3OH$$
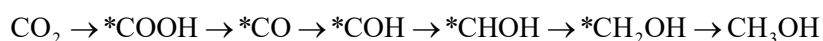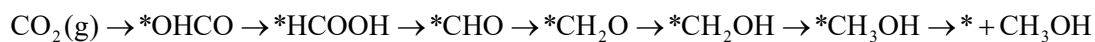
Where the * and *OHCO represent free sites and the adsorption state of OHCO, respectively. The (g) represent the gas phase.

The adsorption energy was calculated by

$$\Delta E = E_{total} - E_{surface} - E_{adsorbents}$$

where E_{total}, $E_{surface}$, and $E_{adsorbents}$ are the DFT-calculated energy for total system, pure surface, and pure adsorbents, respectively.

The reaction free energies of each step were calculated by the following formula:

$$\Delta G = \Delta E + \Delta E_{ZPE} - T\Delta S$$

where ΔE_{ZPE} is the zero-point energy, $T\Delta S$ (T=298.15 K) is the entropy.

3.3 Results and Discussion

3.3.1 Synthesis and Structure Characterization

As shown in **Scheme 3-1**, the targeted 2D nickel organic framework (Ni-2D-O-SA) with abundant carbonyl functional group was solvothermally synthesized by a Schiff-based reaction between 2,5-hydroxyterephthalaldehyde (HBC), nickel acetate and tetramino-benzoquinone (TABQ) in N-methyl-2-pyrrolidone (NMP). The dark-black precipitate obtained from this reaction indicated the formation of a conjugated polymer. This precipitate was vacuum filtrated, washed with water and methanol to remove small molecular mass impurities and finally dried under vacuum at 60 °C. A control sample, without the carbonyl chemical groups (Ni-2D-SA), was prepared using the same reaction process and conditions but replacing TABQ by 1,2,4,5-benzenetetraamine tetrahydrochloride

(TAB) (**Scheme 3-2**).[31]
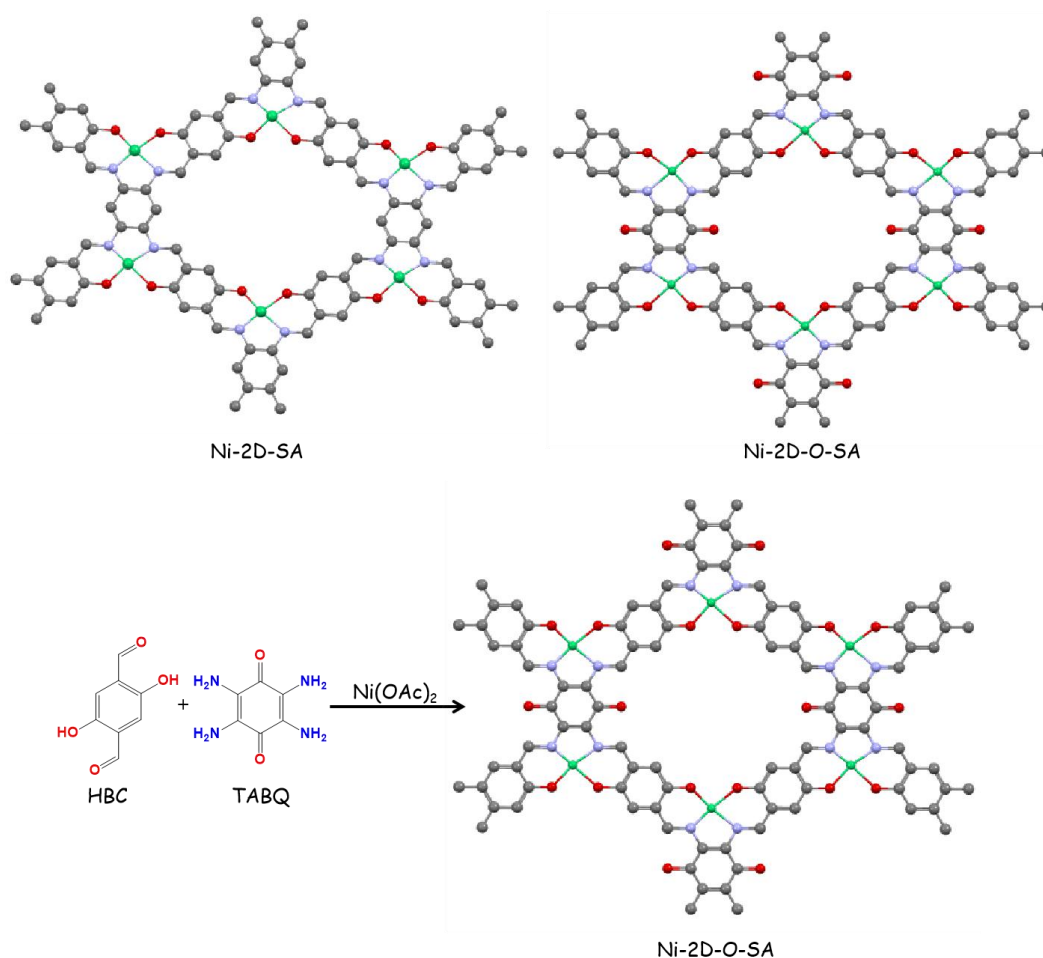
Scheme 3-1 Schematic representation of the synthesis of Ni-2D-O-SA (blue spheres correspond to Ni atoms, red to O, green to Ni and grey to C).

The Ni-2D-O-SA powder exhibited a crystalline and layered structure, as observed by powder X-ray diffraction (XRD) analysis (**Figure 3.2a**). The Ni-2D-O-SA XRD pattern was similar to that of graphite, with a diffraction peak at 26.29° corresponding to the (001) family planes, and thus indicating a π-π layered stacking.[32] In contrast, the XRD pattern of the control sample, Ni-2D-SA, displayed a much lower crystallinity. This result indicates that the introduction of the carbonyl groups enhances the ordering of the nickel organic frameworks.
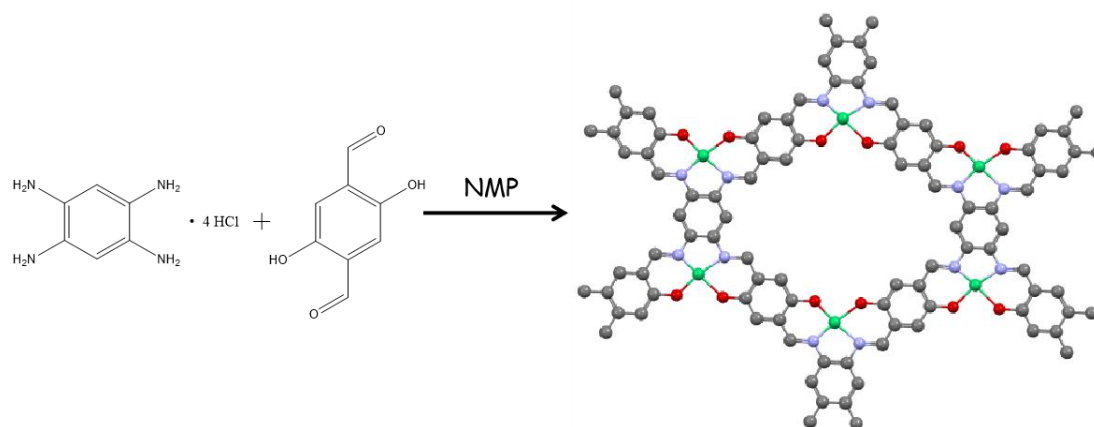
Scheme 3-2 Synthesis scheme of Ni-2D-SA (blue spheres correspond to Ni atoms, red to O, green to Ni and grey to C).

The Fourier transform infrared (FT-IR) spectra (**Figure 3.2b**) of the two samples displayed the footprint of C=N at 1642 cm^{-1} for Ni-2D-SA and 1648 cm^{-1} for Ni-2D-O-SA. At the same time, the characteristic peaks of the N-H stretching vibration (3367-3197 cm^{-1}) disappeared. These pieces of evidence demonstrated the completion of the Schiff-based reaction and the formation of Ni-salophen structural units.[31] The vibration of the carbonyl group (C=O) in Ni-2D-O-SA negatively shifted below 1600 cm^{-1}, where it overlapped with other vibrations. Besides, the vibration peak for the C-(C=O)-C bond in Ni-2D-O-SA, which is characteristic of the TABQ, shifted from 1140 cm^{-1} to 1010 cm^{-1} due to the coordination effect and the attraction between the layers. These results demonstrated the formation of the organic framework containing the carbonyl groups.[33] The solid-state ^{13}C CP/MAS NMR spectrum of the Ni-2D-O-SA catalyst exhibits the presence of C=O, C=N, C=C, with the corresponding signals at 160 ppm, 149 ppm and 123 ppm, respectively. Instead, for the Ni-2D-SA catalyst, the resonance signals of C=N and C=C appear at 150 ppm and 120 ppm, respectively (**Figure 3.2 c-d**).
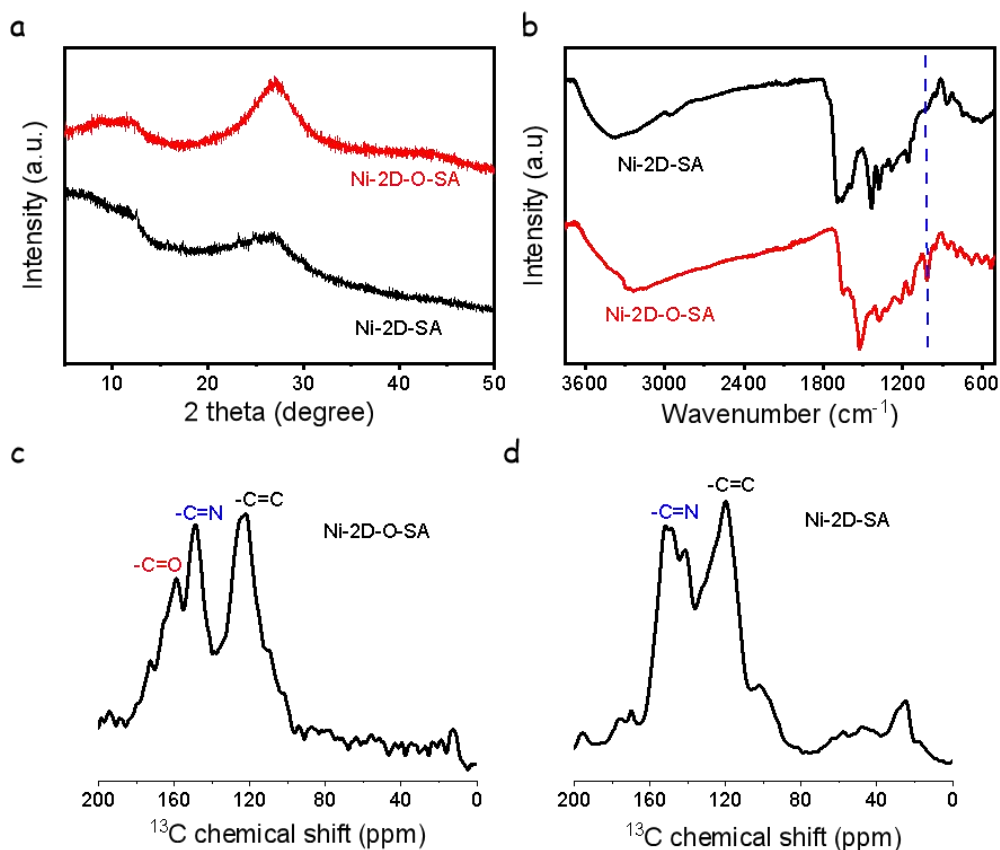
Figure 3.2 (a) PXRD patterns of Ni-2D-SA (black) and Ni-2D-O-SA (red). (b) FT-IR spectra of Ni-2D-SA and Ni-2D-O-SA. chemical shift of ^{13}C SSNMR spectra of Ni-2D-SA (c) and Ni-2D-O-SA (d)

High angle annular dark-field (HAADF)-aberration-corrected scanning transmission electron microscopy (STEM) analysis (**Figures 3.3a-c**) demonstrated the presence of a high density of atomically dispersed and homogeneously distributed nickel atoms. The energy-dispersed X-ray spectroscopy (EDS) elemental mapping shown in **Figure 3.3d** further demonstrated the uniform distribution of Ni, C, N, and O.
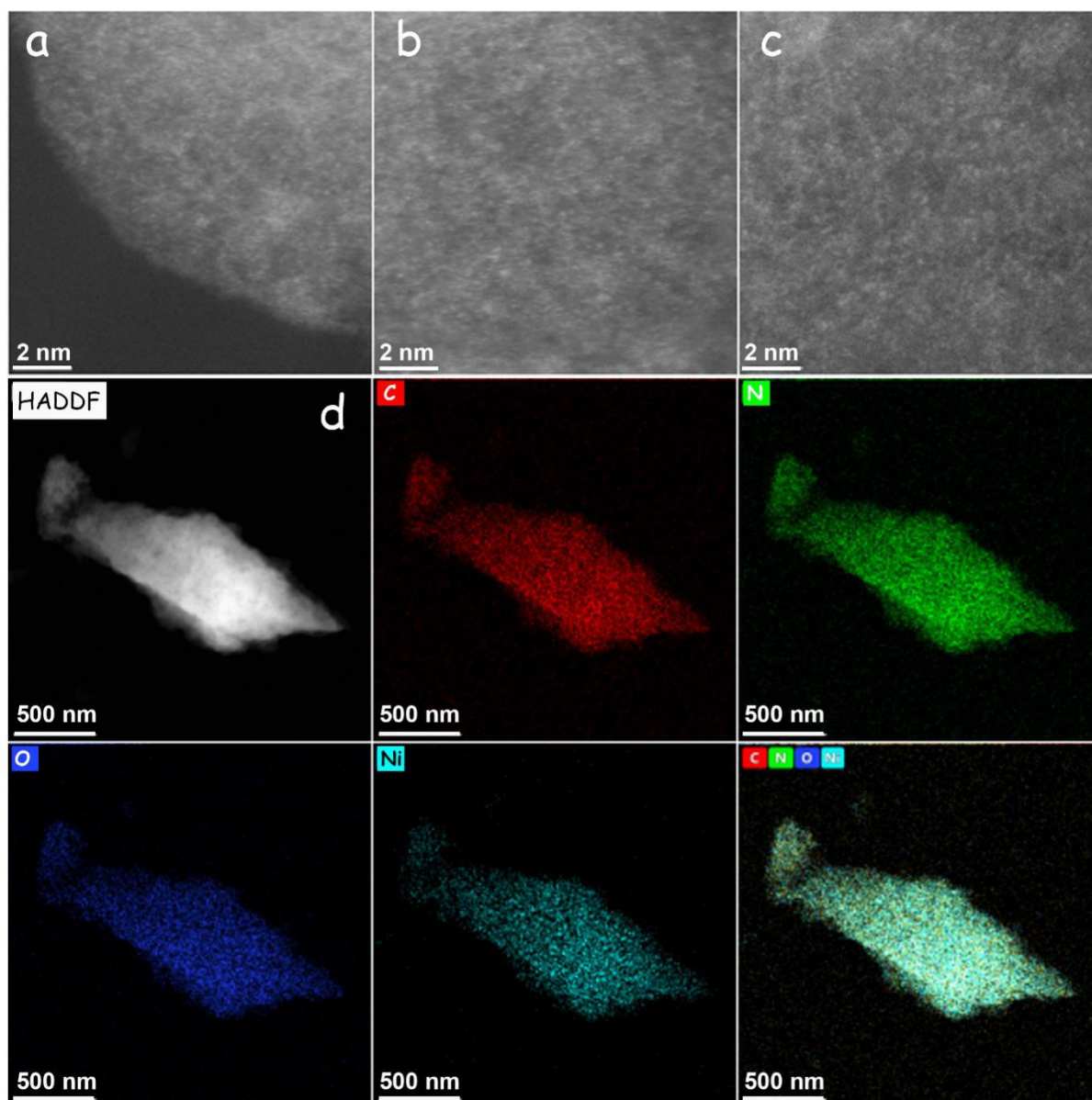
Figure 3.3 (a)-(c) HAADF-STEM images of Ni-2D-O-SA. (d) Low magnification HAADF-STEM image and corresponding EDS elemental maps for C (red), Ni (light blue), N (green) and O (blue), together with the mixed colored map overlapping all the elements.

To further confirm the local coordination environment of Ni active sites in Ni-2D-O-SA, XAFS analysis of the Ni K-edge was conducted (**Figure 3.4**). We first compared the spectral features of Ni-2D-O-SA with those of Ni-2D-SA, NiO, and a model complex Ni-salophen (Ni-SA) at the near-edge (i.e. X-ray absorption near-edge structure, XANES). As shown in **Figure 3.4a**, the absorption energy of near K-edge in XANES spectrum for the Ni-2D-O-SA sample shifted to higher energy compared to

that of Ni-2D-SA, which suggests that the introduction of carbonyl groups resulted in a higher oxidation state of the Ni active centers. The absorption onset of Ni-2D-O-SA occurs at slightly lower energy than that of NiO. Differences are more clearly seen when the first derivative of these spectra are plotted (**Figure 3.4b**). The main absorption peak of Ni-2D-O-SA also has a lower intensity. These features indicate that, compared with NiO where Ni is fully coordinated with O, Ni atoms within Ni-2D-O-SA are surrounded by less electronegative elements, i.e. N substituting O. The EXAFS spectrum was analyzed to obtain more quantitative details of the coordination environment. First the EXAFS spectrum of Ni-SA was fitted well with a NiN_2O_2 coordination structure (**Figure 3.4c** and **Table 3-1**), the Ni-2D-SA was also fitted with a NiN_2O_2 coordination structure (**Figure 3.4d** and **Table 3-2**). The Fourier transformed EXAFS of Ni-2D-O-SA is shown in **Figure 3.4e**. The fitted curve suggests that Ni is coordinated with two N atoms and two O atoms, at a bond length 1.87 Å and 2.05 Å, respectively (**Figure 3.4e**), which matches well the salophen unit structure (NiO_2N_2). The contribution at longer radial distances comes from C atoms with a coordination number of 6 and a bond length of 2.65 Å, which also belong to the Ni...C interaction (**Table 3-3)** and the distance of Ni...Ni interaction is of 3.168 Å which corresponds to the Ni in the layer-layer structure for this type of materials. Thus, the XAFS analysis confirmed the formation of the NiN_2O_2 salophen structure unit within Ni-2D-O-SA frameworks. To confirm the coordination structure stability of Ni-2D-O-SA, the EXAFS spectrum of Ni-2D-O-SA, which was immersed in a $KHCO_3$ aqueous solution for three days, was fitted (**Figure 3.4f** and **Table 3-4**). The Ni-2D-O-SA maintained the NiN_2O_2 coordination structure, indicating its structure stability in the $KHCO_3$ aqueous solution.
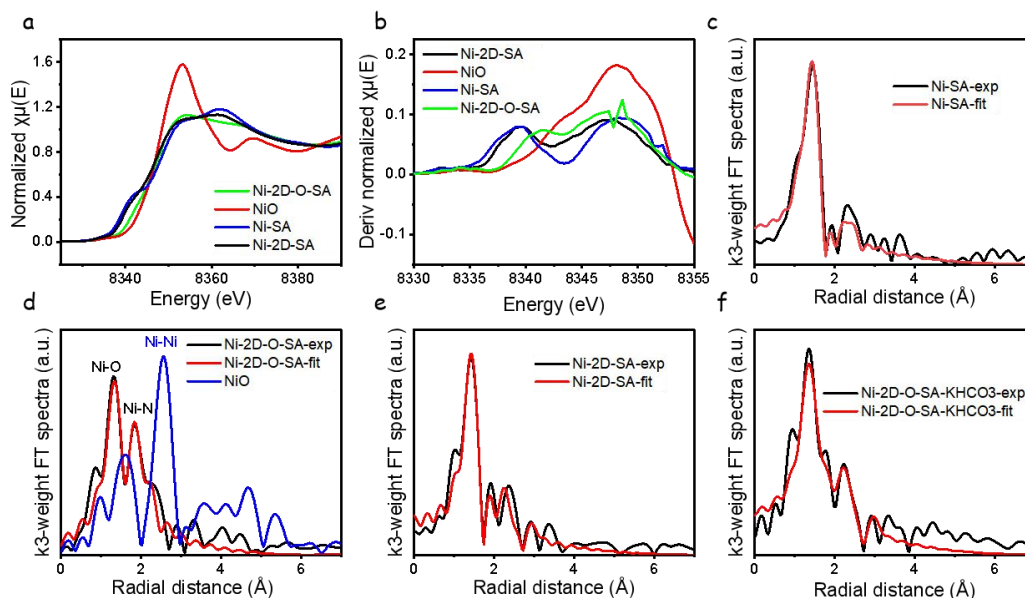
Figure 3.4 (a) Ni K-edge XANES spectrum of Ni-SA, Ni-2D-SA, Ni-2D-O-SA and NiO (commercial powder). (b) First derivative of the Ni K-edge XANES for Ni-SA, Ni-2D-SA, NiO and Ni-2D-O-SA. (c) Fourier transformed Ni K-edge EXAFS spectra of Ni-SA plotted in R-space, Fourier transformed EXAFS spectra in R-space of Ni-SA and fitted curve. (d) Fourier transformed Ni K-edge EXAFS spectra of Ni-2D-O-SA and NiO plotted in R-space, Fourier transformed EXAFS spectra in R-space of Ni-2D-O-SA and fitted curve. (e) Fourier transformed Ni K-edge EXAFS spectra of Ni-2D-SA plotted in R-space, Fourier transformed EXAFS spectra in R-space of Ni-SA and fitted curve. (f) Fourier transformed Ni K-edge EXAFS spectra of Ni-2D-O-SA after immersed in KHCO₃ for three days plotted in R-space, Fourier transformed EXAFS spectra in R-space of Ni-SA and fitted curve.

Table 3-1. The Ni K-edge EXAFS fitting parameters of Ni-SA. R：bond length, CN: coordination

Sample	Bond	R(Å)	CN	σ^2 (10^{-3} Å^2)	ΔE (eV)	R factor
Ni-SA	Ni-O	1.871 (0.015)	2	2 (1)		
	Ni-N	1.820 (0.014)	2	2(1)	4.04 (1.49)	0.03
	Ni...C	2.799 (0.029)	6	10 (4)		

Table 3-2. The Ni K-edge EXAFS fitting parameters of Ni-2D-SA. R: bond length, CN: coordination number

Sample	Bond	R(Å)	CN	σ^2 (10^{-3} Å^2)	ΔE (eV)	R factor
Ni-2D-SA	Ni-O	1.844 (0.015)	2	1 (1)		
	Ni-N	2.070 (0.168)	2	30 (15)	5.04 (1.52)	0.03
	Ni...C	2.760 (0.062)	6	11 (6)		
	Ni...Ni	3.170 (0.091)	1	11 (10)		

Table 3-3. The Ni K-edge EXAFS fitting parameters of Ni-2D-O-SA. R：bond length, CN: coordination number

Sample	Bond	R(Å)	CN	σ^2 (10^{-3} Å^2)	ΔE (eV)	R factor
Ni-2D-O-SA	Ni-O	1.855 (0.024)	2	3 (1)		
	Ni-N	2.084 (0.031)	2	4 (3)	-4.93 (1.53)	0.02
	Ni...C	2.651 (0.052)	6	15 (4)		
	Ni...Ni	3.168 (0.043)	1	10 (5)		

Table 3-4. The Ni K-edge EXAFS fitting parameters of Ni-2D-O-SA-KHCO$_3$.

Sample	Bond	R(Å)	CN	σ^2 (10^{-3} Å^2)	ΔE (eV)	R factor
Ni-2D-O-SA-KHCO$_3$	Ni-O	1.995 (0.021)	2	3 (1)		
	Ni-N	1.851 (0.018)	2	2 (2)	3.35 (1.82)	0.02
	Ni...C	2.790 (0.035)	6	15 (3)		
	Ni...Ni	3.188 (0.050)	1	13 (7)		

The Brunauer-Emmett-Teller surface areas of Ni-2D-O-SA and Ni-2D-SA were calculated at 21 and 83 m^2 g^{-1}, respectively.[40] Thus the presence of the carbonyl functional group decreases the surface area of the material, which is consistent with the higher π-π driven organization of the 2D Ni-2D-O-SA framework observed by XRD analysis. The pore size distribution profiles (**Figure 3.5a-b**) show the

approximate porous structures of Ni-2D-SA and Ni-2D-O-SA, respectively.
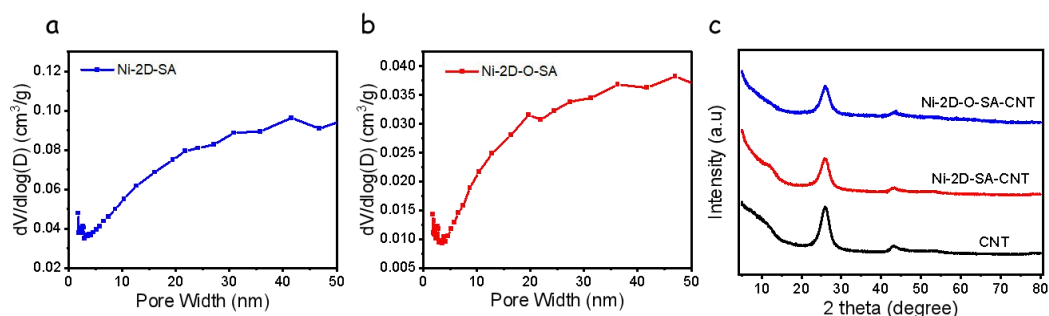
Figure 3.5 Pore size distribution of Ni-2D-SA (a) and Ni-2D-O-SA (b) powder, respectively. (c) PXRD of Ni-2D-SA-CNT, Ni-2D-O-SA-CNT and CNT.

To promote the electrical conductivity of the nickel-based organic frameworks toward their use as efficient electrocatalysts, they were supported on multi-walled CNTs by physical mixing in dimethylformamide. XRD patterns displayed just one broad diffraction peak at about 26° (**Figure 3.5c**), which was assigned to the overlap between the CNT and the nickel organic framework structures. The porous morphology and the homogenous loading of Ni-2D-O-SA on the CNTs within the obtained composites (Ni-2D-O-SA-CNT) were confirmed by STEM images and EDS elemental mapping (**Figure 3.6**).
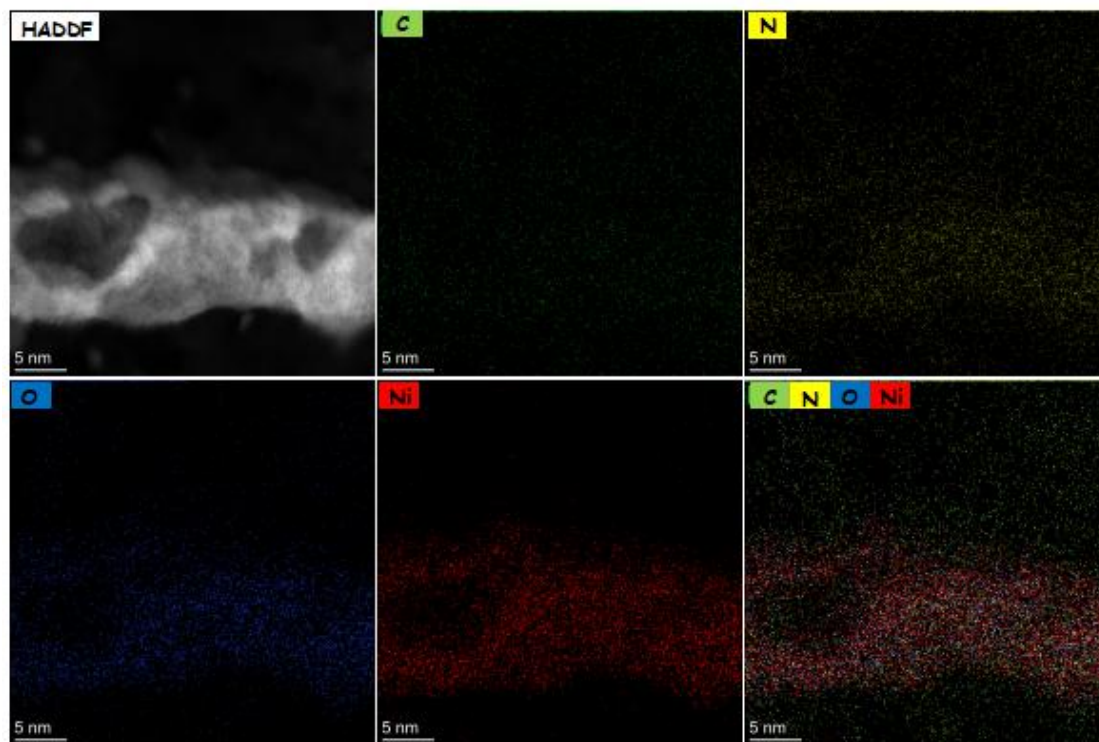
Figure 3.6 HAADF-STEM image and EDS elemental mapping for

Ni-2D-O-SA-CNT.

3.3.2 Electrochemical Characterization

The electrocatalytic properties of Ni-2D-O-SA-CNT toward CO_2RR were tested in a two-compartment electrochemical cell containing a CO_2-saturated 0.1 M $KHCO_3$ electrolyte. As shown in **Figure 3.7a**, the Ni-2D-O-SA-CNT catalyst displayed much higher current densities in the CO_2-saturated electrolyte than in Ar-saturated electrolyte at potentials more positive than -0.9 V *vs* RHE, which indicates a high CO_2RR activity. When the applied potentials were more negative than -0.9 V, the current density in a CO_2-saturated electrolyte was lower than in the Ar-saturated electrolyte due to the HER suppression through CO_2 adsorption.
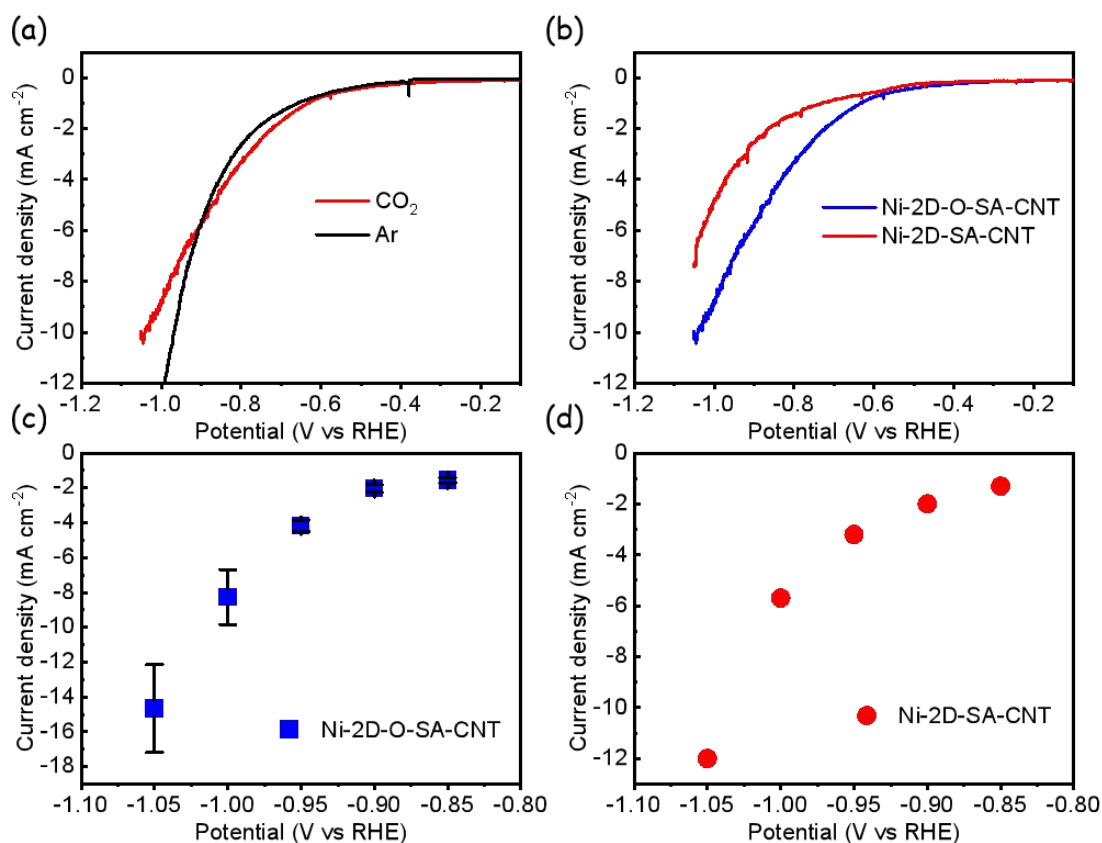
Figure 3.7 Electrocatalytic CO_2RR performance of Ni-2D-O-SA-CNT and Ni-2D-SA-CNT. (a) Linear sweep voltammetry (LSV) curves of Ni-2D-O-SA-CNT at a scan rate of 5 mV s^{-1} in CO_2- and Ar-saturated 0.1 M $KHCO_3$ electrolytes. (b) LSV curves of Ni-2D-O-SA-CNT and Ni-2D-SA-CNT in CO_2-saturated 0.1 M $KHCO_3$ electrolyte. (c and d) Current densities of CO_2RR for Ni-2D-O-SA-CNT and

Ni-2D-SA-CNT at various potentials.

Ni-2D-O-SA-CNT samples displayed much higher current densities than Ni-2D-SA-CNT under the same test conditions (**Figure 3.7b and Figure 3.7c-d**), which demonstrates that Ni-2D-O-SA-CNT has better activity toward CO2RR than that of Ni-2D-SA-CNT. Given that Ni-2D-O-SA-CNT and Ni-2D-SA-CNT were characterized by similar electrochemical double-layer capacitances (**Figure 3.8**), we can conclude that the presence of the carbonyl group within Ni-2D-O-SA organic framework decisively increases its CO_2RR activity.
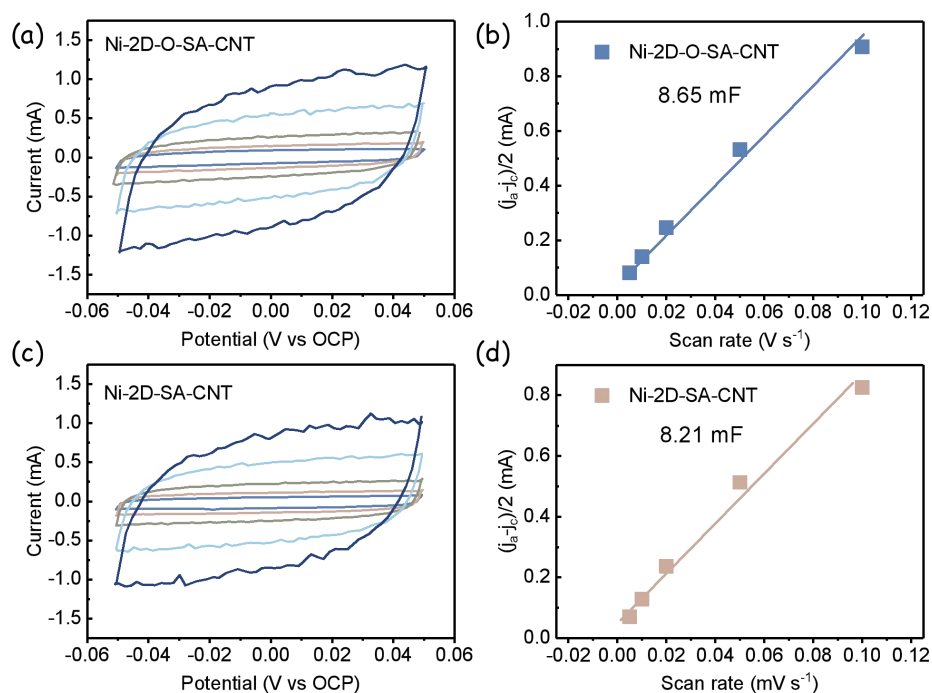
Figure 3.8 (a,c) CV curves on Ni-2D-O-SA-CNT and Ni-2D-SA-CNT with different scan rates (5, 10, 20, 50, 100 mV s-1). (b, d) Current at open circuit potential (OCP) versus scan rates of different samples. The electrode area is 1 cm^{-2}.

The CO_2RR product distribution obtained from Ni-2D-O-SA-CNT and Ni-2D-SA-CNT electrocatalysts at different potentials was evaluated by gas chromatography and nuclear magnetic resonance. The Faradaic efficiency of all products are provided in **Figures 3.9a** and **3.9b**, which show that H_2 is one of the CO_2RR products, too. The Methanol faradaic efficiency was quantified by liquid NMR technology. As shown in **Figure 3.9c** and **3.9d**, Ni-2D-O-SA-CNT and Ni-2D-SA-CNT are characterized by a volcano-shaped Faradaic efficiency (FE)

toward CH$_3$OH in the range of applied potential from -0.85 to -1.05 V. A maximum CH$_3$OH FE of 27% was achieved by Ni-2D-O-SA-CNT at -0.9 V. This excellent performance is in contrast with the nickel organic framework without the carbonyl group Ni-2D-SA-CNT (9.2% FE for CH$_3$OH at -0.95 V, **Figure 3.9d**). The high performance of Ni-2D-O-SA-CNT is also in contrast with all previously developed nickel-based CO$_2$RR catalysts, which mostly yielded CO instead of methanol (**Table 3-5**).[16-17] To the best of our knowledge, only one previous report demonstrated CO$_2$RR to methanol using a Ni-based electrocatalyst but with a moderate activity and selectivity (6% FE).[18] Compared with Ni-2D-SA-CNT, in the potential range from -0.85 to -1 V Ni-2D-O-SA-CNT also exhibited a higher selectivity toward the production of CO, which is an intermediate in the production of methanol (**Figure 3.9e**).[11][14-15]

The catalytic stability of Ni-2D-O-SA-CNT was evaluated at -0.85 V vs RHE (**Figure 3.9f**). We observed the current density to be maintained during an operating period of 5.5 h. Although the selectivity of methanol is decreased after this relatively long electrochemical test, the Ni-2D-O-SA-CNT catalyst could still maintain ~10% FE toward methanol.
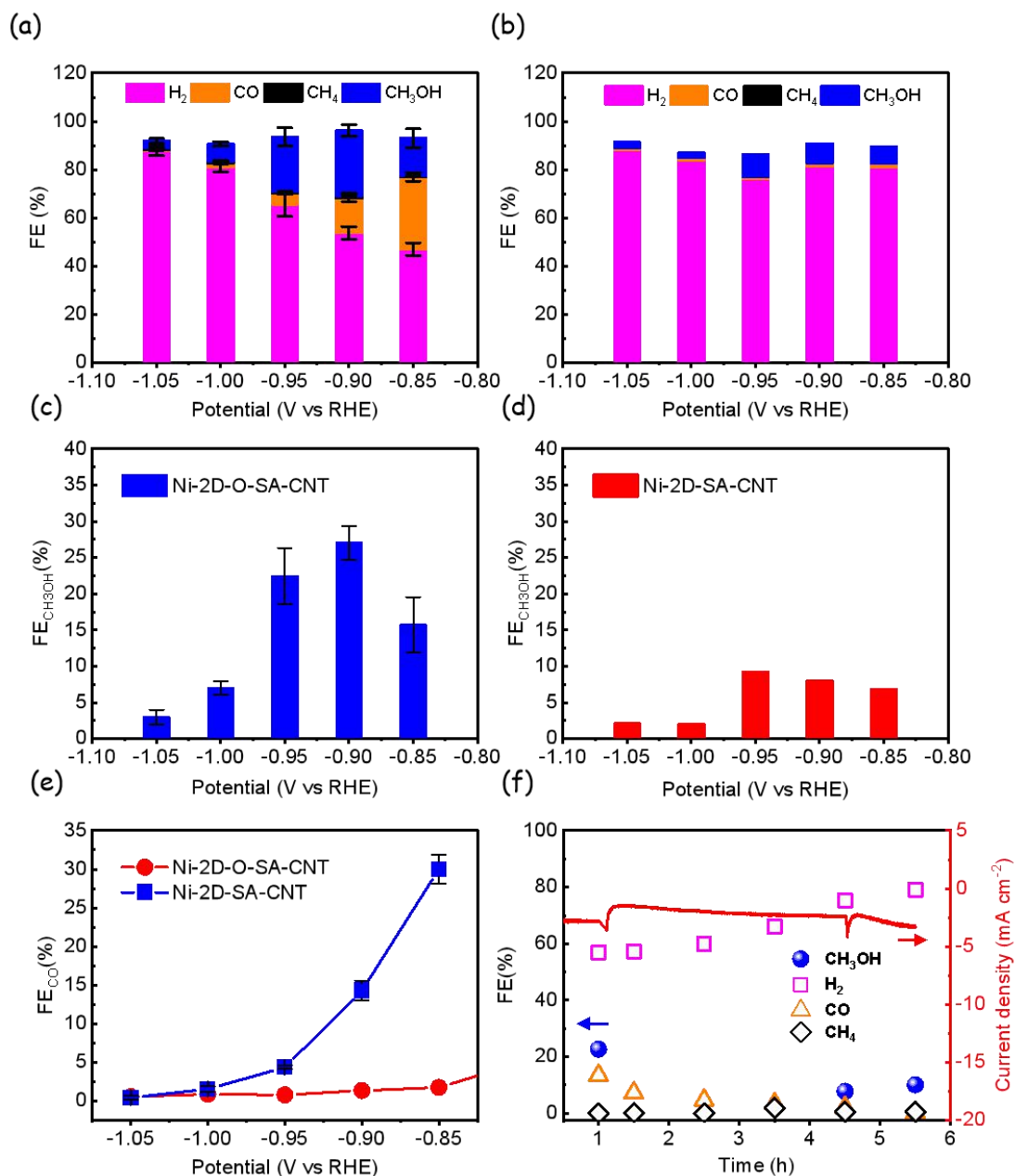
Figure 3.9 (a and b) Product distribution of CO2RR for Ni-2D-O-SA-CNT and Ni-2D-SA-CNT at various potentials. (c, d) FEs of Ni-2D-O-SA-CNT (c) and Ni-2D-SA-CNT (d) toward CH_3OH at various applied potentials, from -0.85 to -1.05 V. (e) CO_2 to CO FE of Ni-2D-O-SA-CNT and Ni-2D-SA-CNT at various applied potentials from -0.85 to -1.05 V vs RHE. (f) Current-time (*i-t*) responses and corresponding FEs of Ni-2D-O-SA-CNT at -0.9 V vs RHE for 5.5 h.

To exclude the possibility that the formation of methanol came from the preparation process or the decomposition of the catalyst, we analyzed the product distribution of the Ni-2D-O-SA-CNT sample in Ar-saturated 0.1 M $KHCO_3$. The

114

obtained results showed that no methanol signal could be found, and that the Ni-2D-O-SA-CNT catalyst could only produce hydrogen in Ar-saturated 0.1 M KHCO₃ (**Figures 3.10**). These results demonstrate the excellent intrinsic catalytic selectivity toward methanol of the Ni-2D-O-SA-CNT sample.
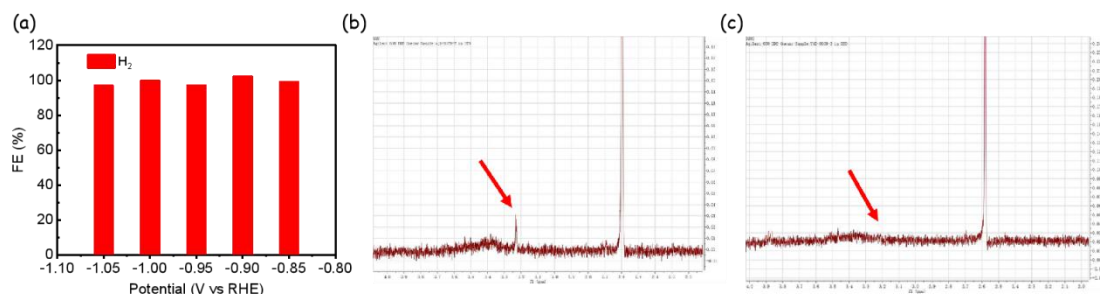
Figure 3.10 (a) Product distribution for Ni-2D-O-SA-CNT under Ar-saturated 0.1 M KHCO₃ electrolyte at various potentials. (b) NMR spectrum of the catholyte after 1 hour of CO₂ reduction on Ni-2D-O-SA-CNT. Potential applied=-0.9 V vs RHE. The peak located at 3.23 ppm is the signal of methanol. (c) NMR spectrum of the catholyte after 1 hour of electro-reduction under Ar environment on Ni-2D-O-SA-CNT. Potential applied=-0.9 V vs RHE.

To understand which are the real active sites for the formation of methanol and the reason of deactivation after the long-term stability test, we analyzed the post reaction sample by XRD, FT-IR, and XPS. From XRD patterns (**Figure 3.11a**), the characteristic peaks of Ni-2D-O-SA-CNT are well maintained after CO2RR test, and no presence of other peaks was observed, suggesting that no Ni-based metal or metal oxide nanoparticles were formed. To investigate the coordination structure of the residual Ni-sites in the catalyst, FT-IR spectra showed that the functional groups of Ni-2D-O-SA-CNT were still maintained after the long-term stability test, implying that the NiN2O2 sites were the real active sites for the formation of methanol (**Figure 3.11b**).
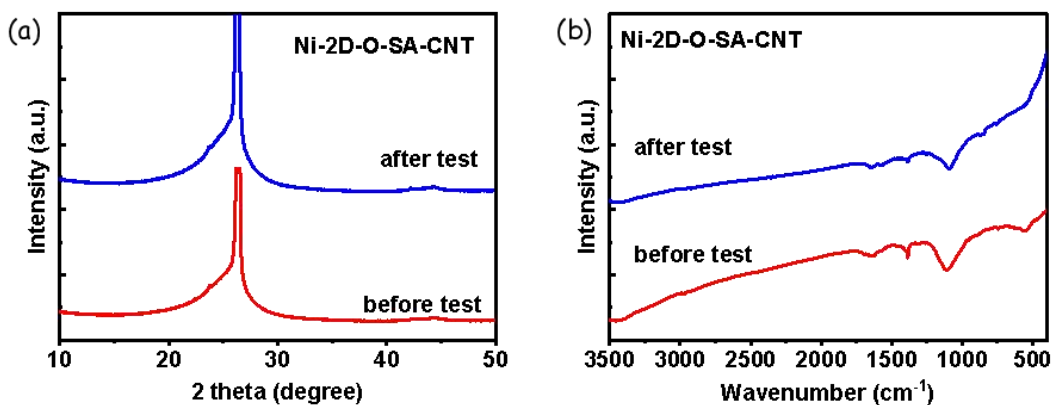
Figure 3.11 (a) XRD patterns and (b) FT-IR spectra of Ni-2D-O-SA-CNT on carbon paper before and after 1 hour of CO_2RR test.

XPS was further conducted to investigate the electronic structure of Ni after CO_2RR (**Figure 3.12**). Interestingly, we found that only a small Ni 2p signal remained after the CO2RR test, indicating that the NiN2O2 sites might be partially decomposed, which could be responsible for the deactivation of our catalyst.
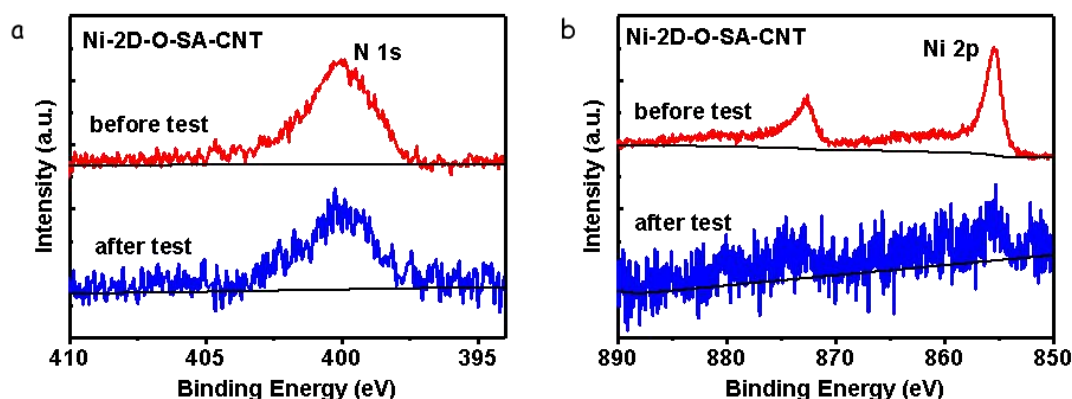
Figure 3.12 XPS spectra of Ni-2D-O-SA-CNT on carbon paper before and after 1 hour of CO_2RR test.

Both electrocatalysts, Ni-2D-O-SA-CNT and Ni-2D-SA-CNT yielded methanol with a significant FE, which indicates that the porous structure, the high densities of nickel active centers, and possibly the short distance between the catalytic active sites resulting in the synergy effect are highly suitable for the electroreduction process of CO_2 to methanol. Furthermore, the presence of the carbonyl group in the ligand between the nickel active centers in the Ni-2D-O-SA-CNT electrode resulted in a very notable enhancement of the FEs for CO_2 reduction to both methanol and CO. Thus, the presence of the carbonyl group clearly favors the electroreduction of CO_2 to CO,

which can be considered as a first step in the formation of methanol. But at the same time, this carbonyl group promotes a deeper electrochemical reduction, which we tentatively attribute to the stronger π-d conjugation that enhances the adsorption of the intermediates generated in the electrochemical reduction process of CO_2 to methanol over the nickel active centers.[15,35] Besides, the strong electronegativity of the carbonyl group could shift the electron cloud in nickel active centers (NiN_2O_2), resulting in Ni ions with a more positive valence than in NiN_4, which usually converts CO_2 to CO. This higher valence has been reported to promote a deeper CO_2 electroreduction in different metals.[36-37]

3.3.3 DFT Calculation

To further understand the effect of the carbonyl group, the differential charge distribution was estimated by density functional theory (DFT) calculations. The electron density difference between Ni-2D-SA and Ni-2D-O-SA (**Figure 3.13a**) illustrates that the charge transfer from Ni ion to ligand appears, which is due to the inductive effect of carbonyl group in Ni-2D-O-SA. These results are consistent to the XANES analysis, which show that the Ni center in Ni-2D-O-SA has a higher oxidation state compared to that of Ni-2D-SA. The absolute free energy of H* on Ni-2D-O-SA is larger than that of Ni-2D-SA, suggesting that the Ni-2D-SA catalyst is more favorable for hydrogen evolution reaction (HER) (**Figure 3.13b**). Furthermore, the free energy diagram in the conversion from *CO to methanol was calculated, and the reaction pathway was proposed based on the previous report.[11] According to our DFT calculation results (**Figure 3.13c**), the conversion of *CO to methanol is thermodynamically more favorable on Ni-2D-O-SA than that on Ni-2D-SA. On the other hand, a second reaction pathway of the conversion from CO_2 to methanol based on another published work [12] was also calculated. As exhibited in **Figure 3.13d**, the free energy in the rate-determining step of the conversion of *OHCO to absorbed *HCOOH is lower on Ni-2D-O-SA. Therefore, we can suggest that Ni-2D-O-SA with carbonyl groups would tend to favor the electrocatalytic reduction of CO_2 to methanol with respect to Ni-2D-SA.
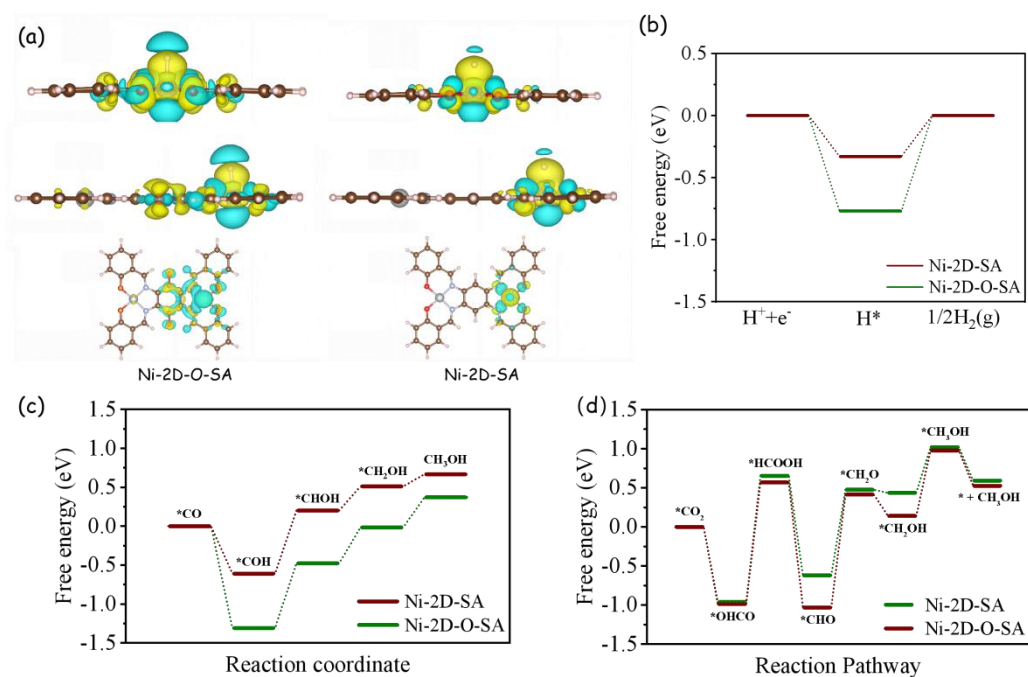
Figure 3.13 (a) Plots of electron density difference for selected segments of Ni-2D-O-SA and Ni-2D-SA. The yellow color corresponds to an isosurface of 0.00120794 e Bohr^{-3} and blue of -0.00120794 e Bohr^{-3}. (b) Free-energy profiles of hydrogen evolution reaction (HER) on selected segments of Ni-2D-SA and Ni-2D-O-SA, respectively. (c) Free energy diagram of *CO to CH$_3$OH on selected segments of Ni-2D-O-SA. (d) Free energy diagram of CO$_2$ to CH$_3$OH on selected segments of Ni-2D-O-SA.

3.4 Conclusion

We have detailed the synthesis and characteristics of an atomically dispersed nickel catalyst consisting of NiN$_2$O$_2$ active sites within a 2D organic framework under mild and controllable reaction condition. A molecular engineering strategy based on modifying the edge ligand environment by introducing a carbonyl group was proposed to tune the electrocatalytic reduction of CO$_2$. The obtained Ni-O-SA-CNT composites exhibited excellent activity and selectivity (27 % FE at -0.9 V vs RHE) toward the conversion of CO$_2$ to methanol due to the synergistic effect of the carbonyl group in the ligand and the nickel active sites. This work not only provides the best nickel-based catalysts so far reported for the electrocatalytic conversion of CO$_2$ to

methanol, but also demonstrates a novel strategy to design and engineer efficient electrocatalysts to convert CO_2 to valuable chemicals through modulating the ligand structures.

References

[1] O. S. Bushuyev, P. De Luna, C. T. Dinh, L. Tao, G. Saur, J. van de Lagemaat, S. O. Kelly, E. H. Sargent, *Joule,* 2018, 2, 825-832.

[2] L. Zhang, Z. J. Zhao, J. Gong, *Angew. Chem. Int. Ed. Engl.*, 2017, 56, 11326-11353.

[3] S. Lin, C. S. Diercks, Y. B. Zhang, N. Kornienko, E. M. Nichols, Y. Zhao, A. R. Paris, D. Kim, P. Yang, O. M. Yaghi, C. J. Chang, *Science*, 2015, 349, 1208.

[4] R. Cao, J. D. Yi, D. H. Si, R. Xie, Q. Yin, M. D. Zhang, Q. Wu, G. L. Chai, Y. B. Huang, *Angew. Chem. Int. Ed.* 2021, 60, 17108-17114.

[5] F. Yang, A. O. Elnabawy, R. Schimmenti, et al. *Nat. Commun.*, 2020, 11, 1088.

[6] S. Gao, Y. Lin, X. Jiao, Y. Sun, Q. Luo, W. Zhang, D. Li, J. Yang, Y. Xie, *Nature* 2016, 529, 68-71.

[7] T.-Y. Chang, R.-M. Liang, P.-W. Wu, J.-Y. Chen, Y.-C. Hsieh, *Materials Letters*, 2009, 63, 1001-100.

[8] E. Andrews, M. Ren,F.Wang, Z. Zhang, P. Sprunger, R. Kurtz, J. Flake, *J. Electrochem. Soc.*, 2013, 160, H841-H84.

[9] X. Sun, Q. Zhu, X. Kang, H. Liu, Q. Qian, Z. Zhang, B. Han, *Angew. Chem. Int. Ed. Engl.*, 2016, 55, 6771-6775.

[10] J. Albo, A. Sáez, J. Solla-Gullón, V. Montiel, A. Irabien, *Applied Catalysis B: Environmental*, 2015, *176-177*, 709-717.

[11] H. Yang, Y. Wu, G. Li, Q. Lin, Q. Hu, Q. Zhang, J. Liu, C. He, *J. Am. Chem. Soc.*, 2019, 141, 12717-12723.

[12] Q. Zhao, C. Zhang, R. Hu, Z. Du, J. Gu, Y. Cui, X. Chen, W. Xu,Z. Cheng, S. Li, B. Li, Y. Liu, W. Chen, C. Liu, J. Shang, L. Song, S. Yang, *ACS Nano*, 2021, 15, 4927.

[13] D. Xiang, D. Magana, R. B. Dyer, *J. Am. Chem. Soc*., 2014, 136, 14007-14010.

[14] E. Boutin, M. Wang,J.C.Lin, M.Mesnage,D.Mendoza, B. Lassalle-Kaiser,C.Hahn, T. F.Jaramillo, M. Robert, *Angew. Chem. Int. Ed.*, 2019, 58, 16172-16176.

[15] Y. Wu, Z. Jiang, X. Lu, et al., *Nature*, 2019, 575, 639-642.

[16] Yang, H.; Hung, SF.; Liu, S. et al. Atomically dispersed Ni(I) as the active site for

electrochemical CO_2 reduction. *Nat. Energy*, 2018, *3*, 140-147.

[17] (a) X. Zhang, Y. Wang, M. Gu, M. Wang, Z. Zhang, W. Pan, Z. Jiang, H. Zheng, M. Lucero, H. Wang, G. E. Sterbinsky, Q. Ma, Y.-G. Wang, Z. Feng, J. Li, H. Dai, Y. Liang, *Nature Energy*, 2020, 5, 684-692.(b) X. Wang, Z. Chen, X. Zhao, T. Yao, W. Chen, R. You, C. Zhao, G. Wu, J. Wang, W. Huang, J. Yang, X. Hong, S. Wei, Y. Wu, Y. Li, *Angew. Chem. Int. Ed.*, 2018, 57, 1944.

[18] J. Liu, D. Yang, Y. Zhou, G. Zhang, G. Xing, Y. Liu, Y. Ma, O. Terasaki, S. Yang, L. Chen, *Angew. Chem. Int. Ed. Engl.*, 2021, *60*, 14473-14479.

[19] D. Kim, J. Resasco, Y. Yu, et al. *Nat. Commun.*, 2014, 5, 4948.

[20] Z. Gu, H. Shen, Z. Chen, Y. Yang, C. Yang, Y. Ji, Y. Wang, C. Zhu, J. Liu, J. Li, T.-K. Sham, X. Xu and G. Zheng, *Joule*, 2021, *5*, 429-440.

[21] Z.-Z. Wu, F.-Y. Gao, M.-R. Gao, *Energy & Environmental Science,* 2021, 14, 1121-1139.

[22] E. Boutin, L. Merakeb, B. Ma, B. Boudy, M. Wang, J. Bonin, E. Anxolabehere-Mallart, M. Robert, *Chem. Soc. Rev.*, 2020, *49,* 5772-5809.

[23] Z. Liang, H. Y. Wang, H. Zheng, W. Zhang, R. Cao, *Chem. Soc. Rev.*, 2021, 50, 2540-2581.

[24] N. Han, Y. Wang, L. Ma, J. Wen, J. Li, H. Zheng, K. Nie, X. Wang, F. Zhao, Y. Li, J. Fan, J. Zhong, T. Wu, D. J. Miller, J. Lu, S.-T. Lee, Y. Li, *Chem*, 2017, 3, 652-664.

[25] X. Zhang, Z. Wu, X. Zhang, L. Li, Y. Li, H. Xu, X. Li, X. Yu, Z. Zhang, Y. Liang, H. Wang, *Nat. Commun.*, **2017**, *8*, 14675.

[26] J. Su, J.-J. Zhang, J. Chen, Y. Song, L. Huang, M. Zhu, B. I. Yakobson, B. Z. Tang, R. Ye, *Energy & Environmental Science*, 2021, 14, 483-492.

[27] Y. Liu, S. Li, L. Dai, J. Li, J. Lv, Z. Zhu, A. Yin, P. Li, B. Wang, *Angew. Chem. Int. Ed.,* 2021, 60, 16409-16415.

[28] P. Shao, W. Zhou, Q. Hong, L. Yi, L. Zheng, W. Wang, H. Zhang, H. Zhang, J. Zhang, *Angew. Chem. Int. Ed.*, 2021, 60, 16687-16692.

[29] H. J. Zhu, M. Lu, Y. R. Wang, et al., *Nat. Commun.*, 2020, 11, 497.

[30] B. Han, X. Ding, B. Yu, H. Wu, W. Zhou, W. Liu, C. Wei, B.g Chen, D. Qi, H. Wang, K. Wang, Y. Chen, B. Chen, J. Jiang, *J. Am. Chem. Soc.*, 2021, *18*, 7104-7113.

[31] T. Li, W.-D. Zhang, Y. Liu, Y. Li, C. Cheng, H. Zhu, X. Yan, Z. Li, Z.-G. Gu, *Journal of Materials Chemistry A*, 2019, 7, 19676-19681.

[32] B. P. Biswal, S. Chandra, S. Kandambeth, B. Lukose, T. Heine, R. Banerjee, *J. Am. Chem. Soc.*, 2013*, 135*, 5328-5331.

[33] L. Wang, Y. Ni, X. Hou, L. Chen, F. Li, J. Chen, *Angew. Chem. Int. Ed.*, **2020***, 59, 22126-22131.

[34] Y. Liao, H. Wang, M. Zhu, A. Thomas, *Adv. Mater.*, 2018, 30, e1705710.

[35] Y. Ni, L. Lin, Y. Shang, L. Luo, L. Wang, Y. Lu, Y. Li, Z. Yan, K. Zhang, F. Cheng, J. Chen, *Angew. Chem. Int. Ed.*, 2021, 10.1002/anie.202104494.

[36] J. Gu, C.-S.Hsu, L. Bai, H.M.Chen, X. Hu*, Science*, 2019, 364, 1091.

[37] J. Wang, H. Yang, Q. Liu, Q. Liu, X. Li, X. Lv, T. Cheng, H. B. Wu, *ACS Energy Letters*, 2021*, 6, 437-444.

[38] X. Kong, Yan.Liu, P. Li, J. Ke, Z. Liu, F. Ahmad, W. Yan, Z. Li, Z. Geng, J. Zeng, *Applied Catalysis B: Environmental*, 2020, 268, 118452*.

[39] X. Kong, J. Ke, Z. Wang, Y. Liu, Y. Wang, W. Zhou, Z. Yang, W. Yan, Z. Geng, J. Zeng, *Applied Catalysis B: Environmental*, 2021*, 290, 120067.

[40] Z. Liang, D. Jiang, X. Wang, M. Shakouri, T. Zhang, Z. Li, P. Tang J. Llorca, L. Liu, Y. Yuan, M. Heggen, R. E. Dunin-Borkowski, J. R. Morante, A. Cabot, J. Arbiol, *Adv. Func. Mater.*, 2021, 2106369.

[41] Y. Wu, Z. Jiang, X. Lu, et al., *Nature*, 2019, 575, 639-642.

[42] B. Ravel, M. Newville, *J. Synchrotron Rad.*, 2005, 12, 537-541.

[43] M. Newville, *J. Synchrotron Rad.*, 2001, 8, 322-324.

[44] Rehr, J. J.; de Leon, J. Mustre.; Zabinsky, S. I.; Albers, R. C. *J. Am. Chem. Soc*. 1991, 113, 5135-5140.

[45] Lyle, S. J.; Osborn Popp, T. M.; Waller, P. J.; Pei, X.; Reimer, J. A.; Yaghi, O. M. *J. Am. Chem. Soc*. 2019, 28, 11253-11258.

[46] Kurt A. W. Wallenfels; Wilfried J. Draber. Darstellung von. *Tet. Lett*. 1959, 13, 24-25.

[47] Z. Luo, L. Liu, J. Ning, K. Lei, Y. Lu, F. Li, J. Chen, *Angew. Chem. Int. Ed. Engl*. 2018, 57, 9443-9446.

[48] R. Manivannan, S. Ciattini, L. C. Kuppanagounder, P. Elango, *RSC Adv.*, 2015, 5, 87341.

[49] S. Stang, A. Lebkücher, P. Walter, E. Kaifer, H. Himmel, *Eur. J. Inorg. Chem.*, 2012, 4833-4845.

[50] T. Li, W. Zhang, Y. Liu, Y. Li, C. Cheng, H. Zhu, X. Yan, Z. Li, Z. Gu, *Journal of Materials Chemistry A*, 2019, 7, 19676-19681.

[51] G. Kresse, J. Furthmüller, *Phys. Rev. B*, 1996, 54, 11169.

[52] G. Kresse, J. Furthmüller, *Comput. Mater. Sci.*, 1996, 61, 15-50.

[53] C. Adamo, V. Barone, *J. Chem. Phys.*, 1999, 110, 6158-6170.

Chapter 4

Molecular Engineering to Tune the Ligand Environment of Atomically Dispersed Nickel for Efficient Alcohol Electrochemical-Oxidation
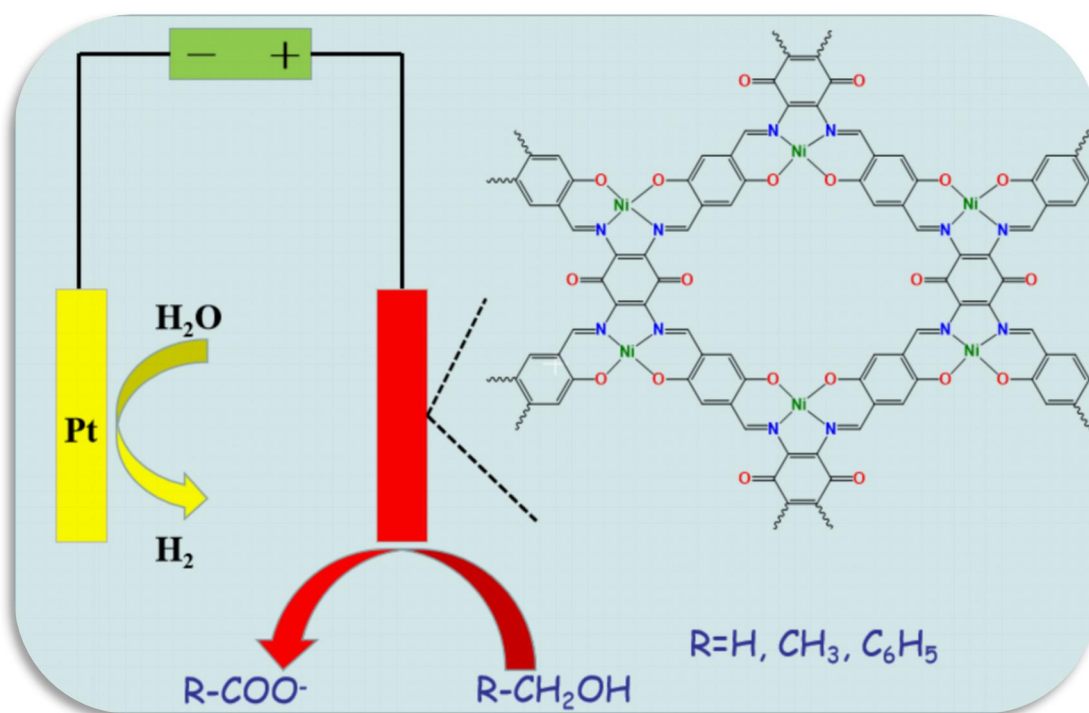
4.1 Introduction

The electrochemical oxidation of alcohols is at the basis of several strategic chemical processes and energy technologies, including electrochemical organic synthesis, biomass and organic waste valorization, and direct alcohol fuel cells (DAFC).[1] The electrooxidation of alcohols offer numerous advantages over competing valorization strategies and energy technologies, such as high energy densities and energy conversion efficiency, operation/reaction at low working temperature with high selectivity, and low fuel cost with easy production, transportation and storage.[1] However, despite their numerous advantages, the deployment of electrocatalytic valorization strategies and DAFCs is hampered by their low cost-effectiveness in large part associated with the use of moderately efficient catalysts based on high-cost and low-abundance elements such as platinum and palladium.[2-3] Besides, current alcohol electrooxidation catalysts become rapidly poisoned with carbon monoxide, which further limits their cost-effectiveness. Thus, the development of efficient and stable alcohol oxidation electrocatalysts based on abundant elements is a topic of major interest.

Several non-precious transition metal catalysts have been proposed for alcohol electro-oxidation.[4-5] Among them, nickel-based catalysts are considered the most promising candidates owing to their high catalytic activity, low price and notable abundance. Numerous Ni-based catalysts, such as $Ni_{0.75}Cu_{0.25}$,[6] NiSn alloy,[7] $Ni_{93}Bi_7$,[8] NiSe,[9] NiO,[10] metal organic frameworks with $Ni(OH)_4$,[11] and Ni-Co hydroxide [12] have been developed and tested for alcohol electrochemical-oxidation. However, the reported onset potentials and stabilities are still not fully satisfactory, which calls for novel strategies to design and engineer nickel-based catalysts with improved performance.

Recently, two-dimensional (2D) covalent organic frameworks and metal organic frameworks (MOF) with highly tunable pore structure and functionality, and high density of active sites, have arisen broad interest as electrocatalysts.[13] Optimized electrocatalysts based on such 2D structures have demonstrated outstanding

performances toward oxygen evolution and reduction,[14] [15] and carbon dioxide reduction.[16-17] However, despite their high potential for alcohol electrooxidation, these 2D materials and particularly a nickel-containing 2D organic framework have yet to be developed and optimized toward this electrocatalytic reaction.

In the present Chapter, we report the synthesis of an atomically-dispersed nickel 2D molecular organic framework containing abundant carbonyl (C=O) functional groups within the nickel ion coordination environment. Its atomic structure and how the outstanding electrocatalytic activities and durabilities obtained for the electrochemical-oxidation of methanol, ethanol and benzyl alcohol were analyzed, which are related to the alcohol adsorption ability of the carbonyl functional groups and the high unsaturated coordination number of the nickel ions within the new catalyst presented here.

4.2 Experimental Section

4.2.1 Materials

Dichloromethane (99%), methanol (99%), N,N-dimethylformamide (DMF, 98%), and hydrazine hydrate (98%) were purchased from Alfa Aesar. Tetrachloro-p-benzoquinone (99%), potassium phthalimide (98%), N-methyl-pyrrolidone (NMP, 99.99%), 2,5-dimethoxyterephthalaldehyde (97%), 1,2,4,5-benzenetetraamine tetrahydrochloride (TAB), hexane (95%), boron tribromide (99.99%), and Nafion (10%) were purchased from Sigma-Aldrich. Benzyl alcohol (99%), nickel acetate tetrahydrate (99%), potassium hydroxide (85%, Acros Organics), acetonitrile (98%) and ethanol (99.5%), were purchased from Honeywell. Commercial Carbon Nanotubes (CNTs) were purchased from Sailing Tech company in Shenzhen (China). All chemicals were used without further purification.

4.2.2 Synthesis of 2,5-dihydroxyterephthalaldehyde (HBC)

2,5-dimethoxyterephthalaldehyde (250 mg, 1.285 mmol) and 25 mL dichloromethane were added to a 50 mL round bottom flask and stirred for 10 min. Then, 3.22 mL BBr3 (1M in hexane) was added to the solution dropwise. After stirring for 3 hours at

room temperature, 5 mL water was added dropwise. Solvents were then removed by argon flow, and the resulting solid was filtrated and washed first with water, and then with acetone to obtain a bright yellow compound, 2,5-hydroxyterephthalaldehyde (HBC) (160 mg, 0.96 mmol, yield 75%). (IR O-H:3260 cm-1, -CHO: 2881, -C=O: 1664 cm-1) 1H-NMR (400 MHz, DMSO-d6, δ): δ 10.33 (m, 4H), 7.25 (s, 2H). [28]
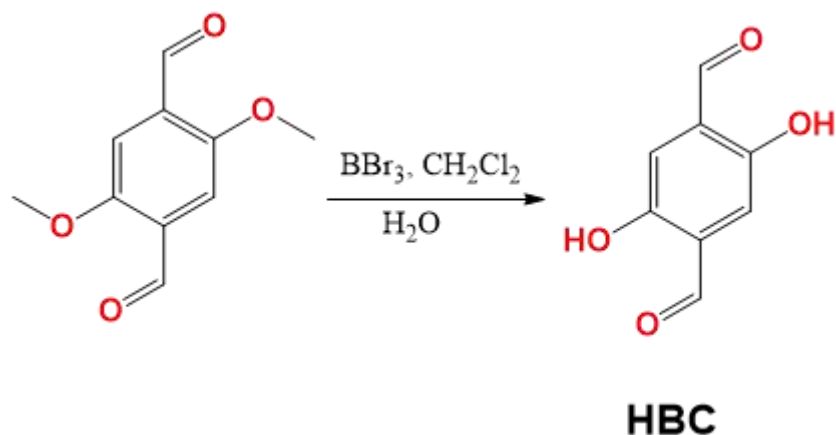
Scheme 4-1. The synthesis of HBC

4.2.3 Synthesis of Tetramino-benzenequinone (TABQ)
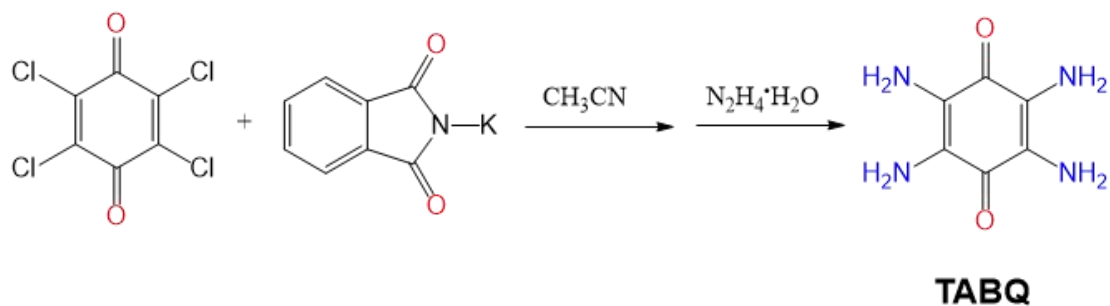
Scheme 4-2. The synthesis of TABQ

5.0 g of tetrachloro-p-benzoquinone and 15.0 g of potassium phthalimide were added to 50.0 mL of acetonitrile under argon and then stirred at 80 ℃ for 12 h. After cooling to room temperature, the products were filtered, and washed with DMF, hot deionized water and ethanol for several times and then vacuum filtered. It was then dried in a vacuum oven at 60 ℃ for 12 h. 10.0 g (yield 71.0%) brown-yellow of tetra(phthalimido)-benzoquinone was obtained.[29] The obtained tetra(phthalimido)-benzoquinone was put into a 100 mL round bottom flask, then 40.0 mL of hydrazine hydrate (98%) was added. After maintained at 65 ℃ for 2 h, purple

tetramino-benzoquinone (TABQ) (1.8 g, yield 26.0%) was obtained. (IR -NH2: 3367 cm^{-1}, -C=O: 1668 cm-1, C-(C=O)-C 1140 cm^{-1}) ^{1}H-NMR (400 MHz, DMSO-d_6, δ): δ 4.55 (s, 8H). [30-31]

4.2.4 Synthesis of Ni-2D-O-SA
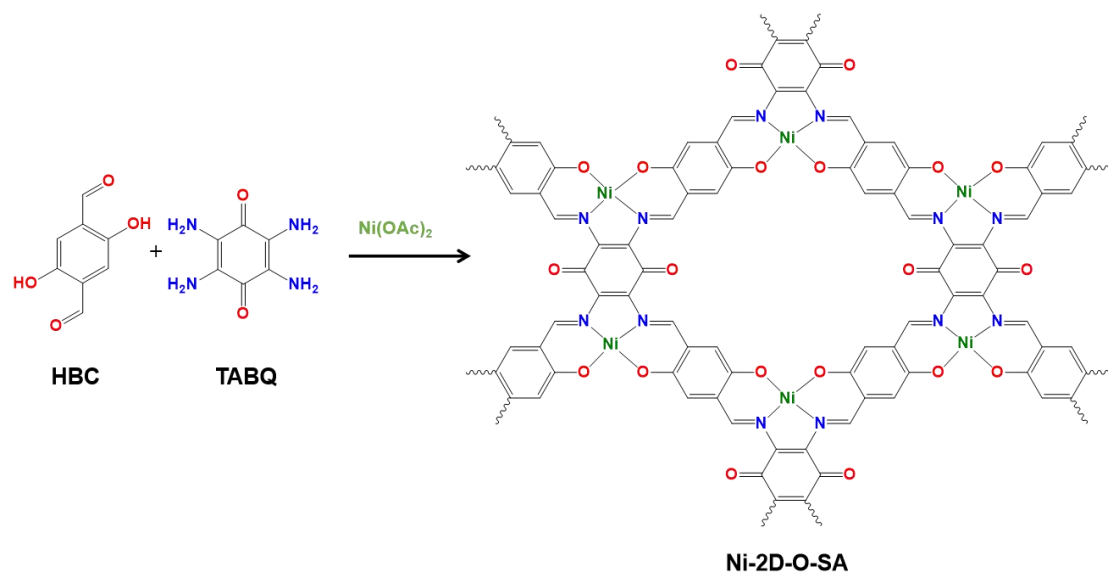
Scheme 4-3. The synthesis of Ni-2D-O-SA

2,5-hydroxyterephthalaldehyde (HBC) (166 mg, 1 mmol) and TABQ (84 mg, 0.5 mmol), excess nickel acetate, and 5 mL dried NMP were added to a 10 mL glass bottle. The resulting solution was sonicated for half an hour to obtain a homogenous dispersion. The glass bottle was transferred into a 25 mL Teflon-lined stainless-steel autoclave. The autoclave was sealed and kept at 120 ºC for 72 h and cooled to room temperature. The resulting black precipitate was collected by filtration and washed with DMF and methanol, Soxhlet extracted by methanol for 24 h, then vacuum dried at 60 ºC for 24 h to give a black powder with ~83% yield ($C_{11}N_2O_3NiH_4$·$2H_2O$, Elemental Analysis, Calculated: C, 43.05 %; H, 2.63 %; N, 9.13 %; Found: C, 42.04 %; H, 3.14 %; N, 8.36 %).

4.2.5 Synthesis of Ni-2D-SA
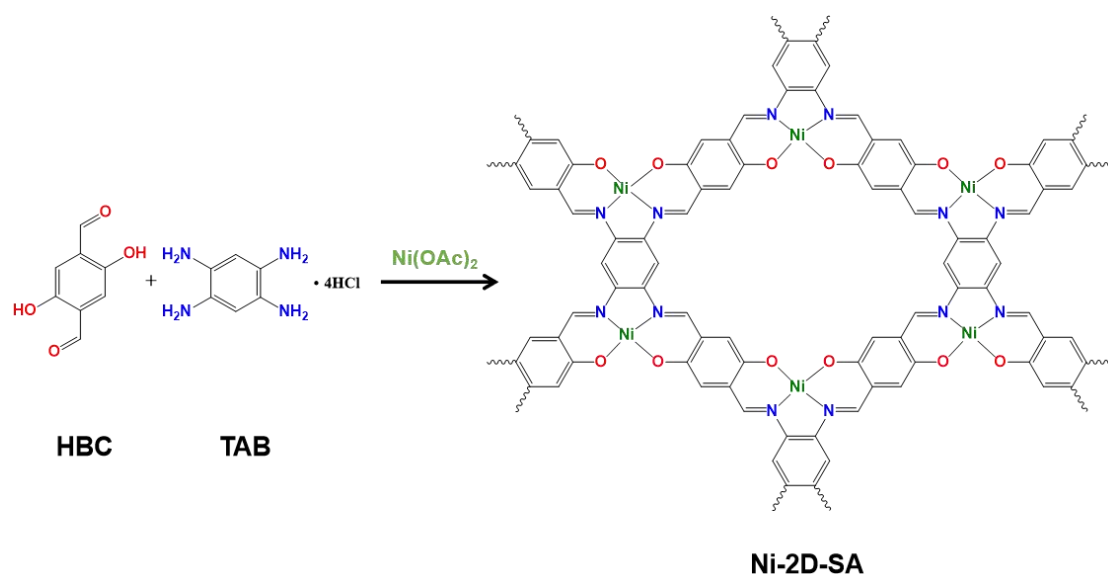
Scheme 4-4. The synthesis of Ni-2D-SA

The synthesis procedure of Ni-2D-SA is similar as Ni-2D-O-SA, just using 1,2,4,5-benzenetetraamine tetrahydrochloride (TAB) to replace TABQ ($C_{11}N_2O_2NiH_5 \cdot H_2O$ elemental analysis Calculated: C, 48.24 %; H, 2.58 %; N, 10.23 %; Found: C %, 47.34 %; H, 3.24 %; N, 9.26 %).[32]

4.2.6 Pre-oxidation of Carbon Nanotubes (CNT)

The Purchased CNT were first calcined at 500 °C in air for 5 h. After cooling to room temperature, the CNT were transferred into a 5 wt% HCl aqueous solution and sonicated for 30 min. The purified CNT were collected by filtration and washed extensively with deionized water and dried for further used.

4.2.7 Synthesis of Ni-2D-O-SA/CNT composites

30 mg Ni-2D-O-SA and 70 mg pre-oxidized carbon nanotube were put into a 15 mL glass vial, then 5 mL NMP was added. The resulting solution was sonicated for half an hour and stirred at 100 °C for 12 h. The resulting black composite was collected by filtration and washed with ethanol, then vacuum dried at 60 °C for 24 h to obtain the final composite.

4.2.8 Synthesis of Ni-2D-SA/CNT composites

Ni-2D-SA/CNT composites were prepared by using the same method as for Ni-2D-O-SA/CNT, just using Ni-2D-SA to replace Ni-2D-O-SA.

4.2.9 Electrochemical Measurements

All the electrochemical measurements were carried out on the Chi760 electrochemical workstation (Shanghai Chenhua, China) at room temperature by using a standard three-electrode setup system without iR compensation. A platinum grid, glassy carbon electrode with 5 mm diameter and Hg/HgO electrode were used as counter electrode, working electrode and reference electrode, respectively. 4 mg of Ni-2D-O-SA-CNT (or Ni-2D-SA-CNT) catalysts and 30 μL of 10% Nafion solution were added to 75 μL isopropanol and 425 μL MiliQ water, then the obtained solution was sonicated for half an hour to obtain a homogeneous solution. 10 μL mixture solution was dropped on the working electrode for drying before the electrochemical tests. All the tests were performed in argon-bubbled 1 M KOH solution with or without alcohol and with magnetic stirring. Linear sweep voltammetry (LSV) curve measurements were conducted in 1.0 M KOH at room temperature with and without 1 M methanol, 1 M ethanol and 0.1 M benzyl alcohol solution, respectively. For oxygen evolution reaction (OER), methanol oxidation reaction (MOR), Ethanol Oxidation Reaction (EOR) and benzyl alcohol oxidation reaction (BOR), the scan rate of LSV curves was 5 mV s^{-1}. The solution resistance estimated from electrochemical impedance spectroscopy (EIS) measurements was recorded under alternating current voltage with frequencies from 0.01 to 10^5 Hz. ^{1}H NMR spectra was recorded on an AVANCE III console (Bruker). In which 1 mL elelctrolyte was added with 200 μL D$_2$O.

4.2.10 Calculation Details

All calculations presented were carried out for the selected fragments using the density functional theory (DFT) with the generalized Perdew-Burke-Ernzerhof (PBE), and the projector augmented-wave (PAW) pseudopotential planewave method as implemented in the VASP code. [33-34] DFT-D3 correction method was employed to

describe van der Waals interaction. The cutoff energy of plane-wave basis was 500 eV. The convergence of energy was set as 10^{-5} eV. A $1 \times 1 \times 1$ k-point mesh was used for the Brillouin Zone sampling. A vacuum region of 15 Å was set between adjacent layers to avoid artificial interactions. The selected fragments for Ni-2D-SA and Ni-2D-O-SA consisting of 66 atoms are shown in **Figure S14**. During the structure optimization, all atoms of the selected fragments are fully relaxed until the force on each of the atoms is less than 0.02 eV Å^{-1}. In order to investigate the adsorption behavior of methanol molecule on the surface of the selected fragment, a single methanol molecule was placed near the potential adsorption sites of the fragments, and adsorption energy (E_{ads}) is defined as $E_{ads} = E_{(methanol+slab)} - E_{slab} - E_{methanol,}$ where E_{slab} is the energy for the selected fragment, and $E_{(methanol+slab)}$ is the total energy for methanol adsorbed selected fragment.

4.2.11 Materials Characterization

The crystal structure was characterized by means of powder X-ray diffraction (XRD) measured in a Bruker AXS D8 Advance X-ray diffractometer. (Cu-Kα radiation, λ = 1.5106 Å, 40 kV and 40 mA; Bruker, Germany). Thermogravimetric analysis (TGA) were performed under argon gas at a heating rate of 5 °C/min using a Thermogravimetric Analyzer Q200. Scanning electron microscopy (SEM) images were obtained in a Zeiss Auriga field emission scanning electron microscopy (FE-SEM) operating at 20 kV. High angle annular dark-field (HAADF)-scanning transmission electron microscopy (STEM) images and elemental mapping were measured in a spherical aberration corrected transmission electron microscope FEI Titan G2 80-200 ChemiSTEM with four energy-dispersive X-ray spectroscopy (EDX) detectors and operated at 80 and 200 keV. X-ray photoelectron spectroscopy (XPS) data was obtained in a Phoibos 150 MCD-9 detector. Ni K-edge X-ray absorption fine structure (XAFS) spectra were measured at the Canadian Light Source, beamline SXRMB. The samples were pressed onto a double-sided carbon tape and the data was recorded in X-ray fluorescence mode. The XAFS data was processed with the Athena program.[35] Extended X-ray absorption fine structure (EXAFS) was analyzed using

the IFEFFIT package[36] and the EXAFS fitting was performed with FEFF6L.[37] For EXAFS fitting, spectra were fitted in R-space, from 1.0 Å to 2.76 Å. The R-space EXAFS signal was obtained by a variable k^n-weighted Fourier transform (n = 1, 2, 3) of the EXAFS signal $\chi(k)$ over a k-range of 3.00 Å^{-1} to 11.7 Å^{-1}. Nitrogen adsorption-desorption isotherms were recorded in a Tristar II 3020 Micromeritics system at 77 K. The specific surface area was calculated by Brunauer–Emmett–Teller (BET) methods.

4.3 Results and Discussions

4.3.1 Preparation and Characterization

The nickel-based 2D organic framework with abundant carbonyl functional groups (Ni-2D-O-SA) was solvothermally synthesized through a Schiff-based reaction between 2,5-hydroxyterephthalaldehyde (HBC) (**Scheme 4-1**) and tetramino-benzoquinone (TABQ) (**Scheme 4-2**) in N-methyl-2-pyrrolidone (NMP) (**Scheme 4-3** and **Figure 4.1**). The dark-black color of the obtained solid indicated the formation of a conjugated polymer, which was washed by water and methanol to remove low molecular mass impurities, and then dried under vacuum. For comparison, a reference nickel-based 2D organic framework without carbonyl chemical groups (Ni-2D-SA) was prepared under the same reaction condition but using 1,2,4,5-benzenetetraamine tetrahydrochloride (TAB) instead of TABQ (**Scheme 4-4**).[18]
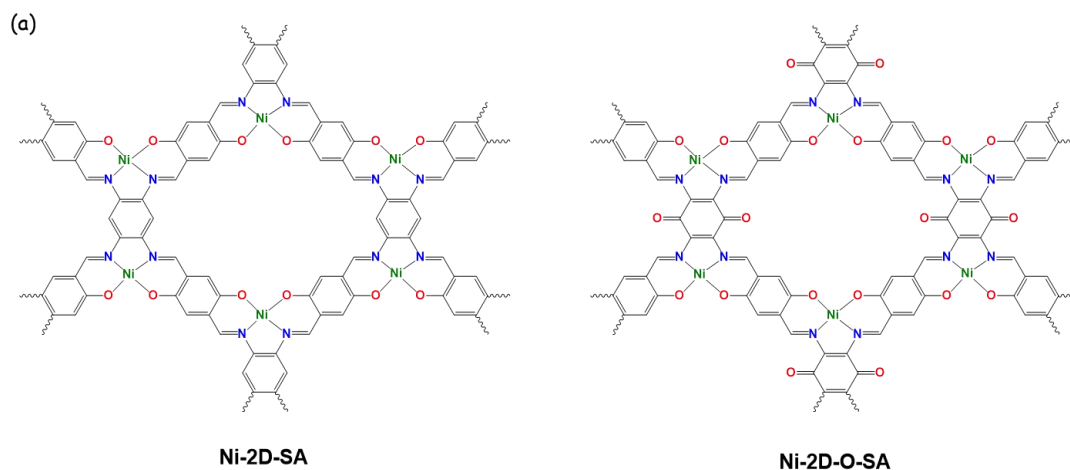
Figure 4.1 (a) Scheme of the synthesis procedure used to produce Ni-2D-O-SA.
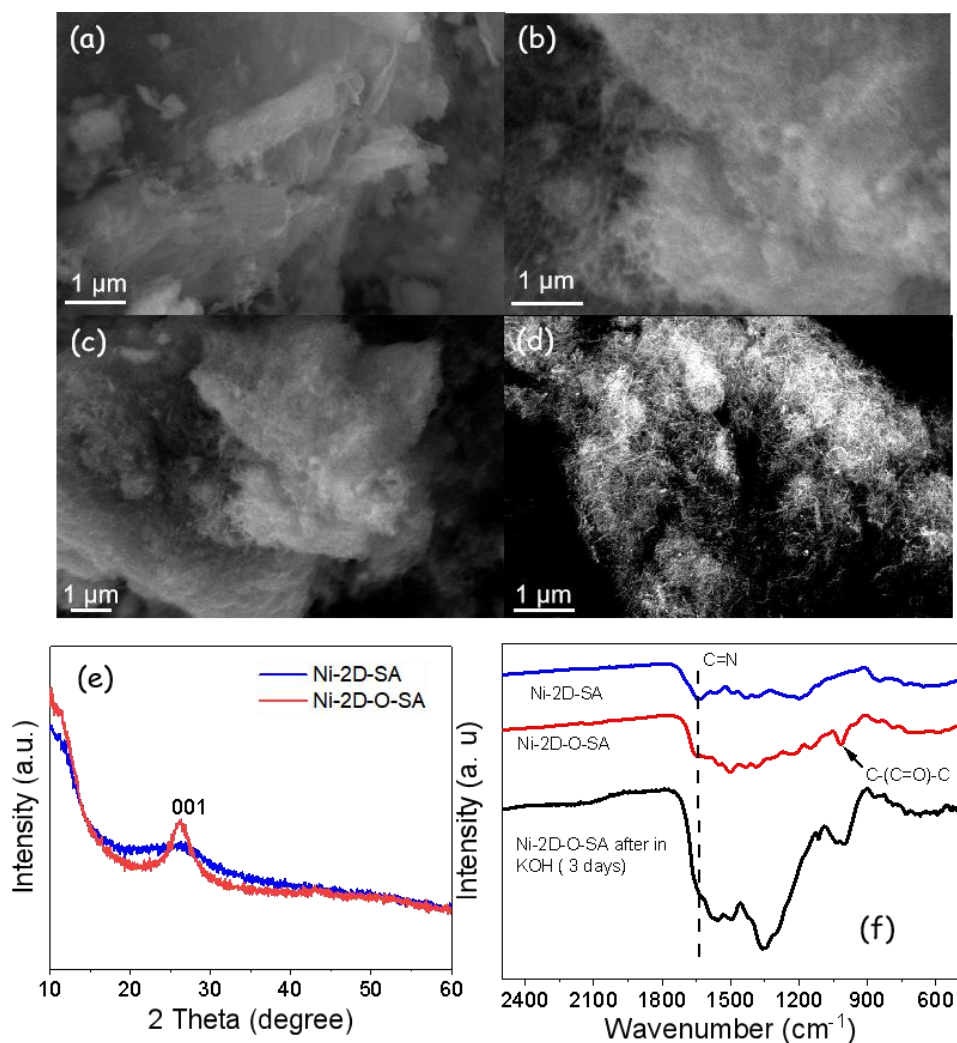
Figure 4.2 SEM images of Ni-2D-O-SA (a,b); Ni-2D-O-SA-CNT (c); Ni-2D-SA-CNT (d). (e) TGA of Ni-2D-O-SA under argon by heating to 600 ℃ at the rate of 5 ℃/min. (f) XRD patterns of Ni-2D-SA (blue) and Ni-2D-O-SA (red)

Scanning electron microscopy (SEM) images (**Figures 4.2a-b**) show that the Ni-2D-O-SA sample has a cotton-like morphology. The X-ray diffraction (XRD) pattern (**Figure 4.2e**) of the Ni-2D-O-SA powder was similar to that of graphite, with a diffraction peak at 26.29° corresponding to the (001) family planes and which indicated π-π layered stacking.[19] In contrast to the clear crystalline and layered structure displayed by Ni-2D-O-SA, the XRD pattern of Ni-2D-SA displayed a much broader and less intense peak at around 26º. This result indicates that the introduction of carbonyl groups enhances the crystallinity of the nickel-based 2D organic framework used here.

Fourier transform infrared (FT-IR) spectroscopy was used to evaluate the chemical structure of the samples (**Figure 4.2f**). Based on the FT-IR spectra, the signal for C=N appeared at 1642 cm^{-1} for Ni-2D-SA, and 1648 cm^{-1} for Ni-2D-O-SA. The vibration of the carbonyl bond (C=O) in Ni-2D-O-SA negatively shifted below 1600 cm^{-1} and overlapped with other vibrations. For Ni-2D-O-SA, the vibration peak for the C-(C=O)-C bond, which is a footprint of TABQ, shifted from 1140 cm^{-1} to 1010 cm^{-1} due to the coordination effect and the attraction between the layers. This result already points out to the successful introduction of the carbonyl groups in the organic framework.[20]
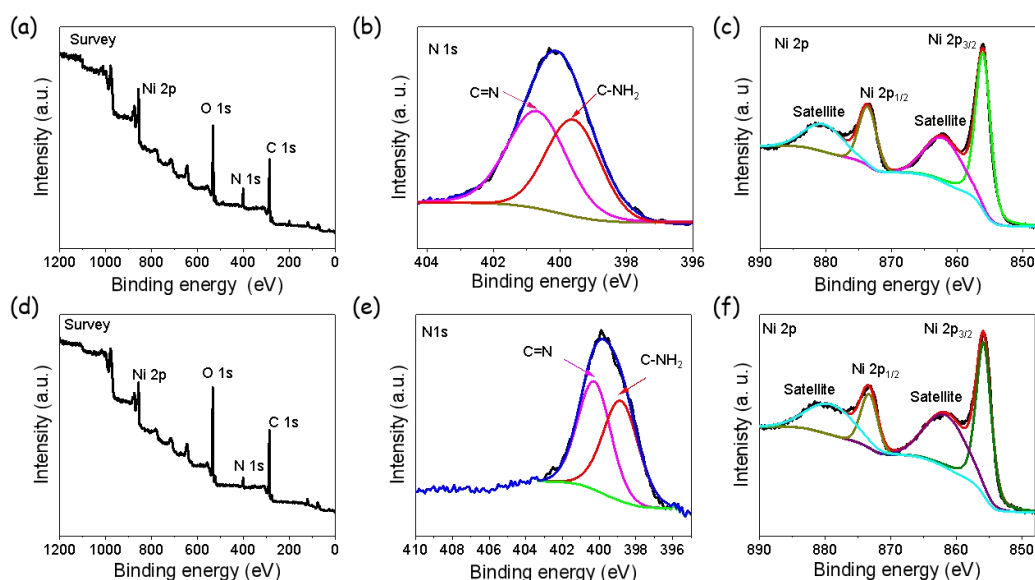
Figure 4-3 (a) Survey, (b-c) high-resolution N 1s, and Ni 2p XPS spectra of Ni-2D-O-SA. (d-f) Survey, high-resolution N 1s, and Ni 2p XPS spectra of Ni-2D-SA.

The survey X-ray photoelectron spectroscopy (XPS) spectra revealed the sole presence of C, N, Ni, O in both samples (**Figure 4.3**).[21] For both samples, the high-resolution Ni 2p spectrum showed a unique doublet at binding energies of 856 eV (Ni 2p$_{3/2}$) and 873.3 eV (Ni 2p$_{1/2}$), significantly above those of NiO.[22-23]
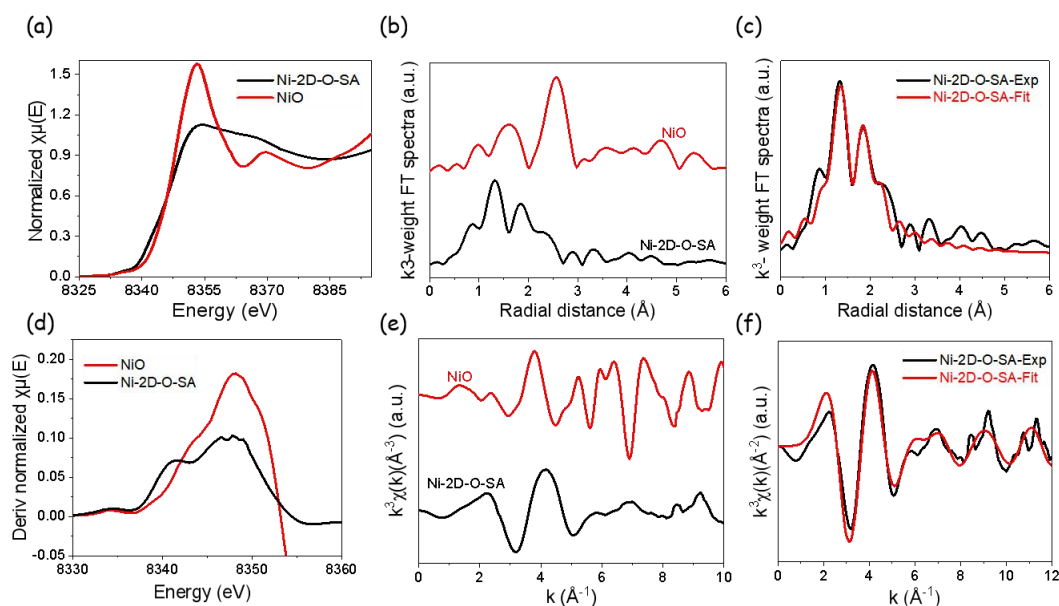
Figure 4.4. (a) Ni K-edge XANES spectrum of Ni-2D-O-SA compared with a commercial NiO powder. (b) Fourier transformed Ni K-edge EXAFS spectra of Ni-2D-O-SA and NiO plotted in R-space. (c) Fitting of the Fourier transformed EXAFS spectrum in R-space of Ni-2D-O-SA. (d) first derivative of XANES spectras. (e-f) Ni K-edge EXAFS oscillations in k-space (k3 × (k)) of Ni-2D-O-SA and its fitted spectrum.

The local environment in Ni-2D-O-SA was further analyzed and compared with that of NiO using X-ray absorption fine structure (XAFS) at the Ni K-edge (**Figure 4.4**). Comparing the spectral features at the near-edge, i.e. the X-ray absorption near-edge structure (XANES), we observe the absorption onset of Ni-2D-O-SA at slightly lower energy than that of NiO (**Figure 4.4b**). Differences are more clearly seen when plotting the first derivative of the two spectras (**Figure 4.4d**). Besides, the main absorption peak of Ni-2D-O-SA has a lower intensity than that of NiO. Both features indicate that compared with NiO, where Ni is fully surrounded by O, within Ni-2D-O-SA Ni atoms are partially surrounded by a lower electronegativity element, i.e. N. A more quantitative picture was obtained by analyzing the extended XAFS (EXAFS) features. The fitting of the Fourier transformed EXAFS spectrum suggests that Ni is coordinated with two N and two O atoms, at a bond length of 1.87 Å and 2.05 Å, respectively (**Figure 4.4b,c**). The contribution at longer radial distances comes from C atoms with a coordination number of 6 and a bond length of 2.65 Å.

The detailed fitting parameters can be found in **Table 4-1**. Overall, XAFS analysis provided strong evidence of the formation of the NiN_2O_2 salophen structure unit in the Ni-2D-O-SA framework.

Table 4-1 Ni K-edge EXAFS fitting parameters for Ni-2D-O-SA. R：bond length, CN: coordination number.

sample	Bond	R(Å)	CN	σ^2 (10^{-3} Å^2)	ΔE (eV)	R factor
	Ni-O	1.87	2	4.7	-3.60	0.03
Ni-2D-O-SA	Ni-N	2.05	2	1.4		
	Ni...C	2.65	6	5.8		
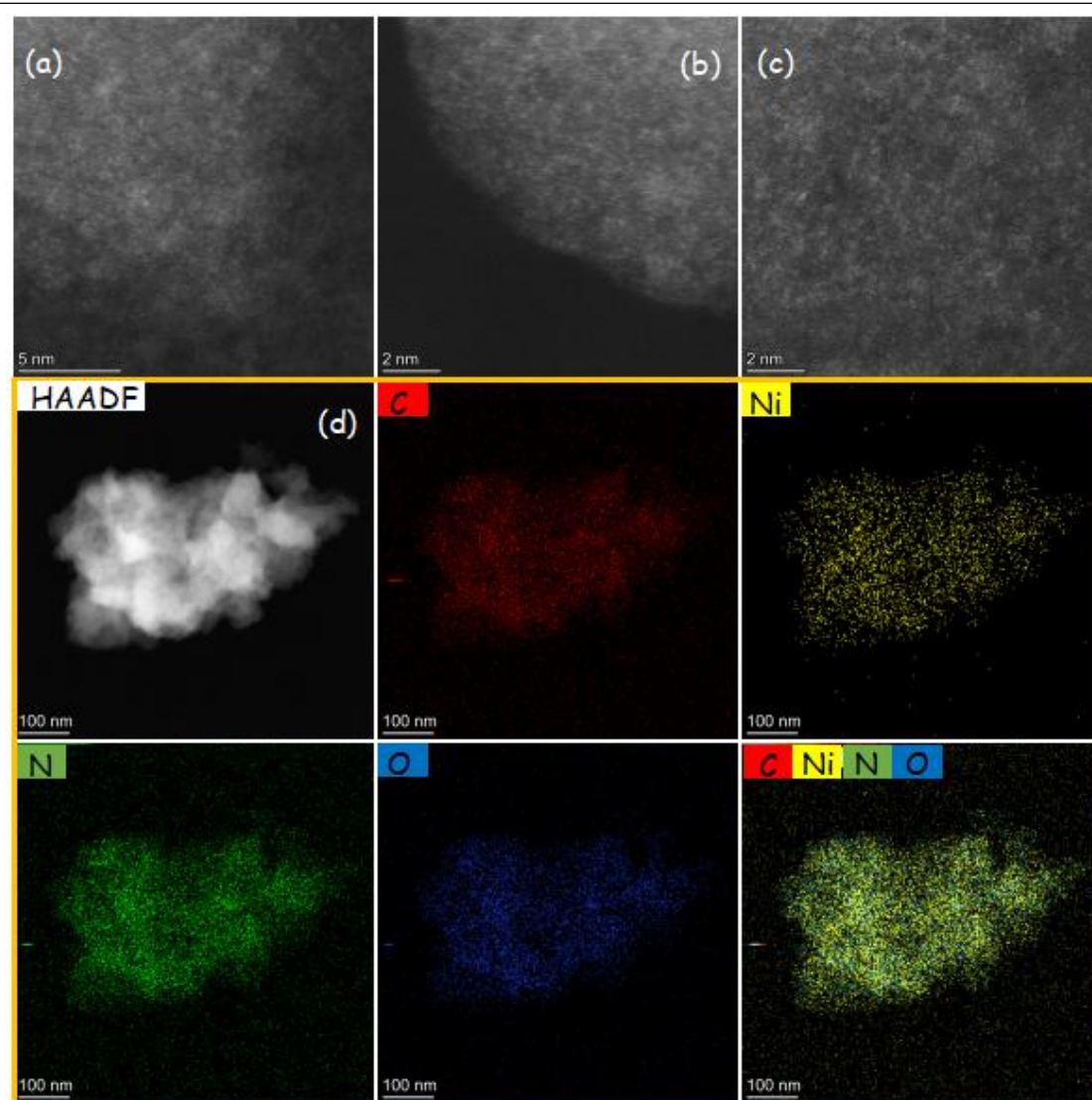
Figure 4.5 (a)-(c) HAADF-STEM images of Ni-2D-O-SA displaying the presence of

atomically dispersed nickel atoms as bright spots. (d) Low magnification HAADF-STEM image and EDS elemental mapping.

High angle annular dark-field (HAADF) aberration-corrected scanning transmission electron microscopy (STEM) was used to analyse the nickel dispersion. As shown in **Figure 4.5a-c**, Ni-2D-O-SA contained a high density of isolated and homogeneously distributed nickel atoms. The uniform distribution of Ni, C, N, and O was further confirmed by energy-dispersed X-ray spectroscopy (EDS) elemental mapping (**Figure 4.5d**).
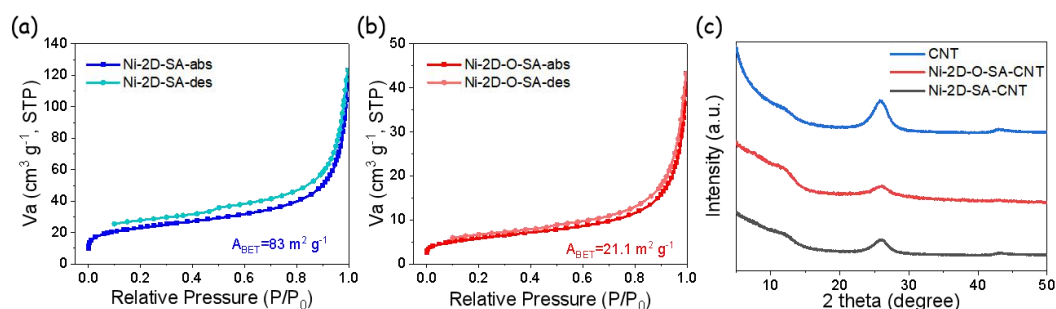
Figure 4.6 N_2 adsorption-desorption isotherm of (a) Ni-2D-SA and (b) Ni-2D-O-SA. (c) XRD patterns of Ni-2D-SA-CNT, Ni-2D-O-SA-CNT and CNT.

The surface area of Ni-2D-O-SA and Ni-2D-SA, evaluated from N_2 adsorption-desorption isotherms at 77 K (**Figure 4.6a,b**) using the Brunauer-Emmett-Teller equation was 21.1 and 83 m^2 g^{-1}, respectively. Thus the introduction of carbonyl functional groups significantly decreased the surface area of the material, which we associate with an enhancement of the layer-layer interaction that results in slightly more densely packed frameworks.

To improve the electrical conductivity of these nickel-based organic frameworks, as required to apply them as electrocatalysts, they were loaded on multi-wall carbon nanotubes (CNTs) through the π-π packing interaction. The XRD patterns of the obtained Ni-2D-O-SA-CNT and Ni-2D-SA-CNT composites, showed a unique peak at about 26° (**Figure 4.6c**), which was assigned to the overlap between the CNT and the organic framework structures. SEM (**Figures 4.2c,d**), STEM images and EDX compositional maps (**Figure 4.7**) showed the composites morphology and confirmed the homogeneous loading of Ni-2D-O-SA on the CNTs.
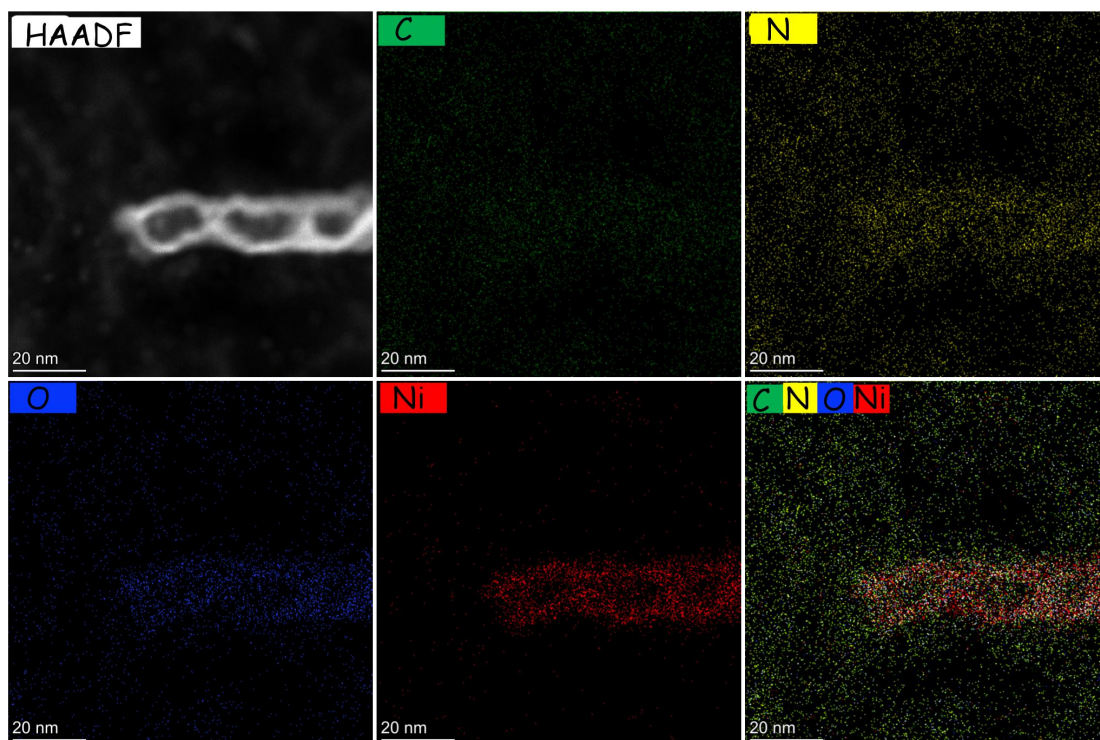
Figure 4.7 Low magnification HAADF-STEM image and EDS elemental maps of the Ni-2D-O-SA-CNT sample.

4.3.2 Electrochemical Performance and DFT Calculation

Figure 4.8a exhibits the cyclic voltammograms (CV) of the two samples in the range from 0 V to 0.65 V in 1.0 M KOH electrolyte with a scan rate of 50 mV s^{-1}. The anodic peak at 0.50 V vs Hg/HgO measured in the forward scan with Ni-2D-O-SA-CNT is attributed to Ni^{2+} oxidation, and the cathodic peak in the backward scan at 0.38 V corresponds to the reduction of Ni^{3+} species. For Ni-2D-SA-CNT, the anodic peak shifted to 0.54 V and the cathodic peak to 0.42 V. The current density at the Ni^{2+} oxidation peak in the Ni-2D-O-SA-CNT electrocatalyst was 19 mA cm^{-2}, which is about 9.5 times higher than that of Ni-2D-SA-CNT, 2 mA cm^{-2}. These results indicate a much higher electrochemical activity of the Ni ions within Ni-2D-O-SA-CNT and their easier oxidation to Ni^{3+}. Besides, the ratio between the anodic and the cathodic peak current densities was close to 1 for both catalysts, indicating a reversible Ni^{2+}/Ni^{3+} redox reaction in both materials.[25]
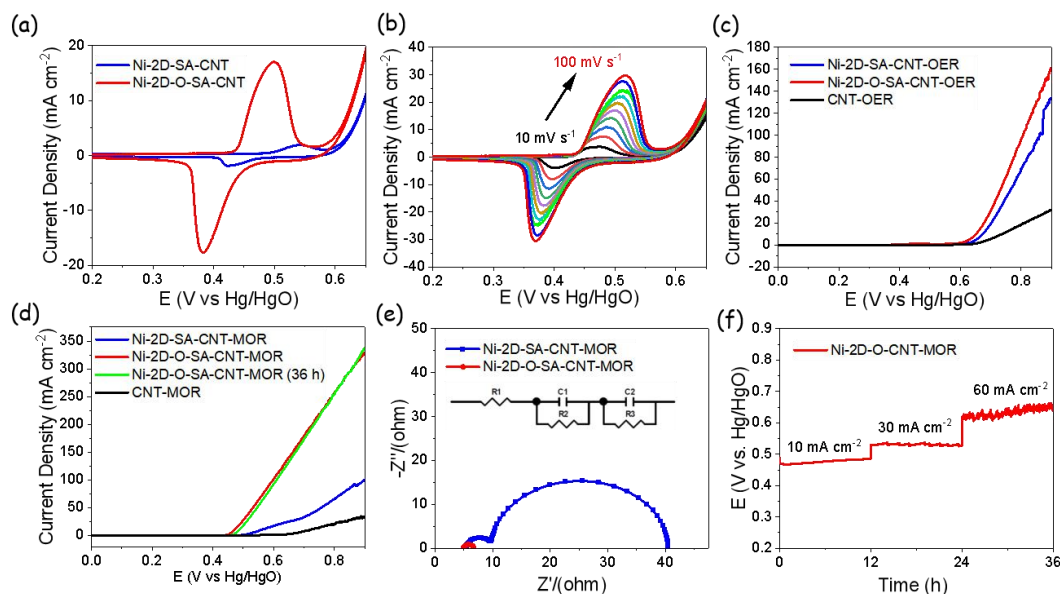
Figure 4.8 (a) CV of Ni-2D-O-SA-CNT and Ni-2D-SA-CNT electrocatalysts in 1 M KOH at 50 mV s^{-1} potential sweep rate. (b) CVs of Ni-2D-O-SA-CNT electrocatalysts in 1 M KOH obtained at an increasing potential sweep rate, from 10 to 100 mV s^{-1}. (c,d) LSV curves obtained with Ni-2D-SA-CNT, Ni-2D-O-SA-CNT and reference carbon nanotubes (CNTs) catalysts in 1.0 M KOH (c) and 1 M KOH + 1 M methanol (d) in the potential range 0 to 0.9 V vs. Hg/HgO and at a scan rate of 5 mV s^{-1}. (e) EIS Nyquist plots at 0.56 V in 1 M KOH + 1 M methanol solution. (f) CP long-term stability of Ni-2D-O-SA-CNT at 10 mA cm^{-2}, 30 mA cm^{-2} and 60 mA cm^{-2}. No iR compensation was applied to the displayed data.

CV of the reduction/oxidation process allowed to estimate the surface coverage (Γ) of Ni^{2+}/Ni^{3+} within Ni-2D-O-SA-CNT to be 1.32×10^{-7} mol cm^{-2}, two orders of magnitude above that of Ni-2D-SA-CNT, 5.17×10^{-9} mol cm^{-2} (Figure 3a, Supporting information Equation S1).[26] **Figures 4.8b** and **4.9** display CV curves at different scan rates, from 10 to 100 mV s^{-1}, obtained with these two catalysts in 1.0 M KOH electrolyte. The variation of the anodic and cathodic peak current densities with the square root of the voltage scan rate was linearly fitted with R^2>0.99 for both samples (**Figure 4.9**), demonstrating the Ni^{2+}/Ni^{3+} redox reaction to be diffusion limited.[25] From this dependence an apparent diffusion coefficient D' was evaluated (see **equation 3**). The D' obtained with Ni-2D-O-SA-CNT is 2.3×10^{-6} g cm^{-1} s^{-1}, which

139

is close to an order of magnitude higher than with Ni-2D-SA-CNT, 3.3×10^{-7} g cm^{-1} s^{-1}.
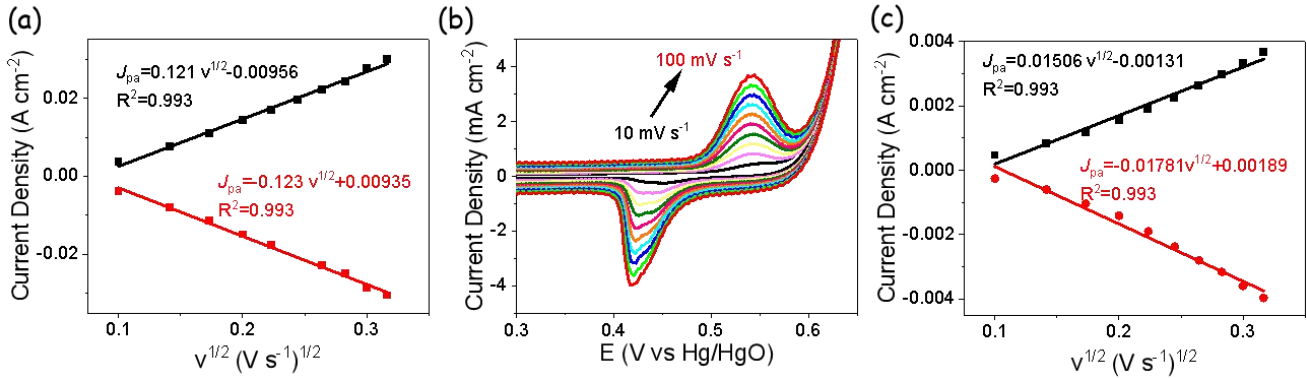
Figure 4.9. (a) Linear fitting of the anodic and cathodic peak current densities to the square root of the sweep rate for Ni-2D-O-SA-CNT. (b) Cyclic voltammograms of Ni-2D-SA-CNT electrocatalysts in 1 M KOH with increasing potential sweep rate from 10 to 100 mV s^{-1}. (c) Linear fitting of the anodic and cathodic peak current densities to the square root of the sweep rates for Ni-2D-SA-CNT.

The surface coverage of Ni^{2+}/Ni^{3+} in these two catalysts was investigated by the following equation.[38-39]

$$\Gamma = \frac{Q}{nFA}$$
(equation 1)

Where Q is the charge from the reduction/oxidation peak, calculated from the average of forward and reverse scan, n is the number of electrons, F is the Faraday constant and A is working geometrical electrode surface area.

Figures 4.9a,c display the good linear relationship of the anodic and the cathodic peak current density of the Ni-2D-O-SA-CNT and Ni-2D-SA-CNT electrode vs the square root of the scan rate. The diffusion coefficient (D) is an important parameter to evaluate the oxidation behavior of electrocatalyst. Normally D was calculated by the following equation:[40]

$$I_p = 2.69 \times 10^5 n^{3/2} A D^{1/2} C v^{1/2}$$
(equation 2)

Where I_p is the peak current, n is the number of transferred electrons, A is the apparent area of electrode, D is the diffusion coefficient, C is the initial concentration of redox species. v is the scan rate.

And here we define an apparent diffusion coefficient (D'):

$$D' = D^{1/2}C \qquad \text{(equation 3)}$$

So the apparent coefficient D' was calculated by the following equation:

$$I_p = 2.69 \times 10^5 n^{3/2} A D' v^{1/2} \qquad \text{(equation 4)}$$

The alcohol electrooxidation performance of Ni-2D-O-SA-CNT and Ni-2D-SA-CNT electrocatalysts was analyzed by linear sweep voltammetry (LSV) in 1 M KOH and 1 M KOH + 1 M methanol solutions using a conventional three-electrode setup (**Figures 4.8c**, **d)**. The OER activity of Ni-2D-O-SA-CNT was just slightly improved compared to that of Ni-2D-SA-CNT. However, the Ni-2D-O-SA-CNT catalysts showed much higher activity toward methanol oxidation reaction (MOR), with current densities increasing from 31 mA cm^{-2} to 106 mA cm^{-2} in the range 0.5-0.6 V versus Hg/HgO, i.e. six-fold higher current densities compared with Ni-2D-SA-CNT. Thus, the introduction of the carbonyl group (C=O) at the ligand environment of the dispersed Ni-atoms active sites clearly results in much higher MOR catalytic activities.

The charge transfer resistances of these two catalysts were evaluated through electrochemical impedance spectroscopy (EIS). The EIS Nyquist plot of Ni-2D-O-SA-CNT (**Figure 4.8e**) presents a smaller semicircle than Ni-2D-SA-CNT at 0.56 V in 1 M KOH + 1 M methanol electrolyte, denoting a lower charge transfer resistance (R_3) and thus a faster MOR kinetics.[27] On the other hand, the charge transfer resistance for OER of Ni-2D-O-SA-CNT is similar to that of Ni-2D-SA-CNT at 0.67 V (**Figure 4.10a**), which is consistent with the similar OER activities of these two catalysts.

As shown in the chronopotentiometry (CP) curve (**Figure 4.8f**), the Ni-2D-O-SA-CNT electrocatalyst maintained constant current densities of 10 mA cm^{-2} and 30 mA cm^{-2} for 12 h without a significant increase in the required potential. When increasing the current density to 60 mA cm^{-2}, the potential raised about 4.8% during 12 h, which is attributed to the methanol consumption. After 36 h chronopotentiometry test, LSV curves recorded with the used electrocatalysts in a

fresh 1 M KOH + 1 M methanol electrolyte (**Figure 4.8d**) showed almost no variation with respect to those obtained with the fresh electrocatalysts, what demonstrates the excellent stability of Ni-2D-O-SA-CNT during MOR. After the stability test, the pH value of the solution was 14.12, which was not significantly changing compared to the initial solution (*pH*=14).
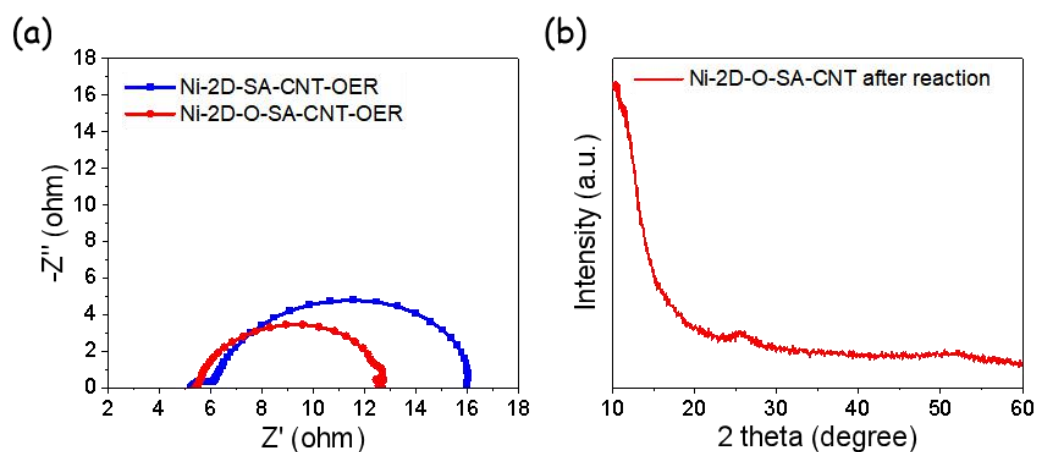
Figure 4.10. (a) EIS spectra of the two catalysts at 0.67 V vs Hg/HgO in 1 M KOH solution. (b) XRD pattern of Ni-2D-O-SA-CNT after MOR electrochemical experiments.

The XRD pattern of Ni-2D-O-SA-CNT after MOR (**Figure 4.10b**) displayed no significant variation with respect to the sample before the electrochemical tests, which confirmed the excellent structural stability of the 2D material and the growth of no additional crystalline phase of the nickel or nickel oxide nanoparticles during the reaction, indicating there is no agglomeration of nickel atom active sites.
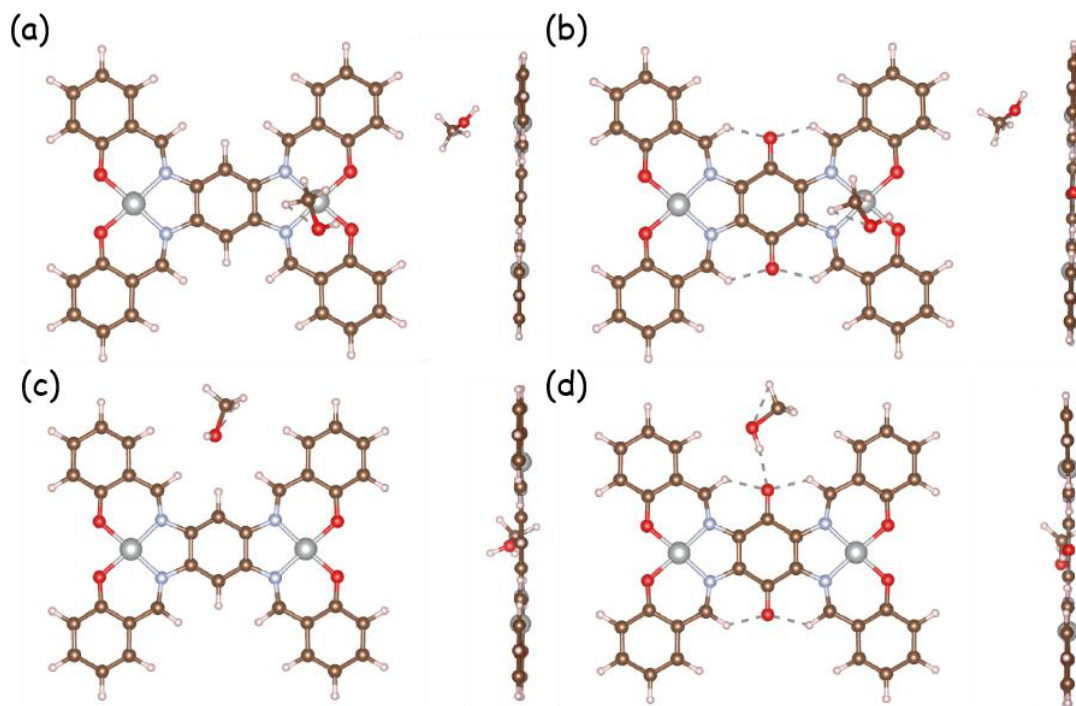
Figure 4.11. (a,b) Optimal methanol adsorption configurations on top of the Ni site in both Ni-2D-SA (a) and Ni-2D-O-SA (b). (c,d) Optimal methanol adsorption configurations on top of the carbonyl site in both Ni-2D-SA (c) and Ni-2D-O-SA (d). (red spheres correspond to oxygen atoms, light blue to nitrogen, grey to nickel, and brown to carbon)

Methanol adsorption is the initial and a limiting step in MOR. To understand the contribution of C=O groups to methanol adsorption, density functional theory (DFT) calculations were carried out. Selected fragments were shown in **Figure 4.11**, which shows the optimal methanol adsorption configurations on top of a Ni site in both Ni-2D-SA and Ni-2D-O-SA. The adsorption energy is -0.248 eV and -0.225 eV in Ni-2D-SA and Ni-2D-O-SA, respectively. The negative adsorption energies suggest that methanol adsorption is thermodynamically favored in both cases. Interestingly, the adsorption distance (d) between the O atom of methanol and Ni in Ni-2D-O-SA is 3.11 Å, which is shorter than in Ni-2D-SA (3.27 Å). Compared with Ni-2D-SA, the 10% lower adsorption energy and 5% shorter adsorption distance indicate a more effective adsorption of the methanol molecule on the surface of Ni-2D-O-SA. What is more, upon adsorption, the $H-O-CH_3$ angle in Ni-2D-O-SA increases from 108.25° to 109.04°, while the $H-O-CH_3$ angle in Ni-2D-SA remains almost unchanged after

optimization. This result indicates that Ni-2D-O-SA can facilitate the activation of the methanol molecule. We also identify the O of the C=O group as a methanol adsorption site. DFT calculations show that the methanol molecule tends to adsorb at such O site with the OH group in methanol parallel to the surface. The shortest distance between the methanol molecule and the surface is 1.87 Å, which is much smaller than in the Ni-2D-SA surface (2.5 Å). Thus, based on the DFT calculations, it is reasonable to conclude that the addition of carbonyl (C=O) groups to the organic framework results in more effective adsorption as well as activation of the methanol molecule, which explains the higher activity of Ni-2D-O-SA toward MOR when compared with Ni-2D-SA.

Beyond MOR, we also examined the electrocatalytic activity of the produced catalysts toward the oxidation of other alcohols. Compared with Ni-2D-SA-CNT, Ni-2D-O-SA-CNT presented significantly higher electrocatalytic performance toward the electrochemical oxidation of both ethanol (EOR) (**Figure 4.12a**) and benzyl alcohol (BOR) (**Figure 4.12b**). Especially for the BOR, the current density at 0.6 V obtained with Ni-2D-O-SA-CNT was about 77 mA cm^{-2}, which is about 8 times higher than that of Ni-2D-SA-CNT (9.7 mA cm^{-2}).
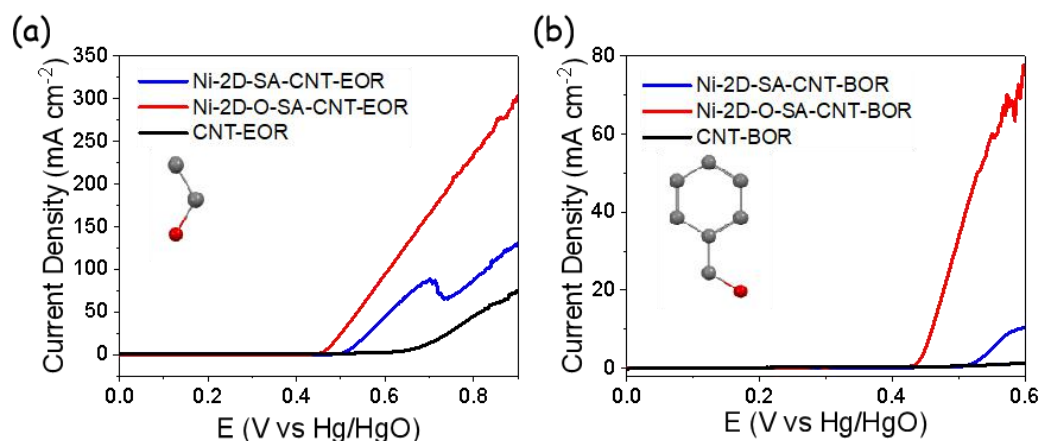
Figure 4.12. (a) LSV of Ni-2D-SA-CNT, Ni-2D-O-SA-CNT and CNT in 1 M KOH+1 M methanol from 0 to 0.9 V vs. Hg/HgO at a scan rate of 5 mV s^{-1}. (b) LSV of Ni-2D-SA-CNT, Ni-2D-O-SA-CNT and the CNT in 1 M KOH+0.1 M benzyl alcohol from 0 to 0.9 V vs. Hg/HgO at a scan rate of 5 mV s^{-1}.

Table 4-2. Summary of the DFT calculation results for methanol adsorption: adsorption energy and distance with Ni and C=O chemical group.

Sample	Adsorption energy (eV) with Ni	Adsorption distance (Å) with Ni	Adsorption distance (Å) with C=O
Ni-2D-SA	-0.225	3.11	2.5
Ni-2D-O-SA	-0.248	3.27	1.87
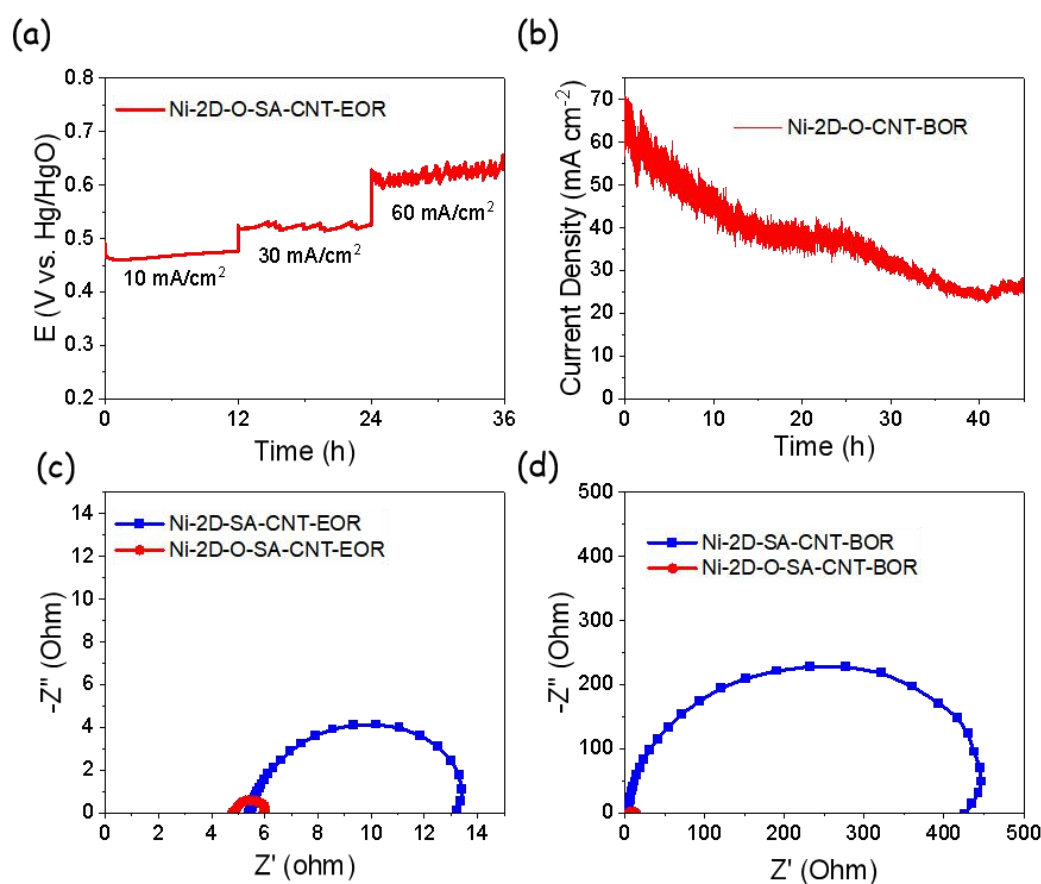
Figure 4.13 (a) CP data showing the long term EOR stability of Ni-2D-O-SA-CNT at 10 mA/cm^2, 30 mA/cm^2 and 60 mA/cm^2. (b) *i-t* curve of Ni-2D-O-SA-CNT at 0.55 V vs Hg/HgO. (c) EIS spectrum at 0.60 V in 1 M KOH+1M ethanol solution. (d) EIS at 0.50 V in 1 M KOH+0.1 M benzyl alcohol solution.

CP measurements were used to test the stability of Ni-2D-O-SA-CNT for EOR. As shown in **Figure 4.13a**, Ni-2D-SA-CNT exhibited excellent long-term stability for EOR, similar to that obtained for MOR. For BOR, chronoamperometric measurements (**Figure 4.13b**) show that the current density decay associated with the

consumption of benzyl alcohol. Notice in this respect that the initial concentration of benzyl alcohol was just 0.1 M since the steric hindrance of benzene may prevent an efficient reaction at higher concentrations. The EIS spectra for EOR and BOR were similar to those obtained for MOR, confirming that Ni-2D-O-SA-CNT is also characterized by a highly efficient charge transfer and a highly favorable EOR and BOR kinetics (**Figure 4.13c,d**).
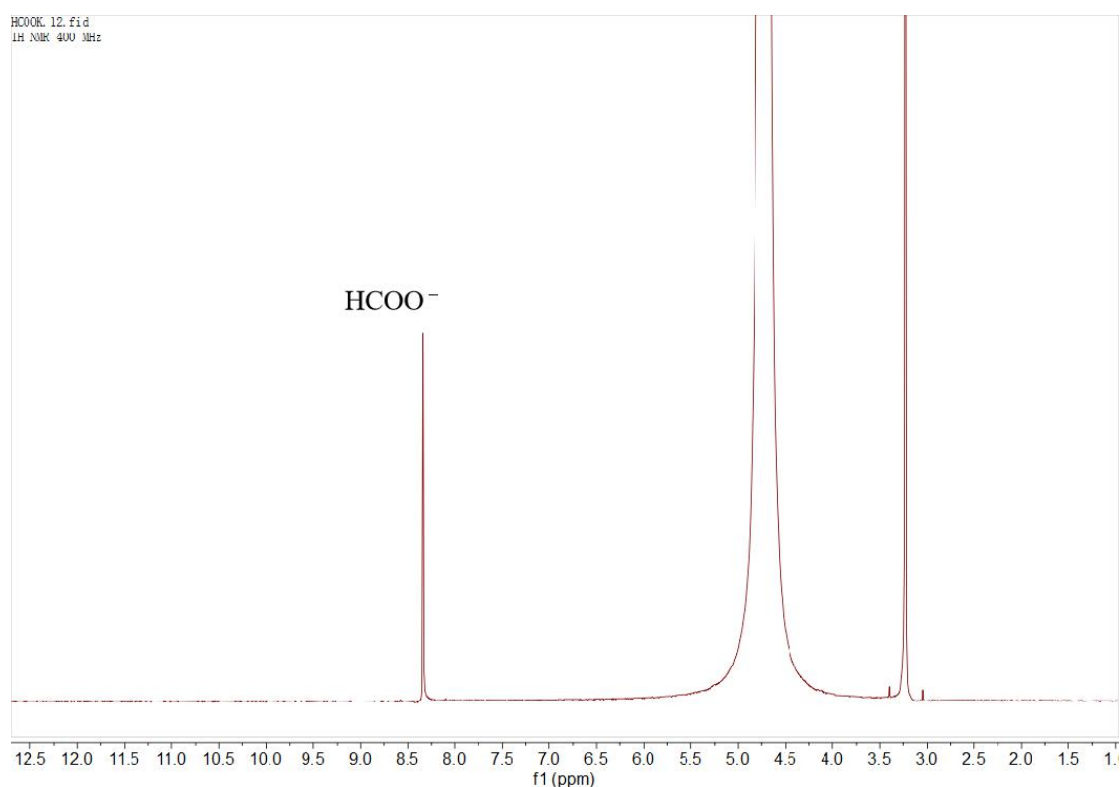
Figure 4.14 ^{1}H NMR spectra of methanol electrochemical oxidation on Ni-2D-O-SA-CNT electrode after 36 h stability test.
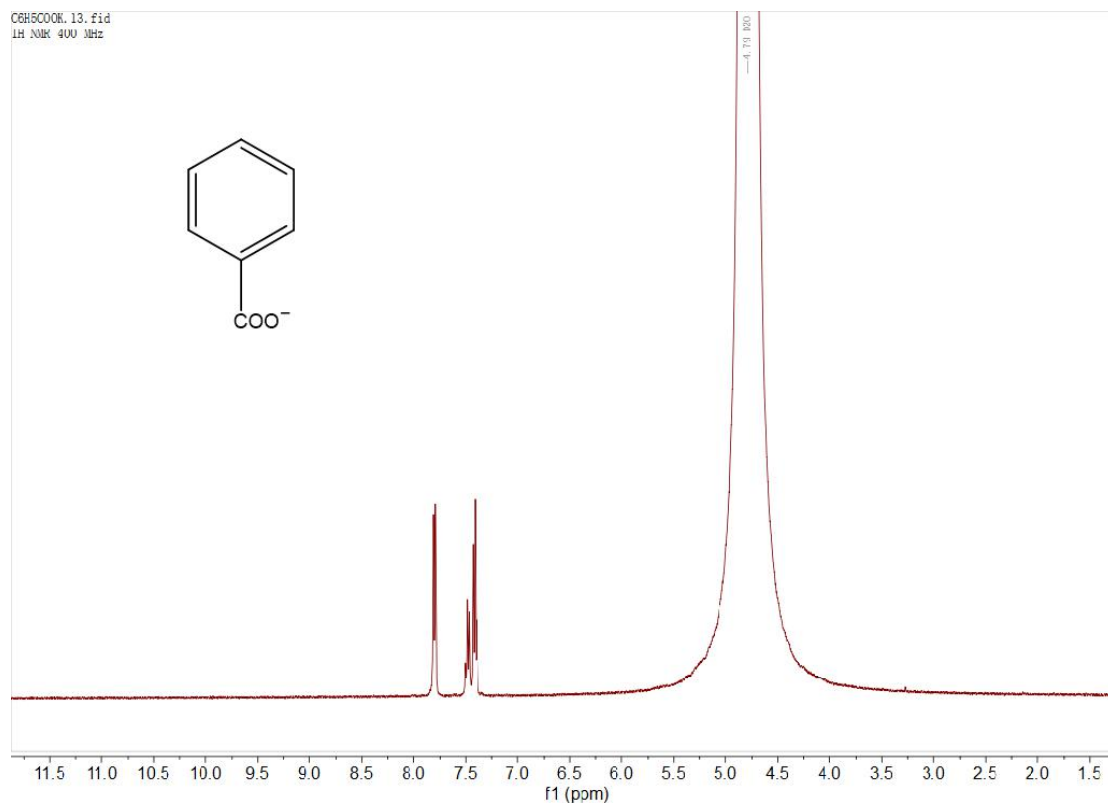
Figure 4.15 ^{1}H NMR spectra of benzyl alcohol electrochemical oxidation on Ni-2D-O-SA-CNT electrode after at 0.55 V vs HgO/Hg untill the current close to zero.
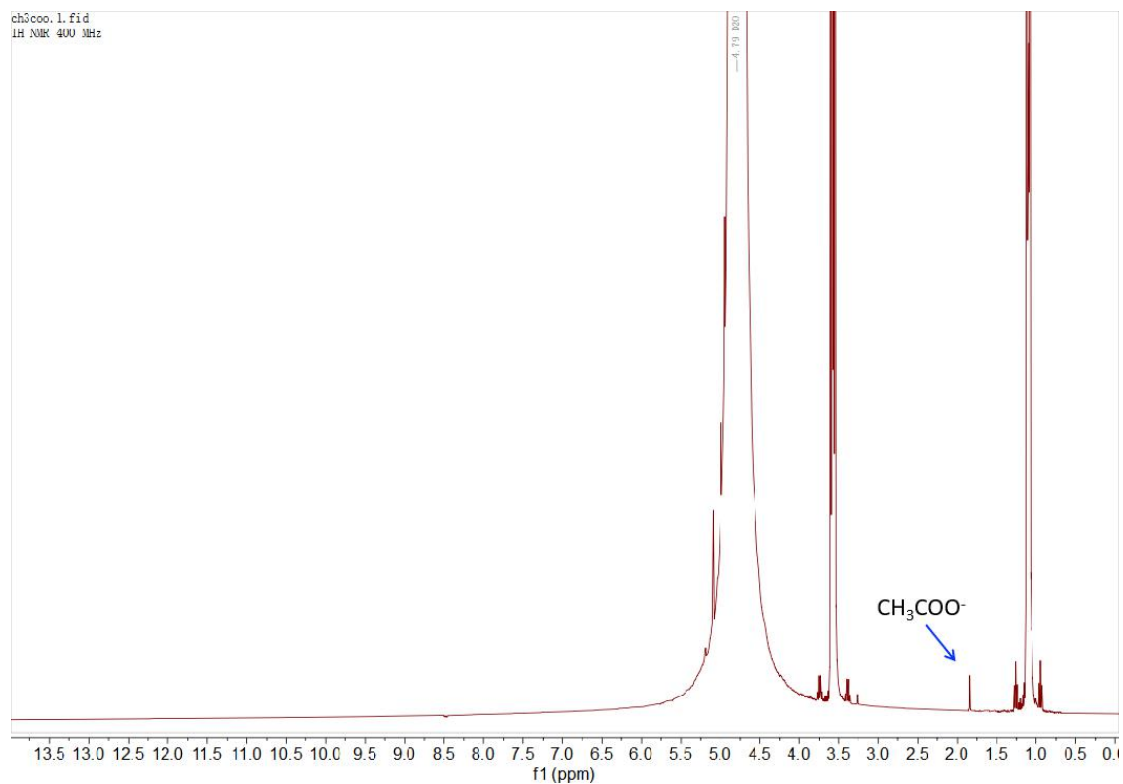
Figure 4.16 ^{1}H NMR spectra of ethanol electrochemical oxidation on

147

Ni-2D-O-SA-CNT electrode after 12 h stability test at 0.7 V vs HgO/Hg.

Finally, in order to confirm the associated product of the electrochemical oxidation of alcohol, Nuclear Magnetic Resonance (NMR) was conducted. As shown in **Figure 4.14,** the NMR spectrum after the MOR stability test displays the characteristic chemical shift of proton of HCOO- at 8.33 ppm, while the characteristic chemical shift of HCHO in the range of 9~10 ppm did not appear, demonstrating that the final product of methanol oxidation is formate ($HCOO^-$). Furthermore, the NMR spectrum (**Figure 4.15**) of the product from benzyl oxidation shows chemical shift in the range of 7~8 ppm, which is assigned to the characteristic chemical shift of the proton in the benzene ring of benzoate. The characteristic chemical shift belonging to the aldehyde (-CHO) of Benzaldehyde did not appeared at the range of 9~10 ppm, demonstrating that the final product of the benzyl alcohol oxidation is benzoate ($C_6H_5COO^-$). The NMR spectra of the EOR electrolyte also display no characteristic chemical shift of the aldehyde (-CHO). The characteristic chemical shift of CH_3COO^- appears at 1.83 ppm (**Figure 4.16**).

Here, We propose the electrochemical reaction of alcohol electrochemical oxidation as follow:

$$RCH_2OH \xrightarrow[\text{1 M KOH}]{\text{Electrocatalysts}} RCOO^-$$

$$R=H, CH_3, C_6H_5$$
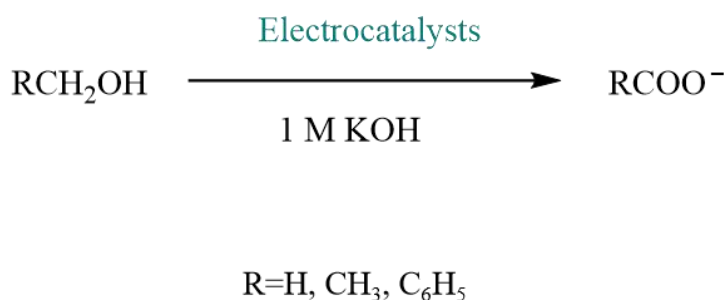
Figure 4.17. Scheme of the electrochemical oxidation reaction of alcohol.

4.4 Conclusion

In conclusion, we detailed the synthesis of a new nickel-based 2D organic framework and proposed a facile molecular engineering strategy to tune the ligand coordination environments of nickel ion centers. Through this strategy, carbonyl (C=O) groups were introduced and proved to decisively contribute to an efficient alcohol electro-oxidation in alkaline solution. EXAFS and XANES analysis confirmed the Ni

salophen unit structure, NiN_2O_2, within the 2D organic frameworks. The atomically dispersed nickel within a framework containing the carbonyl groups displayed outstanding MOR, EOR and BOR performance. DFT calculations suggested that the introduction of the C=O functional groups favor the absorption and activation of methanol molecules, which is at the origin of the improved MOR observed. The present work not only offers novel materials and a promising strategy to design more efficient atomically dispersed nickel-based catalysts for alcohol oxidation, but it could also benefit other research fields related to electrochemical-organic synthesis, energy conversion and storage.

References

[1] (a) E. Antolini, E. R. Gonzalez, *Journal of Power Sources* **2010**, *195*, 3431-3450. (b) K.C. Cheung, W. L. Wong, D. L. Ma, T. S. Lai, K. Y. Wong, *Coord. Chem. Rev.* **2007**, 251, 2637-2385. (c) D. P. Hickey, M. S. McCammant, F. Giroud, M. S. Sigman, S. D. Minteer, *J. Am. Chem. Soc*. **2014**, 136, 15917-15920. (d) N. Kakati, et al. *Chem. Rev*. **2014**, 114, 12397-12429. (e) R. Ciriminna, G. Palmisano, M. Pagliaro, *ChemCatChem* **2015**, 7, 552-558.

[2] Y. Tong, X. Yan, J. Liang, S. X. Dou, *Small* **2021**, *17*, e1904126.

[3] M. A. F. Akhairi, S. K. Kamarudin, *International Journal of Hydrogen Energy* **2016**, *41*, 4214-4228.

[4] (a) S. Rezaee, S. Shahrokhian, *Applied Catalysis B: Environmental* **2019**, *244*, 802-813. (b) A. Badalyan, S. S. Stahl, *Nature* **2016**, 535, 406-410.

[5] G. M. K. Tolba, N. A. M. Barakat, A. M. Bastaweesy, E. A. Ashour, W. Abdelmoez, M. H. El-Newehy, S. S. Al-Deyab, H. Y. Kim, *Journal of Materials Science & Technology* **2015**, *31*, 97-105.

[6] X. Cui, P. Xiao, J. Wang, M. Zhou, W. Guo, Y. Yang, Y. He, Z. Wang, Y. Yang, Y. Zhang, Z. Lin, *Angew Chem Int Ed Engl* **2017**, *56*, 4488-4493.

[7] J. Li, Z. Luo, Y. Zuo, J. Liu, T. Zhang, P. Tang, J. Arbiol, J. Llorca, A. Cabot, *Applied Catalysis B: Environmental* **2018**, *234*, 10-18.

[8] A. Dubale, Y. Zheng, H. Wang, R. Hübner, Y. Li, J. Yang, J. Zhang, N. Sethi, L. He, Z. Zheng, W. Liu, *Angew Chem Int Ed Engl* **2020**, *132*, 13995-14003.

[9] B. Zhao, J. Liu, C. Xu, R. Feng, P. Sui, L. Wang, J. Zhang, J. L. Luo, X. Z. Fu, *Advanced Functional Materials* **2020**, *31*.

[10] C. Liu, W. Zhou, J. Zhang, Z. Chen, S. Liu, Y. Zhang, J. Yang, L. Xu, W. Hu, Y. Chen, Y. Deng, *Advanced Energy Materials* **2020**, *10*.

[11] Y. Wu, J. Tian, S. Liu, B. Li, J. Zhao, L. Ma, D. Li ,Y. Lan, X. Bu, *Angew Chem Int Ed Engl* **2019**, *58*, 12185-112189.

[12] H. Huang, C. Yu, X. Han, H. Huang, Q. Wei, W. Guo, Z. Wang, J. Qiu, *Energy & Environmental Science* **2020**, *13*, 4990-4999.

[13] X. Zhao, P. Pachfule, A. Thomas, *Chem Soc Rev* **2021**, https://doi.org/10.1039/D0CS01569E.

[14] J. Du, F. Li, L.-C. Sun, *Chem Soc Rev* **2021**, 50, 2663-2695.

[15] S. Royuela, E. Martinez-Perinan, M. P. Arrieta, J. I. Martinez, M. M. Ramos, F. Zamora, E. Lorenzo, J. L. Segura, *Chem Commun (Camb)* **2020**, *56*, 1267-1270.

[16] H. Zhu, M. Lu, Y. Wang, S. Yao, M. Zhang, Y. Kan, J. Liu, Y. Chen, S. Liu, Y. Lan, *Nat Commun* **2020**, *11*, 497.

[17] J. Liu, D. Yang, Y. Zhou, G. Zhang, G. Xing, Y. Liu, Y. Ma, O. Terasaki, S. Yang, L. Chen, *Angew Chem Int Ed Engl* **2021**.

[18] T. Li, W.-D. Zhang, Y. Liu, Y. Li, C. Cheng, H. Zhu, X. Yan, Z. Li, Z.-G. Gu, *Journal of Materials Chemistry A* **2019**, *7*, 19676-19681.

[19] B. P. Biswal, S. Chandra, S. Kandambeth, B. Lukose, T. Heine, R. Banerjee, *J Am Chem Soc* **2013**, *135*, 5328-5331.

[20] L. Wang, Y. Ni, X. Hou, L. Chen, F. Li, J. Chen, *Angew Chem Int Ed Engl* **2020**, *59*, 22126-22131.

[21] Y. Liao, H. Wang, M. Zhu, A. Thomas, *Adv Mater* **2018**, *30*, e1705710.

[22] F. L. Li, Q. Shao, X. Huang, J. P. Lang, *Angew Chem Int Ed Engl* **2018**, *57*, 1888-1892.

[23] J. Jin, Y. Zheng, S.-z. Huang, P.-p. Sun, N. Srikanth, L. B. Kong, Q. Yan, K. Zhou, *Journal of Materials Chemistry A* **2019**, *7*, 783-790.

[24] H. Yang, Q. Lin, C. Zhang, X. Yu, Z. Cheng, G. Li, Q. Hu, X. Ren, Q. Zhang, J. Liu, C. He, *Nat Commun* **2020**, *11*, 593.

[25] A. J. Bard, L. R. Faulkner, *Electrochemical Methods Fundamentals and applications* **2001**.

[26] D. Chen, S. D. Minteer, *Journal of Power Sources* **2015**, *284*, 27-37.

[27] Gao. Chen, Y. Luo, L. Ding, H. Wang, *ACS Catal.* **2018**, *8*, 526-530.

[28] S. J. Lyle, T. M. Osborn Popp, P. J.Waller, X. Pei, J. A. Reimer, O. M. Yaghi, *J. Am. Chem. Soc* **2019**, 141, 28, 11253–11258.

[29] Kurt A.W. Wallenfels, Wilfried J. Draber, *Tet. Lett* **1959**, 667, 55

[30] Manivannan, R.; Ciattini, S.; Kuppanagounder, L. C.; Elango, P., *RSC Adv*

2015, 5, 87341.

[31] Stang, S.; Lebkücher, A.; Walter, P.; Kaifer, E.; Himmel, H. J.; *Eur. J. Inorg. Chem*. **2012**, 4833.

[32] T. Li, W.-D. Zhang, Y. Liu, Y. Li, C. Cheng, H. Zhu, X. Yan, Z. Li, Z.-G. Gu, *Journal of Materials Chemistry A* **2019**, *7*, 19676-19681.

[33] G. Kresse, J. Furthmüller. Comput. Mater. Sci. 1996, 6, 15-50.

[34] G. Kresse, J. Furthmüller. Phys. Rev. B: Condens. Matter. 1996, 54, 11169.

[35] B. Ravel, M. Newville, *J. Synchrotron Rad.* **2005**,12, 537–541.

[36] M. Newville, *J. Synchrotron Rad.* **2001**, 8, 322–324.

[37] J. J. Rehr, J. Mustre de Leon, S. I. Zabinsky, R. C. Albers, *J. Am. Chem. Soc.* **1991**, 113, 5135–5140.

[38] A. J. Bard, L. R. Faulkner, *Electrochemical Methods Fundamentals and applications* **2001**.

[39] D. Chen, S. D. Minteer, *Journal of Power Sources* **2015**, *284*, 27-37.

[40] A. J. Bard, L. R. Faulkner, *Electrochemical Methods Fundamentals and applications* **2001**.

Chapter 5

A Novel π-d Conjugated Cobalt Tetraaza[14]annulene Organic Framework for Efficient Electrocatalytic CO$_2$ Reduction
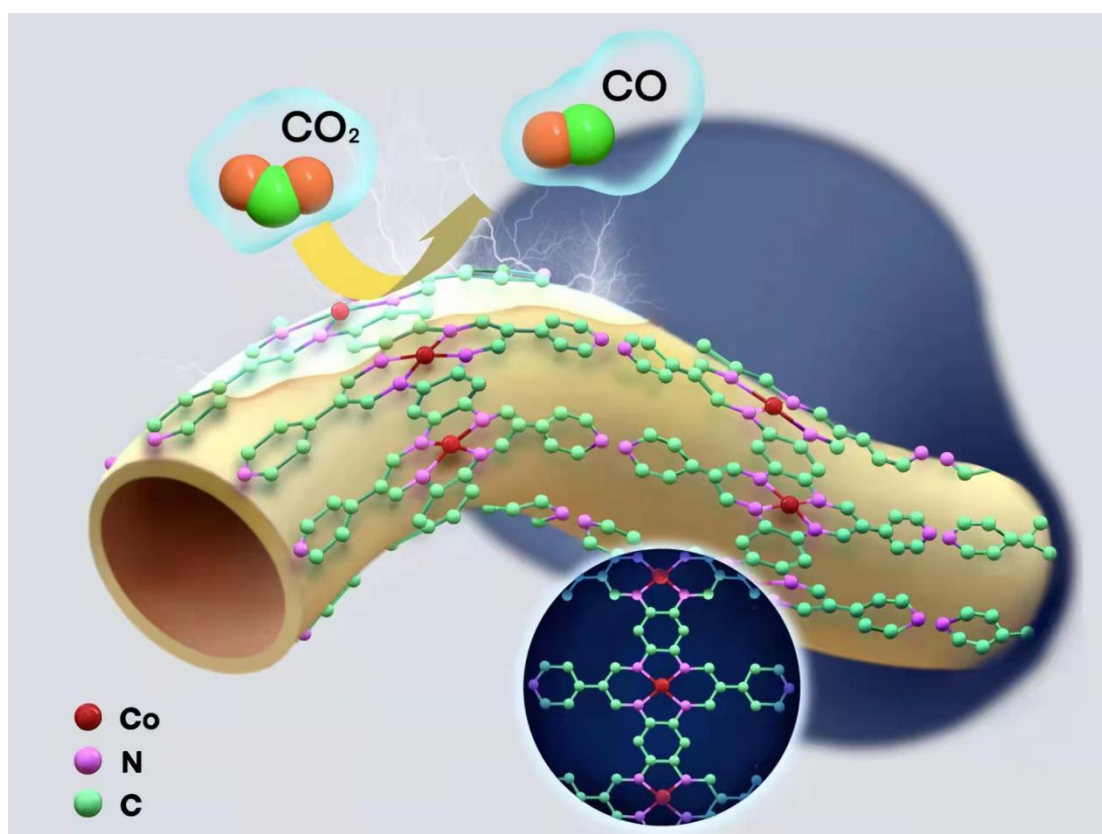
5.1 Introduction

Tetraaza[14]annulenes (TAA) are a type of synthetic macrocycles analogue to porphyrins, which have been much less studied.[1-4] They contain four nitrogen atoms in a central cavity that can be easily deprotonated to coordinate with metal ions to form tetraanulene metal coordination structures. Metal complexes based on TAA have been used in field-effect transistors,[5] CO electrochemical oxidation,[33] as single molecular magnets,[6] catalysts [7] and dye-sensitized solar cells.[8] Most of the previous studies used the metal ion as a template for the synthesis of the TAA complexes. However, this type of macrocycles has been rarely used to build metal organic frameworks because the suitable organic precursors are too short to work as linkage ligands between metal atoms. In addition, to make it more difficult, most of the tetraaza[14]annulene complexes use the template synthesis method, where the metal ion is working as template. Recently, Y. Jiang and co-workers reported the first two-dimensional (2D) Ni(II)-based TAA-linked metal organic framework (MOF) obtained by a template method, and characterized its electrical conductivity and magnetic properties.[9] We believe that these novel structures are excellent platforms for electrocatalytic applications, but a more in-depth exploration of these novel TAA-based metal organic frameworks and study of their relative catalytic performance are needed.

The utilization of renewable energy to drive the electrocatalytic reduction of carbon dioxide to valuable chemicals is a potentially cost-effective strategy to close the carbon cycle. In this direction, the search for electrocatalysts able to efficiently activate the CO_2 reduction reaction (CO_2RR) has a strong interest both scientifically and technologically.[10] Most electrocatalytic materials reported for CO_2RR are nanomaterials,[11-12][40-41][45-46][52-53] even though they have displayed efficient catalytic activity toward electrochemical CO2 reductio,[42] most are not easy to synthesize in large quantities while controlling the active sites under a mild and easy controllable condition and the metal atoms are not 100% utilized. Recently, atomically-dispersed metal-based catalysts, especially those with a coordination

structure of metal-N4, have been successfully applied to high-efficiency electrocatalytic carbon dioxide reduction due to their high catalytic activity and 100% atom utilization.[32][43] However, due to the general high-temperature pyrolysis method for preparation, the active site structure and the ligand structure are not easy to be determined and controlled.[17] In contrast, molecular catalysts also work as a type of atom dispersed catalysts, which can be easily prepared under mild and controllable conditions and provide a well-defined platform that facilitates the understanding of the structure-performance relationships, thus enabling a rational catalyst design and optimization. Combining the merits of these two worlds, the development of stable and high-performance heterogeneous molecular catalysts is raising increasing interest.[13-14]

In recent years, molecular catalysts based on metalloporphyrin and metallophthalocyanine supported on multi-wall carbon nanotubes (CNTs) have shown low overpotentials, high Faradaic efficiencies and excellent selectivity for electrocatalytic CO_2RR.[15-19] However, small molecular catalysts do not easily work for heterogeneous reduction reactions, which limits their application.[20-21] Therefore, it is challenging to develop novel materials and molecular engineering strategies to realize the highly efficient and stable molecular electrocatalysts that a cost-effective CO_2RR would require. Alternatively, π-d conjugated metal organic frameworks (MOFs), with a hybrid interaction between the π orbital of the ligand with the d orbital of the transition metal, have aroused widespread interest in recent years.[33-38] This hybrid interaction is similar to that presented in the π-π conjugated organic frameworks, with the advantages such as their functionalization flexibility through ligand engineering design. However, the π-d conjugated metal organic frameworks have been less studied for electrocatalytic CO_2 reduction. In the present work we combine the π-d conjugated structure and the Tetraaza[14]annulenes macrocyclic structure to design novel metal organic frameworks as efficient catalysts for electrocatalytic CO_2 reduction.

Herein, a non-template synthesis method was used to construct a new type of Tetra[14]annulene based π-d conjugated cobalt organic framework with atomically

dispersed cobalt, namely, Poly-TAA-Co with CoN_4 structure. This molecular complex is loaded on a conductive support, namely multi-wall CNTs, and applied for the efficient electrochemical CO_2RR. The obtained results have been rationalized by means of density functional theory (DFT) calculations.

5.2 Experimental Section

5.2.1 Materials

Methanol (99%), N,N-dimethylformamide (DMF) (98%), hydrazine hydrate (98%) and carbon paper were purchased from Alfa Aesar. 1,2,4,5-benzenetetraamine tetrahydrochloride, potassium thiocyanate (99%), and Nafion (10%) were purchased from Sigma-Aldrich. Cobalt acetate tetrahydrate (99%), potassium hydrogen carbonate (99.7%), 1-butanol (99%), and 2-(4-pyridyl)malondialdehyde (95%) were bought from Acros Organics. All solutions were prepared with Milli-Q water (DI-H_2O, Ricca Chemical, ASTM Type I). Nafion membreanes (N-117 membrane, 0.18 mm thick) was purchased from Alfa Aesar and kept in 0.5 M NaOH solution. All chemicals were used without further purification. Carbon Nanotubes (CNTs) was ordered from Sailed Technology.

5.2.2 Synthesis of Poly-TAA

2-(4-Pyridyl)malondialdehyde (149 mg, 1 mmol), 1,2,4,5-benzenetetraamine tetrahydrochloride (142 mg, 0.5 mmol) and 6 mL 1-butanol were added to a 25 mL three-neck round bottom flask. Then a few drops of acetic acid were added. The resulting solution was sonicated for half an hour to obtain a homogenous mixture. The flask was heated to 110 °C with stirring under argon for 48 h and afterward cooled to room temperature. The resulting brown precipitate was collected by filtration and washed with ethanol, Soxhlet extracted by methanol for 24 h, then vacuum dried at 60 ºC for 24 h to give a black powder with ~63% yield.

5.2.3 Synthesis of Poly-TAA-Co

Poly-TAA (60 mg), cobalt(II) chloride hexahydrate (60 mg) and 6 mL DMF were

added to a 15 mL three-neck round bottom flask. The resulting solution was heated to 130 °C with stirring under argon for 48 h and then cooled to room temperature. The resulting brown precipitate was collected by filtration and washed with ethanol, then vacuum dried at 60 °C for 24 h to give a brown-black powder with ~56% yield.

5.2.4 Synthesis of Co-TAA
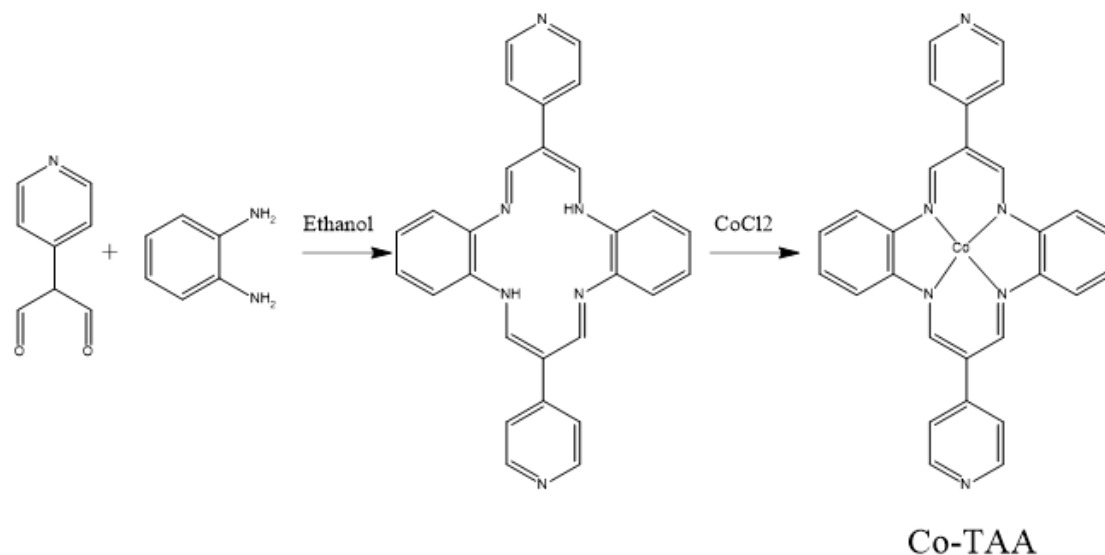
Scheme 5.1 Scheme of the synthesis of Co-TAA

The control sample Co-TAA was prepared following procedures found in the literature.[63]

2-(4-Pyridyl)malondialdehyde (149 mg, 1 mmol), o-Phenylenediamine (108 mg, 1 mmol) and 8 mL Ethanol were added to a 25 mL three-neck round bottom flask, then a few drops of acetic acid was added. The resulting solution was sonicated for half an hour to obtain a homogenous mixture. The flask was heated at 80 °C with stirring under argon for 48 h and cooled to room temperature. The resulting brown precipitate was collected by filtration and washed with ethanol, then vacuum dried at 60 °C for 24 h to give a red-brown powder (**TAA**) with ~80% yield.

Then A mixture of TAA (36.0 mg, 0.08 mmol) and anhydrous cobalt chloride (72.0 mg, 0.55 mmol) in DMF (2 mL) were placed in a Teflon-sealed bomb and then heated to 155 ºC slowly and keep for 10 h and allowed to cool to room temperature slowly. Dark violet needle-shaped complex of **Co-TAA** was obtained, Yield (15%).

5.2.5 Synthesis of Poly-TAA-Co/CNT composites

Poly-TAA-Co and pre-oxidized carbon nanotubes (CNTs) were put into a 15 mL glass vial. Then 3 mL DMF were added. The resulting solution was sonicated for half an hour and stirred at 100 ℃ for 12 h. The obtained black composites were filtrated and washed with ethanol, then vacuum dried at 60 ℃ for 24 h to get the composite.

5.2.6 Electrochemical Measurements

5 mg synthesized different samples and 100 μL 5 wt% Nafion solutions were dissolved in ethanol (1 mL) and ultrasonicated for 30 min to form an evenly suspension for the electrochemical experiments. To prepare the working electrode, 400 μL above as-prepared inks were dropped onto the two sides of the carbon paper electrode with 1×1 cm^2 and then dried at room temperature for a few minutes, resulting in a catalyst loading mass of ~2 mg/cm^2.

The electrocatalytic performance of different catalysts was measured at room temperature by using a gas-tight H-cell with two compartments separated by a cation exchange membrane (Nafion N-117 membrane) with a continuously Ar or CO_2 gas injection. Each compartment contained 70 ml electrolyte (0.5 M $KHCO_3$ made from de-ionized water). In a typical experiment, a standard three-electrode setup in 0.5 M $KHCO_3$ solution was assembled: an Ag/AgCl electrode as reference electrode, a Pt wire as auxiliary electrode and a carbon paper coated with the different samples as working electrode (surface area = 1 cm^2). The potentials were measured versus Ag/AgCl and converted to the reversible hydrogen electrode (RHE) according to the following equation: $E_{RHE} = E^0_{Ag/AgCl} + E_{Ag/AgCl} + 0.059 \times pH$, pH=7.[44] All electrochemical results were showed without iR-compensation by using a computer-controlled BioLogic VMP3 electrochemical workstation. Meanwhile, the *I-t* curves were obtained to reach a stable state at −0.30 V vs. RHE in Ar-saturated 0.5 M $KHCO_3$ (pH=8.5) as supporting electrolyte. The CV and LSV curves were performed at 20 mV s^{-1}. Moreover, electrochemical impedance spectroscopy (EIS) of different samples was carried out in a frequency range from 100 kHz to 100 mHz.

Before the electrochemical CO_2 reduction experiments, an average rate of 20 ml min^{-1}

Ar was injected into cathodic electrolyte in order to form an Ar-saturated solution. During the electrochemical CO_2 reduction experiments, the CO_2 gas was delivered at an average rate of 20 ml min^{-1} at room temperature and ambient pressure, and we measured the downstream by a volumetric digital flowmeter. The gas-phase composition was analyzed by gas chromatography (GC) during potentiostatic measurements every 20 min.

Details concerning the calculation of Faradaic Efficiency (FE) are shown below.[47-48]

The partial current density for a given gas product was calculated as below:

$$j_i = x_i \times V \times \frac{n_i F P_0}{RT} \times (electrode\ area)^{-1} \tag{1}$$

Where x_i is the volume fraction of certain product determined by online GC referenced to calibration curves from three standard gas samples, v is the flow rate, n_i is the number of electrons involved, P_0= 101.3 kPa, F is the Faraday constant, and R is the gas constant. The corresponding FE at each potential is calculated by

$$FE = \frac{j_i}{j} \times 100\% \tag{2}$$

5.2.7 Characterization

The crystal structure information was characterized by means of powder X-ray diffraction (XRD) measured in a Bruker AXS D8 Advance X-ray diffractometer. (Cu-Kα radiation, λ = 1.5106 Å, 40 kV and 40 mA; Bruker, Germany). High-resolution transmission electron microscopy (HRTEM) was conducted in a FEI Tecnai F20 microscope at an operating voltage of 200 keV equipped with an embedded Quantum Gatan Image Filter for electron energy loss spectroscopy (EELS) analyses. High angle annular dark-field (HAADF)-scanning transmission electron microscopy (STEM) images and Energy Dispersive X-Ray Spectroscopy (STEM-EDS) analysis were obtained in a spherical aberration corrected transmission electron microscopy FEI Titan G2 80-200 (ChemiSTEM). It is equipped with four EDX detectors and operated at 200kV. Images have been analyzed by means of Gatan Digital Micrograph software. Thermogravimetric analyses (TGA) were performed
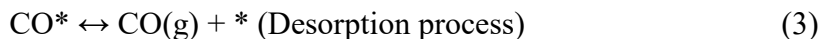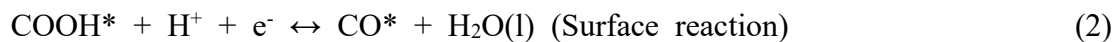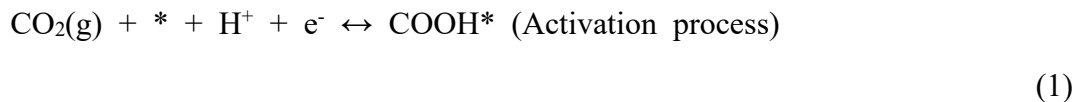
under air at a heating rate of 5 °C/min using a Thermogravimetric Analyzer Q200. X-ray photoelectron spectroscopy (XPS) data was obtained by using 150 W and a Phoibos 150 MCD-9 detector. The X-ray absorption fine structure (XAFS) measurements of the pellet of powder sample were carried out at the BL12C beamline of the Photon Factory, the High Energy Accelerator Research Organization (KEK), under proposal no. 2019G117, 2021G129. Co foil was used for the calibration of Co K-edge. Structural analysis was performed using the Demeter software platform. The samples were pressed onto a double-sided carbon tape and the data was recorded in the X-ray fluorescence mode. The XAFS data was processed with the ATHENA program.[49] The EXAFS was analyzed using the IFEFFIT package [50] and the EXAFS fitting was performed with FEFF6L.[51]

5.2.8 DFT Calculation Details

The lowest unoccupied molecular orbital (LUMO) and highest occupied molecular orbital (HOMO) of cobalt phthalocyanine (CoPc) and Co(II) tetraaza[14]annulenes (CoTAA) structure unit were calculated by using DFT with the hybrid B3LYP functional and the 6-311++G(d,p) basis set.[57-59] For Co atoms the Stuttgart Dresden (SDD) triple zeta effective-core potential (ECP) basis set was used.[60] D3 dispersion correction developed by Grimme was included for weak interactions.[61] These calculations were carried out using the Gaussian16 program package.[62]

The spin-polarized density functional theory (DFT) calculations with projector augmented wave (PAW) method were performed using the Vienna Ab initio Simulation Package code.[54-55] The generalized gradient approximation of Perdew-Burke-Ernzerhof (PBE) with van der Waals correlation was employed to optimize the geometric structures.[56] The convergence criteria was 0.03 eV/ Å in force and 1×10^{-5} eV in energy, while the plane wave cutoff was 500 eV. The Monkhorst–Pack mesh k-point grids was 4×1×1 for all models. All the vacuum thicknesses were higher than 15 Å.

The whole process of CO_2 electrochemical reduction to CO mainly included the following three steps:

$$CO_2(g) + * + H^+ + e^- \leftrightarrow COOH* \text{ (Activation process)}$$

$$(1)$$

$$COOH* + H^+ + e^- \leftrightarrow CO* + H_2O(l) \text{ (Surface reaction)} \quad (2)$$

$$CO* \leftrightarrow CO(g) + * \text{ (Desorption process)} \quad (3)$$

Where the *, COOH* and CO* represent free sites, for the adsorption state of COOH and CO, respectively. The (g) represent the gas phase. The reaction free energies of each step were calculated by the following formula:

$$G = E_{DFT} + E_{ZPE} - TS + E_{sol} \quad (4)$$

Where E_{DFT} is the DFT calculated energy, E_{ZPE} is the zero-point energy, T (=298.15 K) is temperature, S is the entropy, and E_{sol} is the solvation correction, which for CO* was stabilized by 0.1 eV and for COOH* by 0.25 eV.

5.3 Results and Discussions

5.3.1 Synthesis and Structural Characterization
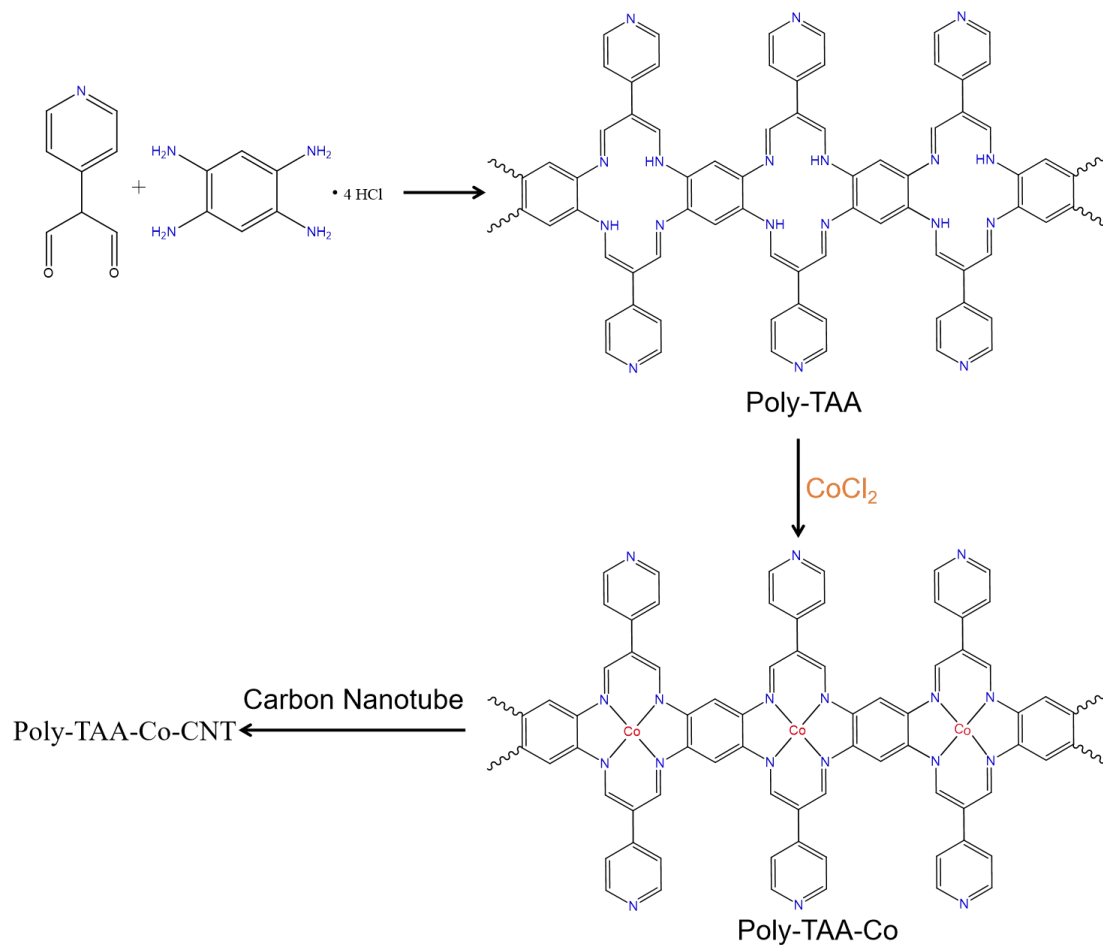
Scheme 5.2. Scheme of the synthesis of Poly-TAA-Co (grey spheres correspond to

carbon atoms, light blue to nitrogen, red to oxygen and purple to cobalt)

The Poly-TAA-Co conjugated framework was prepared in two steps (see **Scheme 5-2**). First, the Poly-TAA was synthesized using a non-template method based on the Schiff base reaction between 2-(4-pyridyl)malondialdehyde and 1,2,4,5-benzenetetramine tetrahydrochloride in 1-butanol with a few drops of acetic acid. The obtained brown precipitate was Soxhlet extracted with methanol to remove the small impurity molecules and dried at 60 °C under vacuum. The brown color of the product was an indication of the formation of a conjugated organic framework. In a second step, Poly-TAA was reacted with cobalt chloride in dimethylformamide (DMF) to yield Poly-TAA-Co.
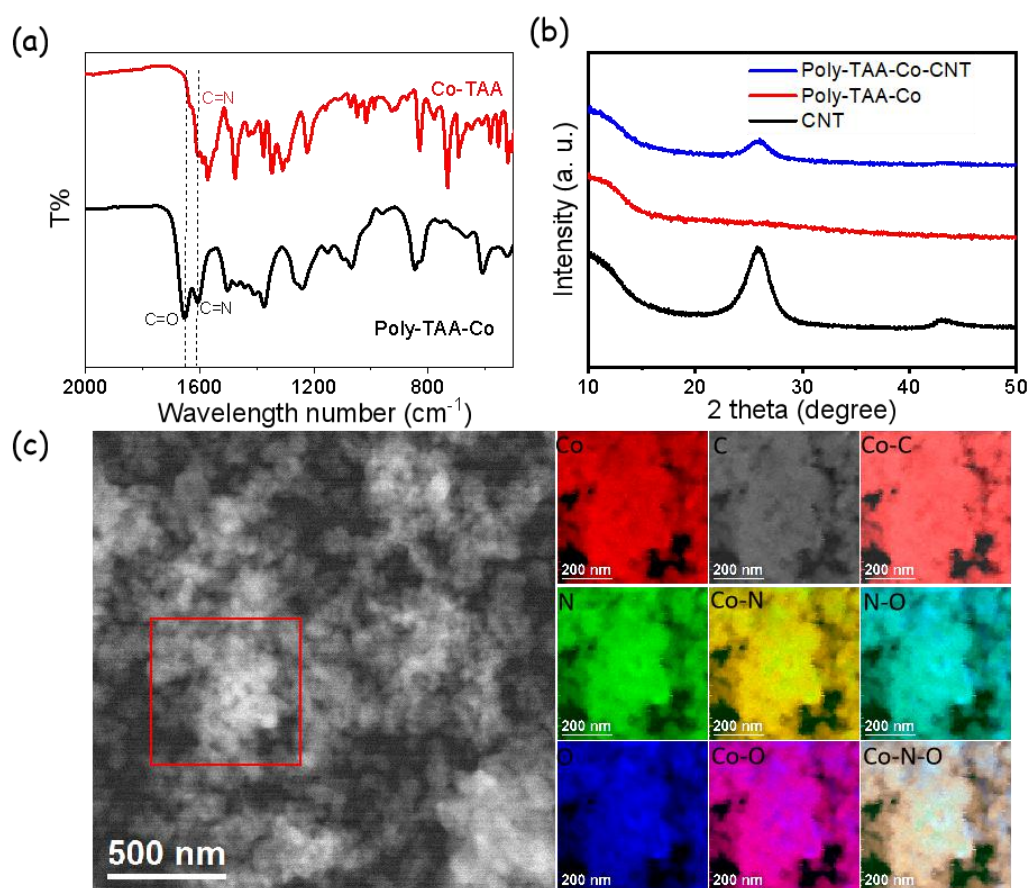
Figure 5.1 (a) FT-IR spectra of the model compound Co-TAA, and Poly-TAA-Co powder. (b) XRD patterns of CNT, Poly-TAA-Co and Poly-TAA-Co-CNT. (c) EELS chemical composition maps from the red squared area of the STEM micrograph. Individual Co $L_{2,3}$-edges at 779 eV (red), N K-edges at 401 eV (green), O K-edges at

532 eV (blue), and C-K edges at 284 eV (grey) and composites of Co-N, Co-O, Co-C, N-O and Co-N-C.

Fourier-transform infrared spectroscopy (FTIR) analysis of Poly-TAA-Co displayed the footprint of C=N at 1606 cm^{-1}, suggesting the formation of Co(II) tetraaza[14]annulene (**Figure 5.1a**).[22] The powder X-ray diffraction (PXRD) pattern of Poly-TAA-Co displayed no diffraction peak (**Figure 5-1b**), which exposed the amorphous nature of the material and discarded the presence of any crystalline Co-based phase. The morphology of Poly-TAA-Co is displayed in **Figure 5-1c**.
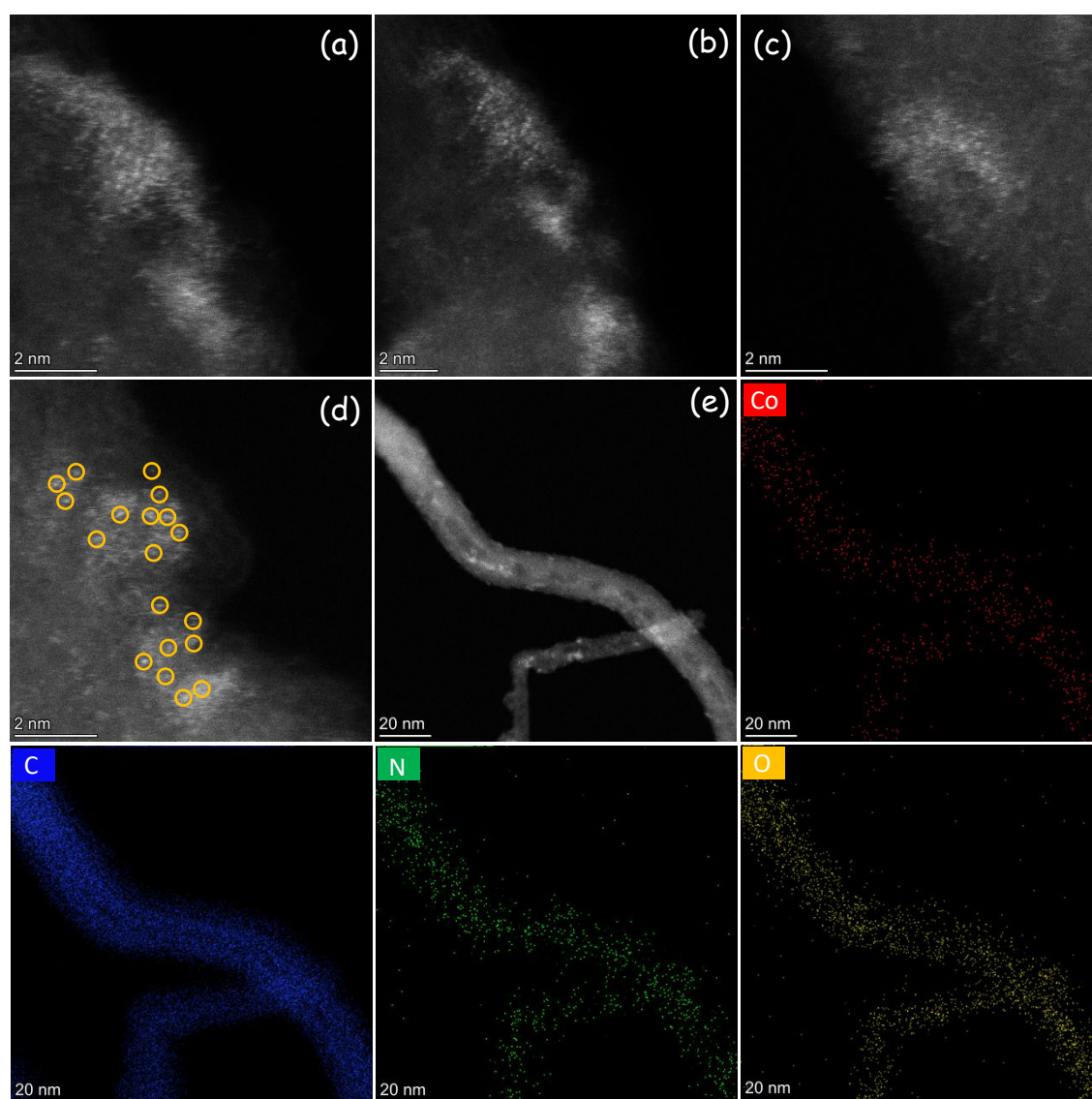
Figure 5.2 (a)-(c) HAADF-STEM images of Poly-TAA-Co-CNT displaying atomically dispersed cobalt atoms. (d) Low magnification HAADF-STEM image and EDS elemental maps for Co (red), C (light blue), N (green) and O (yellow).

To improve the electrical conductivity of Poly-TAA-Co organic frameworks toward their use as efficient electrocatalysts for CO_2RR, they were grafted through π - π interaction to the surface of pre-oxidized multi-wall CNTs by just mixing both materials in DMF (**Scheme 5.2**). The PXRD pattern of the obtained composite (**Poly-TAA-Co-CNT)** showed a unique peak at about 26° (**Figure 5.1b**), which was assigned to the overlap between the CNT and the organic framework structures. Isolated Co atom sites were characterized via high angle annular dark-field (HAADF)-aberration-corrected scanning transmission electron microscopy (STEM) analysis (**Figures 5.2a-d**). The Energy Dispersive X-Ray Spectroscopy (EDS) analysis revealed the homogeneous distribution of Poly-TAA-Co on the surface of CNTs, and the uniform atomic distribution of Co within Poly-TAA-Co (**Figure 5.2e**).
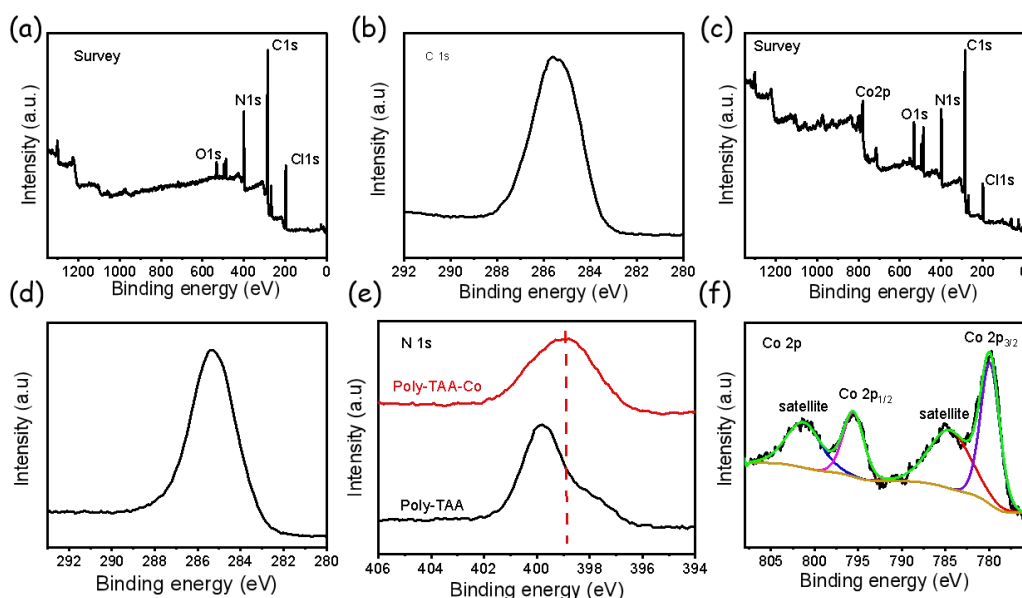
Figure 5.3. (a)-(b) Survey and high resolution C1s XPS spectra of Poly-TAA powder, respectively. (c)-(d) Survey and high resolution C1s XPS spectra of Poly-TAA-Co powder, respectively. (e) N 1s and (f) Co 2p XPS spectra of Poly-TAA-Co powder.

X-ray photoelectron spectroscopy (XPS) analyses displayed the presence of C, N, O, Cl of Poly-TAA and Poly-TAA-Co (**Figure 5.3a,b** and **Figure 5.3c, d**). Compared with Poly-TAA, the high-resolution N 1s XPS spectrum of Poly-TAA-Co is shifted to lower binding energies, which is attributed to the deprotonation of the nitrogen in the TAA cores upon coordination with cobalt ion (**Figure 5.3e**) [9,30]. The high-resolution Co 2p XPS spectrum of Poly-TAA-Co (**Figure 5.3f**) showed two main peaks at 796

eV ($2p_{1/2}$) and 780.3 eV ($2p_{3/2}$), which are assigned to a Co^{2+} chemical state. The respective satellite peaks were also observed [29]. Thermogravimetric analyses (TGA) were performed under air to analyze the Cobalt content of Poly-TAA-Co (**Figure 5.4a**). The small mass lost at about 100 °C corresponds to the solvent (mainly water). The poly-TAA-Co started to decompose at about 350 °C. Finally, after about 650 °C, Poly-TAA-Co fully decomposed to cobalt oxide. From the TGA analysis, we can calculate that the Co content of the Poly-TAA-Co is about 12.6% (the theoretical value was 14%). After loading the poly-TAA-Co on the CNTs, where the CNTs corresponding mass was 70%, the Co mass content in the Poly-TAA-Co-CNT (3:7) is 3.78%.
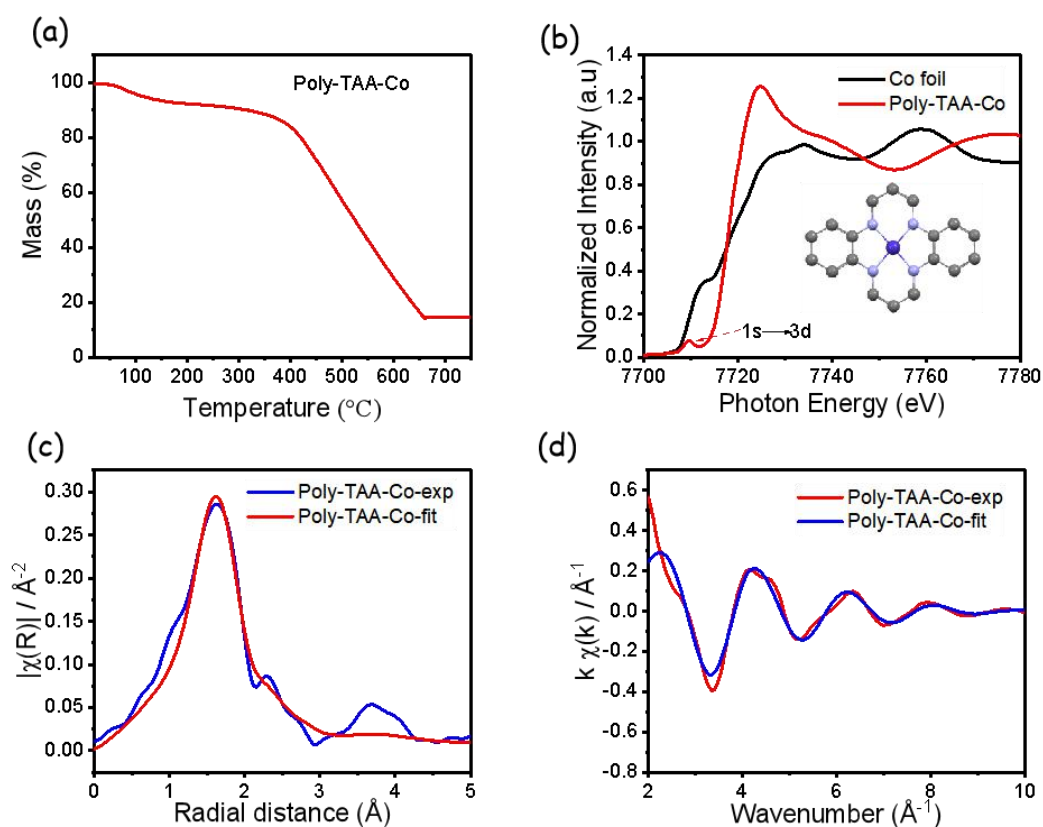

Figure 5.4. (a) TGA analysis of Poly-TAA-Co under argon by heating to 600 °C at the rate of 5 °C/min. (b) Co K-edge XANES spectrum. (c) Fourier transformed EXAFS spectrum and fitted curve. (d) Co K-edge EXAFS oscillations in k-space ($k^3\chi$(k)) of Poly-TAA-Co and its fitted spectrum.

Sample	Bond	R(Å)	CN	R factor (%)
Poly-TAA-Co	Co-N	2.05	3.54±0.5	0.6

Table 5.1. Co K-edge EXAFS fitting parameters for Poly-TAA-Co, R：bond length, CN: coordination number

The coordination structure of cobalt in Poly-TAA-Co was further analyzed by means of X-ray absorption fine structure (XAFS) at the Co K-edge (**Figure 5.4b-c and Figure 5.4d**). The Co K-edge X-ray absorption near-edge structure (XANES) spectrum of Poly-TAA-Co exhibits the fingerprint of CoN_4 at 7709.4 eV assigned to the dipole forbidden 1s to 3d transitions [8]. In addition, we observe the XANES absorption onset of Poly-TAA-Co at higher energy than that of cobalt foil (**Figure 5.4b**). Besides, the main absorption peak of Poly-TAA-Co has a stronger intensity than that of Co foil. These features demonstrate the valence state of Co in Poly-TAA-Co to be higher than that of metallic cobalt, consistently with XPS results. The fitting of the Fourier transformed extended X-ray absorption fine structure (EXAFS) spectrum suggests that Co is coordinated with 4 nitrogen atoms at a bond length of 2.05 Å (**Figure 5.4c and Table 5.1**). Overall, XAFS analysis confirmed the formation of the CoN_4 structure units, thus demonstrating our synthetic route to yield Poly-TAA-Co (**Scheme 5.1**). The surface area of Poly-TAA, Poly-TAA-Co and Poly-TAA-Co-CNT, evaluated from N_2 adsorption-desorption isotherms at 77 K using the Brunauer-Emmett-Teller equation was 4.1, 124.9 and 208.2 m^2 g^{-1}, respectively (**Figure 5.5**).
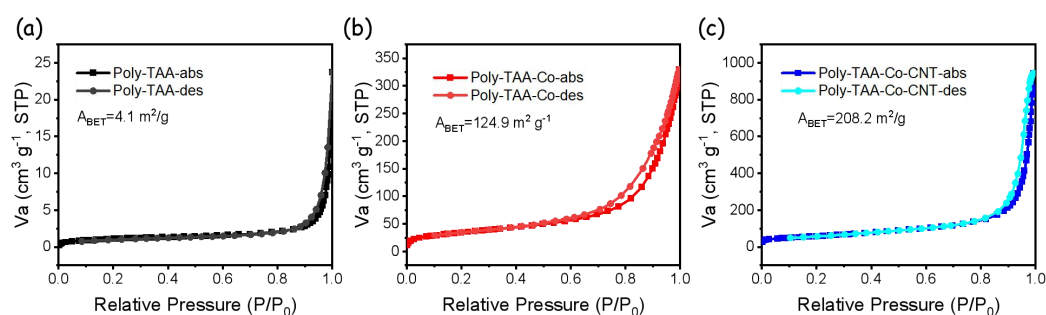
Figure 5.5. N_2 adsorption and desorption of Poly-TAA, Poly-TAA-Co and Poly-TAA-Co-CNT, respectively.

### 5.3.2 Electrochemical CO_2 Reduction Performance

The electrocatalytic activity toward CO_2RR of the Poly-TAA-Co framework and the framework blended with two different amounts of CNTs (Poly-TAA-Co:CNT = 3:7 and 1:1) were investigated using a three-electrode H-cell including an anion exchange membrane and a 0.5 M $KHCO_3$ electrolyte. Gas-phase products were periodically quantified using gas chromatography (GC). Online GC results showed CO and H_2 to be the main gas products for all catalysts. Electrodes were prepared by coating the materials on carbon paper (1 cm×1 cm) with a mass loading of ~2.0 mg cm^{-2}. Electrodes were pretreated at a constant potential of −0.30 V vs. RHE for 15 min until a stable current was reached (**Figure 5.6a**). Then, linear sweep voltammetry (LSV) curves were measured (**Figures 5.6b-d**). The three samples displayed a clear increase of the current density in the presence of CO_2 compared to values obtained in an Ar-saturated electrolyte. Besides, the total current densities significantly increased with the loading of Poly-TAA-CO on CNTs (**Figure 5.7a**), indicating a faster reaction rate in the presence of pre-oxidized CNTs. Electrochemical impedance spectroscopy (EIS) further revealed a much faster electron transfer of Poly-TAA-Co-CNT samples compared with Poly-TAA-Co during CO_2RR (**Figure 5.6**)[23-26].
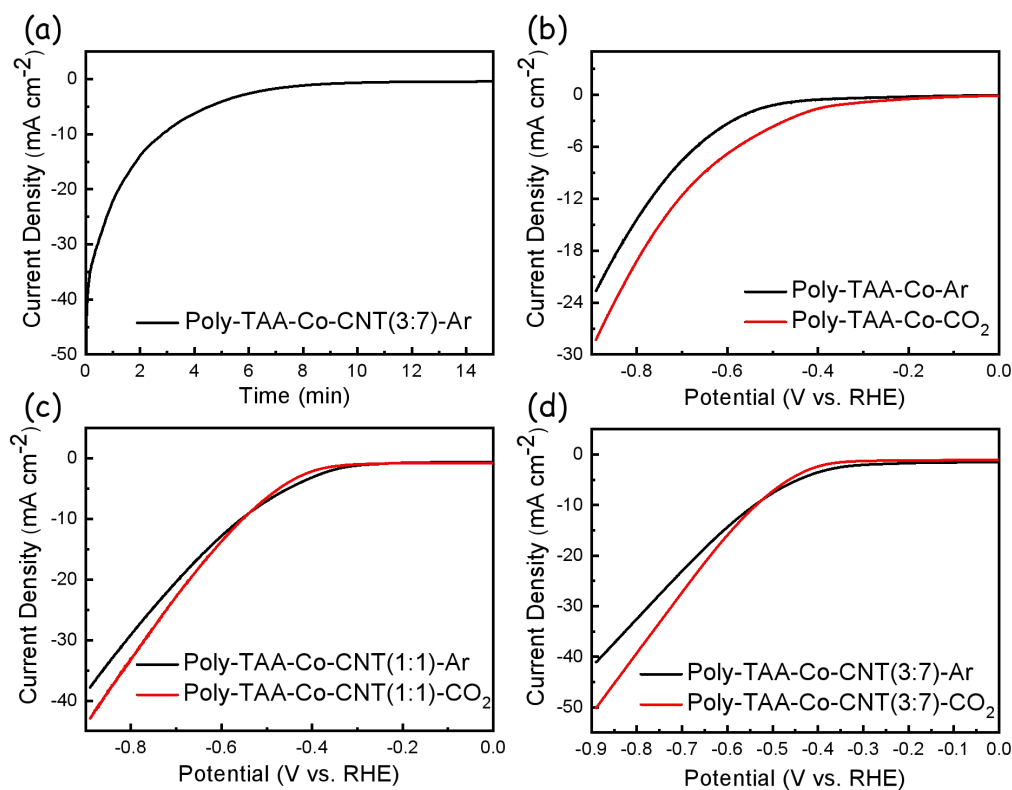
Figure 5.6. (a) Electrode current recorded during reduction of Poly-TAA-Co-CNT(3:7) at −0.30 V vs. RHE in 0.5 M KHCO$_3$ purged with Ar gas. Linear sweep voltammetry (LSV) comparison for (b) Poly-TAA-Co, (c) Poly-TAA-Co-CNT(1:1) and (d) Poly-TAA-Co-CNT(3:7) samples in Ar- and CO$_2$-saturated 0.5 M KHCO$_3$ solution.

The Faradaic efficiency (FE) for CO$_2$ conversion to CO (FE$_{CO}$) and H$_2$ (FE$_{H2}$), and the related current density were determined in the potential range from −0.40 to −0.70 V vs. RHE. **Figure 5.7b** shows the FE$_{CO}$ on these of the Poly-TAA-Co-based cathodes. The FE of bare CNTs can be found in **Figure 5.7b**.
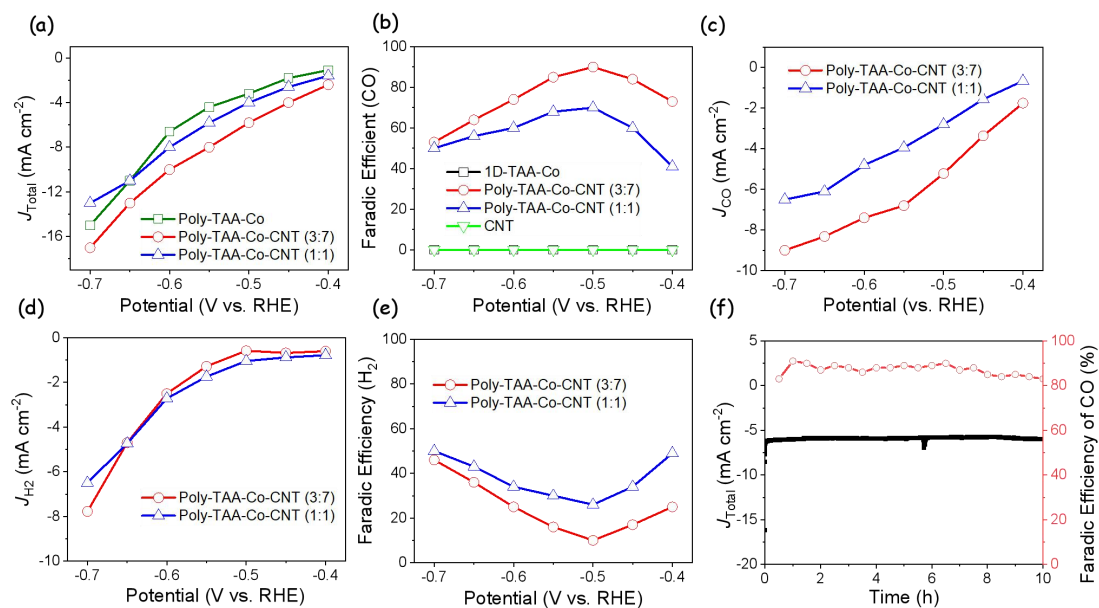
Figure 5.7. (a) Total current density, (b) FE of CO at various potentials, (c) current density for CO production, (d) FE of H_2 at various potentials, (e) current density for H_2 production on Poly-TAA-Co-CNT(1:1) and Poly-TAA-Co-CNT(3:7). (f) Stability test of Poly-TAA-Co-CNT(3:7) at −0.50 V vs. RHE.

For Poly-TAA-Co-CNT(3:7) samples, the CO_2RR to CO started at a potential as low as −0.40 V vs. RHE with a maximum FE_{CO} of 90 % at −0.50 V vs. RHE. This FE_{CO} is clearly above those obtained from Poly-TAA-Co-CNT(3:7) and Poly-TAA-Co-CNT(1:1) samples. Poly-TAA-Co-CNT(3:7) exhibits the highest current densities for CO formation among all the studied electrodes and in the whole range of applied potentials, with a maximum partial current density of −5.8 mA cm^{-2} at −0.50 V vs. RHE. As the potential changed to more negative values (from −0.55 to −0.70 V vs. RHE), the FE_{CO} of Poly-TAA-Co-CNT(1:1) and Poly-TAA-Co-CNT(3:7) gradually decreased and the competitive HER became the dominant reaction, as evidenced in the FE_{H2} and the partial H_2 current densities shown in **Figures 5.7d** and 5.**7e**, respectively. Tafel plots were obtained by calculating the logarithm of current density [log(jCO)] vs. the overpotential (η) to reveal the possible reaction pathway of electrochemical CO_2 reduction (**Figure 5.8a**). We obtained the plot in the linear part of low overpotentials ranging from −0.3 to −0.43 V and −0.28 to −0.38 V for Poly-TAA-Co-CNT(1:1) and Poly-TAA-Co-CNT(3:7), respectively. The Tafel slopes were calculated to be 25 mV dec^{-1} and 21 mV dec^{-1} for Poly-TAA-Co-CNT(1:1) and

Poly-TAA-Co-CNT(3:7), respectively, indicating that the possible rate-determining step is a single electron transfer to CO_2 to generate a $CO_2\bullet-$ intermediate [16, 38]. The EIS spectrum in **Figure 5.8b, c** also confirmed a faster electron transfer when the Poly-TAA-Co was loaded on the surface of CNTs.
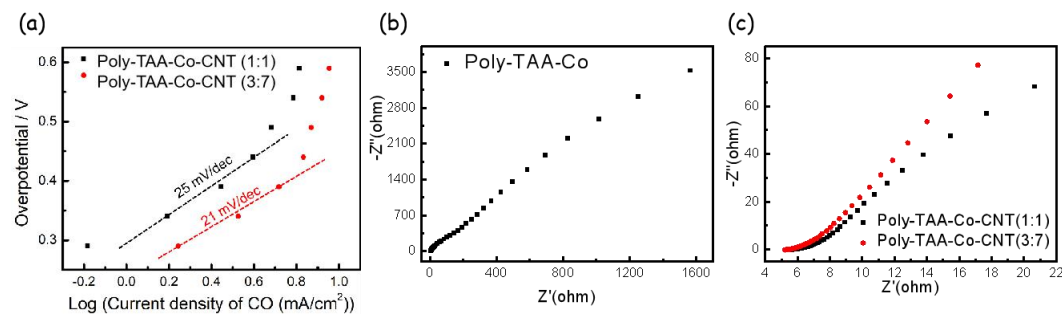
Figure 5.8. (a) Tafel plots (d) of Poly-TAA-Co-CNT (1:1), Poly-TAA-Co-CNT (3:7). Nyquist plots of the electrochemical impedance spectroscopy (EIS) data of (b) Poly-TAA-Co, (c) Poly-TAA-Co-CNT(1:1) and Poly-TAA-Co-CNT(3:7) electrodes after the activation process.

The electrochemical active surface area (ECSA) was determined from the electrochemical double-layer capacitance (C_{dl}) of the active materials. The C_{dl} of Poly-TAA-Co, Poly-TAA-Co-CNT(1:1) and Poly-TAA-Co-CNT (3:7) samples were obtained by CV at different scan rates, from the slope of $\Delta J = J_a - J_c$ against the scan rate (**Figure 5.9 a-c**), the slope which is twice of C_{dl} could be obtained. The C_{dl} of Poly-TAA-Co-CNT(1:1) and Poly-TAA-Co-CNT(3:7) samples are 14 mF cm^{-2} and 19 mF cm^{-2}, respectively, which are significantly larger values than the 3 mF cm^{-2} obtained from Poly-TAA-Co (**Figures 5.9 d-e**). Such different C_{dl} and thus of the related ECSA is a further indication of the higher CO_2RR catalytic activity of Poly-TAA-Co-CNT samples, and particularly of Poly-TAA-Co-CNT (3:7). In addition, the surface roughness factor (R_f) is calculated by taking the estimated ECSA and dividing by the geometric area of the electrode (1 cm^2). Generally, a constant capacitance is used in the same solution, therefore, R_f is linear with C_{dl}. The higher R_f obtained on the Poly-TAA-Co-CNT samples could significantly reduce the adhesion force between the electrode surface and gas bubbles, favoring the CO_2RR [25].
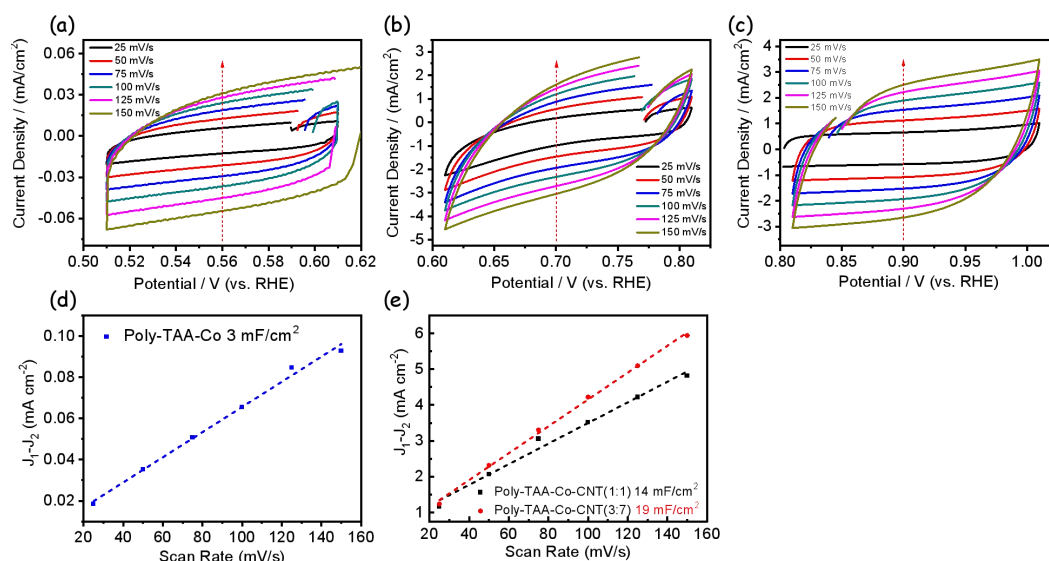
Figure 5.9. Cyclic voltammogram curves for (a) Poly-TAA-Co, (b) Poly-TAA-Co-CNT(1:1) and (c) Poly-TAA-Co-CNT(3:7). Plots of the current density vs. scan rate for (d) Poly-TAA-Co, (e) Poly-TAA-Co-CNT(1:1) and Poly-TAA-Co-CNT(3:7) electrodes.

To further demonstrate the key role of tetraanulene cobalt complex in the CO_2RR, we tested the catalytic activity of the samples after inactivating these sites by adding SCN^- ions, with high affinity to Co, into the solution. As shown in **Figure 5.10**, upon addition of 0.05M KSCN, a significant depression of the catalytic activity of Poly-TAA-Co, Poly-TAA-Co-CNT(1:1) and Poly-TAA-Co-CNT(3:7) was observed. This activity decrease is attributed to the blocking of tetraanulene cobalt sites by SCN^-.
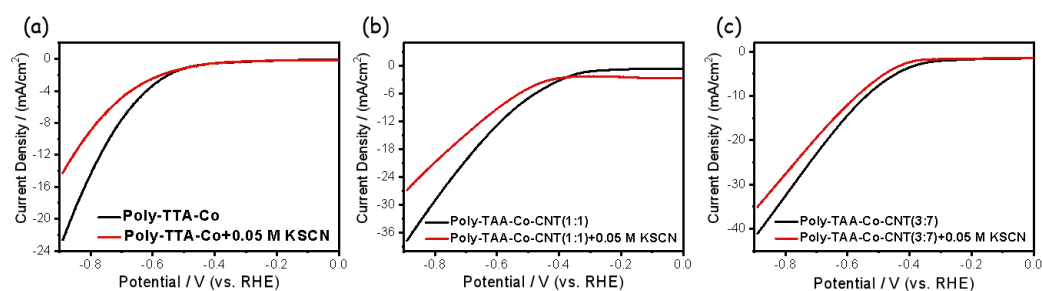
Figure 5.10. Linear sweep voltammetry curves of (a) Poly-TAA-Co, (b) Poly-TAA-Co-CNT(1:1) and (c) Poly-TAA-Co-CNT(3:7) with and without 0.05 M KSCN.

The current density at different HCO_3^- concentrations was measured at a

constant applied potential of −0.50 V vs. RHE to probe the role of HCO_3^- within the reaction. As revealed in **Figure 5.11a-b**, a plot of log (j_{CO}) versus log ($[HCO_3^-]$) showed a slope of 0.72, suggesting that the concentration of HCO_3^- plays a considerable role, influencing the efficiency of the conversion reaction of CO_2 to CO. As observed previously that the HCO_3^- not only acts as a pH buffer and proton donor, but also increases the concentration of CO_2 near the electrode surface [25,27,28].
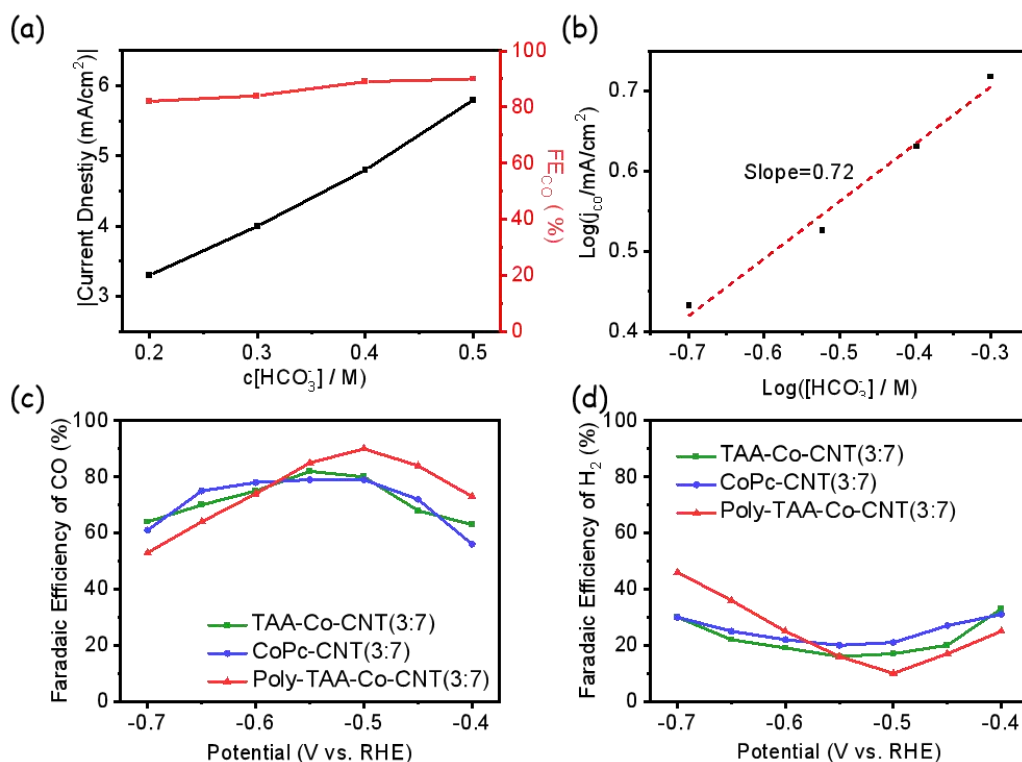
Figure 5.11. (a) Current density and FE of Poly-TAA-Co-CNT(3:7) at different KHCO$_3$ concentrations at a constant potential (−0.50 V vs. RHE). (b) Partial CO current density of Poly-TAA-Co-CNT(3:7) vs. KHCO$_3$ concentration at −0.50 V vs. RHE. FE of (c) CO and (d) H$_2$ at various potentials on TAA-Co-CNT(3:7), CoPc-CNT(3:7) and Poly-TAA-Co-CNT(3:7).

The CO$_2$RR performance of Poly-TAA-Co-CNT(3:7) was also compared with that of commercial cobalt phthalocyanine (CoPc) supported on CNTs (CoPc-CNT) at the same weight ratio (3:7) and with that of non-polymerized Co-TAA molecules supported on CNTs (Co-TAA-CNT(3:7)). As shown in **Figure 5.11c-d**, the maximum FE$_{CO}$ obtained from Poly-TAA-Co-CNT(3:7) was significantly higher than those obtained from CoPc-CNT(3:7) and Co-TAA-CNT(3:7). These results demonstrated

the higher activity of the Tetra[14]annulene cobalt active site in Poly-TAA-Co-CNT, and also the important role of the conjugated frameworks structure, which was proposed to favor the charge transfer during CO_2RR compared with Co-TAA.
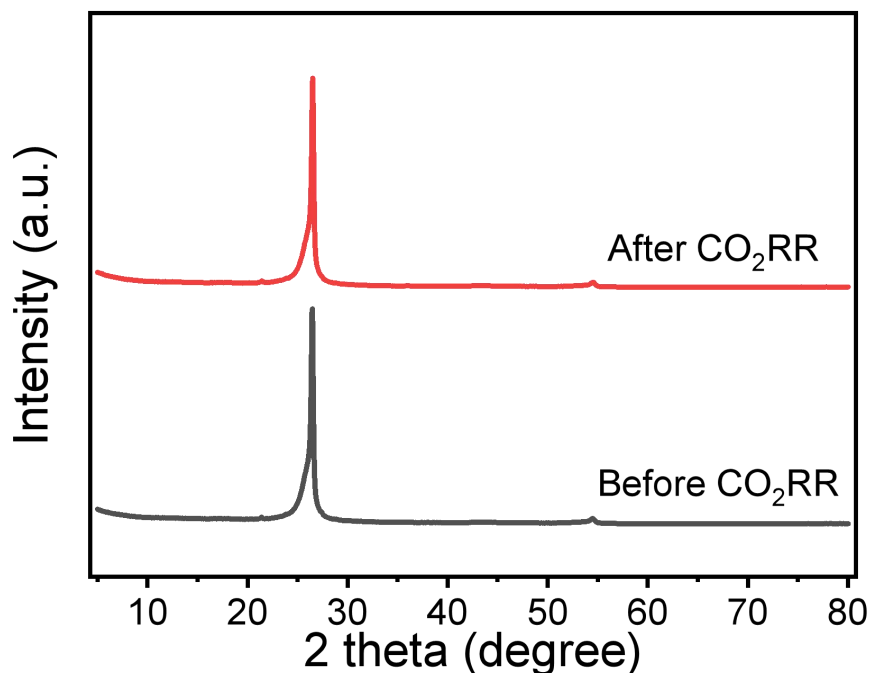
Figure 5.12. XRD patterns of Poly-TAA-Co-CNT loaded on carbon paper before and after CO_2RR.

As a first trial about the stability of the Poly-TAA-Co-CNT(3:7) electrocatalyst, it was evaluated through a 10 h durability test at a constant -0.50 V vs. RHE cathode potential. Outlet gases were analyzed every 30 min by GC to determine the FE_{CO}. The current density of Poly-TAA-Co-CNT(3:7) maintained a steady value of approximately -5.8 mA cm^{-2} with no significant decay (**Figure 5.7f**) during the 10 h test. Besides, the corresponding FE_{CO} just slightly decreased from 90 % to 83 % after the 10 h stability test. From the measurement of the XRD pattern of the electrocatalysts before and after the CO_2RR stability test, no additional diffraction peak was observed, indicating excellent structural stability under CO_2RR conditions (**Figure 5.12**).

5.3.3 DFT Calculation

To further understand the high catalytic activity of the cobalt active site in Poly-TAA-Co for CO_2RR, DFT calculations were conducted. We particularly analyzed the Kohn-Sham molecular orbital of CoPc and the structure unit namely Co-TAA of Poly-TAA-Co (**Figure 5.13a-b**). The energy of the lowest unoccupied molecular orbital (LUMO) of Co-TAA is -5.97 eV, which is below that of the CoPc molecule, -4.95 eV. The lower reduction potential of Co-TAA indicates that it is easier for Co-TAA to accept the charge transfer from the electrode to promote the CO_2RR.
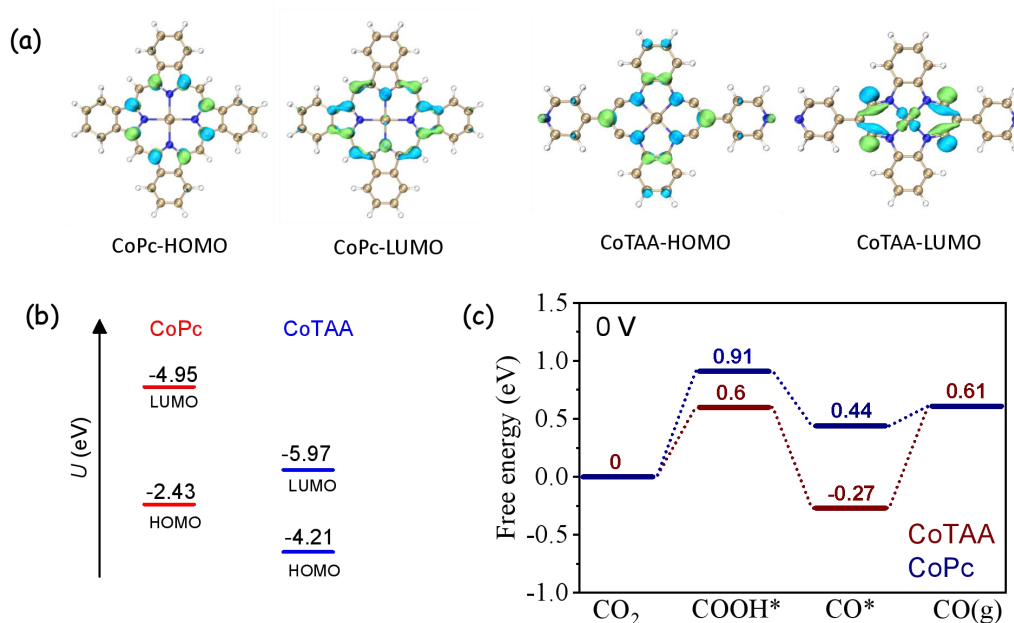
Figure 5.13. DFT calculation results. (a). Calculated energy diagrams for CO_2 to CO conversion on CoPc and Co-TAA molecule, respectively. (b-c). Calculated electron density distribution of the highest occupied molecular orbital (HOMO) and lowest unoccupied molecular orbital (LUMO) levels of CoPc and Co-TAA.

The Gibbs free energy diagram of the CO_2RR for CoPc and Co-TAA are shown in **Figure 5.13c**. The rate-determining step (RDS) for CO_2RR is the adsorption of CO_2 on the cobalt center to form *COOH by a proton-couple electron transfer reaction. At 0 V, the free energy of RDS for Co-TAA is 0.6 eV, which is lower than the 0.91 eV obtained for CoPc. Furthermore, under -0.5 V (**Figure 5.14**), the free energy of RDS for Co-TAA (0.1 eV) is still significantly lower than that of CoPc (0.41 eV). These DFT results are in good agreement with the experimental data.
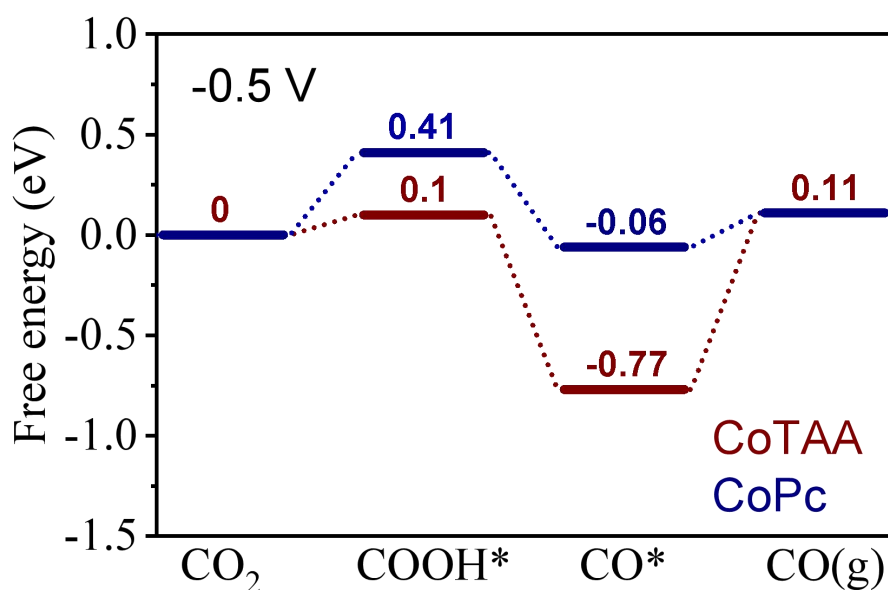
Figure 5.14. Calculated energy diagrams for CO_2 to CO at -0.5 V conversion on CoPc and CoTAA molecule, respectively.

5.4 Conclusions

We have reported for the first time a synthetic route to obtain new π-d conjugated cobalt building blocks based on Tetraaza[14]annulene organic framework by a non-template method. Upon loading the cobalt-based macromolecule complex on the conductive carbon nanotube, the catalyst showed an excellent performance toward electrocatalytic CO_2 reduction, with a FE_{CO} of 90% at a low overpotential (390 mV) and a stable performance (>10 h). DFT simulations revealed the Co-TAA active sites to have the lowest activation energy for CO_2RR, well below that of commercial CoPc. Our results not only demonstrate that the non-template synthesis method can be used to synthesize tetra[14]annulene organic frameworks, but also provide a new strategy to design macrocycle-based covalent metal organic framework for efficient CO_2RR and opens the way to use this type of materials for other applications.

References

[1] A. R. Cutler, D. Dolphin, *Journal of Coordination Chemistry*, 1976, 6, 59-61.

[2] C. W. Marvin, G. Guy, L. G. Virgil, *Inorg. Chem.*, 1977, 16, 305-310.

[3] M. Philip, *Chem. Soc. Rev.*, 1998, 27, 105-115.

[4] F. A. Cotton, C. Joanna, *Polyhedron*, 9 (1990), 2553.

[5] A. M. Whyte, Y. Shuku, G. S. Nichol, M. M. Matsushita, K. Awaga, N. Robertson, *Journal of Materials Chemistry*, 2012, 22, 17967-17975.

[6] Z. Liang, M. Damjanovic, M. Kamila, G. Cosquer, B. K. Breedlove, M. Enders, M. Yamashita, *Inorg. Chem*., 2017, 56, 6512-6521.

[7] A. Chirila, B. Gopal Das, N. D. Paul, B. de Bruin, *ChemCatChem*, 2017, 9, 1413-1421.

[8] A. Q. Ramle, H. Khaledi, A. H. Hashim, M. A. Mingsukang, A. K. Mohd Arof, H. M. Ali, W. J. Basirun, *Dyes and Pigments*, 2019, 164, 112-118.

[9] Y. Jiang, I. Oh, S. H. Joo, O. Buyukcakir, X. Chen, S. H. Lee, M. Huang, W. K. Seong, S. K. Kwak, J. W. Yoo, R. S. Ruoff, *J. Am. Chem. Soc.*, 2019, 141, 16884-16893.

[10] T. Zhang, X. Han, H. Liu, M. Biset-Peiró, X. Zhang, P. Tan, P. Tang, L. Zheng, B. Yang, J. R.Morante, J. Arbiol, *Energy & Environmental Science*, 2021, Accepted Manuscript, DOI: 10.1039/D1EE01592C.

[11] Z. Gu, H. Shen, Z. Chen, Y. Yang, C. Yang,Y. Ji, Y.Wang, C. Zhu, J. Liu, J. Li, T.-K. Sham, X. Xu, G. Zheng, *Joule*, 2021, 5, 1-12.

[12] Z.-Z. Wu, F.-Y. Gao, M.-R. Gao, *Energy & Environmental Science*, 2021, 14, 1121-1139.

[13] S. Lin, C. S. Diercks, Y. B. Zhang, N. Kornienko, E. M. Nichols, Y. Zhao, A. R. Paris, D. Kim, P. Yang, OM. Yaghi, C. J. Chang, *Science*, 2015, 11, 1208-1213.

[14] Y. Wu, Z. Jiang, X. Lu, et al., *Nature*, 2019, 575, 639-642.

[15] Z. Liang, H. Y. Wang, H. Zheng, W. Zhang, R. Cao, *Chem. Soc. Rev*., 2021, 50, 2540-2581.

[16] N. Han, Y. Wang, L. Ma, J. Wen, J. Li, H. Zheng, K. Nie, X. Wang, F. Zhao,   Y.

Li, J. Fan, J. Zhong, T. Wu, D. J. Miller, J. Lu, S-T. Lee, Y. Li, *Chem*, 2017, 3, 652-664.

[17] X. Zhang, Y. Wang, M. Gu, M. Wang, Z. Zhang, W. Pan, Z. Jiang, H. Zheng, M. Lucero, H. Wang, G. E. Sterbinsky, Q. Ma, Y.-G. Wang, Z. Feng, J. Li, H. Dai, Y. Liang, *Nature Energy*, 2020, 5, 684-692.

[18] X. Zhang, Z. Wu, X. Zhang, L. Li, Y. Li, H. Xu, X. Li, X. Yu, Z. Zhang, Y. Liang, H. Wang, *Nat. Commun.*, 2017, 8, 14675.

[19] J. Su, J.-J. Zhang, J. Chen, Y. Song, L. Huang, M. Zhu, B. I. Yakobson, B. Z. Tang, R. Ye, *Energy & Environmental Science*, 2021, 14, 483-492.

[20] M. Zhu, R. Ye, K. Jin, N. Lazouski, K. Manthiram, *ACS Energy Letters*, 2018, 3, 1381-1386.

[21] Z. Jiang, Y. Wang, X. Zhang, H. Zheng, X. Wang, Y. Liang, *Nano Research*, 2019, 12, 2330-2334.

[22] H. Khaledi, M. M. Olmstead, H. M. Ali, N. F. Thomas, *Inorg. Chem.*, 2013, 52, 1926-1941.

[23] O. S.Bushuyev, P. De Luna, C. T. Dinh, L.Tao, G. Saur, J. van de Lagemaat, S. O. Kelley, Sargent, E. H. *Joule*, 2 (2018), 825.

[24] W. Ren, X. Tan, W. Yang, C. Jia, S. Xu, K. Wang, S. C. Smith, C. Zhao, *Angew. Chem. Int. Ed.*, 58 (2019), 6972,

[25] C. Zhao, Y. Wang, Z. Li, W. Chen, Q. Xu, D. He, D. Xi, Q. Zhang, T. Yuan, Y. Qu, J. Yang, F. Zhou, Z. Yang, X. Wang, J. Wang, J. Luo, Y. Li, H. Duan, Y. Wu, Y. Li, *Joule*, 2019, 3, 584.

[26] C. F. Wen, F. Mao, Y. Liu, X. Y. Zhang, H. Q. Fu, L. R.Zheng, P. F. Liu, H. G. Yang, *ACS Catal.*, 2020, 10, 1086.

[27] J. Gu, C.-S. Hsu, L. Bai, H. M. Chen, X. Hu, *Science*, 2019, 364, 1091.

[28] T. Li, C. Yang, J.-L. Luo, G. Zheng, *ACS Catal.*, 2019, 9, 10440.

[29] H. J. Zhu, M. Lu, Y. R. Wang, et al., *Nat. Commun.*, 11 (2020), 497.

[30] Y. Hu, N. Goodeal, Y. Chen, A. M. Ganose, R. G. Palgrave, H. Bronstein, M. O. Blunt, *Chem. Commun.*, 2016, 52, 9941.

[31] S. Yamazaki, M. Asahi, Z. Siroma, T. Ioroi, *ChemCatChem*, 2020, 12,

2717-2720.

[32] H. Yang, L. Shang, Q. Zhang, R. Shi, G. I. Waterhouse, L. Gu, T. Zhang, *Nat. Commun.*, 2019, 10, 4585.

[33] Y. Chen, C. W. Li, M. W. Kanan, *J. Am. Chem. Soc.*, 2012, 134 (2012), 19969-19972.

[34] X. Huang, P. Sheng, Z. Tu, F. Zhang, J. Wang, H. Geng, Y. Zou, C. Di, Y. Yi, Y. Sun, W. Xu, D. Zhu, *Nat. Commun.*, 2015, 6, 7408.

[35] Y. Chen, M. Tang, Y. Wu, X. Su, X. Li, S. Xu, S. Zhuo, J. Ma, D. Yuan, C. Wang, W. Hu, *Angew. Chem. Int. Ed.*, 131 (2019), 14873-14881.

[36] L. Wang, Y. Ni, X. Hou, L. Chen, F. Li, J. Chen, *Angew. Chem. Int. Ed.*, 2020, 59, 22126-22131.

[37] K. Fan, C. Zhang, Y. Chen, Y. Wu, C. Wang, *Chem*, 2021, 7, 1224-1243.

[38] Y. Ni, L. Lin, Y. Shang, L. Luo, L. Wang, Y. Lu, Y. Li, Z. Yan, K. Zhang, F. Cheng, J. Chen, *Angew. Chem. Int. Ed.*, 2021, 60, 16937-16941.

[39] J. Hao, H. Zhu, Y. Li, P. Liu, S. Lu, F. Duan, W. Dong, Y. Lu, T. Liu, M. Du, *Chemical Engineering Journal*, 2020, 404, 126523.

[40] R. Shi, J. Guo, X. Zhang, G. I. N. Waterhouse, Z. Han, Y. Zhao, L. Shang, C. Zhou, L. Jiang, T. Zhang, *Nat. Commun.*, 2020, 11, 3028.

[41] Y.-R. Wang, R.-X. Yang, Y. Chen, G.-K. Gao, Y.-J. Wang, S.-L. Li, Y. Q. Lan, *Science Bulletin*, 2020, 65, 1635-1642.

[42] D. L. T. Nguyen, Y. Kim, Y.J. Hwang, D.H. Won, *Carbon Energy.*, 2020, 2, 72-98.

[43] H. Yang, L. Shang, Q. Zhang, R. Shi, G. I. Waterhouse, L. Gu, T. Zhang, *Nat. Commun.*, 2019, 10, 4585.

[44] Y. Yao, Y. Zhu, C. Pan, C. Wang, S. Hu, W. Xiao, X. Chi, Y. Fang, J. Yang, H. Deng, S. Xiao, J. Li, Z. Luo, Y. Guo, *J. Am. Chem. Soc.*, 2021, 143, 8720-8730 (2021).

[45] Kim, D.; Resasco, J.; Yu, Y.; Asiri, A. M.; Yang, P, *Nat. Commun.*, 2014, 5, 4948.

[46] S. Gao, Y. Lin, X. Jiao, Y. Sun, Q Luo, W Zhang, D. Li, J. Yang, Y Xie, *Nature*, 2016, 529, 68-71.

[47] T. Zheng, K. Jiang, N. Ta, Y. Hu, J. Zeng, J. Liu, H. Wang, *Joule*, 2019, 3, 265-278.

[48] J. Pei, T. Wang, R. Sui, X. Zhang, D. Zhou, F. Qin, X. Zhao, Q. Liu, W. Yan, J. Dong, L. Zheng, A. Li, J. Mao, W. Zhu, W. Chen, Z. Zhuang, *Energy & Environmental Science*, 2021, 14, 3019-3028.

[49] B. Ravel, M. Newville, *J. Synchrotron Rad*. 2005, 12, 537-541.

[50] M. Newville, *J. Synchrotron Rad*., 2001, 8, 322-324.

[51] J. J. Rehr, J. Mustre de Leon, S. I. Zabinsky, R. C. Albers, *J. Am. Chem. Soc.*, 1991, 113, 5135-5140.

[52] H. Hu, J. Z. Ou, X. Xu, Y. Lin, Y. Zhang, H. Zhao, D. Chen, M. He, Y. Huang, L. Deng, *Chemical Engineering Journal*, 2021, 425, 130587.

[53] W. Ye, X. Guo, T. Ma, *Chemical Engineering Journal*, 2012, 414, 128825.

[54] G. Kresse, *Comput. Mater. Sci.* **1996**, *6*, 15-50.

[55] G. Kresse, J. Furthmüller, *Phys. Rev. B: Condens. Matter*. **1996**, *54*, 11169.

[56] C. Adamo, V. Barone, *J. Chem. Phys*. **1999**, *110*, 6158-6170.

[57] P. C. Hariharan, J. A. Pople, *Teor. Chim. Acta* **1973**, *28*, 213-222.

[58] M. S. Gordon, Chem. Phys. Lett. 1980, *76*, 163-168 (1980).

[59 R. Binning, L. Curtiss, *J. Comput. Chem*. **1990**, *11*, 1206-1216.

[60] D. Andrae, U. Häußermann, M. Dolg, H. Stoll, H. Preuß, Teor. Chim. Acta **1990**, *77*, 123-141.

[61] S. Grimme, S. Ehrlich, & L. Goerigk, *J. Comput. Chem*. **2011**, *32*, 1456-1465.

[62] M. J. Frisch, et al. *Gaussian 16* (Gaussian 2016)

[63] H. Ryu, Y. Mulyana, In-H. Park, J. Kim, L. F. Lindoy, S. S. Lee, *CrystEngComm* **2015**,17, 5717-5724.

Chapter 6

Conclusions and Outlook

6.1 General Conclusions

In the present thesis work, I have designed and prepared a series of porous two-dimensional covalent organic frameworks-based atomically dispersed metal atom catalysts with efficient performance in the area of lithium-sulfur batteries, electrochemical CO_2 reduction and electrochemical alcohol oxidation. In more details, as for the lithium-sulfur batteries, the I introduced catalyst based on the iron atoms were atomically dispersed in a porous two-dimensional organic material namely Fe/C_2N catalyst, the materials was probed to be an excellent catalytic host material in the cathode of Li-S cells. I have also developed a strategy to tune the electronic structure of nickel based atomically dispersed catalysts through molecular engineering to enhance the electrocatalytic performance for CO_2 reduction and alcohol oxidation. Additionally, I could also design and synthesize a novel π-d conjugated cobalt tetraaza[14]annulene organic framework for efficient electrocatalytic CO_2 reduction. The main conclusions of this dissertation are presented in the following:

1) A novel catalyst based on atomically dispersed iron in a 2D organic material (Fe/C_2N) has been shown as an efficient sulfur host material for LSBs. A combination of XPS, XANES, EXAFS, atomic resolution HAADF-AC-STEM and DFT calculations confirmed that the synthesized Fe/C_2N presented atomically dispersed iron. Iron atoms, which were in some cases found to be grouped in pairs, are coordinated to nitrogen in the C_2N pores. These atomically dispersed Fe atoms not only improve the material polarity to immobilize the soluble polysulfides, but also act as catalytic active sites to promote the reaction kinetics between sulfur, polysulfide and Li_2S. As a result, S@Fe/C_2N-baed cathodes exhibit excellent electrochemical performance, showing a high capacity and a remarkable rate performance at different current densities, while keeping outstanding cycling stability. This work demonstrates that atomically dispersed metal atoms within the unique C_2N structure can help to achieve excellent electrochemical performance. This strategy can be utilized to engineer active materials not only for LSBs, but also for other energy conversion and storage systems.

2) I have detailed the synthesis and characteristics of an atomically dispersed nickel catalyst consisting of NiN_2O_2 active sites within a 2D organic framework produced under mild and controllable reaction conditions. A molecular engineering strategy based on modifying the edge ligand environment by introducing a carbonyl group was developed to tune the electrocatalytic reduction of CO_2. The obtained Ni-O-SA-CNT composites exhibited excellent activity and selectivity (27 % FE at -0.9 V vs RHE) toward the conversion of CO_2 to methanol due to the synergistic effect of the carbonyl group in the ligand and the nickel active sites. This work not only provided the best nickel-based catalysts so far reported for the electrocatalytic conversion of CO_2 to methanol, but also demonstrated a novel strategy to design and engineer efficient electrocatalysts to convert CO_2 to valuable chemicals through modulating the ligand structures.

3) A facile molecular engineering strategy to tune the ligand coordination environments of nickel ion centers was successfully achieved. Through this strategy, carbonyl (C=O) groups were introduced and proved to decisively contribute to an efficient alcohol electrooxidation in alkaline solution. EXAFS and XANES analyses confirmed the Ni salophen unit structure, NiN_2O_2, within the 2D organic frameworks. The atomically dispersed nickel within a framework containing the carbonyl groups displayed outstanding MOR, EOR and BOR performance. DFT calculations suggested that the introduction of the C=O functional groups favors the absorption and activation of methanol molecules, which is at the origin of the improved MOR observed. This work not only offers novel materials and a promising strategy to design more efficient atomically dispersed nickel-based catalysts for alcohol oxidation, but it could also benefit other research fields related to electrochemical-organic synthesis, energy conversion and storage.

4) I reported the first synthetic route to obtain new π-d conjugated cobalt building blocks based on a Tetraaza[14]annulene organic framework by a non-template method could be reported for the first time. Upon loading the cobalt-based macromolecule complex on the conductive carbon nanotube, the catalyst showed an excellent performance toward electrocatalytic CO_2 reduction, with a FE_{CO} of 90% at a low

overpotential (390 mV) and a stable performance (>10 h). DFT calculations revealed the Co-TAA active sites to have the lowest activation energy for CO_2RR, well below that of commercial CoPc. With these results,I did not only demonstrate that the non-template synthesis method can be used to synthesize tetra[14]annulene organic frameworks, but I also provided a new strategy to design macrocycle-based covalent metal organic frameworks for efficient CO_2RR opening the way to use this type of materials for other applications.

Overall, I developed different novel atomically dispersed metal atom catalysts have been developed for electrocatalysis applications. Additionally, I also displayed a novel tuning strategy between the active sites and the ligand environment could be displayed, which will inspire the future design of new efficient catalysts for applications in different fields.

6.2 Outlook

Due to its 100% metal atom utilization, quantum effect and unsaturated coordination environment, atomically dispersed catalysts show great potential value in catalytic processes, such as lithium-sulfur batteries, electrocatalytic small molecule conversion, etc. The bridge between homogeneous catalysis and heterogeneous catalysis simultaneously plays a very important role in green and low-cost catalysts. Over the past decade, although many important progress has been made in atomically dispersed catalysts, many challenges still remain. Here the outlooks are listed as follow：

1) Green and large-scale synthesis method of atomically dispersed metal atom catalysts.

Currently, the large-scale synthesis of single-atom catalysts with specific coordination structures still faces many challenges. In addition, the metal loading of single-atom catalysts has also a great influence on the overall catalytic performance. Besides, most of the atomically dispersed metal atom catalysts are prepared from high temperature annealing methods, but the surface energy of a single metal atom is very high. Because of these reasons, it is difficult to obtain atomically dispersed catalysts with high loadings during the preparation process. Therefore, it is necessary to find an efficient and green synthesis method to realize the controllable synthesis of ADMACs with high loading for the industrial application.

2) Precise control of the distance between active sites

When the distance between two catalytic sites is reduced to the atomic scale, the synergistic effect between the catalytic sites will greatly improve the intrinsic activity of the catalyst. Therefore, if the distance between the sites of the active center can be precisely controlled to achieve the synergistic effect of neighboring atoms, it is not only beneficial to improve the catalytic performance, but it is also expected to realize a specific catalytic reaction process.

3) Precise control of the coordination structure

The precise control of the coordination environment and coordination number of metal atoms is very important toward catalysis, but this control still faces a great

challenge. Both, reactivity and selectivity are related to the coordination structure of the metal atom active sites. Therefore, the precise control and tuning of the coordination environment and number of atomically dispersed metal atoms will be very critical for their further applications in catalysis and energy. Most preparation methods of atomically dispersed metal atom catalysts are using pyrolysis, which makes it very hard to control the active sites' coordination. So, it is very interesting to develop new types of atomically dispersed metal atom catalysts with controllable coordination structures, such as in MOFs, COFs and molecular-based heterogeneous catalysts.

4) Accurate tuning of the ligand environment

So far, few reports are discussing the influence of the ligand microenvironment around the active center on catalysis. In fact, the ligand microenvironment is also an important factor toward catalysis, not only by regulating the electronic structure of the active centers through the electron withdrawing or electron donating effect, but also by affecting the catalytic process, such as interacting with the reaction intermediate. Therefore, it is worthwhile to study the effect of the ligand microenvironment on the catalytic performance.

5) Advanced techniques for revealing the reaction mechanisms.

Currently, although the characterization techniques used for the structural characterization of SACs such as aberration-corrected HAADF-STEM and XAS spectroscopy are used to confirm the atomically dispersed state, it is still a challenge to reveal the slight coordination structure changes during the catalytic process. More powerful characterization technologies or more advanced analytic methods are necessary to be developed to monitor *in-situ* catalytic processes to understand the reaction mechanisms of atomically dispersed catalysts.

List of publications during PhD period:

1. **Zhifu Liang**, et al. Atomically dispersed Fe in a C₂N Based Catalyst as a Sulfur Host for Efficient Lithium-Sulfur Batteries. *Advanced Energy Materials* 2021, 11, 2003507.

2. **Zhifu Liang**, et al. Molecular Engineering to Tune the Ligand Environment of Atomically Dispersed Nickel for Efficient Alcohol Electrochemical Oxidation. *Advanced Functional Materials* 2021, 31, 2106349.

3. D. Yang+, **Zhifu Liang**+, et al. A High Conductivity One-Dimensional π-d Conjugated Metal-Organic Framework with Efficient Polysulfide Trapping-Diffusion-Catalysis in Lithium-Sulfur Batteries. (**Co-First author**) *Advanced Materials* (**Accepted, DOI: 10.1002/adma.202108835**).

4. **Zhifu Liang**, et al. Non-Template Synthesis of a Novel Cobalt Tetraaza [14] Annulene Macrocyclic Polymer as Efficient Electrocatalyst for CO₂ Reduction. (*Under review*)

5. **Zhifu Liang**; et al. Molecular Engineering to Introduce Carbonyl Between Nickel Salophen Active Sites to Enhance Electrochemical CO2 Reduction to Methanol. (*Under review*)

6. D Yang, **Zhifu Liang**, et al. NbSe2 Meets C2N: A 2D-2D Heterostructure Catalysts as Multifunctional Polysulfide Mediator in Ultra-Long-Life Lithium– Sulfur Batteries. *Advanced Energy Materials* 2021, 2101250.

7. O. B. Ayodele, R. Cai, J. Wang, J. Wang, Y. Ziouani, **Zhifu Liang**, et al. Synergistic Computational-experimental Discovery of Highly Selective PtCu Nanocluster Catalysts for Acetylene Semihydrogenation. *ACS Catalysis* 2020, 10, 451-457.

8. Xiang Wang, Congcong Xing, **Zhifu Liang**, Pablo Guardia, Xu Han, Yong Zuo, Jordi Llorca, Jordi Arbiol, Junshan Li, Andreu Cabot. 8.Activating the lattice oxygen oxidation mechanism in amorphous molybdenum cobalt oxide nanosheets for water oxidation. *J. Mater. Chem. A*, 2022, DOI: 10.1039/D1TA09657E

9. D Yang, C, Zhang, JJ Biendicho, X Han, **Zhifu Liang**, et al. *ACS Nano* 2020, 14

(11), 15492-15504.